Technische Universität München

Fakultät für Elektrotechnik und Informationstechnik

Development of Laser Diode Excitation Source for Optoacoustic Imaging and Sensing

Antonios Stylogiannis

Vollständiger Abdruck der von der Fakultät für Elektrotechnik und Informationstechnik der Technischen Universität München zur Erlangung des akademischen Grades eines

Doktors der Naturwissenschaften (Dr. rer. nat.)

genehmigten Disseration.

Vorsitzender: Prof. Dr. sc.techn. Andreas Herkersdorf

Prüfer der Disseration:

1. Prof. Dr. Vasilis Ntziachristos
2. Prof. Dr. techn. Reinhard Kienberger
3. Prof. Dr.-Ing. Christian Jirauschek

Die Dissertation wurde am 19.04.2021 bei der Technischen Universität München eingereicht und durch die Fakultät für Elektrotechnik und Informationstechnik am 06.02.2022 angenommen.

Abstract

Optoacoustic (OA) imaging and sensing offers many advantages compared to other biomedical imaging methods. OA is a non-invasive modality that uses non-ionizing radiation, offers optical absorption contrast and by detecting the generated Ultrasound (US) waves achieves spatial resolution at higher imaging depths compared to optical imaging. However, current conventional OA lasers present large form factors, expenses and complexity impeding the wide-spread use of OA imaging. Therefore, a lot of attention has been drawn in the last years in developing semiconductor excitation sources for OA imaging and sensing, either Laser Diodes (LDs) or Light Emitting Diodes (LEDs), due to their low-cost of production and small size.

In this thesis, we investigated whether Continuous Wave Laser Diodes (CW-LDs), which are available in the visible and NIR range, can be promising OA light sources when overdriven. We found that it is possible to drive the CW-LDs with a peak current $\gtrsim$ 40-fold higher than its CW absolute maximum value, for only a very short amount of time ($\lesssim$10 ns), with the CW-LDs providing up to 27-fold higher peak power compared to their continuous wave (CW) absolute maximum value, without getting damaged or destroyed, outperforming many Pulsed Laser Diodes and Light-Emitting-Diodes.

Using the overdriven CW-LDs we developed three different OA systems that can be used in various applications in biology, medicine and the environment. We developed a four wavelength Raster Scanning Optoacoustic Mesoscopy system that generated high quality, high spatial resolution and SNR, multi-spectral OA images of a mouse ear and human skin. The system was also used to perform vessel dynamics and monitor relative oxygenation changes and dye diffusion at multiple wavelengths in a mouse ear in-vivo. In order to functionally maximize the overdriven CW-LDs, we removed the stage scanning and developed a single point Spectroscopic OA Sensor for non-invasive measurements of local vascular tissue oxygenations in real-time. Additionally, we used the overdriven CW-LDs and a very sensitive and low-cost US detector, a Quartz Tuning Fork (QTF), to develop a compact and low-cost OA sensor for Black Carbon monitoring in Internal Combustion Engines or the environment. The sensor's novel ellipsoidal chamber design refocuses the OA wave at a distance from its source and enables high SNR detection, high sensor stability, resilience to vibrations and is expected to protect the QTF and the sensitive optical components from contamination from the exhaust gas.

The work in this thesis demonstrates that overdriven CW-LDs can be a viable and attractive alternative to conventional OA lasers and other semiconductor light sources, such as P-LDs and LEDs. Overdriven CW-LDs can play a central role in the near future in the development of low-cost and compact OA systems for various applications in biology, medicine and the environment.

Zusamenfassung

Optoakustische (OA) Bildgebung und Messungen bieten viele Vorteile im Vergleich zu anderen Biomedizinischen Bildgebungsmethoden. OA ist ein nicht-invasives Verfahren, welches mit nicht-ionisierender Strahlung arbeitet und dabei Kontrast durch optische Absorption erzeugt. Zudem wird durch die Detektion von generiertem Ultraschall (US) eine räumliche Auflösung auch für größere Bildgebungstiefen im Vergleich zur Optischen Bildgebung erreicht. Jedoch limitieren Formfaktor, Kosten und Komplexität von aktuellen konventionellen OA Laser eine weitere Verbreitung von OA Bildgebung. Dementsprechend wurde in den letzten Jahren der Entwicklung von Halbleiter-Anregungsquellen, wie Laser Dioden (LDs) und Licht emittierenden Dioden (LEDs), für die OA Bildgebung aufgrund ihrer günstigen Herstellung und kompakten Größe viel Aufmerksamkeit zugewandt.

Im Rahmen dieser Doktorarbeit haben wir untersucht, ob übersteuerte Dauerstrichlaserdioden (CW-LDs), welche im visuellen und nahinfraroten Spektrum verfügbar sind, eine vielversprechende OA Lichtquelle seien können. Im Zuge dessen haben wir herausgefunden, dass es möglich ist CW-LDs mit einem Spitzenstrom von über dem 40-fachen des zugehörigen absoluten Dauerstrich Maximum für nur eine sehr kurze Zeit ($\lesssim$10 ns) zu betreiben. Hierbei erreichen die CW-LDs Spitzenleistungen, welche bis zu 27-mal höher liegen als die zugehörigen Dauerstrich-Maximalwerte, ohne dabei beschädigt oder zerstört zu werden. Schlussendlich übertreffen sie damit viele gepulste Laserdioden und LEDs.

Wir haben drei verschiedene OA System mit implementierten übersteuerten CW-LDs realisiert, welche Anwendung in den Bereichen der Biologie, Medizin und Umweltforschung finden. Unter anderem wurde ein OA Rasterscan-Mesoskopiesystem mit vier Wellenlängen entwickelt, das in der Lage ist multispektrale OA Bilder von Mausohren und humaner Haut in hoher Qualität und mit hoher Auflösung und SNR zu generieren. Das System konnte auch verwendet werden, um die Dynamik in Gefäßen zu analysieren und relative Veränderungen der Oxygenierung und Farbstoffdiffusion in mehreren Wellenlängen in einem in-vivo Mausohr zu beobachten. Um die Funktionalität der übersteuerten CW-LDs zu maximieren, haben wir die Scanplattform entfernt und einen spektralen OA Einzelpunktsensor für nicht invasive Echtzeitmessungen von lokaler vaskulärer Gewebe-Oxygenierung entwickelt. Zusätzlich haben wir mit Hilfe der übersteuerten CW-LDs und einem hoch sensitiven und preiswerten US-Sensor, einer Quarzstimmgabel (QTF), einen kompakten und kostengünstigen OA Sensor für die Überwachung von Rußschwarz in Verbrennungsmotoren und der Umwelt verwirklicht. Der Sensor besitzt ein neuartiges elliptisches Kammerdesign, welches die OA Welle in einem Abstand von ihrer Quelle re-fokussiert und damit die Detektion mit hohem SNR, hoher Sensorstabilität und Widerstandsfähigkeit gegen Vibrationen ermöglicht. Zusätzlich wird so die QTF und sensitive optischen Komponenten von Abgasverschmutzungen geschützt.

Diese Doktorarbeit weist nach, dass übersteuerte CW-LDs eine praktikable und attraktive Alternative zu konventionellen OA Laser und anderen Halbleiterlichtquellen, wie P-LDs und LEDs, sein können. Übersteuerte CW-LDs könnten so in naher Zukunft eine zentrale Rolle in der Entwicklung von preiswerten und kompakten OA Systemen für verschiedene Anwendung in den Bereichen der Biologie, Medizin und Umwelt spielen.

Acknowledgments

I know that it is not possible to mention in this section everyone that has assisted me during the last 5 years that I spent conducting the work presented herein. This is not possible because doing a PhD is not only the research and scientific part, but also me further developing as a person, continuously learning how life works and everybody that I had an interaction with has contributed to this. However, I will try to mention the people that played the most important role and assisted me, one way or another, in my PhD. I want to start with acknowledging the help of Dimitris Karavidas and Dr. Nikos Deliolanis who proposed me to Prof. Dr. Vasilis Ntziachristos.

How could I not thank Prof. Dr. Vasilis Ntziachristos that gave me the opportunity to work in this institute, despite the fact that my previous scientific experience was in Theoretical Physics and Quantum Cosmology. I am very thankful that I got to work in this field and, after so many years, I do not regret my decision. I also want to thank Vasilis for his guidance and support all these years, I really learned a lot from him.

During my first steps in the institute there were three persons that played a very important role in my development, Dr. Andreas Buehler, Prof. Dr. George Sergiadis and Dr. (not yet at that time) Ludwig Prade. Dr. Andreas Buehler was my first group leader and the person that helped me integrate in IBMI and get started. Prof. Dr. George Sergiadis was a visiting professor in IBMI at that time. I am truly grateful that he was there during my first steps, because he was pushing me to study more and learn more in electronics, he was harsh with me when it was necessary and taught me so many things.

A special thank you goes of course to Ludwig Prade, who was still a PhD student back then. We were working together on this project and he, being a senior PhD, was a great source of knowledge to me. He taught me, while we were working together, how to do research, how to use every device in the lab and many, many more things. Together we developed most of the systems presented here and it was a great experience working with him.

Dr. Christian Zakian as my group leader was always there when I needed him. His door was always open for discussions and he would gladly offer advice on how to solve every problem, scientific, administrative or everything else I would ask him about. His experience and guidance really helped me the last 4 years he is in IBMI. Dr. Lucas Mathias Riobo, although he joined IBMI in the last year and a half, he immediately started assisting me in performing various experiments and taught me so many things on electronics design and development. Sarah Isabella Glasl was always there to assist me with in- and ex- vivo mice experiments and her ideas on possible experiments that we could perform were of particular value.

I would also like to thank my colleagues from the Aristotle University of Thessaloniki (AUTH), Nikos Kousias and Giannis Raptis for setting up the soot generator and dilution system and for developing and testing the OA soot sensor together. A big thanks goes to their professor, Prof. Dr. Leonidas Ntziachristos (yes, he is Vasilis' brother) for his advice and guidance in developing this sensor.

How could I forget Philipp Rauschendorfer, my lab colleague that, besides always borrowing my stuff from the lab without asking, was there to discuss and give me his opinion on everything I wanted at any time. I want to thank Andrei Berezhnoi (soon to be Dr.), Francesca Gasparin, Dr. Paul Vetschera and Dr. Georg Wissmeyer for the countless discussions, walks and coffee breaks we had during the last years that made my life so much easier.

For assisting me in various projects I want to thank Dr. Hailong He, Dr. Murad Omar, Roman Shnaiderman, Chen Yang, Yuanhui Huang, Mustafa Qutaiba, Dr. Juan Aguirre and

Dr. Markus Seeger. I also wish Linda Haedrich, Delin Li and Lorenzo Zina the best of luck as they continue working on my projects. Take good care of them! There are so many people working now, or have worked, in the administration team of the Institute of Biological Imaging in Helmholtz-Zentrum Muenchen or the Chair of Biological Imaging in TUM, that is hard to name them all. Thank you all for all of your help!

I want to say thank you and also sorry to everybody who has worked with me because I know I am not an easy person to work with, I get impatient, I am never quite, I can get annoying and loud sometimes. Thank you for being patient with me.

Last but not least I want to thank my wife, Mairy Bolovinou, for being next to me and supporting me in my every step for so many years. Special thanks also go to Dr. Nikos Chatzis for his valuable advice all along. Last but not least I want to thank my family, Sotiris, Maria and Eva Stylogianni.

Thank you all!!!

List of Abbreviations

AC	Activated Carbon
ANSI	American National Standard Institute
AR-PAM	Acoustic Resolution Photoacoustic Microscopy
AWG	Arbitrary Waveform Generator
BC	Black Carbon
BGA	Blood Gas Analyser
CAT	Computer Aided Tomography
CCD	Charged Coupled Device
CMOS-APS	Complementary Metal-Oxide Semiconductor - Active Pixel Sensor
CNR	Contrast-to-Noise Ratio
COMD	Catastrophic Optical Mirror Damage
CPC	Condensation Particle Counter
CW	Continuous Wave
CW-LD	Continuous Wave Laser Diodes
DAQ	Data Acquisition Card
DOA	De-oxygenation Agent
DoV	Depth of View
DPSS	Diode Pump Solid State
EEPS	Engine Exhaust Particle Sensor
FD	Frequency Domain
FMT	Fluorescence Molecular Tomography
FoV	Field of View
FT	Fourier Transform
FWHM	Full Width at Half Maximum
FWMOA	Frequency Wavelength Multiplexed Optoacoustics
GHG	Green House Gases
HB	Haemoglobin
HBO2	Oxygenated Haemoglobin
HEPA	High Efficiency Particle Air
HSM	High Sooting Mode
HWP	Half Wave Plate
ICE	Internal Combustion Engine
IR	Infrared
LD	Laser Diode
LED	Light Emitting Diode
LiDAR	Light Detection and Ranging
LLI	Laser Induced Incadescence

MFP	Mean Free Path
MFT	Mesoscopic Fluorescence Tomography
MIR	Mid Infrared
MPE	Maximum Permission Exposure
MRI	Magnetic Resonance Imaging
MSS	Micro Soot Sensor
NA	Numerical Aperture
NIR	Near Infrared
NIRS	Near Infrared Spectroscopy
OA	Optoacoustic
OCT	Optical Coherence Tomography
OER	Oxygen Extraction Rate
OPO	Optical Parametric Oscillator
OR-PAM	Optical Resolution Photoacoustic Microscopy
PACT	Photoacoustic Computed Tomography
PBS	Phosphate Buffered Saline
PC	Personal Computer
PCB	Printed Circuit Board
pCO2	Pressure of Carbon Dioxide
PEMS	Portable Emission Measurement System
P-LD	Pulsed Laser Diode
PN	Particle Number
pO2	Pressure of Oxygen
PPS	Pegasor Particle Sensor
PSF	Point Spread Function
QEPAS	Quartz Enhanced Optoacoustic Spectroscopy
QTF	Quartz Tuning Fork
Q-factor	Quality Factor
RF	Radio-Frequency
RSOM	Raster Scanning Optoacoustic Mesoscopy
SHG	Second Harmonic Generation
SNR	Signal-to-Noise Ratio
sO2	Blood Oxygen Saturation
SPOAS	Spectroscopic Portable Optoacoustic Sensor
TD	Time Domain
TMFP	Transport Mean Free Path
US	Ultrasound
UST	Ultrasound Transducer
UV	Ultraviolet
XCT	X-Ray Computed Tomography

Contents

Chapter 1

Introduction

1.1 Biomedical Imaging

Until the end of the 19th century medical doctors had no other tools than their human senses to examine and treat patients as well as to perform biological research. The only tools available were simple optical elements, such as spectacles or a magnifying glass, which can be considered as an extension of the human senses, the eye in this case. These tools could not provide significantly more and especially different kind of information to the doctors in order to change the way of doing research and treating patients. The study of physiology and anatomy of the human body was possible either invasive, during a surgery, or postmortem. With the tools of that time it was impossible to study in-depth the functions of the human-body *in-vivo*, i.e. non-invasive, under a variety of different conditions, healthy or diseased .

Medical imaging started with the discovery of X-rays by Roentgen in 1895, when he discovered that some invisible rays were able to penetrate some solids better than others [1] and that this could be used to create maps, images, of the human body and reveal valuable information about the human anatomy and physiology, not available before. Since the discovery of X-rays many medical imaging devices have been developed that utilize various imaging principles and exploit different contrast mechanisms to reveal a variety of information about the human body. The modalities that are today available and allow biomedical imaging and sensing are for example Computer-Aided-Tomography (CAT), Magnetic-Resonance-Imaging(MRI), Ultrasound (US), Advanced Methods in Optical Microscopy, Optoacoustics (OA) etc [2, 3].

Because of the many imaging and sensing devices that exist today, researchers are capable of penetrating deep in the human body and with greater resolution than before, creating images in 3 (x, y, z) or 4 (including t) dimensions to present its inner structure. The fact that these devices have become widely available in research institutes as well as hospitals has allowed for a huge collection of active patient data and basic understanding of many diseases and the way to cure them. Therefore, medical imaging has gained a prominent role and revolutionized patient treatment and basic biological research [2]. Nowadays, a clinician, in order to make a diagnosis, examines many images looking for small changes in the shape, intensity and/or appearance of certain features that are not visible in a healthy tissue. These images often come from a variety of imaging techniques, based on different imaging principles that can provide similar or different kind of information for the same tissue area or type [3].

1.1.1 X-Ray Imaging and Computer Aided Tomography

X-ray planar radiography and Computed Tomography are 2 of the most common and well-known imaging technologies for acute injuries and chronic diseases.

X-rays are produced by an X-ray tube [4]. In the X-ray tube electrons are produced at the cathode, which consists of a thin tungsten wire that is heated up to $\sim 2200^o$C. When the cathode reaches this temperature electrons have enough energy to leave the metal. The free electrons are then accelerated by the voltage difference between the cathode and the anode, that usually is between $25 - 140kV$ and control the energy of the emitted X-rays and vary according to the application. The electrons then hit the anode, that is usually also made by tungsten, and X-rays are emitted by two mechanisms [5]. The first is known as Bremstrahlung, the electrons collide with the bound electrons in the anode metal, change direction and emit high energy photons, X-rays, of a continuous energy spectrum. The second mechanism creates distinct energy peaks in the emitted X-ray spectrum. The free electrons interact with the bound electrons in the anode metal that usually are in the K or L shells of the atoms that leave behind a hole. This hole is usually filled by an electron from the L or M electron shells and emit the X-rays of specific energy [6].

The emitted X-rays travel through the target, the human body, get absorbed differently by different tissues and hit the X-ray detector to form an image. The X-rays interact with the tissue with 2 ways. The first is called photoelectric attenuation and is the main contrast mechanism of X-ray imaging. X-rays are absorbed by atoms in the human tissue and do not reach the detector. The probability of a photoelectric interaction of an X-ray with energy E with a tissue with an effective atomic number Z_{eff} and relative density ρ is:

$$P_{pe} \propto \rho \frac{Z_{eff}^3}{E^3} \tag{1.1}$$

According to equation (1.1) hard tissues like bones with $Z_{eff} \sim 13.8$ and $\rho \sim 2.05$ present much higher X-ray attenuation compared to soft tissues like lipids with $Z_{eff} \sim 7.4$ and $\rho \sim 1$, especially in low energy X-rays [3].

The X-rays can also interact with loosely bound electrons in the outer atomic shells and scatter, an interaction also known as Compton Scattering [7]. The X-ray changes its direction by an angle θ and the energy of the scattered X-ray, E_sc, is given by:

$$E_{sc} = \frac{E_{in}}{1 + \frac{E_{in}}{mc^2}(1 - \cos\theta)} \tag{1.2}$$

where E_{in} is the energy of the incident X-ray. Compton scattering is dominating over the photoelectric effect at higher energies and introduces blurring in the images. To reduce this blurring effect anti-scatter grids have been introduced right before the X-ray detector.

In the past, X-rays were detected using an X-ray film, that is a gelatin-covered polyester film base that is coated at both sides with a ting silver halide crystals that are sensitive to X-rays. Nowadays, the X-ray films have been replaced with digital detectors. The X-rays interact with a scintillator and are converted into lower energy photons, which are converted into voltage by 2D grid of photodiodes. The modern detectors offer higher quality images and allow data to be stored in the PC, processed and shared much easier [8].

X-ray planar radiography has a large variety of applications [3]. It can detect fractured bones in the scull, hands, arms, legs, feet and air cavities in the lungs [9]. Digital X-ray mammography is commonly used to detect tumors in breasts [10, 11]. X-ray imaging can also be used to image

the vascular structure with an iodine-based contrast agent injection [12]. By using a different contrast agent, barium sulphate, X-ray radiography can image the gastrointestinal track and help in the treatment of various disorders [3, 13].

Computed Aided Tomography (CAT) is a 3 dimensional version of planar X-ray radiography. In simplified terms, one or many X-ray planar radiography devices can be rotated around the sample. The acquisition of many X-ray line-signals at different angles around the sample can be mathematically reconstructed in the computer to form 2 dimensional images of the tissue. The name Computed Tomography comes exactly from the need to perform computer reconstruction of the signal to present tomographic slices of the sample. By performing many scans at different positions in the body, or by applying helical scans to increase imaging speed, full body tomographic images can be generated [14].

Some of the most common clinical applications of CAT are cerebral scans to detect acute trauma, oedemas and skull fractures, aneurysm ruptures, internal bleeding, or to detect and monitor the progression of brain tumours [15]. CAT is also used to outline the size and the shape of nodules in the lunges after they have been confirmed by planar X-ray radiography images. Using CAT the whole liver can be imaged very fast at high resolution and lesions in the liver can be revealed with the use of an iodine-based contrast agent [16]. The same agent can be used with CAT to image the heart and assess calcification in the coronary artery when other methods such as MRI cannot be applied due to cardiac pacemakers [3].

X-ray imaging, that includes X-ray planar radiography and Computed Tomography, has the advantage of the unique inherent contrast between soft and hard tissue provided by the use of high energy photons. X-ray imaging can offer exceptional imaging depth as the high energy photons can penetrate the whole tissue without significant absorption nor scattering, at least compared to optical imaging. For such high imaging depth X-ray planar radiography or CAT can provide very good spatial resolution that varies from 150um to 1mm according to the various types of instrumentation [17].

However, X-ray imaging involves the use of ionizing radiation and has to be used with caution. The ionizing radiation has two effect on the tissue. The deterministic effect refers to cellular damage that leads to loss of tissue function the more cells get damaged. The deterministic effect becomes more severe the higher the radiation dose. The stochastic effect refers to random mutations that can happen with any radiation dose and can lead to the development of cancer. Therefore, strict rules have been applied by the authorities in all countries that limit the exposure to ionizing radiation for patients and clinicians that perform X-ray imaging [18–20].

1.1.2 Magnetic Resonance Imaging

In contrast to X-ray imaging that offers exceptional contrast between soft and hard tissues and uses ionizing radiation, Magnetic Resonance Imaging (MRI) offers very good contrast between soft tissues without the use of ionizing radiation maintaining the high penetration depth to image the whole body.

MRI images the amount of hydrogen nuclei in the body. MRI uses three main components to create an image, a superconducting magnet, a set of magnetic field gradient coils and a set of radio frequency (RF) transmitters and receivers [3].

The super conducting magnet forms a uniform magnetic field, B_0, that is usually 1.5 or 3 Tesla, i.e. up to 60 000 times stronger than the magnetic field of the Earth. The magnetic field causes the protons in the body to precess, rotate, around B_0 at a very specific frequency ω, called the Larmor frequency, the value of which is

$$\omega = \gamma B_0, \tag{1.3}$$

where γ is the gyromagnetic ratio and it varies for different atoms according to the number of proton in their nuclei. MRI is looking for Hydrogen atoms and thus the Larmor frequency is $127.7MHz$ for a 3 Tesla magnet [21, 22].

The magnetic field gradients are responsible for the image formation. They alter the strength of the magnetic field as a function of space. Therefore, the Larmor frequency, ω, is different for different space points allowing MRI devices to create images.

The RF transmitter and receiver is responsible for the excitation and detection of the signal in MRI. As the protons precess around B_0 they cause a magnetic flux Φ on the RF receiver that creates a detectable signal at the same Larmor frequency (1.3) through Faraday induction. The strength of the signals depends on the density of protons M_0 in the tissue [23].

In MRI, the RF coils are also used to generate a RF pulse at the same frequency, that is absorb by the precessing protons. The RF pulse has a direction 90° to B_0 that causes the net magnetization of the protons to flip from the z plane to the $x-y$ plane. The excited protons now will re-emit this energy following two relaxation mechanisms that induce contrast to MRI.

The protons re-align with B_0 with a characteristic relaxation time T_1. T_1 relaxation affects only the z magnetization and is also called spin-lattice relaxation. After a 90° RF excitation the value of the magnetization detected in the z axis is given by

$$M_z(TR) = M_0(1 - e^{-\frac{TR}{T_1}}), \tag{1.4}$$

where M_0 is the net magnetization of each tissue and TR the time between successive spin flips. Representative values of T_1 relaxation times for a 3 Tesla magnet for different tissues are, 0.36 sec for subcutaneous fat, 0.80 sec for liver, 1.1 sec for brain white matter, 1.6 sec for brain gray matter and 1.42 sec for skeletal muscle [24–27].

The second relaxation time, T_2, affects only x and y magnetization and represents the time the protons need to stop precessing coherently and relax to their thermal equilibrium values of zero. If an RF pulse is applied along the x axis then at time TE after the excitation the magnetization along the y axis is given by

$$M_y(TE) = M_0 e^{-\frac{TE}{T_2}}, \tag{1.5}$$

where T_2 is the relaxation time. Representative values of T_2 relaxation times for a 3 Tesla magnet for different tissues are, 130 m sec for subcutaneous fat, 40 m sec for liver, 60 m sec for brain white matter, 80 m sec for brain gray matter and 30 m sec for skeletal muscle. T_2 is always a much slower process than T_1 relaxation [25, 27, 28].

Now by combining equations (1.4) and (1.5) the MRI signal is given by the following equation:

$$S(TR, TE) = M_0(1 - e^{-\frac{TR}{T_1}})e^{-\frac{TE}{T_2}}. \tag{1.6}$$

Notice that the values of T_1 and T_2 depend on the tissue being imaged but the values TE and TR can be chosen to yield different contrast in MRI. If we choose $TR \gg T_1$ and $TE \sim T_2$ then we create a T_2 weighted image, i.e. contrast comes from T_2 relaxation process. If we choose $TR \gg T_1$ and $TE \ll T_2$ then we create a M_0 weighted image, i.e. contrast comes from the proton density in the tissue. This mechanism offers the lowest contrast in MRI. If we choose $TR \sim T_1$ and $TE \ll T_2$ then we create a T_1 weighted image, i.e. contrast comes from the T_1 relaxation mechanism. If we choose $TR \sim T_1$ and $TE \sim T_2$ then we create a mixed T_1 and T_2 weighted image, a choice rarely made in MRI, [3, 29].

We notice that the T_1 relaxation time is large, at the order of seconds, resulting in long acquisition times for MRI. In order to reduce the acquisition times in MRI, slice imaging and

multi-slice imaging can be applied. The magnetic gradient coils alter the magnetic field spatially along with the Larmor frequency, ω_s. Excitation with a RF with frequency ω_s and bandwidth $\Delta\omega_s$ will only excite a z slice in which the Larmor frequency is in the bandwidth of the RF pulse. Phase encoding and frequency encoding techniques can be applied to excite, record and separate the signals from different points in the x and y direction. Since T_1 relaxation time is longer than T_2 relaxation, the time during one acquisition and the next excitation, $TR - TE$, images from nearby slices can be acquired to lower the total imaging time in MRI. By using RF coil arrays and advanced techniques imaging speed can be increased even more. By rotating the magnetic gradient coils and the RF coils, slices in any direction can be acquired. MRI can therefore image the whole body, as tissues are transparent to RF radiation, and the typical imaging resolution is around 0.5mm [30, 31].

MRI can image almost all of the parts of the human body. Neurological conditions can be diagnosed using MRI [32]. By the use of a contrast agent, brain imaging can detect intracranial mass lesions such as tumors [33]. Vasogenic or cytoxic oedemas are easily seen in T2-weighted MRI imaging. MRI can also image the liver and detect lesion in fatty livers, such as hepatic adenomas or liver cirrhosis [34, 35]. The musculoskeletal system is usually imaged by MRI to evaluate the cartilage integrity of the knee, to monitor degenerative diseases in the spinal cord etc [36]. The heart can also be nicely imaged using MRI due to the high contrast between the myocardium and the myocardial wall itself and is widely used to detect and monitor a variety of heart diseases [37].

MRI offers multiple advantages compared to other imaging modalities. MRI has an excellent penetration depth that can scan the whole human body and provides good resolution. MRI offers unique contrast between soft tissues that is necessary to image a large variety of conditions in almost all parts of the human body. MRI can provide images at any position and orientation in the human body. MRI does not use ionizing radiation, is non-invasive and no adverse effects have yet been reported.

Besides the excellent contrast of soft tissues, MRI has very poor contrast in hard tissues; bones, teeth, metallic objects, even air, appears black in MRI. MRI requires huge and expensive equipment to build, operate and maintain. MRI instrumentation is noisy and takes a long time to form an image that causes many patients to develop claustrophobia or feel uncomfortable. Moreover, due to the use of strong magnets, MRI instrumentation requires good shielding to reduce the electromagnetic interference to other medical devices in the clinics. In addition, due to the use of strong magnets, patients with metallic implants or pace-makers cannot be imaged using MRI.

1.1.3 Ultrasound Imaging

In comparison to X-ray and MRI, Ultrasound (US) imaging is less expensive and can be easily miniaturized. US offers good contrast between tissues to provide morphological and structural information with minimal to no safety concerns. US imaging can also offer fast, real time imaging and with Doppler US the blood flow and velocity can also be monitored and measured. Therefore, US is extremely useful in many clinical applications and is widely used as a first, easy imaging tool [38].

US is a mechanical pressure wave that oscillates along the transmission axis forcing the tissue to compress and expand periodically, i.e. it is a longitudinal wave. US imaging usually exploits frequencies between 1-15MHz that correspond to a wavelength between ~ 0.1 to 1 mm for a speed of sound in tissue of $\sim 1540\ m/s$. However, the speed of sound is not the same for all tissues and it depends on the tissue density ρ and the tissue compressibility κ, and its value

is given by the following equation

$$c = \frac{1}{\sqrt{\kappa\rho}}. \tag{1.7}$$

Another metric that is commonly used to characterize tissues in US imaging is the characteristic acoustic impedance Z:

$$Z = \sqrt{\frac{\rho}{\kappa}}, \tag{1.8}$$

with dimensions $gcm^{-2}s^{-1}$. Air, that can be located in lungs has the lowest acoustic impedance of 43 $gcm^{-2}s^{-1}$ while strong structures like bones have an acoustic impedance of $7.8 \cdot 10^5$ $gcm^{-2}s^{-1}$. Other tissues like blood, fat, muscle, liver, kidney have intermediate values of acoustic impedance of 1.59, 1.38, 1.7, 1.65 and 1.62 $10^5 gcm^{-2}s^{-1}$ respectively [3]. The difference in the acoustic impedance, or speed of sound, in different tissues provides the contrast in US imaging.

When US waves face a surface that is the boundary between two tissues of different acoustic impedance do two things. One part of the incident wave reflects back and is detected to form the image. The other part is transmitted further into the tissue changing its direction slightly. The angle of incidence, reflection and refraction as well as the US wave intensities are connected through the Snell's law. In the two extreme cases of air pockets and bones most of the signal will be reflected back, with a 180° phase shift for the air pockets case, giving a very strong US signal, i.e. excellent contrast. However, there is only a very small portion of the incident signal that is transmitted and no signal can be detected from any structures behind the air pockets or bones. In the other case of soft tissue, due to the small difference in the acoustic impedance at the interface, only a small part will be scattered back and detected and most of the signal will be transmitted deeper in the tissue and reflected back by deeper structures giving rise to signals from multiple tissues. For this reason US imaging requires a very strong excitation pulses to perform imaging. However, very few safety considerations have to be taken care of, that allow the use of strong pressure waves in US imaging.

It is important to note that US waves face only limited scattering when they travel through tissues. Small structures that are of the size or smaller than the ultrasound wavelength will scatter the ultrasound wave in all directions, destroying the US wavefront [3]. A common small scatterer of US in tissues are red blood cells. However, since red blood cells are usually located very close together, the US wave that is scattered by many of them interferes constructively and the red blood cells can be considered as a uniform bigger object. However, if small particles are located further apart, the resulting scattered wave is a combination of constructive and destructive interference and is considered as undesirable noise. This property of US waves is of particular importance for Optoacoustic Imaging as it will be discussed later.

US waves can also be absorbed by the tissue with two mechanisms. The first mechanism is relaxation absorption and is characterized by the relaxation time τ that the particles need to return to their equilibrium position after being displaced. The second mechanism is classical absorption and is a consequence of friction. US exhibits low absorption through tissue of about 1 dB cm^{-1} MHz^{-1}. This means that for every 3 cm of tissue the US wave lose approximately half of their value per MHz, i.e. the higher the frequency the stronger the US attenuation is [39, 40].

US imaging is performed by sending an US pulse at a central frequency f_0 with a bandwidth of Δf and wait until the signal is transmitted into the tissue, reflected back and detected. This is the only limitation as far as imaging speed is concerned; the US wave needs time to travel back and get detected. The device that generates and detects the US waves is called an Ultrasound Transducer (UST) and it is made by a piezoelectric material that can convert an electrical voltage into pressure and vice versa. The USTs are easy and cheap to manufacture and single

elements can be made flat or curved to focus the ultrasound for higher spatial resolution. As a rule of thumb, the higher the frequency used, the higher the axial and the lateral resolution gets but the shallower the imaging depth. Moreover, many small UST elements can be combined in one dimension or even 2 dimensional arrays that work together using linear array or phased array techniques to form an image [41, 42].

There are three modes of US imaging or sensing. A-mode refers to the use of a single element that fires an US pulse wave and detects the back-scattered echo. This is a very common application to measure the axial length of the eye and the corneal thickness when high frequencies are used [3]. When acquiring many such A-lines and displaying them side by side, M-mode imaging is performed, and it is used to display fast movement of objects like in cardiac or foetal cardiac sensing. The most common US imaging mode is Brightness (B-) mode. B-mode US imaging uses an UST array in either one or two dimensions to generate the US wave and detect the pulse-echo. By employing beam-forming reconstruction algorithms 2D or 3D images can be formed respectively [43].

In US imaging the Doppler effect can be exploited to detect and quantify the blood flow speed. The blood flow will increase the frequency of the back scattered wave if blood is flowing towards the UST array or will decrease the frequency of the detected US wave if the blood is flowing in the opposite direction, away from the UST array. Doppler US imaging gives rise to Duplex or triplex image acquisition [44–47].

US imaging is a safe technique; only the Mechanical Index and the Thermal Index have to be considered. The Mechanical Index predicts the possibility of cavity generation in tissue and only the maximum rare-factional pressure is a critical parameter. The Thermal Index estimates the potential of harmful biological effects due to the rise of temperature in soft tissue and bones, usually limiting the temperature rise to $1.5°C$. Both Mechanical and Thermal Indexes are only approximations of the risk of biological damage and not exact quantifiable parameters [3, 48, 49].

US imaging is widely used in gynecology and obstetrics, to monitor the health and development of the foetus. 3D US imaging can also produce high resolution images of the foetus face. US can also be used from breast imaging to avoid radiative expose to X-rays. Musculoskeletal structures, such as tendons and nerves can be imaged with US. B-mode US imaging is used to determine ventricular size and function in heart imaging [50], to identify early signs of cardiac arythmia, valve disease or cardiac embolisms and infractions [51–53].

US imaging has many advantages. US is a low-cost method, in comparison to MRI and X-rays and its instrumentation is compact and small in size. It can provide high frame-rate images, in 2D or 3D, for a long time as it is using no ionizing radiation. US can be widely used as it has no contradictions, such as MRI with patients with metallic implants.

US can image deep in the tissue, up to many cm's in the tissue. However, US cannot image the whole body as X-ray imaging and MRI can. US can provide high spatial resolution, usually $\sim 100um$ with a significant trade-off between resolution and imaging depth; the higher the imaging depth the lower the spatial resolution and vice-versa. US can only provide morphological information about the tissue and cannot effectively differentiate between different kinds of soft tissue nor provide functional information.

1.2 Optical Imaging

The imaging technologies that we have discussed so far offer different kind of advantages and disadvantages in terms of contrast, resolution, penetration depth, imaging speed, cost. Optical imaging, i.e. use of non-ionizing photons to investigate the tissue, offers a unique set of characteristics that make it a necessary tool for biomedical imaging. The use of non-ionizing

photons makes it a safe modality to use without major limitations. Tissue contains many biological molecules that interact with light, the main ones being oxygenated and de-oxygenated haemoglobin, usually called absorbers or chromophores, or scatter light, usually called scatterers. The biological molecules interact with light at a wide range of wavelengths, from ultraviolet (UV) to mid-Infrared (MIR), offering great contrast between soft tissues and the ability to reveal biochemical information and study different functions of the human body, or even gene activity [54]. First, We are going to focus on light scattering and the techniques used to reduce its effect. Then, we are going to discuss light absorption and re-emission of photons and fluorescence.

1.2.1 Light Scattering

Light, as it propagates in tissue, can be scattered by the different cellular structures or get absorbed by them. In biological tissue scattering dominates over absorption in the UV to NIR region. Elastic scattering occurs when a photon gets absorbed and re-emitted at the same wavelength, without loss of energy, but with a possible change of direction. The scattering coefficient μ_s denotes the probability of a photon being scattered in a unit length, and is measured in $1/cm^{-1}$. The reciprocal of the scattering coefficient is called scattering mean free path (MFP) and indicates the average distance a photon travels between 2 successive scattering events. For biological tissue the scattering MFP is of the order of $100\mu m$, although it can vary with tissue type [54].

When a photon is scattered, it has a higher probability of maintaining its original direction. The more scattering events the photon undergoes, the more it loses its original direction and becomes diffusive. For this reason the anisotropy coefficient has been introduced, g, that defines the degree of forward scattering, with a typical value of $0.8 - 1$ and the reduced scattering coefficient is defined as $\mu_s' = \mu_s(1 - g)$. The transport mean free path (TMFP) is given by TMFP$= 1/\mu_s'$ and it represents the distance that the photons travel before losing relation to the original propagation direction, i.e. become diffusive [55].

Scattering is the major limiting factor in optical imaging, as it dominates the interaction events in the UV to NIR region. Scattering limits the number photons that remain at their original path, thus limiting the achieved resolution at higher depths. Scattering is the reason why optical imaging is limited in only superficial depths. Many new techniques have been developed in order to extend the optical imaging depth beyond the ballistic regime ($<$ MFP) [54, 55].

A general classification of the different optical imaging methods has been done according to their imaging depth measured in TMFP units. *Microscopy* images at penetration depths below 1 TMFP ($\sim 0.5 - 1$ mm); *mesoscopy* images at depth between 1 and 10 TMFP (~ 0.5 mm -1 cm) and *macroscopy* at depths larger than 10 TMFP ($>$ 1 cm) [55].

1.2.2 Optical Microscopy and Ballistic Imaging

Optical microscopy is a well established biological tool. Microscopy uses a light source to illuminate the sample, a combination of optical elements (lenses, mirrors, pinholes, etc.) to manipulate the light and a light detector (the human eye, a photographic film or a digital camera) to record the light [56].

The modern cameras are based on semiconductor materials that are sensitive to light absorption. The material absorbs light, which creates a small current through the photoelectric effect that can be recorded. Two of the most popular sensor used in microscopy today are CCD (charged-coupled-device) and CMOS-APS (complementary metal-oxide semiconductor active

pixel sensor) [57]. Both type of sensors consist of a rectangular array of sensitive elements, called pixels, that detect the incident light at different locations. The size of each pixel, the number of pixels and the size of the sensor affect the SNR (signal-to-noise ratio) of the image, the FoV (field of view) and the resolution of the final image. Each pixel can capture the total incident light, irrespective of the wavelength; this type of sensor is usually called monochromatic because it can generate only gray-scale images. Most cameras, however, use a color filter array that allows red, green and blue colors to pass at specific pixels that are arranged in a specific pattern, such as a Bayer filter mask [58, 59], in the sensor array [60].

The quality of the image depends on the sensor to effectively capture the incident light. However, the most important component of an optical microscope is the objective lens, the first optical element that the light encounters after the sample and is responsible for primary image formation. The quality of the objective lens and its characteristics define the magnification and the resolution a specific camera can achieve.

The total FoV acquired by a microscope is defined by the camera sensor size and the magnification of the objective used as

$$FoV = \frac{\text{Camera Sensor Size}}{\text{Magnification of Objective}}. \tag{1.9}$$

The numerical aperture (NA) of the objective is defined as $NA = n\sin(\theta)$, where n is the refractive index of the medium, usually air or oil, for oil immersion objectives, and θ the one-half angular aperture of the objective. The NA defines the ability of the objective to collect light and resolve fine details in the sample.

The image of a point source is not a single point, rather the intensity is distributed over an area on the image plane, i.e. it appears blurred. This happens because any practical system is never ideal but has imperfections. The distribution of the point-like source is called point spread function (PSF) and its shape depends on the wavelengths and the numerical aperture of objective lens. When two point-like objects are very close to each other, they cannot be distinguished any more. The two points can be distinguished if their distance is larger than the full width at half maximum (FWHM) of the point spread function of the system. Therefore, the resolution of a microscope is defined by

$$r = \frac{0.5\lambda}{\text{NA}} \tag{1.10}$$

where λ is the wavelength of the incident light and NA the numerical aperture of the objective. This means that the shorter the wavelength, the smaller the structures that can be resolved [61].

There are two equivalent ways to perform optical microscopy depending on how the light is delivered and collected from the sample [62].

• **Bright Field Microscopy**

In a conventional bright field microscope an incoherent large-area source is illuminating the whole sample simultaneously through a condenser lens. The transmitted (or reflected) light passes through the objective lens that forms the image on the light detector. The light detector is usually a camera, and each pixel of the camera acts as a point detector. As discussed above the objective lens is responsible for forming the image, defines the resolution, the condenser plays only a secondary role [62].

• **Scanning Optical Microscopy**

In a scanning optical microscope the sample is illuminated by a point source that is focused in the scattering medium by the objective lens. The transmitted (or reflected) light is collected on a large-area detector by a collector lens. The point source is scanned in two

dimensions to form an image. The quality of the image is still controlled by the objective lens, only now it is responsible for focusing the light on the sample, rather than collecting it from the sample and forming the image. Scanning optical microscopy is equivalent, but reversed, to bright field microscopy and have therefore identical characteristics. Both modalities are sensitive to light absorption and scattering in the tissue, that is their contrast mechanism [63].

Scattering imposes the biggest limitation for optical microscopy, as scattered photons diverge from their original direction, destroying the original wavefront and the focusing ability of the objective and the microscope. This is the reason why optical microscopy has very good resolution but only at shallow imaging depths [55].

Ballistic imaging refers to imaging using unscattered or singly back-scattered photons. In practice, however, the detector will detect also quasi-ballistic photons that will increase the signal but reduce the resolution of the system. Non-ballistic photons, i.e. multiply scattered photons, have different characteristics than ballistic or quasi-ballistic photons. Multiple techniques have been developed that use those different characteristics to reject no-ballistic photons and only collect ballistic ones. Some of them are presented below [56, 60]:

• **Time-Gated Imaging** Time-gated imaging takes advantage of the fact that ballistic photons arrive at the photodetector earlier than non-ballistic photons. A usual time-gated imaging setup consists of an ultrafast collimated laser beam that illuminates the sample. Between the scattering sample and the optical detector a time gate is positioned that is synchronized with the laser pulse, allowing only early photons to enter the camera and be detected. The early photons are attenuated only along the optical axis and the whole system can be raster scanned in the transverse directions to create a 2D image of the sample. The duration that the time gate stays open affects the image quality. The longer it stays open, more non-ballistic photons can enter the detector that will increase the signal but will deteriorate the resolution at the same time. There is, therefore, a trade-off between the signal quality and the image resolution [64, 65].

• **Spatiofrequency-filtered imaging**

Ballistic photons have different spatial frequency distributions to non-ballistic photons due to the multiple scattering events that they undergo. Spatiofrequency-filtered imaging utilizes a collimated laser source to illuminate the sample and uses a lens, or a pair of lenses, after the sample to focus the light in a diffraction limited spot at which a pinhole is placed. The pinhole allows the ballistic photons to pass through and rejects the non-ballistic photons that cannot be focused in the diffraction limited spot. After the pinhole the light is collected by a light detector. Similar to time-gated imaging, each pixel of the image represents a line through the scattering medium and a raster scanning can be performed to generate 2D images of the sample. A trade-off between signal intensity and resolution exists here as well, as with a bigger pinhole, more heavily scattered photons can reach the detector, increasing the signal and reducing the resolution [66].

• **Confocal Imaging**

Ballistic photon have a better defined wavefront than non-ballistic photons. Confocal microscopy is a special type of point scanning microscopy that uses a point source to illuminate a small region of the sample through an objective lens. A second objective lens is collecting the light from the same focal spot and focuses it through a pinhole onto a point detector. In a different configuration, the same objective lens is used to collect the back-reflected light from the sample and direct it through a mirror to the pinhole and the point detector. Confocal microscopy offers several advantages over conventional microscopy. As the light is focused and collected from one point, only photons that pass through the focal spot can be detected, the rest are rejected from the pinhole. Stray light is also rejected due to the pinhole in front of the

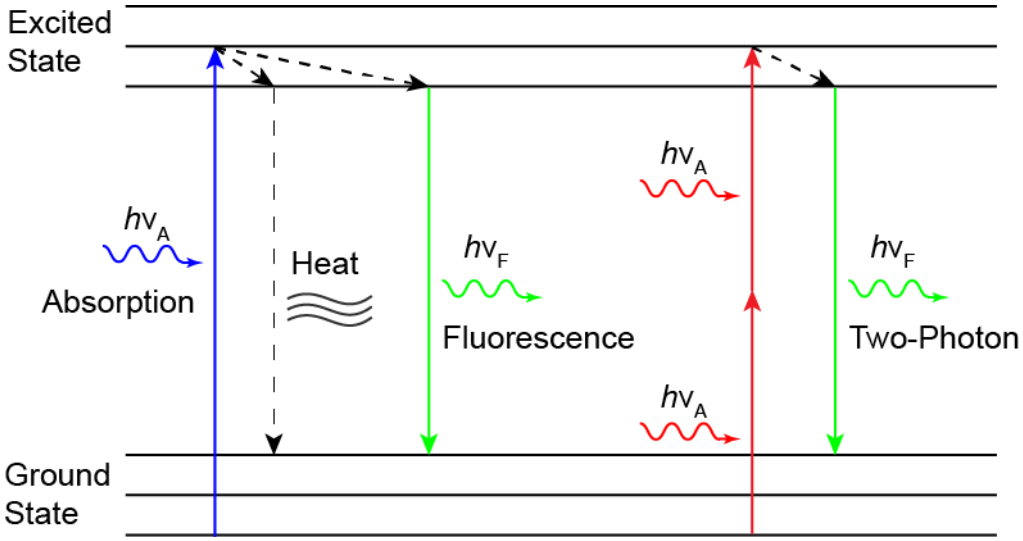

Figure 1.1: Jablonski Diagram. The main electronic absorption and emission processes are presented for non-radiative relaxation, fluorescence and two photon excitation.

detector that helps increasing the resolution and the image SNR. This microscopy modality offers a slight increase of the spatial resolution as both the illuminating objective and the collector objective lens play a role in the image formation. In addition, confocal microscopy offers depth discrimination and a three dimensional scan can be performed to generate a 3D image of the object. However, the three dimensional point scanning of the sample leads to long acquisition times [67, 68].

1.2.3 Light Absorption and Fluorescence Imaging

Similar to the scattering coefficient, the absorption coefficient μ_a is defined as the probability of a photon being absorbed in a unit length. The reciprocal of the absorption coefficient is called mean absorption length and is the average length a photon travels before being absorbed by a biomolecule. Moreover, the extinction coefficient, or total interaction coefficient, is the sum of the scattering and the absorption coefficient, $\mu_t = \mu_s + \mu_a$, and the reciprocal of it is called the extinction mean free path [54, 55].

Photons that get absorbed by a molecule elevate an electron from its ground state to an excited state, this process is called *excitation*. For this to happen, the energy of the excitation photon needs to be exactly the same as the energy difference between the excited and the ground state. After the excitation there are several possible outcomes. The electron can then relax back to a ground state by either generating heat, a process called non-radiative relaxation, or by emitting another photon, a process called luminescence. Figure 1.1 presents the Jablonski diagram for some of the main photon absorption and emission processes [69]. The diagram shows the different discrete energy levels of a biomolecule, the ground and the excited state, as well as their different vibrational levels. The photon absorption and the different kinds of relaxation, non-radiative and fluorescence, as well as a non-linear process, called two photon excitation, are presented. In two photon excitation the biomolecule absorbs two photons of low energy simultaneously to be excited and later emit a fluorescent photon of twice the energy [69].

In fluorescence imaging the emission photon is typically of less energy than the excitation photon, it is red-shifted, a phenomenon called Stokes effect. The three important parameters of fluorescence are the quantum yield, the lifetime and the molar extinction coefficient [70].

The quantum yield is the ratio of the number of the emitted photons relative to the number of the absorbed photons. The biomolecules in the excited state can return to the ground state either by emitting a photon (fluorescence) or through non-radiative relaxation. The quantum yield represents the fluorescence efficiency of a biomolecule, usually called fluorophore [71].

The absorption of a photon happens in the femtosecond scale. It is followed by a vibrational relaxation, an internal conversion, that does not emit a photon, which happens in the picosecond scale. The biomolecule stays at this state for a specific period of time until it returns to the ground state and emits a fluorescent photon. This phenomena happen in the nanosecond scale. Therefore the fluorescent lifetime is at the order of nanoseconds. Fluorescence lifetime is the average time a molecule spends in the excited state before emitting a photon [72].

The quantum yield and the lifetime are parameters that depend on the micro-environment the fluorophore is in, such as local temperature, pH etc. This property can thus be used to detect small changes in these parameters during different biological phenomena and processes and provide biochemical information about the sample.

The molar extinction coefficient represents the ability of a fluorophore to absorb photons of a specific wavelength in a unit of length. The concentration and the molar extinciton coefficient of a fluorophore can provide molecular and morphological information about the sample [73].

Fluorescent imaging is one of the most rapidly expanding techniques in biological optical imaging. The existence of many endogenous fluorescent biomolecules as well as the development of many external fluorescent agent has heavily contributed to the expansion of fluorescence microscopy. It can provide excellent sensitivity for low fluorophore concentration and information on morphology as well as dynamics and interactions of the bioassembly.

Some of the most important fluorescence imaging techniques are presented below [55, 70, 74]:

• **Fluorescent Molecular Tomography**

Fluorescence Molecular Tomography (FMT) can generate three-dimensional images of the distribution of different fluorophores in small animals and tissues. FMT is a tomographic technique, that illuminates the sample with a point source, to increase the resolution, over several illumination angles and collects the fluorescent diffusive light with a light detector. The raw signals from the different projections are reconstructed based on different theoretical models of light propagation in tissue to improve the resolution and create the three-dimensional image [75, 76]. FMT can be combined with X-Ray Computed Tomography (XCT), in a hybrid FMT-XCT system. The XCT images, besides the new contrast they introduce, can also be used to form prior knowledge of the sample that can increase the image resolution. FMT can therefore offer imaging depths of several millimetres to centimetres but the dominant light scattering in biological tissues limits its spatial resolution (1mm to 1cm) [77, 78].

A simpler version of FMT is Mesoscopic Fluorescence Tomography (MFT) that uses volumetric tissue illumination and a CCD camera with a lens to collect the light, from multiple angles. Mathematical model of light propagation are also used but in this case the imaging depth is reduced to around 1 TMFP and the resolution is increased to hundreds of μm's [79].

• **Wide-field and Single Photon Excitation Confocal Fluorescence Microscopy**

Wide-field and Single Photon Excitation Confocal Fluorescence Microscopy are very similar to the wide-field and confocal microscopy, respectively, that were discussed above. By adding an optical filter and a dichroic mirror to a wide-field or a confocal microscope, it is possible to separate the excitation from the emission spectrum and only record the emitted, fluorescent, photons. In this way it is quite simple to combine two detectors and also record, simultaneously, both the RGB image as well as its fluorescent counterpart. Wide-field fluorescence imaging is very simple and the most widely used fluorescence technique [80].

Similar to confocal microscopy, single photon excitation confocal fluorescence microscopy

uses two confocal objective lenses to illuminate and detect the light and a pinhole to minimize out-of-focus photons. Single photon excitation confocal fluorescence microscopy, therefore, offers a significant increase to the resolution and the addition of depth sectioning compared to wide-field fluorescence microscopy. In confocal single photon excitation fluorescence microscopy a photomultiplier tube is usually used to increase the sensitivity of the system [81].

• **Two-Photon Excitation Microscopy**

Two photon fluorescence microscopy takes advantage of the two photon excitation phenomenon. The two photons need to be in the absorption cross-section of the molecule at the same time to be absorbed and therefore the extinction probability depends on the square of the instantaneous light intensity [82, 83].

A typical two photon excitation microscopy setup is similar to that of single photon excitation fluorescence confocal microscopy. However, two photon excitation microscopy uses light with twice the wavelength compared to single photon excitation fluorescence confocal microscopy, that leads to reduced scattering and increased depth. Two photon excitation microscopy uses a very fast femtosecond laser to excite the sample and increase the probability of absorption at the focal spot. Moreover, the use of a pinhole before the detector is not necessary, as photons can only be emitted by the focal spot, where the two photon absorption takes place. The use of a pinhole, however, can increase the spatial resolution at the expense of signal strength [56].

• **Fluorescent Lifetime Imaging**

As already explained above, the fluorescence lifetime of a biomolecule depends on the local micro-environmental conditions. Measuring the lifetime of a specific fluorophore can provide valuable information on different conditions and processes that takes place in the vicinity of the biomolecule [84, 85].

Fluorescence lifetime imaging uses a pulsed light source to illuminate and excites the sample. A very high speed photodetector is synchronized with the pulse light source and collects the fast decaying fluorescent light. As the fluorescence lifetime is of the order of nanoseconds, the response of the detector and the electronics needs to be at the order of a few tens to hundreds of picoseconds. The signal acquisition can take place point by point if a single point detector is used, that however will slow down the total acquisition. New high speed cameras, such as gated image intensifier cameras, or streak cameras, can be used to parallelize the acquisition [70].

Fluorescence lifetime imaging can also provide fluorescence intensity information, if the signal is integrated over the period, providing extra flexibility. Moreover, the lifetime signal is insensitive to the light intensity fluctuations, fluorophore concentrations and light scattering, as it only measures the lifetime of the fluorophore.

Optical imaging provides excellent contrast for the study of biological tissues and different bio-processes within, at low costs and without the use of ionizing radiation. Light can undergo many processes when interacting with the tissue that provide different kinds of contrast, in the UV, visible and NIR region. However, light scattering dominates light absorption in this wavelength range. Therefore, the use of light to visualize the tissue leads to high spatial resolution, μm to sub-μm, but only at shallow depths, a few hundreds of μm, due to scattering.

1.2.4 Optical Coherence Tomography

Optical Coherence Tomography (OCT) is the optical equivalent to ultrasonic imaging for biological applications. Similar to US imaging, OCT depends on the back-reflection of light from the interface of different tissues; it provides structural information about the sample, non-invasively, with high sensitivity and at a depth between $1 - 2$ mm. However, for high

resolution imaging that is required in biological imaging, e.g. $10\mu m$, and due to the much higher speed of light compare to US, the time resolution required is 30 fs, that is much lower than the detection limit of the current electronics. Therefore, to achieve this kind of high resolution the use of interferometry is necessary [86, 87].

OCT is based on a Michelson interferometer, but it uses a low coherence light source, a white light source. The coherence length is the length over which an electric field remains coherent, substantially correlated. The coherence length, l_c is defined as

$$l_c = \frac{4\ln 2}{\pi}\frac{\lambda_0^2}{\Delta\lambda}, \tag{1.11}$$

where λ_0 is the center wavelength of the source and $\Delta\lambda$ is the source's FWHM bandwidth. The coherence length in OCT defines the resolving ability of the system. A monochromatic source, with low wavelength bandwidth, has a longer coherence length while a broadband source has a small coherence length, i.e. better resolving ability.

The simplest way to perform OCT is in Time Domain (TD). TD-OCT uses a white light source, that is split using a beam splitter in two arms. The first arm, the reference arm, is reflected back from a mirror that is positioned on a linear stage. While the mirror is moving back and forward the reference path length can be varied. The second arm is directed into the sample. Some of the light is back reflected from within the sample, at its different interfaces and boundaries. The back reflected light follows a specific path length that is different for the different reflecting surfaces. The reference arm and the sample beam are recombined through the beam splitter and interfere on a photo-detector. If the reference arm and the sample arm have exactly the same path length, then the broadband light interferes constructively on the photo-detector. If the reference arm path length differs from the sample arm path length then the interference is destructive. The reference arm is then scanned to interrogate different depths in the sample. Then the interrogation point besides the axial scan can be scanned in the two lateral direction to create full 3 dimensional images of the sample.

One of the most important advantages of OCT is that the axial resolution is decoupled from the lateral resolution. The axial resolution depends on the coherence length of the source and it is given by

$$\Delta z = \frac{l_c}{2}, \tag{1.12}$$

with l_c given by equation (1.11). The lateral resolution is defined by the objective lens used to focus the light into the sample and is given by

$$\Delta x = \frac{2\lambda_0}{\pi \mathrm{NA}}, \tag{1.13}$$

where NA is the numerical aperture of the lens, defined as the $1/e^2$ Gaussian beam waist. This lateral resolution stands over a specific region around the focal spot, called depth of field, which is given by

$$\Delta d = \frac{\pi \Delta x^2}{2\lambda_0}. \tag{1.14}$$

There is, therefore, a trade-off between the lateral resolution and the depth of field, a higher NA objective provides high lateral resolution but only over a small depth of field.

TD-OCT is simple to develop, however, it is slow as it requires a three dimensional scan and the moving mirror in the reference arm introduces motion artifacts that can blur the image.

Frequency Domain Optical Coherence Tomography (FD-OCT) is the Fourier domain equivalent OCT modality. In FD-OCT instead of scanning the reference arm mirror to interrogate

different depths in the sample, the reference arm is kept stable and a dispersive element separates the wavelengths so that they can be all detected simultaneously by a detector array. In an alternative FD-OCT system a variable wavelength light source is used, which constantly changes the wavelength that is detected by a single detector. FD-OCT offers higher sensitivity and imaging speed compared to TD-OCT.

In OCT the choice of the wavelength determines the overall system's performance. Usually wavelengths between 650 nm and 1.4 μm are used due to the low water absorption in this range, as water is the main component of tissues. Imaging at wavelengths around 830 nm offers high axial and lateral resolution at the expense of imaging depth due to increased scattering in tissues. Imaging at 1300 nm is the most common as it offers good penetration depth, due to reduced scattering of light at this wavelength and low absorption from blood and melanin, as well as good resolution. Imaging at 1050 nm is commonly used for application of OCT in ophthalmology [88].

OCT is a promising biological imaging modality as it offers high resolution imaging, at significant depth that can be performed in a non-invasive manner. Modern FD-OCT system can provide high frame rate images of the tissue. An additional advantage is the ability to develop OCT system using optical fibers, which has pushed OCT in smaller and cheaper form factors and has enabled endoscopic OCT system. OCT finds applications [87] in ophthalmology [89], cardiology [90, 91], gastrenterology [92, 93], urology [94, 95] and neurosurgery [96, 97].

1.3 Optoacoustic Imaging

Optoacoustic (OA) imaging, also referred to as Photoacoustic, is an emerging powerful imaging modality of optical absorption in tissues. It is based on the photoacoustic effect that was discovered by Alexander Graham Bell in 1880 [98]. OA imaging was further developed in the last two decades due to the development of strong and fast lasers as well as of high frequency and sensitive ultrasound transducers [99].

OA imaging combines the optical absorption of light and contrast with the ultrasonic imaging depth and spatial resolution. OA imaging uses a short laser pulse to excite the tissue. The photons are absorbed by the biomolecules that emit heat through the non-radiative relaxation. This instantaneous temperature change gives rise to a pressure wave, through the thermoelastic effect, that propagates through the tissue. US waves are scattered much less than photons in biological tissues, thus enabling larger penentration depths compared to optical imaging, while maintaining the same optical absorption contrast between soft tissues.

OA imaging overcomes the problem of light scattering in tissue by detecting the ultrasound wave. Scattering just changes the direction of the photons and does not remove them from the medium, as absorption does. Therefore, scattered or diffusive light can still generate an OA signal as long as there are enough photons to be absorbed by the target and give rise to an OA signal that can be detected by the Ultrasound Transducer (UST), if it is sensitive enough.

1.3.1 Optoacoustic initial pressure

The initial OA pressure rise can be calculated using basic thermodynamic principles as presented in [100]. The local fractional volume expansion, dV, that results from a short laser pulse as the tissue heats up can be given by

$$\frac{dV}{V} = -\kappa p(\mathbf{r}) + \beta T(\mathbf{r}), \tag{1.15}$$

β is the thermal coefficient of volume expansion, p the pressure and T the temperature. κ is the isothermal compressibility and can be expressed as

$$\kappa = \frac{C_P}{\rho \upsilon_s^2 C_V}, \tag{1.16}$$

with ρ denoting the mass density, υ_s is the speed of sound in tissue (that is mostly water), C_P and C_V the specific heat capacities at constant pressure and volume, respectively.

There are two important time scales to take into account in order to simplify eq.(1.15), that are connected to the characteristic scale of the phenomenon, d_c, that is the heat heterogeneity dimension, the size of the optically absorbing area. Heat takes time to diffuse out of the excited volume and the characteristic time scale is called *thermal relaxation time*

$$\tau_{th} = \frac{d_c^2}{\alpha_{th}}, \tag{1.17}$$

where α_s is the thermal diffusivity. The initial pressure will travel out of the excited volume in the characteristic time scale called *stress relaxation time*,

$$\tau_s = \frac{d_c}{\upsilon_s}. \tag{1.18}$$

As long as the excitation pulse width t_p satisfies the thermal and stress confinement limit, i.e

$$t_p < \tau_s < \tau_{th}, \tag{1.19}$$

the volume expansion can be neglected and eq.(1.15) is simplified

$$p_0 = \frac{\beta T}{\kappa}, \tag{1.20}$$

with p_0 the initial pressure rise. The temperature rise in the excitation volume can be expressed as

$$T = \frac{\eta_{th} A}{\rho C_V}, \tag{1.21}$$

where A is the absorbed energy and η_{th} is the portion the absorbed energy converted into heat, and is inversely related to the fluorescence quantum yield of a biomolecule. We can also define the dimensionless Grueneisen parameter

$$\Gamma = \frac{\beta}{\kappa \rho C_V}, \tag{1.22}$$

and eq.(1.20) is converted into

$$p_0 = \Gamma \eta_{th} A. \tag{1.23}$$

The absorbed energy A can also be expressed as $A = \mu_\alpha C_0 \Phi$, where μ_α is the optical absorption coefficient and C_0 the concentration of a specific absorber and Φ the optical fluence, i.e. the illuminated energy per unit volume on the sample over a defined time interval. Then the initial pressure rise is given by

$$p_0 = \Gamma \eta_{th} \mu_\alpha C_0 \Phi. \tag{1.24}$$

This equation tells us that the initial pressure rise is proportional to the Gruenseisen parameter, the amount of light absorbed, i.e. the optical flunce, the absorption coefficient, the chromophore concentration and the amount of the absorbed energy converted into heat.

1.3.2 Optoacoustic wave equation

The general optoacoustic wave generation and propagation equation is [101]

$$\left(\nabla^2 - \frac{\gamma}{v_s^2}\frac{\partial^2}{\partial t^2}\right) p(\mathbf{r},t) = -\frac{\alpha\gamma}{v_s^2}\frac{\partial^2 T(\mathbf{r},t)}{\partial t^2}, \tag{1.25}$$

where γ is the specific heat ratio, α is the pressure expansion coefficient given by $\alpha = \left(\frac{\partial P}{\partial T}\right)_V$. The general heat diffusion equation is

$$\frac{\partial}{\partial t}\left(T - \frac{\gamma-1}{\gamma\alpha}p\right) = \frac{K}{\rho C_P}\nabla^2 T + \frac{H}{\rho C_P}, \tag{1.26}$$

where K is the thermal conductivity and $H = \eta_{th}\mu_\alpha\Phi$ the heat source term. For common fluids γ approaches unity and if the thermal confinement limit is satisfied $K \to 0$. The pressure expansion coefficient is also expressed by $\alpha = \rho\beta v_s^2/\gamma$. The coupled differential equations (1.25) and (1.26) decouple and can be combined into

$$\left(\nabla^2 - \frac{1}{v_s^2}\frac{\partial^2}{\partial t^2}\right) p(\mathbf{r},t) = -\frac{\beta}{C_P}\frac{\partial H(\mathbf{r},t)}{\partial t}. \tag{1.27}$$

The left hand side of this equation is the propagation term of the pressure wave. The right hand side is the source term, that is proportional to the first time derivative of the heat term. This means that only a varying source term generates an optoacoustic signal. A constant heating source does not generate an optoacoustic signal and the higher the transient absorbed power the stronger the generated optoacoustic signal.

It has been proven [102,103] that for a point-like source and a time dependent light intensity of the form $I(t) = \frac{\Phi}{\theta}f(t/\theta)$, with θ a pulse width parameter, the resulting pressure wave is given by

$$p(t) = a_1\frac{\Phi}{\theta^2 r}\frac{d}{d\hat{\tau}}f(\hat{\tau}), \tag{1.28}$$

where a_1 is a coefficient that can be found in [102, 103],r the distance from the source to the detector and $\hat{\tau} = \frac{t-r/c}{\theta}$. This equation shows that for a point like source the optoacoustic pressure is inversely proportional to the distance from the excitation volume dropping with $1/r$ as it has spherical symmetry, inversely proportional to the pulse width parameter squared, proportional to the optical fluence of the illumination source and proportional to the time derivative of the light intensity profile.

1.3.3 Optoacoustic Absorption Spectra

Figure 1.2 demonstrates the optical absorption spectra of the main endogenous biological absorbers. Melanin has an almost flat spectrum in the ultraviolet (UV) and visible region that slowly drops with increasing wavelength. Although, melanin has a very strong absorption in this wavelength range, it is mainly confined in the epidermis layer of the skin and the eye retina and is of importance for dermatological [104, 105] and opthalmological [106] and other clinical applications [107].

Haemoglobin (HB) and oxygenated haemoglobin (HBO2) are the main endogenous absorbers located in the blood vessels and micro capillaries. The difference in spectra between HB and HBO2 provides the ability to OA Imaging to estimate the blood oxygen saturation of hemoglobin (sO2), one of the most important parameters for OA. Many diseases can alter the oxygenation

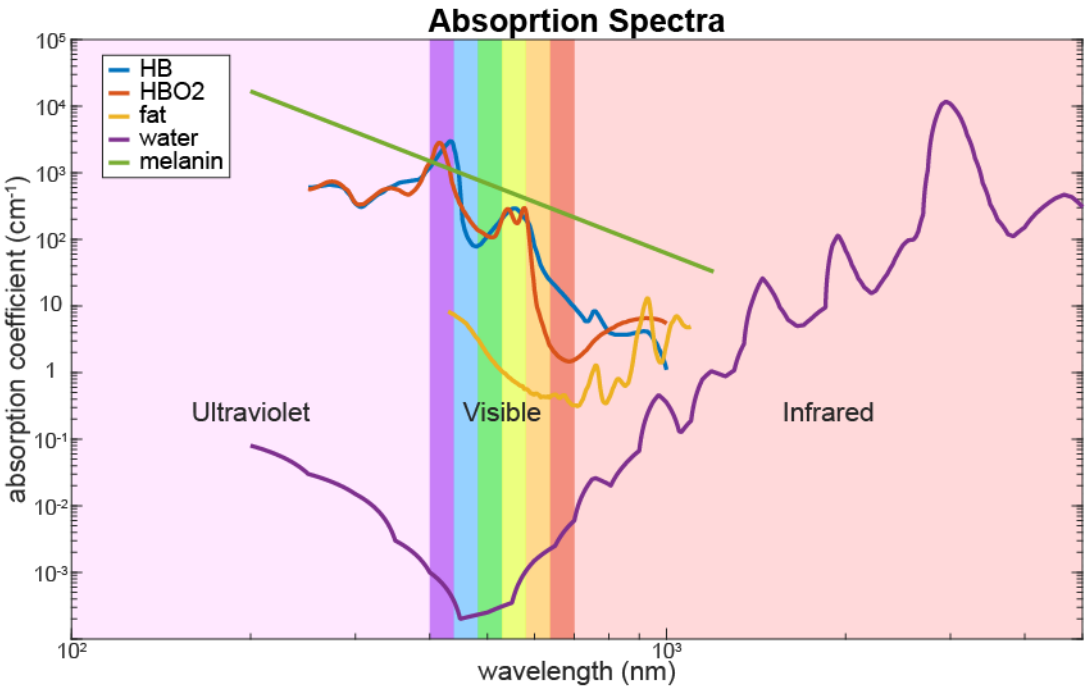

Figure 1.2: Absorption Spectra. Optical absorption spectra of main biological absorbers, haemoglobin (HB), oxygenated haemoglobin (HBO2), fat, water and melanin.

level of blood, can cause lack of oxygen supply through the blood to the various tissues, that can lead to tissue necrosis, or even death [108, 109]. Of particular importance is the monitoring of the vascularization of a tumor area, as a growing tumor consumes more oxygen that leads to agniogenesis, i.e. the development of new vessels on the outer area, and at the same time presents low oxygenation values in its core (hypoxia) [110, 111]. Monitoring of blood oxygenation is also particularly important in the brain and OA Imaging is an interesting imaging modality in neuro-sciences.

Fat and lipids can also be detected using OA Imaging with a peak absorption wavelength around 930 and 1210 nm. Fat is usually located under the skin and subcutaneous fat morphology correlates with cardiovascular risk factors [112, 113].

The human body mainly consists of water. Water is almost transparent in this wavelength region, with 5 to 6 orders of magnitude lower absorption coefficient compared to blood in the visible range. This optical window allows OA Imaging to image all the other chromophores despite the high concentration of water in the tissue. However, at higher wavelengths, in the NIR region water is absorbing light and its distribution in the human body can be imaged [112].

By imaging the tissue at multiple wavelengths we can differentiate the various absorbers by means of linear un-mixing methods. The acquired OA signal at wavelength λ_i, $P(\lambda_i)$ can be expresses as

$$P(\lambda_i) = \sum_{k}^{N} \mu_{a,i}^{k} C_k \Phi(\lambda_i), \tag{1.29}$$

where k runs for all the different N absorbers, endogenous or exogenous, in the tissue, C_k represents the local concentration of each absorber, $\mu_{a,i}^{k}$ its absorption coefficient and $\Phi(\lambda_i)$ the local light fluence at each wavelength. For N different chromophores we need to acquire the OA signal using at least N wavelengths to construct a system of N equations, similar to eq.(1.29), with N unkowns, the C_k's. It is also possible, and most times desirable, to acquire the OA signal in more than N wavelengths and perform a linear spectral fitting methods, such as the least

square method or any other, in order to increase the accuracy of our measurement [114, 115].

Un-mixing methods are important in correctly measuring the blood oxygen saturation as [114]

$$sO_2 = \frac{C_{HBO_2}}{C_{HBO_2} + C_{HB}} \times 100\%, \tag{1.30}$$

where C_{HBO_2} and C_{HB} are the concentrations of oxygenated and de-oxygenated haemoglobin. However, the optical fluence is not the same for all the wavelengths deeper in the tissue. Although, we can measure and correct the differences in the laser energy per pulse for each wavelength, the optical fluence depends on the light absorption of the particular wavelength at the upper tissue layers as well as the different scattering coefficient in tissue of each wavelength. For this reason, several methods have been developed to overcome this problem and are explained in [109], such as the optical transport model based method [116], the acoustic spectrum based method [117, 118], the eigenspectra optoacoustic tomography method [119] and others.

1.3.4 Optoacoustic Modalities

Optoacoustic imaging is versatile and OA systems have been developed that can image superficial structures with high resolution as well as deeper structures but with lower resolution with optical absorption contrast.

OA systems usually consist of the pulsed laser source that should provide short nano-second range pulses with the desired energy per pulse and wavelength. The light output is usually conditioned by the use of optical elements to illuminate the sample at the desired way. The generated OA ultrasound wave is detected by an UST or an UST array that is coupled with the tissue using water or ultrasound gel to match the acoustic impedance of tissue and increase the SNR. The detected electrical signal of the UST is usually amplified by the use of a low noise amplifier and recorded by a high-speed digitizer.

The signal is usually recorded at multiple positions either with the use of mechanical stages, that transport the illumination and detection system or the sample, galvanometric mirrors that scan the illumination point on the sample or with the use of UST arrays. In most of the cases, in order to form an OA image from the multiple recorded signal image reconstruction is necessary. Image reconstruction forms images by numerically shifting the signal back in time for a given speed of sound, to its initial position in space, i.e. its source, by using an inverse Radon transformation [120–124]. In the process the sensitivity field of the UST, either focused, flat, cylindrical or an array, has to be taken into account in order to increase spatial resolution and sensitivity [125, 126].

From the solution of the OA wave equation (1.27) [100] we know that smaller objects generate higher frequencies than larger objects that generate low frequencies. We also know that the generated OA signal from a light pulse with a definite pulse width results from the convolution of the OA signal generated by a Dirac delta excitation (the Green's function) and the excitation pulse. For this reason, it is important to match the excitation pulse width to the size of the object that we want to detect, as long as it satisfies the thermal and stress confinement limit. Moreover, the bandwidth of the UST should match, as much as possible, the bandwidth of the generated OA signal, in order to increase the SNR and the spatial resolution [69].

The developed OA systems can be split in three main categories based on their imaging depth and spatial resolution and they have different requirements on laser pulse width, laser energy per pulse, UST design and frequency range.

- **Optoacoustic Macroscopy or Photoacoustic Computed Tomography (PACT)**

Optoacoustic Macroscopy is usually called Photoacoustic Computed Tomography (PACT) and can provide deeper imaging at lower spatial resolution compared to the other OA modalities.

PACT uses expanded light beams that illuminate a wide area on the sample surface. Light delivery is usually achieved with the use of fiber bundles. Diffusive light can penetrate deep into the tissue that gives rise to the OA signal that is detected by the UST array. In PACT the use of an UST array, either 1-D or 2-D, ensures that the acquisition of an image, either 2-D or 3-D with a single light pulse. The frame rate then depends on the pulse repetition rate of the laser and a few tens of Hz up to a couple of hundred Hz ($50 - 200$ Hz) are enough [127].

The wide field illumination lowers the energy density on the sample surface, which is defined as the energy per illuminated area. In addition, diffusive light will generate the OA signal deep in the tissue and for these reasons, in PACT, high energies per pulse, usually more than 10mJ, are required [69].

The acoustic frequency range of the UST array is generally low, 1 - 10MHz, since lower acoustic frequencies attenuate less in tissue compared to higher frequencies but provide lower spatial resolution. Therefore, PACT can offer imaging depth up to a few cm's [128, 129] in tissue and spatial resolutions of $50 - 200\mu$m [55]. The optical pulse width of a PACT system needs to satisfy the thermal and stress confinement limits, which for the larger structures that are ususally detected in PACT, can be as long as $\sim$50 ns, for a 100μm object.

The laser wavelength in PACT is usually tunable to provide functional and molecular multispectral OA imaging and to be able to detect and quantify the concentration of the different absorbers in the tissue [127]. PACT uses mostly excitation wavelengths in the NIR region that can penetrate the tissue easier and provide larger penetration depth. Therefore, Q-switched Nd:YAG lasers with an Optical Parametric Oscillator (OPO), TI-Sapphire and dye laser systems are commonly used, since they can provide the high pulse energies, the pulse widths and the repetition rates that are required.

In summary, PACT provides video frame-rate imaging, that depends on the repetition rate of the laser, the wavelength switching speed and the wavelength multiplexing scheme used, at cm depths with spatial resolution of hundreds of μm's with high field of view. Image reconstruction is necessary to create the 2-D or 3-D images and increase the SNR and the spatial resolution in all depths. PACT systems are easy to be combined with an US pulse echo imaging system [130, 131].

PACT systems, such as the Multispectral Optoacoustic Tomography (MSOT) [127], have been extensively used in life sciences lately, in functional brain mapping [132], cancer research, diagnosis or treatment [133–136], cardiovascular disease management [137], monitoring of oxygenation [108, 109] and tissue perfusion [138], thyroid imaging [139], systemic sclerosis diagnosis [140] etc.

• Optoacoustic Microscopy or Optical Resolution Photoacoustic Microscopy (OR-PAM)

Optoacoustic Microscopy is a microscopic OA modality that can provide very high resolution OA imaging at shallow depths. OA Microscopy focuses the light tightly in the tissue, usually with the use of an objective lens, similar to a scanning optical microscope. Usually a spherically focused UST is confocally aligned with the optical focus to detect the OA signal. Optoacsoutic Microscopy is also called Optical Resolution Photoacoustic Microscopy (OR-PAM) since the optical focus is tighter than the acoustic focus and the lateral resolution relies on it. Therefore, OR-PAM can offer very high, diffraction limited resolution of a few μm [141], but only at shallow depths, a few 100 μm's [142], limited by light scattering in tissue.

Point scanning is usually performed in OR-PAM with the use of galvanometric scanning, that provides high scanning speed and small field of view (FoV) or with sample scanning that is slower but with bigger FoV, or a combination of the two. Therefore, in OR-PAM the scanning speed depends mainly on the laser pulse repetition rate, usually more than 400kHz [69].

Due to the very high lateral resolution of OR-PAM, high frequency UST's are used, usually 1-100 MHz [55, 141, 143]. In OR-PAM, the axial resolution depends on the frequency of the UST because of the detection of US waves that travel along the same axis. The spatial resolution is not homogeneous in OR-PAM with the lateral resolution being tighter than the axial resolution [69]. OR-PAM requires a very small excitation optical pulse width, usually 1 ns or even less, to be able to satisfy the stress and thermal confinement limits, eq. (1.19), and to be able to generate the high frequencies required to image such small objects.

Since the light is tightly focused on the sample, the energy density is very big and not that much energy per pulse is required from the laser, usually in the tens to hundreds of nJ's per pulse [69, 142]. In OR-PAM no image reconstruction is necessary, since the OA signal can only originate from the optical focal spot where the energy density is large enough to generate a detectable OA signal. However, signal and image processing techniques can enhance the image SNR and resolution [141].

OR-PAM provides high spatial resolution 3-D images, with good axial resolution, but with low depth of focus. Depending on the setup, the laser pulse repetition rate, the galvanometric mirror or stages speed, the chosen FoV and the averaging required to increase the SNR, OR-PAM can provide images with high frame rate and small FoV or slow frame rate and with a high SNR and FoV.

The advantage of OR-PAM is that it is only sensitive to light absorption and not scattering, in comparison to optical microscopy. OR-PAM is also quite easy to combine it with other optical microscopy modalities, such as Scanning Optical or Wide Field Microscopy, Two Photon Excitation etc [144]. OR-PAM finds applications in cell biology because it can image single cells [145, 146], it can image circulating tumor cells in the blood stream [147–149], or track single red blood cells loading and unloading oxygen *in-vivo* [150], etc.

• Optoacoustic Mesoscopy or Acoustic Resolution Photoacoustic Microscopy (AR-PAM)

Optoacoustic Mesoscopy bridges the gap between OA Microscopy and Macroscopy by providing imaging depths and spatial resolutions in the range between the other two OA modalities.

Optoacoustic Mesoscopy is also called Acoustic Resolution Photoacoutic Microscopy (AR-PAM) because the acoustic focus is tighter than the optical focus. Therefore, both the lateral and the axial resolution depend on the UST, in its ability to focus the ultrasound and its frequency bandwidth, respectively.

AR-PAM commonly uses a tightly focused UST with high acoustic NA, in order to increase the lateral resolution and detect a bigger part of the acoustic signal and increase the SNR. The UST usually has frequencies 1-100 MHz [110], to detect both the low and the higher frequency content of the signal in order to visualize the larger as well as the smaller structures in the sample [110, 151].

In AR-PAM the illumination area is smaller than in PACT but bigger than in OR-PAM, usually 0.5-4 mm^2. Therefore higher energies per pulse are demanded to generate a detectable OA signal, usually more than 10 μJs per pulse [152]. The light delivery to the sample is usually performed with fiber bundles or single core multimode fibers and is co-aligned with the UST focal spot. Since AR-PAM targets to detect both smaller and larger structures the excitation pulse shall include small and high frequencies that is achieved with a short nano-second duration pulse, usually 1-6 ns [153].

Scanning is usually performed by stage scanning of the illumination and detection system over the sample to detect the signal at multiple points. Image reconstruction is necessary to achieve homogeneous lateral resolution in all depths and create a 3-D image. AR-PAM can

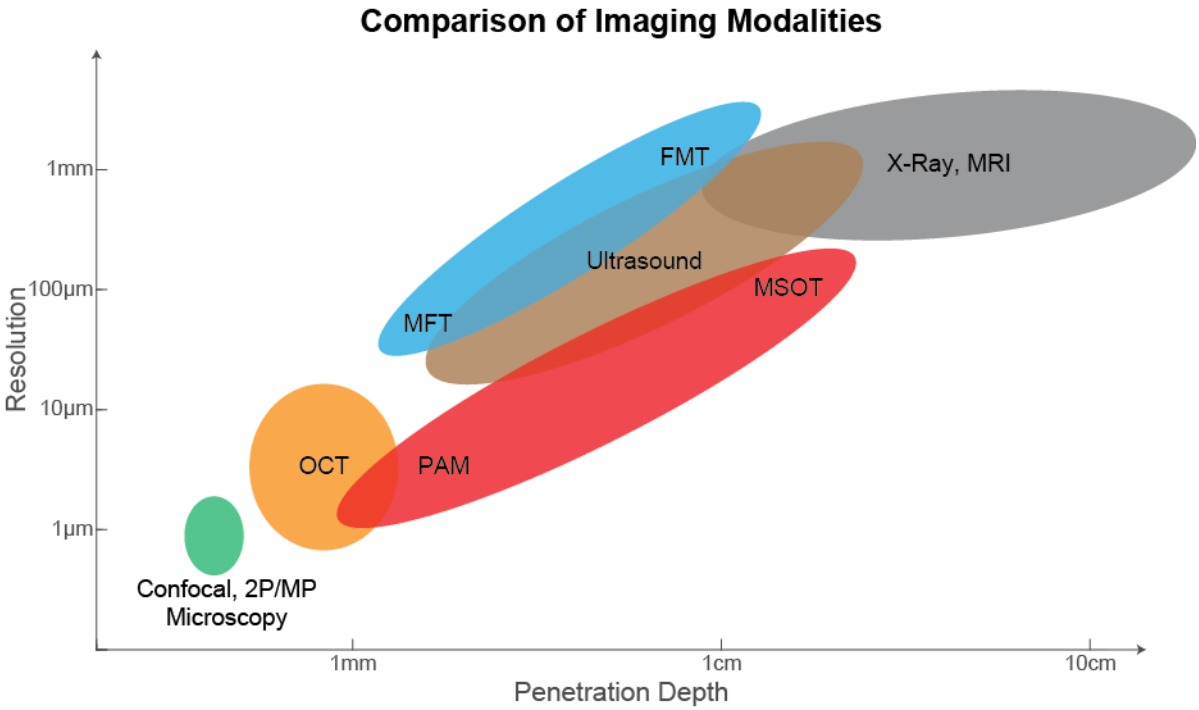

Figure 1.3: Imaging Modalities Comparison. A comparison between the different imaging modalities in terms of the penetration depths and the spatial the can provide. *MRI*, Magnetic Resonance Imaging, *FMT*, Fluorescence Molecular Tomography, *MFT* Mesoscopic Fluorescence Tomography, *MSOT* Multispectral Optoacoustic Tomography, *PAM* Photoacoustic Microscopy, *OCT* Optical Coherence Tomography, *2P/MP Microscopy*, Two Photon/Multi-photon Microscopy.

achieve large FoV and the scanning speed depends on the stages moving speed, the laser pulse repetition rate, that is usually larger than ∼1 kHz, and the averaging necessary to increase the SNR. However, since imaging in AR-PAM is usually slow, requiring seconds to minutes to acquire an image, AR-PAM images suffer from artifacts caused by the patients movements. For this reason, motion correction algorithms have been developed [154, 155].

AR-PAM finds extensive applications mainly in dermatology [156], as its depth and spatial resolution match the range needed in this field and it provides excellent endogenous contrast of melanin and blood in the human skin [157] and can reveal the skin morphology [158]. AR-PAM has been used to monitor melanoma development [159], cancer angiogenesis [110], to asses psoriasis in patients [160], to increase accuracy of allergy patch testing [161], to assess hyperthermia induced vasodilation [162] and to quantify the skin sensitivity of UV light [163], etc.

Figure 1.3 presents a summarized comparison of all the presented imaging modalities in terms of their penetration depth and spatial resolution. X-Ray and MRI provide large penetration depths with low spatial resolution; X-Ray imaging provides excellent contrast between soft and hard tissues while MRI between soft tissues. US imaging provides higher spatial resolution but at shallower depths and provides only structural information of the soft tissues. Fluorescence imaging offers good optical absorption and fluorescence contrast that gives functional information about the tissue but suffers from light scattering and presents relatively low resolution and imaging depth compared to the other imaging modalities. OCT can achieve high resolution at low imaging depths and images structures within biological tissues. Confocal Microscopy and Two Photon or Multi-photon Microscopy have the highest spatial resolution but only at very low imaging depths while providing excellent optical contrast. X-Ray, MRI, US and OCT imaging

are commonly used in applications that structural information are necessary. Fluorescence, confocal and functional MRI (fMRI) also offer functional information about the tissue .

Optoacoustic Imaging, by being a hybrid modality, utilizes the excellent optical absorption contrast that can give functional and structural information about the tissue and achieves a wide range of spatial resolutions and imaging depths. For this reason OA is a rapidly developing modality and can serve as a valuable tool in the hand of clinicians and medical doctors for diagnosis, developement or treatment monitoring of various diseases.

1.4 Lasers for Optoacoustic Imaging and sensing

1.4.1 Laser Light

Laser, or L.A.S.E.R., stands for Light Amplification by Stimulated Emission of Radiation. Laser is a specific kind of light source that is useful in many applications, including biomedical imaging and treatment as well, because it has some specific characteristics. These are *monochromaticity*, *directionality* and *phase consistency*, i.e. laser light is *coherent*. Coherence is what differentiates laser light from all other light sources, such as the sun or a light bulb [164].

Laser light is monochromatic, it includes only one wavelength, or in order to more precise, it contains only very few wavelengths around a central wavelength, i.e. its emission bandwidth is very small, even down to 1 nm for a He-Ne laser [165, 166]. All the photons in the laser beam move in almost the same direction. In other words, the divergence of a laser beam is very small. Last but not least, all the waves in a laser beam oscillate with the same phase, i.e. laser light presents a specific wave-front [164, 167].

These characteristics make laser light useful for biomedical imaging. All the waves in the laser beam have almost the same wavelength, which is particularly useful for biomedical imaging since it can probe specific biomolecules or fluorophores in the human tissue. A laser beam can be focused in a diffraction limited spot through the use of proper optics, e.g. an objective lens, to provide better spatial resolution and to also increase the energy density. Using a laser source ultra short light pulses can be generated. Laser light is coherent, both spatially and temporally [164].

1.4.2 Energy Levels and Inverse Population

Modern Quantum Mechanics teaches us that the energy levels of an atom or a molecule are quantized, the energy stored in an atom or molecule cannot take all possible values but rather only specific discrete value. In addition, matter interacts with light by exchanging only discrete amounts of energy.

There are three major interactions that take place in an energy level system of interest for laser light generation [168, 169].

• **Photon Absorption**. An atom's or a molecule's electron that is at an energy state with energy E_1 can transition to a higher energy state with energy E_2 by absorbing a photon with energy $E_2 - E_1 = hf = hc/\lambda$, where f is the photons frequency, c the speed of light in vacuum, h the Planck's constant and λ the photon wavelength. If the photon has an energy different than the energy difference of the two levels, the transition cannot happen.

• **Spontaneous Emission**. An excited atom, i.e. an atom whose electron is not in the ground state E_0 but has absorbed energy and is at an excited state E_1, after some characteristic time for each atom, called spontaneous emission lifetime τ_{sp}, will return to the ground state by emitting a photon of energy $E_1 - E_0$ at a random direction and with a random phase.

• **Stimulated Emission**. An excited atom at an energy level E_1 can interact with a photon with energy $E_1 - E_0$ before it spontaneously emits a photon. In the case of stimulated emission the excited atom returns to its ground state E_0 and at the same time it emits a second photon with energy $E_1 - E_0$, therefore with the same wavelength, at the same direction and at the same phase as the photon that caused the stimulated emission. The light is thus amplified in a coherent way. This process is the basis of laser light production.

A medium that consist of a particular type of atoms or molecules will have its own discrete energy levels. In thermal equilibrium some of the atoms or molecules will occupy some energy levels and other atoms or molecules will occupy different energy levels. Then the population of atoms or molecules in the ground state will be larger than the population of atoms or molecules in any excited state. This situation that exists in thermal equilibrium is a stable state for the entire population and can remain in that state until disturbed. If additional thermal energy is added, then more atoms or molecules move to excited states but the population of the ground state is always larger than that of any other excited state. It is obvious that a system in thermal equilibrium cannot be used to exploit stimulated emission of radiation, cannot be used to generate laser light [170].

However, if we can pump external energy in a way that we can create an excited energy state, say E_2, with more population, N_2 ,than a lower state, say E_1 with N_1 atoms or molecules, for some time, then it becomes possible to create laser light. Such a situation, i.e. a system of atoms or molecules with $N_2 - N_1 > 0$, is called *inverse population* and it is a necessary requirement to generate laser light [171].

In most cases, in order to create population inversion the active medium presents four energy levels, E_0, E_1, E_2 and E_3, that take part in the process. The energy pumped excites the electrons from the ground state E_0 to the pump level E_3. The electrons stay at that state for a very small time and spontaneously decay to the upper laser level E_2 with internal conversion that does not generate a photon. The upper laser level is usually a metastable level, i.e. it has a long spontaneous decay rate, the electrons can stay in this level for a significant amount of time. This is an important requirement for a medium to be able to provide enough *gain* in order to generate laser light. The spontaneous emission and the stimulated emission happens between the upper laser level and the lower energy level, E_1, that later decays to the ground level with internal conversion. Systems with three levels also exist. In this case, the upper laser level is the same as the pump level or the lower laser level coincides with the ground level [170, 172].

There are several ways of pumping energy in a system of atoms or molecules in order to create population inversion. It is not possible to create population inversion without external excitation of the system. The most common techniques are the following. In electrical pumping the laser medium is placed in an electron beam and the fast moving electrons collide with the atoms or the molecules and transfer part of their energy to inverse the population. Another form of electrical pumping is electric discharge, similar to fluorescence lamps. Some gas lasers are pumped with radiofrequency waves. Semiconductor lasers are pumped with current that pushes the electrons and the holes in the p-n junction. A lot of lasers are optically pumped by a lamp or another laser whose photons have the right amount of energy, or the right wavelength. Chemical energy can also be used to create population inversion [170].

1.4.3 Laser resonator cavity

An active medium that has been externally pumped with energy and has created population inversion is nothing more than a light amplifier. For laser light to be produced, the presence of a

resonator cavity is necessary. The active medium can be enclosed between two mirrors, one that has 100% reflection and the other allows a small amount of the light to escape, usually $\lesssim 5\%$, and serve as the output. The cavity is used to extend the distance the photons travel through the active medium by forcing the light to bounce continuously back and forth in the active medium that is continuously pumped to maintain the necessary population inversion. The light intensity will experience losses and gain at each round-trip. Losses occur from the output mirror transmittance, the light absorption by the medium, from scattering in the medium and on the imperfect surfaces etc. If the gain of the medium is higher than the losses during a round trip in the cavity, that is defined as the threshold gain, then the light intensity will be increased or at least maintained. Therefore, laser light is created [173].

Therefore, we have seen so far that in order to build a laser an active medium, an external pump source that will create a population inversion and a resonant cavity are necessary. The active medium is enclosed in a resonant cavity, and the external pump generates the population inversion. Initially, at the absence of photons in the medium, spontaneous emission dominates and photons are emitted in the medium. The emitted photons stimulate other excited molecule into emission of coherent photons and, like an avalanche, laser light is created. This is a continuous wave (CW) laser.

However, the presence of the resonant cavity has some more implications. The energy cannot be stored in the cavity in any way, it can only oscillate in specific ways, called modes. There are two kind of spatial modes in a resonator, transverse and longitudinal modes [174, 175].

The transverse modes can be visualized be detecting the shape of the output beam of the laser. The most important mode is the TEM_{00}, that is the mode that presents the smallest transverse diameter and a Gaussian shape. It is also called the Gaussian mode, the fundamental mode or the diffraction limited mode. In addition to the TEM_{00} higher order mode can oscillate in the resonant cavity as well. These modes, TEM_{ij} present i number of dark stripes in their spatial energy distribution in one transverse direction and j number of dark stripes in the other. Their spatial energy distribution is larger compared to the TEM_{00}. For this reason it is very common to include a small pinhole, of the correct size, in the cavity so that only the TEM_{00} can fit through it. Therefore, as the light bounces in the cavity only this transverse mode will be amplified.

The longitudinal modes govern the distribution of energy along the oscillation axis. The existence of the mirrors forces the electromagnetic wave to have nodes at the boundaries, at the mirrors. Therefore, not all frequencies, not all wavelengths, can oscillate in the cavity. It can be proved that there is a specific frequency spacing between the allowed oscillating frequencies equal to

$$\Delta f = \frac{c}{2l}, \tag{1.31}$$

where c is the speed of light in the medium and l the length of the resonator cavity.

1.4.4 Laser Bandwidth

As we have already discussed, lasers are almost monochromatic sources, they have a small but finite bandwidth, that is usually measured halfway from the peak of the central laser line, at Full Width at Half Maximum (FWHM). The finite bandwidth comes from the fact that the laser lines are not razor sharp but are broadened, due to several mechanisms. Doppler broadening and pressure broadening are common sources of bandwidth broadening in gas lasers. Doppler broadening comes from the fact that the gas atoms move at high speed and at random directions in the medium that effects the emitted wavelengths through the optical Doppler effect. The higher the temperature of the medium, the faster the atoms move, the stronger the

Doppler broadening is. Pressure broadening results from the collisions of the particles with themselves. The higher the pressure of the gas, the more particles exist in the medium, the more frequent they collide, the broader the bandwidth. In solid-state active mediums, higher temperature means that the molecules vibrate more, broadening their energy levels and thus the laser bandwidth. Imperfections in the host crystal structure also contribute to laser bandwidth broadening [172, 176].

However, reducing the temperature or the pressure will reduce the laser bandwidth, it will also reduce the output power. The most common way of reducing the laser's bandwidth is to reduce the bandwidth of the feedback gain of the resonator, i.e. reduce the gain in specific oscillating modes and allow only a small number of modes to oscillate. This is done by including a prism in the cavity that reflects all wavelengths but a few, in every round trip, out of the medium. Alternatively, replacing a mirror with a grating can also reduce the gain bandwidth of the cavity in the same way. Installing an etalon, that is a Fabry-Perot interferometer, in the cavity has the same result. The etalon will allow only frequencies that are separated by $c/2L$ to oscillate, where L is the length of the etalon. By choosing the length of the etalon to be big enough so that its frequency spacing is bigger than the lasers bandwidth then only one or few modes will be allowed to oscillate. This is called a single-mode laser.

In this way, the resonant wavelength of the laser can be tuned by changing the angle of the prism, the grating or the etalon. This technique allows only slight wavelength tuning over a short range of wavelengths [176].

1.4.5 Laser Technology

Up to now we have discussed CW lasers. However, in many biomedical applications, such as optoacoustics, a pulsed laser is necessary. In addition wavelength tunability over a large range of wavelengths is highly desirable for most biomedical applications. In this section we discuss three basic techniques to generate fast and strong pulsed laser, Q-switching, cavity-damping and mode-locking, and two ways to change the wavelength of the laser based on non-linear optics, second harmonic generation and optical parametric oscillation.

• **Q-Switching**.

The Q-factor of a laser resonant cavity is proportional to the rate of change of the energy stored in the resonator and the energy loss per round trip in the resonator. The Q-factor is usually defined as $Q = f_0/\Delta f$, where f_0 is the central oscillation frequency of the laser and Δf the bandwidth of the laser. A high Q-factor is a high quality resonator, a resonator that has low losses, amplifies the light in a round trip.

In Q-Switching, to create a pulse from a CW laser the lasing action needs to be disrupted for a short amount of time to allow energy to build up, and then suddenly release it in a very short time, in a huge pulse. This can be done by either eliminating the population inversion or the cavity resonance. Since energy must be stored in the medium the cavity feedback is disrupted, i.e. the Q-factor is lowered. While the Q-factor is low the energy is stored in the active medium's inverse population. When the Q-factor is suddenly increased for a short amount of time the stored energy is released, the laser field oscillates and build up and escapes through the low transmittance output mirror. This is why this technique is called, Q-switching.

Q-Switching works only with optically pumped solid state lasers, because the spontaneous lifetime of the upper laser level is long enough to allow the energy to build up. Q-switching is usually achieved by placing a mechanically rotating mirror in the one end of the cavity that provides feedback only when it is perfectly aligned with the other mirror. Acousto-optic modulators are also used, that diffract the light out of the cavity to prevent feedback form the

mirror according to the frequency of the UST in the Acousto-optic modulator. Electro-Optic modulators take advantage of the polarization of the light to prevent it from resonating. Dye Q-switches absorb all the light until it reaches a specific intensity threshold and then become transparent.

Q-switched lasers usually provides pulses at the nano-second range at low pulse repetition rates of up to a few hundred Hz. Therefore, these lasers are of interest for Optoacoustic Imaging. However, each material has its own population inversion constant that determine the maximum pulse repetition rate and the minimum pulse width for Q-switched lasers [177, 178].

• **Cavity-Dumping**.

Cavity-dumping is a Q-switching technique that is also called pulse-transmission mode Q-switching.

Q-switched lasers have a low Q-factor to reduce the cavity feedback and store energy in the medium's inverse population. The Q-factor is increased for a short time to allow laser light to be generated and leave the cavity. Inversely, in a cavity dumped laser the Q-factor is maintained at a very high level, with the use of 100% mirror at both ends. In this way, laser light is built up in the cavity and the energy is stored in the resonator and not in the medium's inverse population as in Q-switching. When the laser light intensity in the cavity reaches a very high value the Q-factor is lowered to release all the energy in a very short time. Usually an electro-optic (EO) modulator and a polarizer are used to achieve it. The EO modulator and the polarizer allow the light to oscillate in the high Q-factor mode. The EO modulator changes the polarization of the light that is totally reflected out of resonator through the polarizer and not one of the two mirrors, as in Q-switching. Therefore, the pulse width of a cavity-dumped laser is equal to the round trip time of the cavity $2L/c$. Cavity-dumped lasers present lower pulse widths and higher pulse repetition rates than Q-switched lasers [179, 180].

• **Mode-locking**.

Mode-locking a laser can be used simultaneously with Q-switching and cavity-dumping and creates very short pulses at extremely high repetition rate.

In mode-locking the reflectivity of the mirrors is that of a normal CW laser, one is 100% reflective and the other $\gtrsim 95\%$. A Q-switching element is introduced in the cavity, this can be an AO modulator, an EO modulator or a dye switch. The Q-switching element allows light to pass through and resonate only once per round trip, creating a pulse front. Another way to explain modelocking is to do it in frequency domain. In a CW laser the different modes will oscillate freely in the cavity. However, in a mode-locked laser, the different longitudinal laser modes are forced to be in phase at all times, by the use of a fast optical gate. The different modes interfere constructively only at one point of cavity and destructively at all other point, creating a pulse. Therefore, all of the energy in the cavity is confined at a single pulse that bounces between the mirrors and a small part of it leaves the cavity through the lower reflectivity mirror once per cycle. Therefore, the repetition rate of a mode-locked laser depends on the size of the resonant cavity, $f_{rep} = c/2L$. Mode-locked lasers can reach repetition rates of tens of MHz.

The duration of the pulse depends on the bandwidth of the laser. Inside the cavity multiple modes can oscillate. However, all these different modes will be in phase only at one point in the cavity, at which they will interfere constructively. Therefore, the longer the laser bandwidth is, the more modes are present in the cavity and the shorter the pulse width will be. High bandwidth lasers can achieve femto-second pulses [179, 180].

• **Second Harmonic Generation**.

We have discussed ways to generate a pulse from a laser. Non-linear optics are used in order to change the wavelength of the laser. As light passes through a linear material it interacts with the electrons that are bound to the lattice structure, that absorb and re-emit part of the

light energy and reduce the speed of light in this material. However, non-linear optics use non-linear materials, such as a birefringent material, the refractive index of which depends on the polarization and the propagation direction of the light [181]. Non-linear materials can be used in optical mixing, where the material absorbs two photons at different wavelengths, λ_1 and λ_2, and they re-emit one photon at a new wavelength, λ_3. This procedure needs to satisfy the law of conservation of energy, from which follows that

$$\frac{hc}{\lambda_1} + \frac{hc}{\lambda_2} = \frac{hc}{\lambda_3}. \tag{1.32}$$

Conservation of the momentum of the three photons must also be satisfied, which is achieved with phase matching, that in do not discuss here.

Second-harmonic generation (SHG), or frequency doubling, involves the absorption of two photons of the same, long, wavelength and the re-emission of one photon of half the wavelength, or double the energy. The efficiency of SHG is proportional to

$$P_{SH} \propto l^2 \frac{P_{in}^2}{A} \left[\frac{\sin^2 \Delta\phi}{(\Delta\phi)^2} \right], \tag{1.33}$$

where P_{SH} is the power of the second harmonic, l the length of the non-linear crystal, P_{in} the incident power, A the cross-sectional area of the incident beam on the crystal and in the bracket a phase matching factor. We observe that the efficiency of SHG is proportional to the square of the incident power, the square of the non-linear crystal length and inversely proportional to the area of the beam. Therefore, the use of SHG is more efficient when used with pulses, that have much higher power compared to CW lasers, and mostly the TEM_{00} that can be focused more efficiently. However, it is very expensive to create very long non-linear crystals and thus impractical.

It is very common that these crystals are positioned in the laser cavity, since the oscillating power is much higher in the cavity than the small amount that leaves the cavity in every cycle. In order to do so, the output mirror needs to perfectly reflect the initial long wavelength and perfectly transmit the shorter converted wavelength, i.e a dichroic mirror is used [182, 183].

• **Optical Parametric Oscillator**.

The Optical Parametric Oscillator (OPO) consists of a non-linear optical crystal and an optical resonator. The OPO is used to convert the energy of one photon, the incident or pump photon with wavelength λ_1, into two new photons, the transmitted or signal photon with wavelength λ_2, and the idler photon with wavelength λ_3. Following equation (1.32) the transmitted wavelength is given by

$$\lambda_2 = \frac{\lambda_1 \lambda_3}{\lambda_3 - \lambda_1}. \tag{1.34}$$

The non-linear optical crystal are placed in a resonator to force the signal or the idler waves to resonate. The pump wave is inserted in the OPO and passes through the non-linear crystals. By adjusting the angle between the incident light and the non-linear crystals the signal and idler wavelengths can be fine tuned. The intensity of the pump wave is reduced and the intensity of the idler and signal waves is increased, as light passes through the non-linear crystals. The resonator allows only the idler and signal waves to oscillate and the gain from the non-linear crystal allows the idler and signal waves to amplify and compensate for the losses in the round-trip. Additional prisms or diffraction gratings are used to reduce the bandwidth of the cavity feedback and reject the idler waves, allowing only the signal wave to oscillate and amplify. As it is typical with non-linear optics the conversion efficiency from the pump waves to the signal wave is higher for higher pump powers. Therefore, OPOs are usually coupled with

pulsed lasers in order to provide high output powers at multiple wavelengths that can be finely tuned. OPOs can only generate two wavelengths at the same time, idler and signal, and possibly a third, the pump. However, these systems are extremely complicated, precise and simultaneous control of the position of the non-linear crystals and the prisms is required, that is achieved with computer control. Therefore, generation of new wavelengths is slow, due to the change in the orientation of the optics in the OPO. OPOs are thus expensive and complex devices but are extensively used in applications where multiple excitation wavelengths are necessary [182–184].

1.4.6 Lasers Used in Optoacoustics

There are many materials that can be used as the active medium, gases that are used in gas laser or in a crystal structure used in solid state lasers. As we have already discussed earlier, Optoacoustic Imaging requires short pulses, usually in the order of a few nanoseconds, with high peak power and high repetition rate, according to the application, OR-PAM, AR-PAM or PACT. Wavelength tunability is necessary to fine tune the wavelength to match the optical absorption line of different molecules, as it is for all optical imaging modalities. Some of the most common lasers used in Optoacoustics are solid state lasers [135], such as the Nd:YAG laser [151], the Ti-Sapphire laser, dye lasers [69, 185]. It is very common that some of these lasers are coupled with an OPO to increase the wavelength tuning range [69].

• **The Nd:YAG laser.** The Nd:YAG laser consists of an YAG ($Y_3Al_5O_{12}$) crystal that is doped with Nd particles at a density of $0.1 - 1\%$. The population inversion is created at the Nd^{3+} ions and it is a 4-level system. The spontaneous lifetime of the upper laser level is very long, 230μs, that makes the Nd:YAG laser a great candidate to be Q-switched. It is optically pumped using either a flash lamp or a laser diode at 808nm. The characteristic output wavelength is 1064nm with a relative bandwidth of 10^{-5}. The wavelength can be up-scaled to 532nm with a Second Harmonic Generator. The existence of these 2 lines make it very easy to couple it with an OPO to generate a tunable wavelength laser. Nd:YAG lasers are used as continuous wave (CW) lasers or as pulsed lasers. Q-switched Nd:YAG lasers can produce 10ns pulses, with 100mJ - 1J or pulse energy at repetition rates or a few hundred Hz. This means that the peak power they can provide is 10-100MW, with a mean power of 1-10W. A Q-switched diode pumped Nd:YAG laser coupled with an OPO is an common laser that is used in Optoacoustic Imaging [184, 186, 187].

• **The Ti:Sapphire laser.** The Ti:Sapphire laser consists of a Al_2O_3 crystal doped with Ti atoms at a 1% density. The distance between the Ti^{3+} ions in the crystal affects the energy levels that have a vibronic nature. The Ti:Sapphire lasers is a 4-level system; levels 0 and 2 are the ground vibronic state of the ground and first excited electronic state respectively and levels 1 and 3 are the excited vibronics states of the ground and the first excited electronics states respectively. Due to the existence of the multiple vibronic states, the relative emission bandwidth of the Ti:Sapphire laser is very large, in the order of 10^{-1}, with a central wavelength of 790nm that can vary between 660 and 1180nm. The emission wavelength can be tuned by reducing the cavity feedback with a pair of prisms at different angles. The addition of an OPO can extend the emission wavelength range of the Ti:Sapphire laser. The spontaneous lifetime of the upper laser level is short at 3.8μs. Therefore, the Ti:Sapphire is not a very good candidate for Q-switching, but can produce ultra-fast pulses, through modelocking, due to its very wide emission bandwidth. It is optically pumped usually with frequency doubled (SHG) Nd:YAG laser (532nm), whether it is CW or in pulsed mode. The Nd:YAG laser can be Q-switched to pump the Ti:Sapphire laser in order to generate a 10ns pulse and provide 100mJ at around 800nm at repetition rates of a few hundred Hz. Its characteristics and its stability make it a

very appealing option for Optoacoustic Imaging and especially PACT [184, 186, 187].

• **Dye lasers.** Dye lasers consist of different dyes that are solved in water or alcohol. Different dyes can provide emission of different wavelengths in the range of 300-1500nm. Dye lasers are 4 level systems that also have vibronic nature, offering a wide emission and tuning range of 5% by the use of an etalon, a grating or both. The spontaneous emission lifetime is very short, 1-5ns lifetime, that makes Q-switching impractical for dye lasers. They are optically pumped by a lamp for cw operation or by a Nd:YAG laser that can be Q-switched to provide nanosecond pulses. The broad emission bandwidth makes them excellent candidates for modelocking that can provide 1ps pulses with 200nJ energy per pulse at 50MHz, with a peak power of 20kW and 1W mean power. However, the dye decays and decomposes with time and needs frequent maintenance. In addition, the dye needs to be changed in order to provide different emission ranges. The dye lasers were the first wide bandwidth lasers and that is the reason the have been used in Optoacoustic Imaging. However, nowadays the Ti:Sapphire is more stable and can offer a wider bandwidth and has replaced the dye lasers [184, 188].

These lasers are quite powerful and flexible providing many advantages in their use in Optoacoustic Imaging in the laboratory and well founded scientific research. However, they are still impractical for extended use in the clinics and fast commercialization of Optoacoustic systems. This happens for various reasons. Most important aspect is the high price and the big size of such laser systems. Optically pumping such lasers often require a second pump laser, that increases the cost, or a lamp that is not efficient for continuous use and generates a lot of heat that needs to be removed somehow. Often the cooling system in a laser is the most bulky component. These laser systems are very complex devices with multiple wavelength measuring and control components that further increase the cost of the overall system. Cooling systems are also necessary to cool not only the optical pump system but the active medium as well. In order to control these systems sophisticated control software is also necessary that adds to the cost and complexity. Frequent maintenance and re-alignment of the optical components is also necessary. For all these reasons there is a lot of research in developing smaller, lower cost, simpler laser sources for Optoacoustic Imaging.

1.4.7 Semiconductor Lasers or Laser Diodes

Semiconductor lasers are a special kind of solid state lasers, the active medium of which is based on a semiconductor material. Laser diodes, as they are mostly called, are a very attractive kind of laser for modern biological, and optoacoustic imaging, because they offer several advantages. Laser diodes offer small dimensions and ease of manufacturing that leads to the low-cost of these devices. In addition, laser diodes can provide a variety of available wavelength covering the whole range of UV to IR emission spectrum. Moreover, they are current pumped lasers, they convert current directly to laser light, that leads to high efficiency. However, their light output and beam characteristics, as well as their output power is worse compared to other types of lasers discussed above [189]. In any case, especially due to their small size and low-cost, semiconductor lasers have attracted a lot of attention lately and there are a variety of optical biomedical imaging techniques that use laser diodes [185, 190].

In order to understand how laser diodes work we need to shortly discuss first the basics of semiconductors. In a solid material the electrons are no longer bound to a specific atom, but rather are bound to the atom lattice structure. In a conductive material the electrons are "loosely" bound to the structure and they are allowed to move more freely in the whole medium in order to conduct current. In an undoped semiconductor material, such as silicon that has 4

electrons in its outermost shell, in 0K temperature the electrons completely fill the valance band and the conduction band is completely empty. There is an energy gap E_g between the valance band and the conduction band. At higher temperatures, some of the electrons are excited from the valance band to the conduction band leaving behind an empty spot in the valance band that other electrons can occupy. Instead of following the electrons moving in the valance band and occupying the empty spots, it is easier to follow the hole moving in the valance band. Therefore, the electrons in the conduction band and the holes in the valance band can move in the presence of an electric voltage and conduct current [191].

If we replace a few of the silicon atoms in the lattice with other atoms with 5 electrons in the outermost shell, like arsenic atoms, then the lattice will have an abundance of free electrons. This type of material is called an n-type semiconductor, it has plenty free negative charge carrier. If instead of an atom with 4, or 5, electrons in its outermost shell we dope the semiconductor with atoms with 3, or 2, electrons in the outermost shell, then we create a p-type semiconductor material. This material has plenty of positive charge carriers, that are the holes, to conduct current.

When the two semiconductor material types are brought in contact then the free electrons in the n-type and the holes from the p-type are electrically attracted to the junction and recombine, emitting either heat or a photon. The photons in this case will have a wavelength that corresponds to the energy gap between the conduction and the valance band, E_g. Light can interact with the electrons and the hole of a semiconductor material and can force excitation of an electron from the conduction band to the valance band leaving a hole behind, as well as stimulate an electron-hole pair to recombine by re-emitting a coherent photon. This is the basis of laser generation in a semiconductor material.

As we have already discussed, in order to create a laser light we need an active medium, population inversion and cavity feedback. We have already discussed what the active medium is in the case of semiconductor lasers. We need now to create population inversion and introduce cavity feedback. Most semiconductor lasers use a small layer of undoped material sandwiched between the n- and p-type materials to create a, p-i-n, a double-heterostructure. The energy band gap of the undoped material is lower compared to the band-gap between the n- and p-type materials, and this band-gap defines the emitted wavelength. A forward biased current pushes electrons from the n-type material and holes from the p-type material into the undoped material, that after a short lifetime, at the order of a few nanoseconds, recombine by emitting a photon. Therefore, the inverse population is created directly by applying a forward current at the p-i-n heterostructure [189, 192, 193].

The undoped area acts as the active material that amplifies the light through stimulated emission. Moreover, the double heterostructure active region, offers two more advantages. Since the energy band gap is lower than the n-p type the electron-hole pairs are confined in the undoped material and are forced to recombine, offering high material gain. In addition, the middle undoped material has a higher refractive index compared to the n- and p-type materials that act as a waveguide to confine the photons in the active medium. Therefore the active medium acts as a naturally built Fabry-Perot resonator that offers the necessary cavity feedback to the laser field. By controlling the refractive index of the materials the reflectivity of the once facet is usually kept high, $> 99\%$, and the output facet is usually uncoated with a natural reflectivity of 30-40%.

Laser diodes are available in a big variety of wavelengths form the UV to visible and the IR region. The emission wavelength depends on the materials used to develop the p-i-n junction and different materials or different concentration ratios of materials can offer various band gaps and emission wavelengths. Some of the most common materials along with their emitted wavelengths

are the following: Gallium nitride/ Indium gallium nitride (GaN/InGaN) emits between 375-480nm, Aluminum gallium indium phosphide / Gallium arsinide (AlGaInP/GaAs) emits between 620-680nm, Gallium aluminum arsinide/ Gallium arsenide (GaAlAs/GaAs) between 750-880nm, Indium gallium arsenide/ Gallium arsenide (InGaAs/GaAs) between 905-1050nm etc. However, there is a gap in the spectral region between 480 and 620 nm. The development of laser diodes that emit in new wavelengths depends on the development of new materials that offer this band gap. Only recently laser diodes that emit in the green and yellow area of the visible spectrum have become available, but still in low output cw power [189, 192, 193].

Semiconductor lasers are current driven devices and the current controls the medium gain, by controlling the amount of inverse population. Therefore, at low current values not enough population inversion has been achieved and spontaneous emission dominates, making the laser diode emit incoherent radiation, i.e. function as a Light-Emitting-Diode (LED). However, when the current exceed a threshold value (I_{th}) then the stimulated emission dominates and laser field is amplified. The input current and the optical output power, after the threshold value, present an almost linear relationship until it reaches saturation.

By modulating the input current the output power will also be modulated accordingly. However, there will be a delay due to the fact that the laser field needs to oscillate a couple of times in the cavity, that, for a 1mm optical cavity length, corresponds to a few tens of GHz, maximum modulation frequency. Therefore, it is straightforward to create a strong and short pulse using semiconductor lasers, by applying a short and strong forward current to the laser diode. However, generating short and high current pulses requires sophisticated electronics as we are going to discuss later. Generating a strong pulse using semiconductor lasers is usually achieved using gain-switching, as the medium's gain is changing from low to high in order to generate a strong pulse. Gain-switching is similar to Q-switching in the sense that the energy is stored in the medium's inverse population. In the case of gain-switching it is faster and simpler to create the inverse population, since semiconductor lasers are current driven devices and do not require external optical pumping to generate the inverse population. Moreover the cavity feedback in the case of gain-switching is not disrupted, as it is in Q-switching, because the inverse population build up is faster because of the current applied. Gain-switched semiconductor lasers can generate nanosecond pulses at repetition rates of a few hundred kHz [193].

However, the fact that semiconductor laser are current driven devices has some drawbacks. Current flowing through any resistor will generate heat. However, there is no perfect material that presents zero resistance and laser diodes are no exception to this rule. Therefore, every laser diode has a small but finite resistance, of the order of $\sim 0.5\Omega$ that generates heat when the laser diode is emitting light. The semiconductor material is very sensitive to heat that changes the physical and optical size of the cavity causing instabilities on the laser diode function and operation of laser diodes demands good temperature control. Moreover, the emitted wavelengths slightly change due to a different longitudinal mode dominating at different optical wavelength of the cavity. In addition, at higher temperatures the threshold current increases and the efficiency of the laser, drops. This is particularly important for continuous wave laser diodes; all laser diodes are build on top of small heat sinks to dissipate the generated heat. If heat management is implemented laser diodes offer stable and reliable operation for over 10000 hours [192, 193].

The active region of a laser diode usually has a rectangular shape. The height of the active region is defined by the size of the undoped material between the n- and p- type semiconductor material and is usually very small, at the order of 1 μm for double heterostructure laser diodes, at the order of nm for quantum well laser diodes. The length of the active region has to be long to increase the gain of the medium, with the optical cavity length (i.e. nL, with n the refractive index of the medium) to be around 1 mm. The width can vary to control the threshold (and

operating) current along with the gain of the medium and usual values are between 5 - 400 μm depending on the designed laser diode application as we will discuss later [194].

The shape of the active region in laser diodes affects the output laser beam quality. The difference in size between the active region height and width results in different beam divergence, around 6-12^o in the slow axis and up to 15-40^o in the fast axis. However, the fast axis is the short axis and vice versa. In addition, the rectangular shape of the active region causes astigmatism, i.e. the beam appears to come from two different spots; the fast axis waist appears closer to the active layer facet than the waist of the slow axis by 3-10μm for single mode laser diodes and 10-50μm for multi-mode laser diodes [194].

The output beam quality is often quasi-Gaussian as it appears more divergence and bigger waists compared to a Gaussian beam. For this reason, and due to the big laser diode divergence angle (and big numerical aperture, NA) aspheric lens are used to collimate the laser diode output, as they offer very high NAs of up to 0.6. A pair of anamorthic prisms or a pair of two cylindrical lenses can also be used that will correct the cylindrical output beam shape, and make it spherical. This approach comes at the cost of harder alignment and higher motion and vibration sensitivity [195].

There are two main types of laser diodes developed for different applications with distinct design characteristic. These are the continuous wave laser diode (CW-LDs) and the pulse laser diodes (P-LDs) [196].

• **Continuous Wave Laser Diodes.** Continuous wave laser diodes are designed for continuous use, which means that they require a continuous electrical current to maintain the population inversion. The continuous pumping current generates heat that is the main limiting factor in CW-LDs. Therefore CW-LDs are designed to be able to manage and dissipate the generated heat. The length of the active region needs to be increased to allow better heat removal through the heat sink.

The threshold current, and therefore the operating current as well, needs to be kept low. For this reason the active region width is kept low, at the order of 5 to 35 μm, modern high power laser diodes go up to 100μm. However, the low operating current means low population inversion and low medium gain. To increase the medium gain the cavity feedback needs to increased by increasing the output facet reflectivity. CW-LDs offer mean output power of a few mili-Watts up to a few Watts.

CW-LDs can be modulated with frequencies up to a few GHz. CW-LDs are current driven devices and the light output is directly proportional to the driving current temporal profile. Therefore, CW-LDs can be arbitrarily modulated to produce light oscillating as a sine wave, a triangle or a square pulse etc. However, up to now, the instantaneous peak current does not exceed the maximum current the CW-LDs can achieve in CW operation. In any case, heat management is still the main limitation in driving the CW-LDs with higher currents and achieving higher output peak power.

The small size of the active region increases the output beam divergence, that reaches 35-45^o for the fast axis. However, with proper optics that offer high NA, the small size of the active region makes it easier and more efficient to focus the output beam and increase the energy density.

CW-LDs are available in many wavelengths over the whole emission spectrum over the UV, visible and the IR.

• **Pulsed Laser Diodes.** In order to address the problem of low output power in applications where strong pulses are necessary Pulsed Laser Diodes have been developed. P-LDs are designed for pulsed operation with very low duty cycles, usually less than 1%. Therefore, heat removal is not a critical issue any more and their cavity design differs from that of a CW-LD.

Since heat is not a critical issue any more in P-LDs, the threshold and operating currents of the P-LDs can be increased. The width of the active area in P-LDs can also be increased to reach up to 400μm or even more. The increased active area size increases the medium gain, but also increases the amount of oscillating modes that get amplified. For this reason, all P-LDs are multi-mode laser diodes. P-LDs are pumped with very high peak currents, tens of amperes, at short bursts, of a few nanoseconds up to a maximum of 200 ns. The very high pump current creates a very high instantaneous gain, due to the very high inverse population. Therefore, P-LDs provide much higher peak power than the CW-LDs. However, the pump current pulse requires sophisticated electronics to create such high peak current at such short pulse widths.

The output facet reflectivity of P-LDs is reduced to allow the laser field to drain fast and keep the light pulse width low, that has a minimum of around 3 ns due to the round trip time. However, the instantaneous high photon density can cause damage on the facet, and burn a spot lowering the efficiency of the P-LD, that is called Catastrophic Optical Mirror Damage (COMD), and specific precautions need to be taken. COMD usually happens in the nanosecond scale and without any previous indication or degradation of the P-LDs performance. Heat management is the limiting factor in CW-LDs while COMD is the limiting factor in P-LDs in the effort to achieve higher output peak power from these LDs.

The length of the active region of P-LDs is shorter than that of CW-LDs and the width much wider. Therefore, the output beam divergence is smaller, at about 25^o. Multiple active regions can be stacked on top of each other that increases the output power up to 650W peak power [197]. However, the big active area shape makes it quite hard and inefficient to focus the light in a small spot and increase the energy density. P-LDs are only available at the NIR range, a wavelength range that the market demands for Light Detection And Ranging (LiDAR) applications.

Semiconductor lasers and specifically laser diodes are versatile laser devices that offer many advantages for miniaturization and commercialization of biomedical devices and specifically Optoacoustic imaging. For this reason there is a lot of work that focuses on developing laser diode Optoacoustic systems [198, 199]. The main disadvantage of the LDs for OA imaging is their low output power, since OA imaging requires fast and strong energy transients to generate a detectable OA signal.

1.5 Objective of Thesis

Optoacoustic imaging overcomes the light scattering problem in tissue by detecting ultrasound waves generated by short optical transients instead of backscattered or transmitted light. Therefore, OA imaging offers optical absorption contrast at higher depths in tissue compared to pure optical imaging methods. However, OA requires very short and strong optical pulses, ideally at multiple wavelengths to perform multi-spectral OA imaging. These pulses are usually generated by optically pumped Q-Switched Nd:YAG lasers or optically pumped Ti:Sapphire lasers equipped with an OPO, especially in Photoacoustic Computer Tomography methods, where a lot of energy is necessary. In Optoacoustic Microscopy, either Acoustic Resolution or Optical Resolution, the same kind of lasers dominate, as they offer enough energy and high repetition rates to generate a detectable Optoacoustic signal. However, these lasers present large form factors, often require cooling and frequent re-alignment, they are very complex machines and therefore come at high cost of manufacturing and maintenance. These lasers hinder, thus, the wider use of Optoacoustic devices and the need for low-cost, miniaturized light sources that can generate a strong OA signal emerges.

For this reason, a lot of attention has been drawn lately in developing semiconductor laser sources for OA imaging. These light sources, as discussed above, offer high efficiency, very small size and low manufacturing and maintenance costs but suffer from their low output power and poor laser beam characteristics. P-LDs have been considered as an attractive alternative due to their higher output power, compared to CW-LDs, but their big emitter size confines their use to Optoacoustic tomography and their wavelength, available only in the NIR region, limits the optoacoustic signal strength from blood due to its low light absorption in this wavelength. OR-PAM has also been developed using P-LDs but the lateral resolution achieved is lower compared to more advanced lasers. CW-LDs have been considered only for OR-PAM because of their low output power. LED's have also been considered for Optoacsoutic Tomography because of their huge emitting areas and long pulse width that they offer.

In this frame, the scope of the current work is to **develop a laser diode excitation source for Optoacoustic imaging and sensing**. I investigated whether there are new ways of using LDs in order to increase their output power and generate a strong OA signal for various applications.

In light of this motivation, this thesis has focused in four parts:

1. CW-LDs are available in a wider wavelength range, compared to P-LDs, that is highly attractive for Optoacoustic Imaging. We investigated whether we can **overdrive** the CW-LDs, i.e. *exceed the manufacturer specified absolute maximum current value for a short duration in order to achieve higher peak power than the manufacturer specified absolute maximum power value without destroying the CW-LDs.* We had to prove that the overdriven CW-LDs can provide enough energy per pulse in order to generate a strong OA signal.

   Different possible applications for the overdriven CW-LDs have been investigated.

2. Laser Diodes have not been used so far for Optoacoustic Mesoscopy and overdriven CW-LDs are an excellent candidate for LD-Raster Scanning Optoacoustic Mesoscopy, because of their output power, beam characteristics and availability in multiple wavelengths.

3. Overdriven CW-LDs due to their small size and low-cost can be used to develop a single point, miniaturized, Optoacoustic oximeter, that can accurately monitor, non-invasivley, the local vascular oxygenation in tissue.

4. Single point detection finds also applications in environmental sciences as well. Photoacoustic Spectroscopy is well known in gas and particle detection for environmental studies. Overdriven CW-LDs can contribute in developing low-cost and miniaturized OA sensors for on-board detection of black carbon (soot) and Green House Gases (GHG), such as Nitride Oxides (NOx), in Internal Combustion Engine (ICE) exhaust streams.

1.6 Structure of Thesis

Following the research objectives this dissertation is structured in six parts:

Chapter 1 discusses the main biomedical imaging modalities, non-optical and optical, used nowadays and introduces Optoacoustic imaging in this context. Identifies as one of the main limitation in OA imaging the laser sources because of their big size, complexity and high cost.

Discusses semiconductor lasers as an alternative light source for OA imaging and points at their low output power as their main disadvantage.

Chapter 2 presents the current state of laser diode systems that have been previously developed and indicates that CW-LDs can be overdriven to provide enough power to be used as an OA light source. A custom-made laser diode driver is presented and the multiple CW-LDs have been characterized when overdriven. A single wavelength RSOM system has been developed and OA images from a mouse ear and human skin have been captured.

Chapter 3 builds upon the work presented in Chapter 2 and a 4 wavelength LD-RSOM system is demonstrated. A unique way of multiplexing different wavelengths in the Time Domain with signal processing in the Frequency Domain, previously developed [200], is optimized and presented here as well. The multispectral LD-RSOM achieves high resolution images of mouse ears *in-vivo* as well as fast vessel dynamics during injection of extrinsic contrast agents.

Chapter 4 shows a low-cost and miniaturized dedicated OA oximeter. Overdriven CW-LDs at two wavelengths can be used in order to monitor with high accuracy the local blood oxygenation non-invasively in tissues *in-vivo*. By removing the need to generate images, that requires some kind of scanning, the overall cost and the complexity of the device can be reduced and the low-cost and small size of the overdriven CW-LDs can make the device portable and hand-held.

As a last application of overdriven CW-LDs, Chapter 5 presents a miniaturized OA sensor for monitoring black carbon emissions, as well as NOx, in ICE exhausts on board or as a distributed network of sensors for environmental air pollution monitoring. Optoacsoutics has already presented its potential in detecting soot and GHG but the existing systems are bulky and expensive. A unique sensor chamber design is presented in this chapter that in combination with the overdriven CW-LDs make the developed OA sensor suitable for on-board monitoring, something that was not previously possible.

Chapter 6 summarizes the work and discusses the main advantages of overdriven CW-LDs over other semiconductor lasers for OA signal generation. It highlights the potential that overdriven CW-LDs have in contributing to the development of future low-cost and miniaturized OA systems with applications in many fields. The drawbacks of the overdriven CW-LDsLDs are also discussed and possible solutions are proposed.

Chapter 2

Overdriving Continuous Wave Laser Diodes

2.1 Introduction

The work presented in this chapter has been separately published and the Figures and Tables are adapted versions from [201][1], with permission from the Journal.

As already explained in the previous chapter, OA imaging requires strong energy transients, i.e. short and high intensity pulses, in order to satisfy the stress and thermal confinement limits [eq. (1.19)]. The high peak power of the excitation pulse and the short pulse width are proven to generate high signal-to-noise (SNR) OA signal, since the OA signal strength depends on the first derivative of the heating function [eq. (1.27)]. In addition, high repetition rates ensure higher SNR through averaging and/or fast imaging. The delivered energy per pulse is another parameter that can characterize the performance of an OA system. We have already discussed that PACT system require very high energies per pulse, hundreds of mJ, since a broad area on the sample is illuminated simultaneously and they need to achieve high penetration depths. In contrast, OA mesoscopy systems, require less energy per pulse, tens to hundreds of μJ, since they illuminate a much smaller area and the achieved imaging depth is at the order of a few millimeters. OA microscopy requires less energy per pulse, tens to hundreds of nJ per pulse, as the light pulse is tightly focused on the sample surface and the imaging depth is only superficial, only a few hundred μm.

For all these applications, up to now high-end lasers have been used, such as Q-switched Nd:YAG, Ti:Sapphire, dye laser coupled with an OPO to fine tune the wavelength. As explained above, these lasers can produce high energy, very short pulses at multiple wavelengths, making them suitable for developing and testing OA in the laboratory. However, these lasers present large form-factors, require extensive cooling, are complex devices and therefore require high cost of manufacturing and maintenance. These drawbacks, render these lasers unsuitable for miniaturization, cost-reduction and vast commercialization of OA devices.

For this reason, there has been a lot of work on developing alternative light sources for OA imaging [202–204]. The focus has been in using semiconductor lasers that are miniaturized,

[1] Antonios Stylogiannis developed the laser diode driver presented here and characterized the overdriven laser diodes. Dr. Ludwig Prade developed the raster scanning imaging system. Antonios Stylogiannis and Dr. Ludwig Prade integrated the laser diode illumination source into the raster scanning imaging system and performed the imaging experiments. Dr. Juan Aguirre processed the human skin images. Dr. Andreas Buehler, Dr. George Sergiadis and Dr. Vasilis Ntziachristos helped with extensive discussions and guidance in conducting this research.

low-cost and are available in multiple wavelengths. Semiconductor light sources are commercially available, do not require extensive cooling and present stability, high efficiency and versatile operation, as they are all current driven devices. However, their output peak power and energy per pulse is orders of magnitude lower than the traditional laser sources used in OA. Light-Emitting-Diodes (LEDs), Pulsed Laser Diodes (P-LDs) and Continuous Wave Laser Diodes (CW-LDs) have been used for OA imaging.

LEDs are incoherent light sources that have almost the same operating principle as a semiconductor laser; light generation is dominated by spontaneous photon emission. In LEDs the output facet reflectivity is low, there is no cavity feedback and thus stimulated emission does not take place. LEDs are available in multiple wavelengths covering the whole visible and NIR range. They feature large emitting areas of approximately $1 \times 1mm^2$ in order to achieve higher output power and big divergence angles, as all semiconductor sources, that makes attempts of focusing their output light very hard and inefficient. In addition, LED can be pulsed but their output optical pulse width is relatively long due to the longer spontaneous lifetime of the electron-hole recombination. Therefore, LEDs are mainly used in PACT applications [202–204].

LEDs emitting at the range of 420-620 nm were overdriven with up to 50A, 20-fold their nominal CW value, 200ns pulses at 500Hz, that is 0.01% duty cycle in order not to damage the LED [205]. The LEDs provided up to 9 μJ per pulse. By the use of low frequency, 3.5MHz, cylindrically focused UST, that present high efficiency, signal had to be averaged between 1.000 and 10.0000-fold to achieve good SNR when imaging blood filled tubes immersed in an Intralipid suspension. However, LEDs even when overdriven present low repetition rates and require extensive averaging to increase the SNR that slows the image acquisition down and increases the imaging time. A commercial handheld LED dual US and PACT system uses 4 rows of 36 LEDs (144 total LEDs) at four different wavelengths, 470, 620, 690, 850 nm in order to increase the energy per pulse [206]. The LEDs arrays are driven with 20A, 35-150 ns pulses of up to 16kHz providing up to 200 μJ per pulse, for the 850 nm LED array, and signal averaging of 384 times had to be employed. This system has been tested in human *in-vivo* in imaging peripheral microvascular function and dynamic changes.

P-LDs utilize large emitting areas, usually stacks of multiple p-i-n junctions. Although their beam divergence is relatively low, focusing the output of P-LDs into a small focal spot is inefficient. P-LDs are commercially available in the NIR region and despite the fact that blood is the most dominant absorber in this region, the blood absorption in this range is a few orders of magnitude compared to the blood absorption in the visible region, specifically in the blue. Therefore, despite their high energy output the OA SNR from blood vessels using P-LDs is still low.

The possibility of using P-LDs in OA Imaging has been extensively investigated in PAT [207–209] and OR-PAM [210–213]. PLDs emitting in the 803-905 nm region, that achieve peak power of hundreds of Watts, pulsed with long pulse widths of 130-500 ns and offer high pulse energies of 0.87-1.4 mJ at repetition rates of 2-10 kHz, have been used in PAT systems that utilize a low frequency UST of 2-7.5 MHz [207–209]. These systems have imaged phantoms with dye filled tubes [207], tissue mimicking phantoms [209], in-vivo human finger joint [208]. However, these systems offer low spatial resolution, as they perform PAT, and they require heavy averaging, up to 5000 pulses [207], that slows the imaging speed. OR-PAM systems used PLDs emitting at 905 nm with high peak power of up to 140 W, pulsed with long pulse widths of 35-124 ns at repetition rates of 0.8-10 kHz [210–213], offering 0.33-5.6 μJ per pulse. Low frequency USTs of 2-10 MHz have also been used here, due to their increased sensitivity. These systems offered lateral resolution of 1.5-500 μm when imaging phantoms and ex-vivo samples. Extensive averaging, 128-5000 averages, is necessary to increase the SNR that in combination

with the low pulse repetition rate increases the acquisition time drastically.

CW-LDs are an attractive alternative to LEDs and PLDs as they are commercially available in the visible region where blood absorption is strong and due to their smaller emitting area that, despite their large output beam divergence, can be efficiently focused in small diffraction limited spots. Their drawback is the very small peak power that has limited their application in OR-PAM.

CW-LDs that emit at the blue/violet region, 405 nm, have been used in OR-PAM systems. The CW-LDs have been pulsed with 10-174 ns pulses, at peak powers not exceeding 300 mW, at 1-30 kHz repetition rates providing up to 52 nJ of energy per pulse. One of the systems used a low frequency UST of 3.6 MHz and imaged a carbon fiber phantom and a mouse ear ex-vivo with 0.95 μm lateral resolution [214] and the other used a higher frequency 50 MHz UST to image red blood cells and a mouse ear in-vivo with lateral resolution of 1 μm [215]. However, both systems used extensive averaging of 512-3000 times to increase the SNR at the expense of reduced the imaging speed. A CW-LD emitting at 784 nm and a peak power of 120 mW has been modulated with a sine wave at 2.45 MHz and generated an OA signal of the same frequency that was detected with a 2.45 MHz UST [216]. However, excitation with a sine wave lack the high energy transient of an optical pulse and this results in low SNR. This system offers no axial resolution, 1 mm lateral resolution and has imaged rabbit blood vessels.

Semiconductor laser sources, LEDs, P-LDs and CW-LDs have proven their ability to generate a detectable OA signal in various applications, including biological in-vivo samples. However, LEDs lack the focusing ability and can only provide long pulse widths to be used in mesoscopic applications. P-LDs are only available in the NIR where blood absorption is very low to generate a good SNR signal. CW-LDs suffer from low energy output and thus low OA SNR. All these sources have, therefore, required a lot of averaging that in combination with the low pulse repetition rates increases the acquisition time.

In this work, we hypothesized that we can overdrive the CW-LDs in order to increase their peak power and the pulse repetition rate, without destroying and damaging them. We overdrove CW-LDs with ultra short currents pulses, with peak currents exceeding the nominal CW-LD absolute maximum limits imposed by their manufacturer in cw operation in order to achieve higher output peak power than the absolute maximum value of the CW-LDs in cw operation mode. We also achieved much higher repetition rates than previously reported, speeding up the acquisition time. We developed a raster-scanning mesoscopy imaging system using the overdriven CW-LDs and imaged phantoms and biological samples in-vivo. We proved that it is possible to capitalized on the advantages of CW-LDs, low-cost, small size, small emitting area and wavelengths availability and overcome their previous limitation, i.e their low output power, and used CW-LDs in OA imaging systems in order to further push the miniaturization and cost reduction of such systems that will help their fast commercialization.

2.2 Materials and Methods

2.2.1 Pulsed Laser Diode Driver

We developed a custom laser diode driver, that is an updated version of the pulsed laser diode driver developed form radar applications in [217]. This circuit delivers high current, nanosecond pulses at very high repetition rate to the laser diode LD. Figure 2.1a shows the pulsed laser diode circuit. The capacitor bank C is charged through the charging $R_C - C - D_1$ circuit at high voltage HV, when the MOSFET Q_1 is not conducting. When Q_1 (DE275-501N16A; IXYS, USA) is triggered with a 15 V square pulse conducts and allows the capacitor bank C to

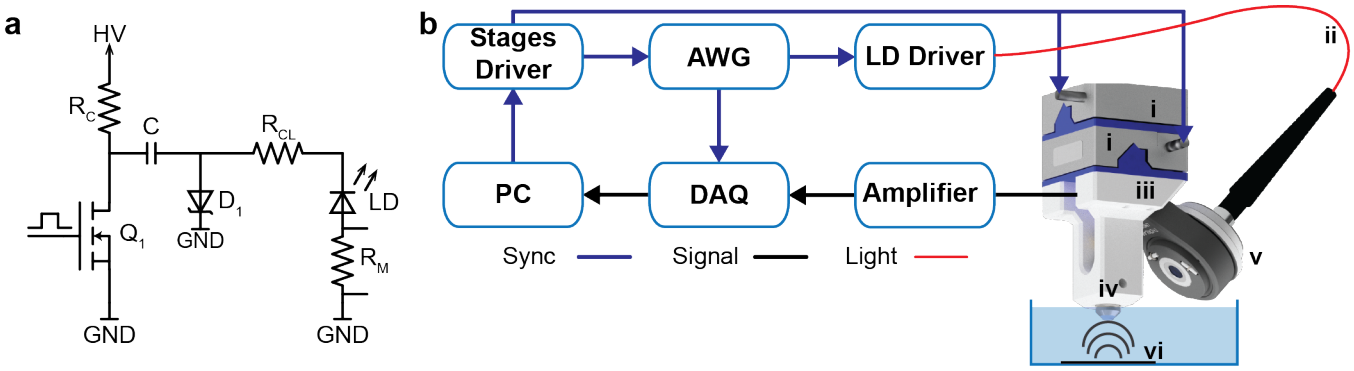

Figure 2.1: **(a)** Schematic of the laser diode driver developed. **(b)** Schematic of the laser diode-based optoacoustic imaging system. DAQ, data acquisition card; PC, personal computer; AWG, Arbitrary Wavefunction Generator; LD, Laser Diode; **i**, Stages, **ii**, 3D printed hodler; **iii**, UST, Ultrasound Transducer; **iv**, focusing optics and tip-tilt mount; **v**, optical fiber; **vi**, sample in water for optimal coupling. Adapted with permission from [201].

discharge through the LD via the $C - Q_1 - R_M - LD - R_{CL}$ circuit. The value of the charging resistor R_C, 3.4 kΩ, and the capacitance of C, 400 pF, defines the charging time constant of the $R_C - C$ circuit and thus the maximum repetition rate this driver can provide, since the capacitor bank C needs to be fully charged at HV before the next trigger arrives, to discharge again. The current limiting resistor R_{CL}, 1 Ω, is limiting the current through the LD and the monitor resistor R_M, 0.1 Ω, is positioned in series with the LD to allow easy monitoring of the driving circuit output current. The maximum current that this circuit can deliver is defined by the total resistance of the the discharge circuit, $R_t = R_{CL} + R_Q + R_M + R_{LD}$, where R_Q is the conducting resistance of the MOSFET, 0.4 Ω, and the R_{LD} is the dynamic resistance of each CW-LD. The duration of the pulse width is constant and cannot be externally controlled in this circuit. The rise time of the current pulse is determined by the turn on time of Q_1 and the fall time by the R_tC time constant of the discharge circuit. All the components used can be operated with high voltages up to 500 V. This pulsed laser diode driver can provide peak currents of up to 50-60 A, electrical pulse widths of ∼10 ns at high repetition rates of 500kHz, a combination that commercial laser diode drivers cannot offer.

2.2.2 Diode Characterization

Using the pulsed laser diode driver presented above we tested six CW-LDs emitting in the visible and NIR region that are presented in Table 2.1 along with their package type, emitting wavelength, rated power and operating current as well as their manufacturer or provider. The capacitor bank C was charged at various voltages ranging from 10 to 270 V by a variable high voltage supply (EA-3050B; EA, Germany) that has a maximum supply voltage of 300 V. To trigger the pulsed laser diode driver we used an Arbitrary Waveform Generator (AWG, 33522B; Keysight, USA), that provided a square Transistor-Transistor-Logic trigger pulse to the pulsed laser diode driver at 50 kHz. To monitor the optical output of the CW-LDs we used a biased photodiode (DE10A/M; Thorlabs, USA) and recorded the signal with a high speed digital oscilloscope (DPO 7254; Tektronix, USA). At the same time, at another channel of the digital oscilloscope, the output monitor of the pulsed laser diode driver was connected to record the current pulse through the CW-LD under test. The two signals were recorded and averaged 1000 times to reduced noise and the Full-Width-at-Half-Maximum (FWHM) of the optical pulse as well as the peak current were recorded. In order to measure the energy per pulse of the lasers

we used a handheld power meter (Edmund Optics, USA) and recorded the mean output power of the CW-LDs, that when divided by the repetition rate provides the energy per pulse. To measure the output wavelength of the CW-LDs we used a USB spectrometer (Ocean Optics Spectrometer 2000, Ocean Optics, USA).

Table 2.1: Characteristics of the laser diodes used with the driver. The "CW Power" and "CW Current" columns indicate the manufacturer-specified absolute maximum power and current in CW operation, respectively. Adapted with permission from [201].

Laser Diode	**Package Type (TO Can)**	**Wavelength (nm)**	**Power (W)**	**Current (A)**	**Manufacturer Provider**
NDB7K75	∅9mm	445	3.5	3.0	Nichia, Japan
TB450B	∅5.6mm	450	1.6	1.6	Osram OS, Germany
HL63193MG	∅5.6mm	638	0.7	1.0	Oclaro, USA
RTL780-1000G	∅9mm	780	1.0	1.4	Roithner LaserTechnik, Austria
L808P1000MM	∅9mm	808	1.0	1.5	Thorlabs, USA
RTL830-1.5G	∅9mm	830	1.5	2.1	Roithner LaserTechnik, Austria

2.2.3 Laser Diode Imaging System

In order to test the CW-LD in OA imaging we developed a laser diode raster scanning imaging system [126, 151], the schematic of which is presented in Fig. 2.1b. Matlab (Matlab 2016b, Mathworks, USA) was installed in a Personal Computer (PC) and was controlling the system. The stages driver (C-867.260; Physik Instrumente, Germany) was controlling the movement of the two stages (M-663; Physik Instrumente, Germany) that were mounted at 90^o with respect to each other to form an X-Y scanner (**i** in Fig.2.1b). The stages were moving in a sweeping snake-like motion with x being the fast axis and y the slow axis. The x-axis is moving from the starting position to the end position in one direction at a constant speed (performing a B-Scan), recording signals at multiple x-positions in between (that are called A-Scans) at the same y-position. Then the slow y-axis is moving to the next y-position and the fast axis is moving in the opposite direction performing the next B-Scan. When the fast axis was moving a distance equal to the desired step size, the stages driver was sending a TTL trigger signal to the AWG and to the Data Acquisition Card (DAQ, Razor Express 14x2 CompuScope; Dynamic Signals, USA) to trigger the laser pulse train and signal acquisition. The AWG, upon trigger, was sending a pulse train of N_{avg} pulses at the required repetition rate f_{rep} to the pulsed laser diode driver, with N_{avg} the number of pulses to be averaged. The OA signal from the UST was amplified by a low noise amplifier (AU-1291-R; Miteq, USA) before being recorded with 200 MS/s Sampling Rate.

The CW-LD was mounted on the pulsed laser diode driver and was coupled into a multimode glass fiber (**ii** in Fig.2.1b, M45L01; Thorlabs) of 400 μm core diameter and 0.5 Numerical Aperture (NA), that was achieved by immobilizing the CW-LD emitting window against the fiber tip. The coupling efficiency achieved is $\sim$ 80%, due to the big fiber diameter and high NA

and the small distance between the CW-LD emitting area and the fiber tip. The stages where holding a custom 3D-printed holder (**iii**) that was hosting the UST (**iv**) and the focusing optics (**v**). The spherically focused UST has a central frequency of 28.8 MHz, 112% relative bandwidth and an f-number of 1.07 (SNX160333 HFM29; Sonaxis, France). The fiber was coupled to a fiber collimator (F220SMA-532; Thorlabs) with focal length of f_1=10.9 mm and a focusing lens (A260-A; Thorlabs) with focal length of f_2= 15.29 mm. The magnification ratio (f_2/f_1) of this lens pair is 1.4 and an illumination spot of 560 μm is expected. The fiber and the focusing lens pair were mounted on a tip-tilt mount (KAD11F; Thorlabs) for easy alignment of the optical and ultrasound focal spots on the sample (**vi**). We measured the optical illumination spot on the sample using a Charge-Coupled-Device (CCD) camera (daA1920-30um; Balser AG, Germany). The FWHM of the illumination spot was an ellipse with 880 and 720 μm diameter in the two directions, due to the big illumination angle of $\sim 60^o$ between the illumination and the detection axes. The illumination area is estimated to be 0.63 mm^2.

2.2.4 Experimental Measurements

For all the imaging experiments we used the blue CW-LD (TB450B) for two reasons; we were only able to couple the ∅5.6 mm package CW-LDs and due to the strong blood absorption at 450 nm. The applied voltage on the pulsed laser diode driver was set to 300V, the pulse energy was measured to be 72 nJ after the focusing optics and the pulse width was 10 ns.

In order to characterize our system's performance and resolution we employed a suture phantom that consisted of 3 sutures with different diameters of 20, 30 and 50 μm, crossing one another, immersed in clear water. All sutures were perpendicular to the detection axis, that is the axis of the UST. Imaging the suture phantom was performed using a pulse train of 200 pulses at 625 kHz repetition rate, imaging a Field of View (FoV) of 4x4 mm^2 at a step size of 5 μm.

To test the ability of the overdriven CW-LDs to generate a strong OA signal in biological applications we imaged the ear of a healthy, adult CD-1 albino mouse under anaesthesia. In this case, we used a repetition rate of 625 kHz and 500 averages, imaging a 5x5 mm^2 FoV and a step size of 25 μm.

We also measured the median surface of the lower forearm of a healthy human volunteer to test the overdriven CW-LDs in a possible real world application. Here, a repetition rate of 156 kHz was used, in order to reduce the moving speed of the stages and to avoid motion artefacts caused by that, the signal was averaged 500 times, a FoV of 5x5 mm^2 was imaged and a step size of 25 μm was used.

All procedures with animals and humans were approved by the District Government of Upper Bavaria.

The optoacoustic signals acquired at different points had to be reconstructed into an optoacoustic image in order to achieve constant resolution at all depths [218]. To do this, we used a 3D beam forming algorithms that takes into account the directivity and sensitivity field of the UST for enhanced performance. The voxel size of the reconstructed image was chosen 20x20x5 μm^3 for the suture phantom and 20x20x10 μm^3 for the biological images.

In order to estimate the imaging depth of our system we calculated the Contrast-to-Background Ratio (CNR) in the human arm image at 14 different points (volume elements), that were located on blood vessels of the reconstructed image, at different depths. The CNR was calculated as

$$\mathrm{CNR} = 10 \log \left(\frac{S - B}{B} \right), \tag{2.1}$$

where S is the root mean square of the signal volume point at each depth and B the standard deviation of the background noise [219].

2.2.5 Longevity Testing of Laser Diodes

In order to test the performance and stability of the laser diodes over extended periods of times, we used the two visible CW-LDs (TB450B and HL63193MG) coupled to the multimode fibers. The CW-LDs were pulsed with a pulse train containing 500 pulses at 625 kHz repeated every 2.4 ms. The HV at the pulse laser diode driver was set at 300V. This configuration was chosen to mimic the real imaging application of the mouse ear imaging session. The light output of the fiber was attenuated with an absorptive Neutral Density Filter (optical density of 2; NE20B-A; Thorlabs, USA) in order to avoid saturation of the photodiode signal, that was recorded with the same biased photodiode as above. The signal recorded with the high speed digital oscilloscope at 2.5 GS/s and averaged 500 times. For each pulse train we recorded the peak voltage and the FWHM of the optical pulse width as recorded by the photodiode. Measurements were performed over 140 hours, in many intermediate sessions over a course of 2 weeks.

2.2.6 Maximum Permissible Exposure Limits

For the experimental conditions in the in-vivo experiments the energy density on the sample at a single pulse is calculated to be 4.6 μJ/cm^2 and the mean power density to be 3.18 W/cm^2, both well below the limits imposed by the American National Standards Institute [220] of 20 mJ/cm^2 and 18 W/cm^2.

2.3 Results

2.3.1 Laser Diode Characterization

We tested the 6 CW-LDs presented in Table 2.1 with the pulsed laser diode driver demonstrated in Fig.2.1a. The CW-LDs were overdriven with peak current up to 45-fold higher than their manufacturer-specified absolute maximum operating current [221] and at repetition rates 21-fold higher than ever previously reported [216].

Fig.2.2A presents the results of the CW-LD overdriving characterization. All CW-LDs were tested with a voltage between 10 and 270 V with 10 V steps applied to the pulsed laser diode driver. This value was chosen to avoid damage on the L808P100MM and RLT780-1000G as they presented strong peak power saturation at these voltages. The TB450B and HL63193MG, however, presented stable operation up to 300 V. The difference in the peak current for each CW-LDs results from the different internal dynamic resistance of each CW-LD. Fig.2.2A shows the energy per pulse, the optical peak power, the optical pulse width and the emitted wavelength of each CW-LD as a function of the driver peak current. The CW-LDs when overdriven can provide as high as 200 nJ per pulse and peak power up to 27-fold higher peak power than the manufacturer-specified absolute maximum limit. While the current pulse is always around 8 ns (data not shown) the optical pulse width is around 10 ns. Inductance in the Printed Circuit Board (PCB) is a major limitation in further reducing the current pulse width and increasing the peak current and therefore reduce the optical pulse width and increase the optical peak power. The pulse width of the L808P1000MM CW-LD presents non-monotonic behavior with a maximum around 20 A. Since the pulse width changes as a function of the applied peak current the relationship between the Peak Power and the Energy per Pulse is not linear. The emitted

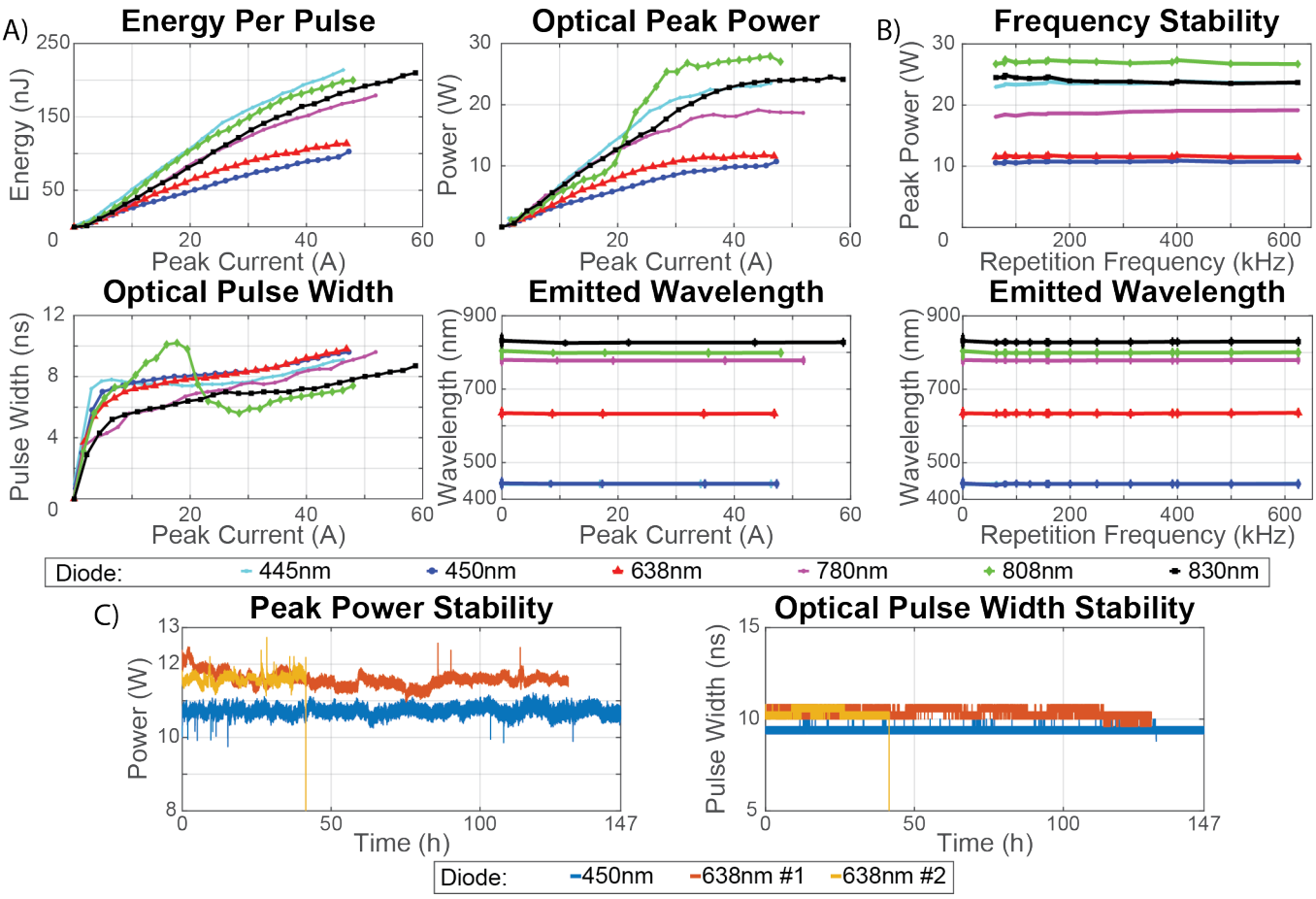

Figure 2.2: **Performance comparison of laser diodes emitting nanosecond pulses.** (a) Energy per pulse, optical pulse width, optical peak power and wavelength vs peak current. The data for the 445 nm and 450 nm diodes in the "Emitted Wavelength" graph overlap. (b) Optical peak power and wavelength vs repetition rate. The data for the 445 nm and 450 nm diodes in the "Emitted Wavelength" graph overlap. (c) Longevity test of three laser diodes (TB450B, HL63193MG-#1 and HL63193MG-#2), showing peak power and pulse width as a function of total working hours. The wavelength emitted at CW operation is plotted at Peak Current and Repetition Frequency "0". Adapted with permission from [201].

wavelength presents a small drop of ∼3 nm compared to the datasheet reported value when overdriven with higher than the designed current. This may happen due to mode hopping in the laser cavity. However, the emitted wavelength remains constant for all different applied operating currents.

Fig.2.2B demonstrates the optical peak power and the emitted wavelength when a HV of 270 V is applied to the pulse laser diode driver. No change in the peak power and the emitted wavelength is observed at higher repetition rates, indicating a stable overdriving performance of the pulsed laser diode driver and the CW-LDs.

The output divergence of the CW-LD is greater when overdriven compared to their nominal operation (data not shown). As long as the output beam NA is smaller than the fiber NA and the beam size at the fiber tip is smaller than the fiber core diameter the coupling efficiency should not be affected. However, this effect does not influence our results since the CW-LDs, when used in biological imaging, are fiber coupled and any drop in coupling efficiency is taken into account.

Fig.2.2C shows the results of the longevity experiments and specifically the peak power and the optical pulse width as a function of the laser operating time. In this experiment we used 3 CW-LDs, one TB450B and two of the HL63193MG. We observe that the HL63193MG-1 was destroyed after ∼40 hours of operation without any previous sign of degradation. This indicates that this CW-LD got destroyed by COMD, due to the high optical peak power in the CW-LD facet. For this reason we installed another HL63193MG and continued the longevity experiment. The two CW-LDs, TB450B and HL63193MG, presented stable operation for more than 140 hours in a real world imaging scenario. No peak power or pulse width drop is observed throughout the experiment time and the values remained stable around 11 W. The standard deviation of the optical peak power was less than 2% for all 3 CW-LDs. The discontinuities observed at the peak power graph coincide with the end and the beginning of a new experiment session. The slight increase in the peak power of TB450B and slight drop in the power of HL63193MG at the beginning of each session disappear after the CW-LD reach their thermal equilibrium. During these experiments no special heat removal precautions have been taken. The CW-LDs are being passively cooled by the CW-LD - fiber connector and only a small metal heat sink has been installed on the MOSFET. The MOSFET and the R_C resistor remained at a stable temperature of $\sim 60^o$C and the CW-LD at ambient temperature.

2.3.2 Imaging Performance

Fig.2.3 shows the imaging results with the overdriven CW-LDs. The scale bars in all images are 1 mm long. Fig.2.3a presents the maximum intensity projection images along the vertical direction of the reconstructed images from the Suture phantom. Fig.2.3b and Fig.2.3c present the lateral and axial profiles, respectively, of the Hilbert-transformed optoacoustic signal along the 50 μm sutures at the point indicated in Fig.2.3a. The lateral resolution of the system is calculated as 110 μm and the axial 33 μm, calculated as res $= \sqrt{s_m^2 - s_r^2}$, where s_m is the size of the object as measured by the system as FWHM and s_r the real object size.

In order to test our system's ability to image biological tissues, a mouse ear *in-vivo* was imaged. Fig.2.3d and e present the maximum intensity projections of the reconstructed images along the vertical and horizontal directions, respectively. It is important to mention that to acquire this images, with a FoV of 5x5 mm^2 and a step size of 25 μm only 97 seconds were required. In both images, the vasculature is well resolved and even smaller vessels have become visible.

Next, we tested the overdriven CW-LDs in imaging thick biological samples, such as the lower forearm of human skin *in-vivo*, and investigated the imaging depth they can achieve. Fig.2.3f and g show the maximum intensity projections of the reconstructed optoacoustic images along the vertical direction at different depths from the skin surface, 0-280 and 280-550 μm, respectively. In Fig.2.3f the epidermis structure is evident and in Fig.2.3g microvasculature in the dermis region of the human skin is visible. This results indicates that overdriven CW-LDs can be used to differentiate the epidermis from the dermis in human skin.

Fig.2.3h demonstrates the CNR of the reconstructed optoacoustic images of different vessels located at different depths in the human skin. The CNR achieved was 15-20 dB for the first 100 μm and dropped fast with increased depth. This is due to the use of blue light that is strongly absorbed by blood and melanin, that is located at the upper layers of the skin, and is heavily scattered in human tissue. Use of other wavelengths, at the green region, can increase the penetration depth in human skin.

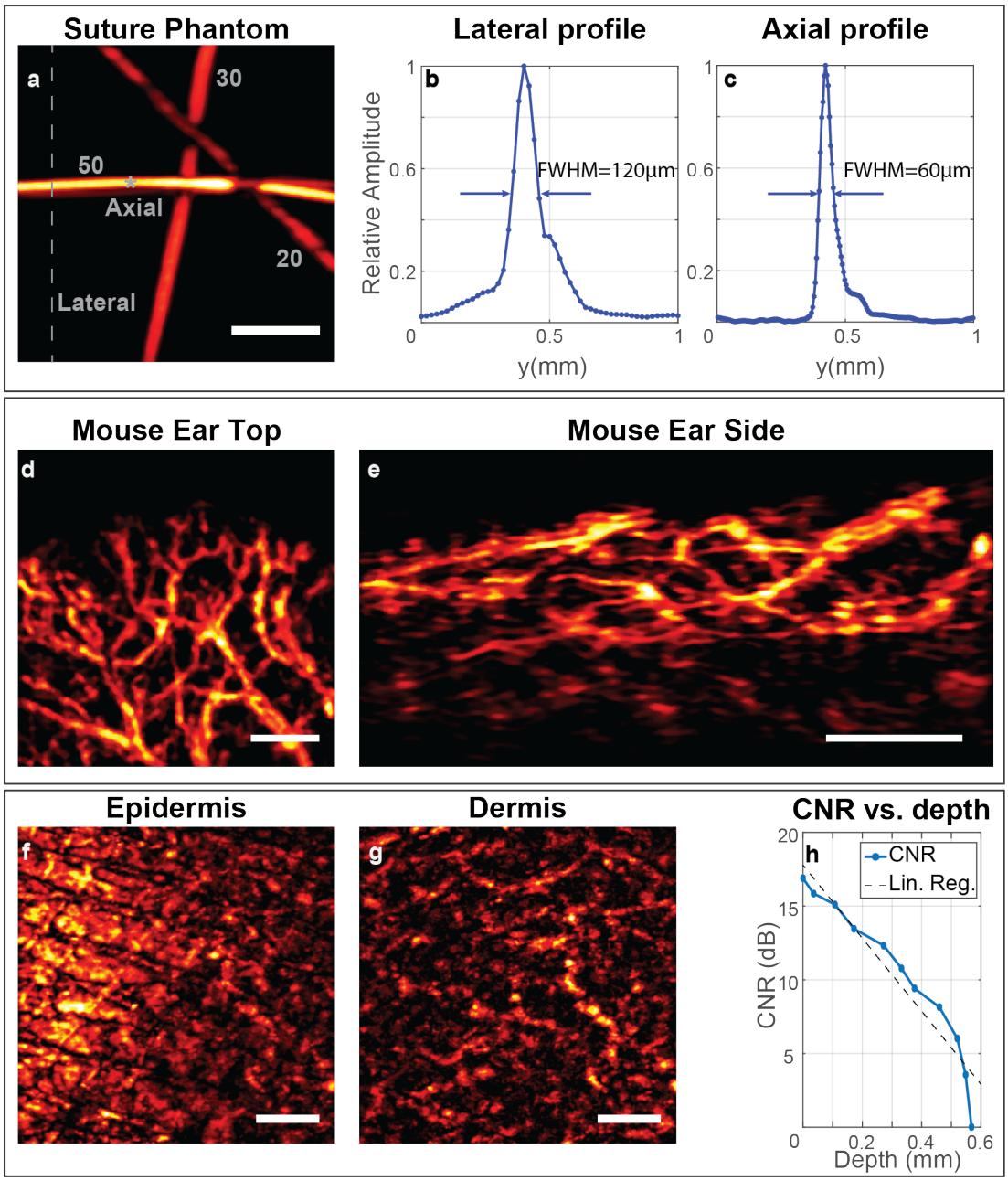

Figure 2.3: **Performance of the overdriven CW laser diode system for optoacoustic imaging.** (a) Top view of the Suture Phantom. Suture diameters are indicated in μm. (b) Profile of the lateral line shown in panel a. (c) Profile of the axial point shown in panel a. (d-e) Maximum Amplitude Projection images of a mouse ear showing vasculature, including smaller vessels. (f-g) Coronal maximum-amplitude projections of human forearm imaged at depths ranging from 0-280 um (epidermis) and from 280-550 um (dermis). The two skin layers show different patterns, with microvasculature evident in the dermis. (h) Contrast-to-noise ratio (CNR) as a function of penetration depth when imaging the human forearm. A best-fit line calculated by linear regression (Lin. Reg.) is shown for reference. Scale bars, 1 mm. Adapted with permission from [201].

2.4 Discussion

In this Chapter, we have developed a pulsed laser diode driver to deliver high current, ultra short pulses at high repetition rates to CW-LDs. The CW-LDs when overdriven with current up to 45-fold their nominal value for a few nanoseconds can deliver up to 27 time more peak power than their nominal value without getting destroyed or damaged. We also discovered that it is possible to pulse the CW-LDs at repetition rates of up to 625 kHz in order to increase the SNR through averaging without further increasing the acquisition time. We proved that overdriven CW-LDs can generate good OA signal from biological samples, such as blood vessels in a mouse ear or even thicker samples like human skin.

In order to understand how it is possible to sustainably overdrive CW-LDs we need to understand their two main damage mechanisms. The first damage mechanism is thermal damage, that results from high electron density that dissipates heat and if not properly removed burns the CW-LD and is dominant when CW-LDs are operated in cw mode. The other mechanism is COMD, that results from high photon density in the active region and the facet that can get a very high value momentarily at a small point on the facet and burn it. COMD is happening at the nanosecond scale, without previous indication, and does not completely destroy the LD but rather degrades it, there is still emitted light but of less intensity. COMD is dominant at P-LDs, that due to their very low pulsing duty cycle do not suffer from thermal damage. It is also reported that the maximum peak power a LD can provide in pulsed mode before being damaged from COMD is inversely proportional to the inverse square root of the pulse width, $P \propto \frac{1}{\sqrt{t}}$ [221–223]. This indicates that it is possible to increase the LD peak power by lowering the pulse width. According to our experience, for overdriven CW-LDs, that are designed for cw operation that requires efficient heat removal from the LD, the two damage mechanisms, thermal and COMD, are independent. This means that we can pulse the CW-LD with very high currents close to their limit, imposed by the inverse square root law for COMD, and at very high repetition rate, close to their thermal limit for thermal damage, at the same time without damaging the CW-LD.

These results, suggest that we can further increase the repetition rate as long as the mean output power is below the nominal value. For the CW-LD that provided the highest power, the NDB7K75, we achieved ∼200nJ per pulse and at extremely high repetition rates of 1 MHz, the mean output power is 200 mW, much lower than their nominal value of 3.5 W in cw operation. Therefore, if the pulsed laser diode driver can sustain it, it is possible to further increase the repetition rates to acquire more averages at the same time and increase the SNR. In this work, we achieved a repetition rate of 625 kHz and duty cycles of 0.6% that is 6-fold higher than the theoretical maximum limit of PLDs, 0.1%. We were also able to acquire 500 averages in only 0.8 ms, that is 60-fold faster than previously reported [216].

We also tested the overdriven CW-LDs in long operation of more than 135 hours, that is $\sim 10^{11}$ pulses in total, under challenging, real world application conditions, i.e. at bursts of 500 pulses at 625kHz with a period of 2.4 ms and with a peak current of about 50A. Our results demonstrate that the CW-LDs presented stable operation without any degradation. One of the CW-LDs got destroyed after ∼40 hours of operation, without any previous indication or degradation. However, we replaced it with another CW-LD of the same kind, HL63193MG, that did not get damaged after ∼130 hours. This suggests, that this might be due to internal manufacturer defects that were not present in the second red CW-LD. In the course of the experiments performed during this study and the studies presented in the following chapters, no other overdriven CW-LD has been destroyed. Even in the case of a damaged CW-LD, it is faster and cheaper to replace a CW-LD than calibrating or replacing a burnt DPSS laser or one

equipped with an OPO.

Our data from the overdriven CW-LD raster scanning system show that operating CW-LD this way, has several advantages for OA imaging. Semiconductor lasers suffer from low pulse energies and low beam quality at the same time. This means that PACT applications, that require a lot of energy to illuminate a large area, and OR-PAM applications that require diffraction limited illumination spot, are hard to be implemented with LEDs, P-LDs or CWLDs. However, AR-PAM or mesoscopic applications require loosely focused light and pulse energies in between microscopic and macroscopic applications, and are better suitable for semiconductor laser or light sources. In addition, LEDs that are available in many wavelengths in the UV, visible and NIR region can only offer long pulses, that reduce the spatial resolution, and cannot be focused due to their large emitting area. On the other hand, P-LDs that can offer very high pulse energies are only available in the NIR region where the blood and other important biological absorbers do not absorb strongly. Overdrive, CW-LD can fill this gap, due to their small emitter size, wavelength availability, high pulse energies and very high repetition rates the overdriving technique can now provide.

However, as with all semiconductor sources, although they are available in many wavelengths in the UV, visible and NIR region, it is not possible to achieve all the wavelengths in this range. Due to the specific band gap of the semiconductor active material, only very specific wavelengths are available. That makes it hard to finely fit the optoacoustic wavelength to the peak absorption wavelengths of the specific biological absorber in order to maximize the SNR. Nevertheless, this study introduced a way to use CW-LD more effectively in AR-PAM that brings even more available wavelengths to choose from. Future developments in semiconductor material will introduce new wavelengths into the market, especially in the green region, that will allow to increase the penetration depth in human skin, due to reduced scattering in these wavelengths compared to the blue region.

In the next chapters, we aim to use these overdriven CW-LDs in order to capitalize on the advantages they bring and develop different system for different applications in biology, medicine and the environment. The next steps will aim to solve the drawbacks of the system presented in this Chapter:

- We need to find a way to couple the ∅9 mm CW-LD into multimode fibers so that we can use the achieved higher energy per pulse and emitting wavelengths provided by these CW-LDs for OA imaging.
- We need to find a way to efficiently illuminate the sample with the output of multiple overdriven CW-LDs at different wavelengths, in a multispectral system.
- We can improve the pulsed laser diode driver in order to achieve shorter pulses but with higher peak power and energy per pulse to increase the OA SNR achieved.
- A shorter pulse width in combination with a higher frequency and bandwidth UST will improve the spatial resolution.
- We observed a discrepancy between the measured and the theoretical expected axial and lateral resolution. The axial and lateral resolution should be 20 and 82 μm [224, 225], respectively, and they were measured to be 33 and 110 μm, respectively. This is a result of the steep illumination angle, 60^o between the acoustic and the optical axis, that results in an inhomogeneous illumination, especially deeper in the tissue. This is inconsistent with the assumption made in the 3D beam-forming reconstruction algorithm of homogeneous illumination, and results in degraded image spatial resolution [126, 218].
- The use of optics that are positioned above the water surface renders the use of the system complicated as it is necessary to re-align the optical focal spot with the acoustic spot every time before a measurement, often even during a measurement session. An improved system should

be easier to use and should provide more consistent results.

• Multiple wavelength measurements will require a simultaneous pulse per pulse monitoring of the CW-LDs in order to correct the time jitter and energy fluctuations before spectral un-mixing of the different biological absorbers [109, 119].

In conclusion, we have proven that the miniaturized and low-cost CW-LDs when overdriven can generate a strong OA signal that can be used as OA light sources that enable fast multispectral OA imaging for various applications in biology, medicine and the environment.

Chapter 3

Multispectral overdriven CW-LD RSOM

3.1 Introduction

This chapter is published in a separate journal article [226][1].

Overdriven CW-LDs can offer a low-cost and miniaturized alternative to conventional expensive and bulky lasers used in OA imaging so far. OA imaging at multiple wavelengths requires either multiple solid state lasers emitting at different wavelengths that is expensive and impractical, or coupling a solid state laser with an OPO, that is the most common choice but increases the complexity of the system and slows down the acquisition as a single source can emit multiple wavelengths only sequentially. As CW-LDs are available in many wavelengths across the UV, visible and NIR spectral regions, they can be used to develop a multiple wavelength illumination system that is also low-cost, compact and can provide fast, high resolution and good SNR optoacoustic mesoscopy images. The existence of multiple illumination sources at different wavelengths enables the implementation of different multiplexing techniques to further reduce the acquisition time at multiple wavelengths, such as the Frequency Wavelength Multiplexing algorithm [200], shortly presented herein.

In order to capitalize on the advantages offered by the overdriven CW-LDs presented in the previous chapter, we further developed the system presented in Fig.2.1. We managed to couple all CW-LDs, ∅5.6 mm and ∅9 mm CW-LDs with high coupling efficiency. We developed a multiple wavelength excitation system, we increased the spatial resolution of the system and ease of use and alignment of the system for faster and easier sample preparation. The system's performance has been characterized using resolution phantoms and showcased concurrent high-resolution, fast, multi-wavelength OA imaging of vasculature and lymphatic vessels in mouse ear as well as diffusion and circulation of dyes in the blood vasculature system of a mouse. We also demonstrated that multi-wavelength, cross-sectional images of human skin can be obtained at high resolution.

[1]Dr. Ludwig Prade developed the Frequency Wavelength Multiplexing signal processing technique [200]. Antonios Stylogiannis and Dr. Ludwig Prade together developed the multiple wavelength RSOM system. Antonios Stylogiannis further worked on the Frequency Wavelength Multiplexing algorithm, developed the overdriven CW-LD excitation source, performed the imaging experiments and processed the data. Sarah Glasl assisted Antonios Stylogiannis in performing the mice experiments. Mustafa Qutaiba reconstructed the optoacoustic images. Dr. Christian Zakian and Dr. Vasilis Ntziachristos helped with extensive discussions and guidance in conducting this research.

3.2 System Development

3.2.1 Multispectral overdriven CW-LD RSOM

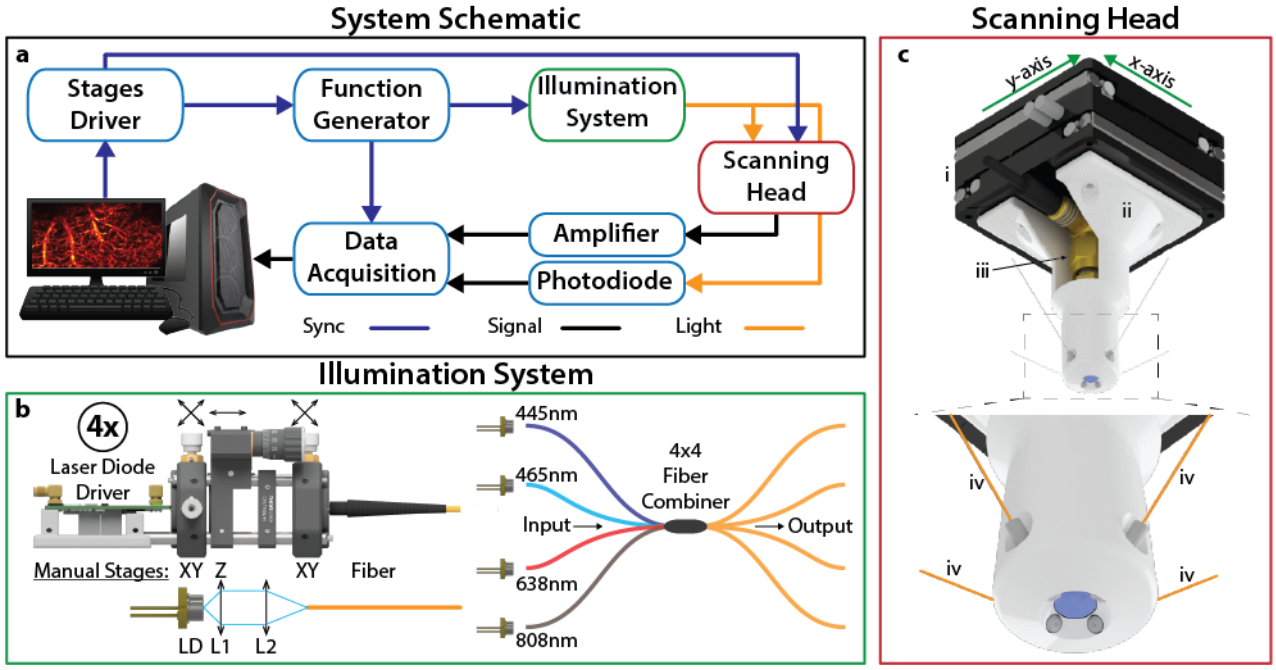

Figure 3.1: The 4-wavelength CW-LD RSOM system. **(a)** The Schematic of the system with all the electrical connections, synchronization and signal, and the light delivery. **(b)** The illumination system presenting the CW-LD coupling into the fiber and the 4x4 fiber combiner; L1 and L2, lens 1 and lens 2. **(c)** The Scanning head consisting of the x-y scanning stages (**i**), the 3D printed holder (**ii**), the Ultrasound Transducer (**iii**) and the 4 fibers for light delivery (**iv**). Adapted version from [226].

Figure 3.1 presents the multi-wavelength CW-LD RSOM system, that is an updated version of the system presented in Fig.2.1. In this chapter we will discuss only the updates compared to the single wavelength system presented in the previous chapter.

Fig.3.1a presents the schematic of the system, the electrical connections between the different components and the illumination path. The stages driver is the same as in Chapter 2 and is still triggering the AWGs and the DAQ at every assigned position to start sample illumination and signal acquisition. We are using two of the same AWGs in order to trigger four CW-LDs, using pulse trains of N_p pulses that will later be averaged. We are still using the same low noise amplifier and the same DAQ to amplify and digitize the OA signal.

A small portion of the light pulses of all four overdriven CW-LDs is directed into a photodiode (DET10A/M, Thorlabs, USA) that is recorded simultaneously with the OA signal using the second channel of the DAQ. The photodiode signal is used in order to correct the pulse per pulse energy variation and time jitter of the light pulses.

Fig.3.1b presents the Illumination System of the multispectral CW-LD RSOM. The pulsed laser diode driver PCB layout has been updated compared to the one presented in Fig.2.1a, in order to achieve updated performance in terms of pulse width and peak power. The updated PCB layout offers overall smaller footprint and lower inductance on the current delivery line, and thus achieves lower pulse width and higher peak current. The value of the charging resistor R_C (see Fig.2.1a) has been lowered to 50Ω to allow higher repetition rates, in the case up to

10 MHz. However, heat removal from the pulsed laser diode driver, specifically from R_C and Q_1, becomes critical when high repetition rates are used. For this reason, a custom-made heat spreader has been mounted between R_C and Q_1 that spreads the generated heat into a bigger heat sink that is cooled with an air flow caused by a fan.

Each of the four used CW-LDs is mounted on a separate pulsed laser diode driver and coupled into a fiber using a 2 lens system. Each CW-LD is mounted on a manual X-Y positioning stage (CXY1, Thorlabs, USA) using LD mounts for either the ⌀5.6 mm TO-Can CW-LDs (S1LM56, Thorlabs, USA) or the ⌀9 mm TO-Can CW-LDs (S1LDM9, Thorlabs, USA). The collimating lens (C340TMD, Thorlabs, USA) is positioned on a manual Z translating stage (SM1Z, Thorlabs, USA) and has a focal distance of 4.03 mm and an NA of 0.64, that is larger than the NA of the CW-LDs used. The focusing lens (C560TME, Thorlabs, USA) is kept stable and has a focal distance of 13.86 mm and an NA 0.18. The magnification ratio of the lens pair is 3.44, that results in a focal spot with a size of approximately 172 μm for a 50 μm big axis size of the CW-LD. Therefore, a 200 μm core fiber (larger that 172 μm) and 0.22 NA (bigger than 0.18 NA of the focusing lens) has been chosen to ensure high coupling efficiency.

In order to combine the output of 4 CW-LDs into a single path and illuminate the same spot on the sample with all four wavelengths, we used a 4x4 fiber combiner (MPC-4-M21-M41-P23, Lasfiberio, China). This fiber combiner has 4 input fibers, each with 200 μm core diameter and 0.22 NA, and 4 output fibers, each with 200 μm core diameter and 0.22 NA. Each output fiber contains 25% of each input to achieve homogeneous sample illumination with all four wavelengths. One of the outputs was connected to a custom-made 95-5% fiber splitter (LTL 500-93310-95-1, LaserComponents Germany GmBH, Germany) and the 5% fiber was connected to the photodiode. The other 3 output fibers of the fiber combiner and the 95% fiber of the fiber splitter were terminated with a 1.25 mm ferrule (SFLC230, Thorlabs, USA) and directed to the Scanning head.

The Scanning Head is presented in Fig.3.1c. New stages have been used (i, U-723 XY, Physik Instrumente, Germany) that are lighter and faster than the ones used in Chapter 2. A 3D printed holder (ii) hosts the new UST (iii, HFM23, Sonaxis, France) that has a central frequency of 50 MHz and 110% relative bandwidth and an f-number of 1.07. The higher central frequency UST is expected to increase the spatial resolution of the system. The four fiber tips are located around the UST with 90^o compared to each other with their outputs designed to cross at the focal spot of the UST to achieve maximum energy density on the sample and homogeneous illumination. In this case there is no lens to focus the light onto the sample, and the system relies on the short distance between the fiber tip and the sample as well as the relatively low output NA of the fibers. The advantage of such a design, stems from the fact that the fiber tips can be submerged into water without disturbing the illumination scheme of the system, as it would be if lenses were used. Therefore, the UST and the fiber tips are submerged into water already confocally aligned to illuminate and detect from the same point and there is no need to re-align the system for every measurement, achieving more consistent results every time we use the system.

3.2.2 CW-LD Characterization and Maximum Permissible Exposure Limits

We used 4 CW-LDs emitting at 445 nm (LDM-445-6000, LaserTack, Germany), 465 nm (LDM-465-3500, LaserTack, Germany), at 638 nm (HL63283HG, Ushio, Japan) and at 808 nm (K808D02FN, BWT, China) named laser 1, 2, 3 and 4 respectively. Each CW-LD was driven with a pulse train of 100 pulses at ∼200 kHz and delivered 189, 137, 142 and 153 nJ per pulse,

respectively, as measured by a stabilized thermal power meter (PM160T, Thorlabs, USA) at the sample position. The pulse width of the laser diodes was estimated as 6.7, 6.7, 10.2 and 10.2 ns, that results in a peak power of 28.2, 20.4, 13.9 and 15 W, for lasers 1, 2, 3 and 4 respectively. We observe that the updated version of the pulsed laser diode driver, along with the new CW-LDs used delivered higher peak power compared to the CW-LD used for imaging in Chapter 2.

Using a USB CCD camera (daA1920-30um; Basler AG, Germany) the illumination spot on the surface of the sample was measured to be a circle with a diameter of 1mm. Using the above mentioned repetition rates for each laser diode and a scanning speed of 10mm/s for a scanning step size of 10um we can calculate the sample exposure.

The total exposure of the sample for simultaneous illumination with all 4 wavelengths is calculated to be 19.8 μJ/cm^2 per pulse and 3.96 W/cm^2 mean exposure, well below the MPE limits of 20 mJ/cm^2 and 18 W/cm ^{2}, imposed by the American National Standards Institute [220].

We recorded the emission spectra of the 4 laser diodes used in the multispectral laser diode RSOM with a spectrometer (USB4000, OceanOptics, UK) and the peak emission wavelengths were 444.3, 460.1, 636.8, 804.9 nm with a variance of 1.6, 1.7, 1.9, 2.2 nm respectively and an R^2 confidence level higher than 0.96 for all cases. In the following, we also use their nominal wavelength to refer to these CW-LD (namely 445, 465, 638, 808 nm).

These wavelengths were chosen because they offer interesting endogeneous and exogeneous contrast. Lasers 1 and 2 are strongly absorbed by oxygenated and de-oxygenated hemoglobin (see Fig.1.2) with de-oxygenated hemoglobin absorption being higher than oxygenated hemoglobin [227] at laser 1, and vice-versa at laser 2. Therefore, the ratio of the signal strength of laser 2 over the signal strength of laser 1, S_2/S_1, is proportional to the blood oxygen saturation. Lasers 3 and 4 absorb blood weakly and blood vessels present low SNR; most times blood vessels are invisible, in these wavelengths. Laser 3 is strongly absorbed by Evan's Blue [228, 229] and laser 4 by Indocyanine Green (ICG) [230], two dyes that we will use in the experiments as discussed below. Laser 3 is also absorbed by ICG and ICG will appear in the OA images of laser 3.

3.2.3 Experimental Measurements

In order to characterize the lateral resolution of the multispectral RSOM we imaged a standardized resolution phantom, the Siemens Star (R1L1S3P, Thorlabs, USA) [231, 232]. The Siemens Star consists of 72 dark bars over 360^o in a bright background and the lateral resolution of the system can be determined by noting how close to the center the radial lines can be resolved by their neighboring lines. This phantom offer a minimum resolution of 435 μm at the outer circle and a maximum resolution at the center circle of 8.7 μm. To measure this phantom a Field of View (FoV) of 5x5 mm^2 is used and a step size of 10 μm.

Next, in order to examine whether the multi-wavelength CW-LD RSOM can produce high quality images of in-vivo samples we imaged a mouse ear. In addition, we introduced exogeneous contrast by intradermal injection of 5 μL Evan's Blue and 5 μL Indocyanine Green (ICG), both 1% concentration solution, in order to visualize lymphatic structures and vessels along with the blood vessels.

For our experiments we employed two 5 to 6-week old female Athymic nude- Foxn1nu mice (Envigo, Germany). During all measurements, the mice were anesthetized by 1.6% Isoflurane (cp-Pharma, Germany) with 0.8 lpm carrier gas flow and kept on constant body temperature with a red lamp and a heating plate. For all mouse ear experiments the FoV was set to 10x10 mm^2 and the step size to 10 μm.

Moreover, to investigate whether our system can detect fast biological changes in multiple

wavelengths we imaged a mouse ear and selected an artery-vein vessel pair and performed additional continuous B-Scans (on a line of length 2 mm and a step size of 10 μm). During the B-Scan we were recording with all four wavelengths and performed two experiments. First, an oxygen stress test where the mouse was breathing alternatively 0.8 lpm of 100% oxygen (O_2) and 0.6 lpm medical Air (20% O_2) plus 0.2 lpm carbon dioxide CO_2, in order to monitor fast changes in the oxygenation of the main artery and the the main vein. Second, we injected the two dyes in the tail vein (100 μL solution of 5 mg/mL of ICG and a 100 μL of 1% concentration of Evan's Blue) and monitored the dye perfusion on the artery-vein vessel pair.

Both mice were sacrificed immediately after imaging by cervical dislocation. All mouse experiments were performed according to the committee on Animal Health and care of Upper Bavaria, Germany.

Last, in order to examine the system's ability to image thicker samples we imaged the lower forearm of a healthy human volunteer with a FoV of 2x4 mm^2 and a step size of 10 μm.

The back projection algorithm is implemented in Fourier domain [233] to recover acoustically diffraction limited images. The resulting image is also corrected by the system's total (electric and spatial) impulse response [234, 235] and further processed with a vesselness filter for display purposes [236, 237]. The raw data of a single B-Scan do not allow for 3D image reconstruction. Therefore, a simplified version of the back-projection algorithm was developed, which operates in two-dimensions and approximates the transducers sensitivity field as a conic section along the B-Scan direction only.

3.3 Frequency Wavelength Multiplexed Optoacoustics

Optoacoustic Imaging is usually performed in Time Domain (TD), i.e. using pulses to excite the sample, due to the high energy transient that they offer. TD-OA offers a high SNR and by recording the time-of-flight of the ultrasound waves by a high speed digitizer, high axial resolution is achieved. However, multi-wavelength excitation and acquisition is not straight forward and usually requires increased acquisition time.

Frequency Domain OA (FD-OA) uses a sinusoidal light wave to excite the tissue and records the OA signal at the same frequency by means of analog demodulation techniques to acquire the amplitude and the phase of the signal [238–240]. The advantages of FD are the overall simpler and more economic hardware required, the high repetition rates of the lasers used and easy concurrent illumination using frequency multiplexing [216, 241, 242], i.e. each laser is modulated at a different frequency. However, FD-OA techniques lack the high SNR of TD-OA due to the much lower energy transient of a sine wave compared to a light pulse and lack of axial resolution. However, it is recently shown [243] that it is possible to achieve axial resolution and high image quality if FD-OA signal at multiple discrete frequencies is acquired, at the expense of increased imaging time.

In this section, we present a new hybrid technique, that was previously developed in [200], that merges the advantages of TD- and FD-OA, termed Frequency Wavelength Multiplexed Optoacoustics (FWMOA). FWMOA is presented in Fig.3.2. We used laser 1 to illuminate a black varnish layer on a petri-dish as the sample using a pulse train of $N_p = 100$ pulses at $f_{rep} =$ 200 kHz.

Fig.3.2a shows the raw OA signal as a function of time as it was recorded by the DAQ. In TD averaging the first step is to separate the signal in N_p pieces of period $T = 1/f_{rep}$ as presented in Fig.3.2b. Then we averaged all the pieces to reduce the noise power and increase

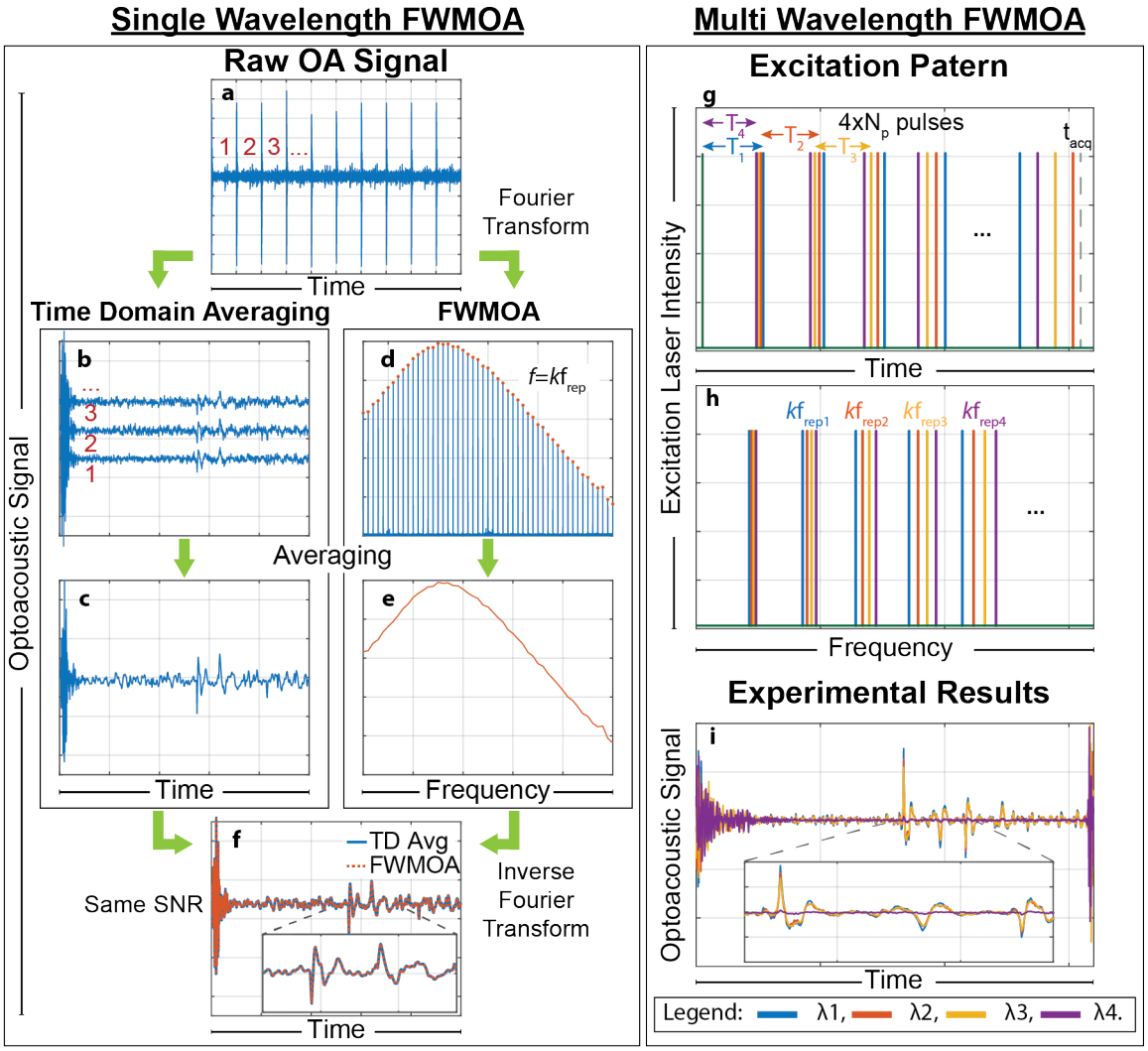

Figure 3.2: The Frequency Wavelength Multiplexed Optoacoustics (FWMOA) signal processing algorithm for single wavelength and multiple wavelength OA Imaging. **(a)** The raw optoacoustic signal recorded using a pulse train. **(b-c)** present the normal averaging in TD. **(b)** The train of pulses is split in chunks of period $T = 1/f_{rep}$ and they are averaged **(c)** point by point. **(d-e)** The FWMOA processing of the same signal. **(d)** is the Fourier transform of the raw optoacoustic signal **(a)** with many discrete frequencies that are all harmonics ($k * f_{rep}$ with k positive integer) of the base repetition rate f_{rep}. We perform the average in FD by choosing only the harmonics of f_{rep} and discarding all the other frequencies that contain only noise and no signal **(e)**. **(f)** By performing the inverse Fourier Transform in **(e)** we recover the TD signal that matches perfectly with the one in **(c)**. The 4 laser excitation pattern using the FWMOA algorithm presented in the Time Domain **(g)** and in the Frequency Domain **(h)**, where each laser diode has a different repetition rate $f_{rep,j}$, j the number of each laser. **(i)** The optoacoustic signal where FWMOA is used. Signal from all 4 wavelengths has been recovered without any cross-talk between the lasers and correctly co-registered in time. Adapted version from [226].

the SNR as a function of $\sqrt{N_p}$ (Fig.3.2c). Mathematically this operation can be expressed as

$$S_a(t) = \frac{1}{N_p}\sum_{k=1}^{N_p} S_{r,k}(t) = \frac{1}{N_p}\sum_{k=1}^{N_p} S_r(t) * \delta(t + KT), \tag{3.1}$$

where $S_a(t)$ is the averaged OA signal, N_p the number of pulses or periods that will be averaged, $S_{r,k}(t)$ the k-th period of the recorded signal, $S_r(t)$ the complete recorded signal and $*$ denotes convolution by the Dirac-delta function, $\delta(t+kT)$, i.e. a shift in time.

The FWMOA algorithm for a single wavelength works as follows. The raw OA signal (Fig.3.2a) will be Fourier transformed to yield the same signal in Fourier space (Fig.3.2d). In Fourier space the signal presents multiple peaks at the harmonics of the repetition rate, i.e. at integer multiples of the kf_{rep}, with k a positive integer, since the signal is periodic. In this case, the OA signal can also be written in the form

$$S(\omega) = S_0(\omega) \sum_{m=-\infty}^{\infty} \delta(\omega - m\omega_0), \tag{3.2}$$

with $S(\omega)$ the Fourier Transform of a signal $S(t)$ and $S_0(\omega)$ the Fourier Transform over one period, the 0-th in this case, of the periodic signal $S(t)$. The multiplication in FD with a series of Dirac-deltas confines the periodic signal to the harmonics of the repetition rate ($m\omega_0$, with m a positive integer and $\omega_0 = 2\pi f_{rep}$).

In order to average now the signal in FD we need to apply the Fourier Transform on eq.(3.1) and get

$$S_a(\omega) = \frac{1}{N_p} \sum_{k=1}^{N_p} S_r(\omega) e^{jk\omega T} = \frac{1}{N_p} S_r(\omega) \sum_{k=1}^{N_p} e^{jk\omega T}, \tag{3.3}$$

where $S_a(\omega)$ is the Fourier Transform (FT) of the averaged signal and $S_r(\omega)$ the FT of the recorded OA signal. However, since we know that $S_r(t)$ is periodic with frequency f_{rep} we can multiply eq.(3.3) with $\sum_{m=-\infty}^{\infty} \delta(\omega - m\omega_0)$ to get

$$S_a(m\omega_0) = \frac{1}{N_p} S_r(\omega) \sum_{k=1}^{N_p} e^{jk\omega T} \sum_{m=-\infty}^{\infty} \delta(\omega - m\omega_0), \tag{3.4}$$

where $S_a(m\omega_0) = \sum S_a(\omega)\delta(\omega - m\omega_0)$. For k and m integers $e^{jk\omega T} = e^{ikm2\pi} = 1$ and $\sum_{k=1}^{N_p} e^{jk\omega T} = N_p$ and eq.(3.4) becomes

$$S_a(m\omega_0) = S_r(\omega) \sum_{m=-\infty}^{\infty} \delta(\omega - m\omega_0). \tag{3.5}$$

Eq.(3.5) tells us that the FT of the averaged signal can be acquired by taking the FT of the recorded signal and restricting it only to the harmonics of its repetition rate.

By applying the operation shown in eq.(3.5) to the Fourier transformed signal in Fig.3.2d we get the signal in Fig.3.2e that is the FT of the TD averaged signal in Fig.3.2c. By applying the Inverse Fourier Transform on the signal in Fig.3.2e we get the TD signal after averaging usign the FWMOA algorithm that matches with the TD averaged signal (Fig.3.2f).

This shows us that the FWMOA algorithm shows equivalent performance for a single excitation wavelength, both signals offer exactly the same SNR. However, the advantages of FWMOA arise when multiple light sources emitting at different wavelengths are used simultaneously. Similar to frequency multiplexing in FD-OA with multiple wavelengths, in FWMOA different wavelengths are assigned slightly different repetition rates, and thus different harmonics, that when the signal is processed in the FD can be correctly recovered.

Fig.3.2g-i shows how the FWMOA algorithm works in the case of 4 excitation wavelengths. Each laser has a slightly different repetition rate to all other lasers, $f_{rep,j} = f_{rep,1} + (j-1)\delta f$, where $f_{rep,1}$ is the repetition rate of laser 1 and j the number of the laser, 1 to N for N

wavelengths used, with $\delta f \ll f_{rep,1}$. All lasers excite the sample simultaneously and are recorded using a single UST (Fig.3.2g), the signal is Fourier transformed (Fig.3.2h) and the FWMOA algorithm presented above is applied to each wavelength separately to recover the signal from each wavelength (Fig.3.2i) without any cross-talk between the wavelengths, with a high SNR and perfectly aligned in time.

However, there are some limitations imposed on the number of pulses in each pulse train as well as the small frequency shift δf in order to avoid cross-talk between the signal from each wavelength. The signal is recorded over an acquisition time defined by $t_{acq} = N_p/f_{rep,1}$, where N_p is the number of pulses in the pulse train of laser 1. When performing the FT on the recorded signal the frequency resolution is defined by $df = 1/t_{acq}$, i.e. the frequencies that are separated by less than df cannot be resolved.

The UST used detects frequencies that fall in its bandwidth defined by the -6dB cut off points, f_{low} and f_{high}. In order to recover the signal from all wavelengths correctly we need to ensure that the harmonics of all lasers can be resolved by all the harmonics of all other lasers, for all frequencies that fall in the UST bandwidth.

For laser 1, we can find the first harmonic k_s that is bigger than f_{low}, $k_s \cdot f_{rep,1} > f_{low}$, and the last harmonic k_f that is lower than f_{high}, $k_f \cdot f_{rep,1} < f_{high}$. This is true for

$$k_s = \text{ceil}\left(\frac{f_{low}}{f_{rep,1}}\right) \text{ and } k_f = \text{floor}\left(\frac{f_{high}}{f_{rep,1}}\right), \tag{3.6}$$

where ceil(x) defines the nearest integer greater than x and floor(x) the nearest integer smaller than x.

At the lower end of the UST bandwidth the k_s harmonic of laser 1 will be located very close to the k_s harmonic of laser 2. Their difference has to be greater than the frequency resolution df, i.e.

$$\Delta f = k_s \cdot f_{rep,2} - k_s \cdot f_{rep,1} = k_s \cdot (f_{rep,1} + \delta f) - k_s \cdot f_{rep,1} = k_s \cdot \delta f > df. \tag{3.7}$$

This leads to $\delta f > df/k_s$ which defines a minimum limit on the small frequency shift

$$\delta f_{min} = \frac{df}{k_s}. \tag{3.8}$$

At the upper end of the UST bandwidth the k_f harmonic of laser 1 will be located very close to the $k_f - 1$ harmonic of laser N. Their difference has to be greater than the frequency resolution df, i.e.

$$\begin{aligned} \Delta f = k_f \cdot f_{rep,1} - (k_f - 1) \cdot f_{rep,N} &= k_f \cdot f_{rep,1} - (k_f - 1) \cdot (f_{rep,1} + (N-1)\delta f) \\ &= f_{rep,1} - (k_f - 1) \cdot (N-1) \cdot \delta f > df. \end{aligned} \tag{3.9}$$

This leads to $\delta f < (f_{rep,1} - df)/[(k_f - 1) \cdot (N-1)]$ which defines a maximum limit on the small frequency shift

$$\delta f_{max} = \frac{f_{rep,1} - df}{(k_f - 1) \cdot (N-1)}. \tag{3.10}$$

We need to ensure that $\delta f_{min} < \delta f_{max}$ in all cases, which imposes a minimum limit on the number of pulses in the pulse train of laser 1 in the case $\delta f_{min} = \delta f_{max}$, as

$$N_{p,min} = \text{ceil}\left(\frac{(k_f - 1) \cdot (N-1) + k_s}{k_s}\right). \tag{3.11}$$

Any number of pulses greater than $N_{p,min}$ is valid and defines the range of valid small frequency shifts, δf, between δf_{min} and δf_{max}.

In the case presented in Fig.3.2, of $N = 4$ wavelength, $f_{rep,1} = 200$ kHz and an UST bandwidth between $f_{low} = 22$ MHz and f_{high} =78 MHz, $N_{p,min} = 12$. We have chosen $N_p = 100$ to further increase the SNR that defines the range of valid δf between 18.2 and 169.7 Hz. We have chosen δf =125 Hz as a good representative value in the middle of the valid range. Therefore, the repetition rate of all four lasers are $f_{rep,1} = 200000$ Hz, $f_{rep,2} = 200125$ Hz, $f_{rep31} = 200250$ Hz and $f_{rep,4} = 200375$ Hz. Moreover, the number of pulses in each pulse train is adjusted to fit as many pulses in the defined acquisition time, $t_{acq} = N_p/f_{rep,1}$, as possible, *i.e.* $N_{p,1} = 100$, $N_{p,2} = 101$, $N_{p,3} = 101$ and $N_{p,4} = 101$.

In this way, FWMOA manages to excite the sample with multiple wavelength simultaneously without the need to compromise the Depth of View (DoV) for each wavelength [200, 226], the number of averages, and thus the SNR, or the acquisition time. FWMOA OA enables multi-wavelength, high SNR imaging especially when semiconductor sources are used that is necessary to average to increase the SNR.

3.3.1 Frequency Wavelength Multiplexesd vs Frequency Domain Optoacoustics

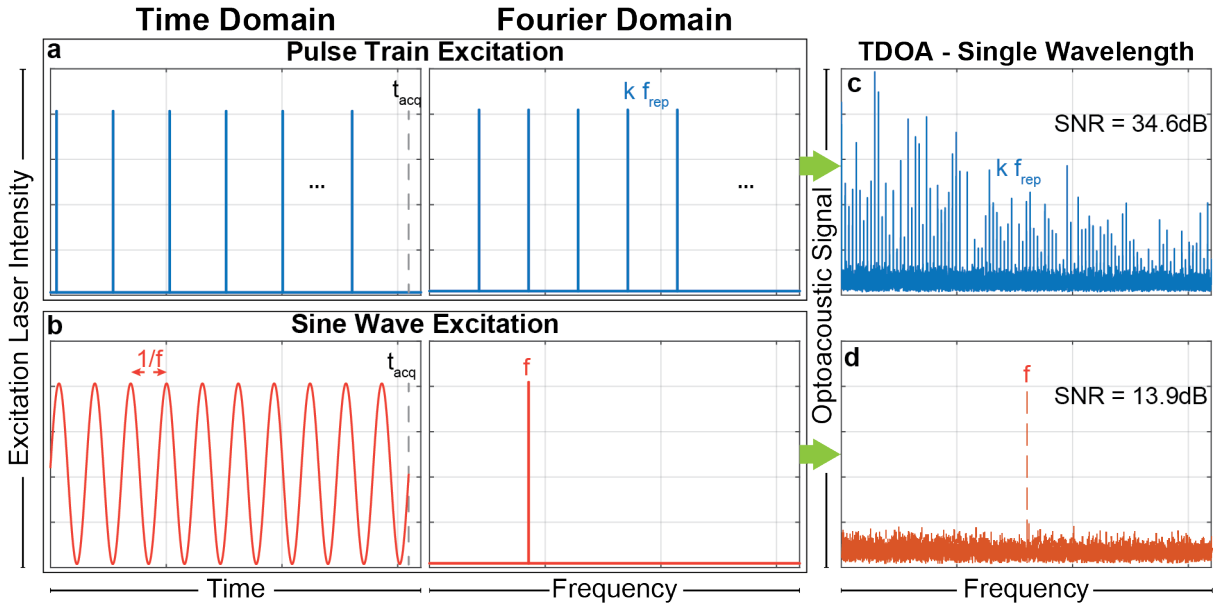

Figure 3.3: SNR Comparison between FWMOA and Frequency Domain (sinusoidal) excitation at a single wavelength. **(a)** The pulse train excitation in Time and Frequency Domain. **(b)** The sinusoidal excitation presented in Time and Frequency Domain. **(c)** The OA signal from the FWMOA excitation in **(a)** in the Fourier Space showing multiple peaks at the harmonics of the base repetition rate f_{rep}. **(d)** The OA signal from the sinusoidal excitation in **(b)** with only one peak at the frequency of the sine wave and 20.7 dB less SNR. Adapted version from [226].

In order to compare FWMOA with FD-OA we used a fiber-coupled 450 nm laser diode (FBLD-450-0.8W-FC105-BTF; Frankfurt Laser Company, Germany) connected to an analogue laser diode driver (BFS-VRM 03 HP; Picolas, Germany). The output fiber of the 450 nm laser was connected to the same input fiber of laser 1, also emitting at 445 nm, to ensure the same illumination path for both lasers. The sample was the black varnish phantom on a petri-dish.

The excitation pattern of laser 1 is presented in Fig.3.3a in the Time Domain and in the Frequency Domain. The analogue laser was modulated using a sine wave at 20 MHz (Fig.3.3b)

and adjusted its mean power to match the mean output power of laser 1, emitting 7 ns, 189 nJ pulses at 200 kHz, as measured by the stabilized thermal power meter. The mean power for both lasers was 37.8 mW.

The OA signal resulting from the excitation pattern in Fig.3.3a is presented in Fig.3.3c in the Frequency Domain and exhibits multiple peaks at the harmonics of its repetition rate. The OA signal resulting from the excitation pattern in Fig.3.3b is presented in Fig.3.3d and exhibits a single peak at its modulation frequency. FD-OA achieved 13.9 dB SNR and FWMOA demonstrated 20.7 dB higher SNR (34.6 dB) compared to FD-OA due to the higher energy transient of a pulse compared to the energy transient of the sine wave. Moreover, FWMOA records multiple frequencies simultaneously that also results in high axial resolution compared to no axial resolution in FD-OA.

3.4 Results

3.4.1 Spatial Resolution

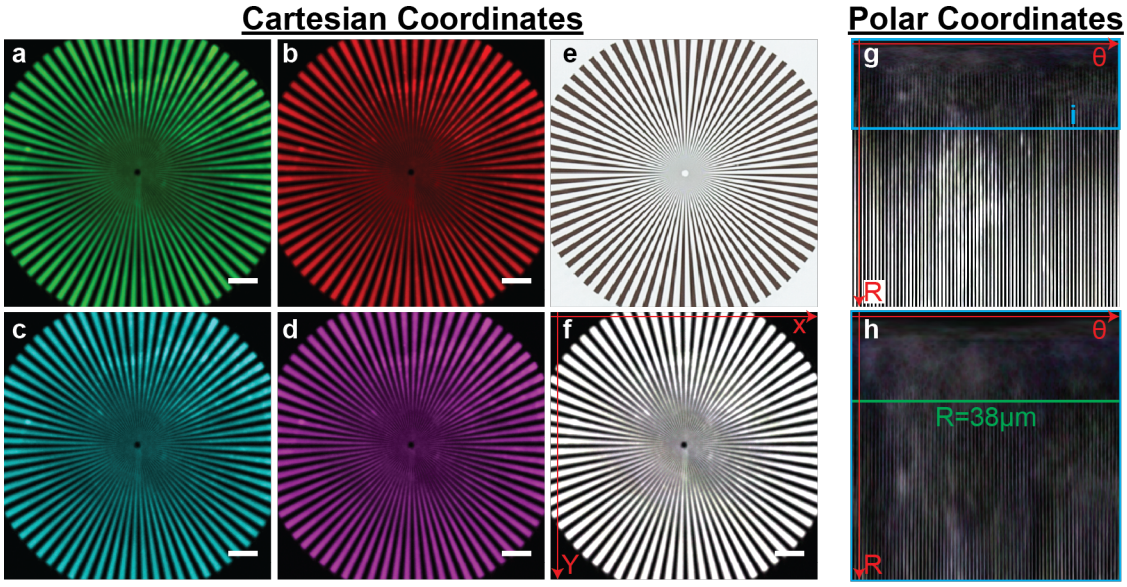

Figure 3.4: OA images from the Siemens Star Resolution phantom. **(a)-(d)** The maximum intensity projections of the reconstructed OA images in Cartesian coordinates from wavelengths 445, 465, 638, 808 nm, respectively. **(e)** The bright field image of the original Siemens Star phantom. **(f)** The Composite OA image of the same phantom in Cartesian coordinates. All scale bars are 1 mm wide. **(g)** The Composite OA image from **(f)** presented in polar coordinates. **(h)** A zoomed images from the cyan box marked with **i** in **(g)**. The green line indicates the smallest radius that all lines can be well resolved which results in a spatial resolution of 38 μm. Adapted version from [226].

Fig.3.4 presents the maximum intensity projection of the reconstructed OA images of the Siemens Star resolution phantom along the vertical direction at wavelengths 445, 465, 638 and 808 nm (Fig.3.4a, b, c and d respectively). Fig.3.4e shows an image of the original phantom and Fig.3.4f the composite image that consists of all four wavelengths; the display color is green, red, cyan and magenta for lasers 1, 2, 3 and 4, respectively. Since the image SNR is strong for all wavelengths the contrast in the composite image appears as white. All images up to now

are presented in Cartesian coordinates. However, in order to correctly estimate the system's resolution, the images have been transformed into polar coordinates; Fig.3.4g demonstrates the composite image in polar coordinates and Fig.3.4h a close up version of the cyan rectangle in Fig.3.4g indicated with **i**. The green line in Fig.3.4h shows the smallest radius where all 72 lines can be resolved, at 38 μm, which is the estimated system's lateral resolution.

3.4.2 High Resolution Mouse Ear Imaging

Fig.3.5 presents the results of the mouse ear imaging experiments. Fig.3.5a-c shows the results of the first mouse ear imaged. The maximum intensity projections along the vertical axis of the reconstructed images from the two blue wavelengths (green for 445 nm and red for 465 nm) are presented (Fig.3.5a and b). Fig.3.5c showcases the superposition of these two images, where red indicates a higher oxygenation region than green. We can differentiate many vessels at different oxygenation levels; we also observe that the main vessels usually come at pairs of oxygenated (main artery) and de-oxygenated (main vein) vessels.

In order to visualize multiple structures in the mouse ear, we imaged a second mouse ear and injected Evan's Blue and ICG intradermally to introduce external contrast at lasers 3 and 4. The OA images generated by our system allows us to simultaneously reveal blood vessels (Fig.3.5d,e) and lymphatic vessels (Fig.3.5f,g), since there is a significant uptake of the two dyes from the lymphatic vessels, which reveals them in lasers 3 and 4, that were previously invisible. We notice that there is significant diffusion of Evan's blue around the lymphatic vessels that is visible in the OA image (Fig.3.5f) and the bright field image of the mouse ear (Fig.3.5h). The injection points for Evan's Blue and ICG is visible in lasers 3 and 4. The composite image of all four wavelengths (Fig.3.5i) allows for co-localization of blood and lymphatic vessels for the first time using CW-LDs.

3.4.3 Fast multipectral Imaging and Sensing - Vessel Dynamics

Next, we examined whether we can take advantage of the high repetition rate of the CW-LDs and the FWMOA technique to record OA signals from multiple wavelengths simultaneously at high rates and detect dynamic biological changes in the mouse ear. First, we scanned the mouse ear (in Fig.3.6a a composite image from laser 1 and laser 2 is shown) and we identified, close to the base of the mouse ear, an artery vein vessel pair. We performed continuous B-Scans of 2 mm length at a rate of $\sim$4 Hz, as shown in Fig.3.6a by the small blue box; a single B-Scan is also presented (**i**) and the artery (red) and the vein (green) are indicated with arrows.

Next, we performed the oxygen stress test. Fig.3.6b presents the ratio of the signal intensity of laser 2 over the signal intensity of laser 1, which is proportional to the blood oxygen saturation, for the main artery (red line) and the main vein (green line) over time. The oxygenation is always higher in the artery compared to the vein, as expected. We also observe that the oxygenation remains constant throughout the first "O_2" period and drops, with a small delay, during the "Air" periods. The oxygenation drops earlier, faster and at higher percentage in the artery than in the vein. The oxygenation recovers to approximately the same values during the "O_2" periods.

We also calculated the Oxygen Extraction Rate (OER) as [244]

$$\mathrm{OER} = \frac{O_{ca} - O_{cv}}{O_{ca}}, \tag{3.12}$$

where, O_{ca} is the oxygenation of the central artery and O_{cv} the oxygenation of the central vein. The OER is an estimation of the amount of the oxygen extraction by the cells and the tissue.

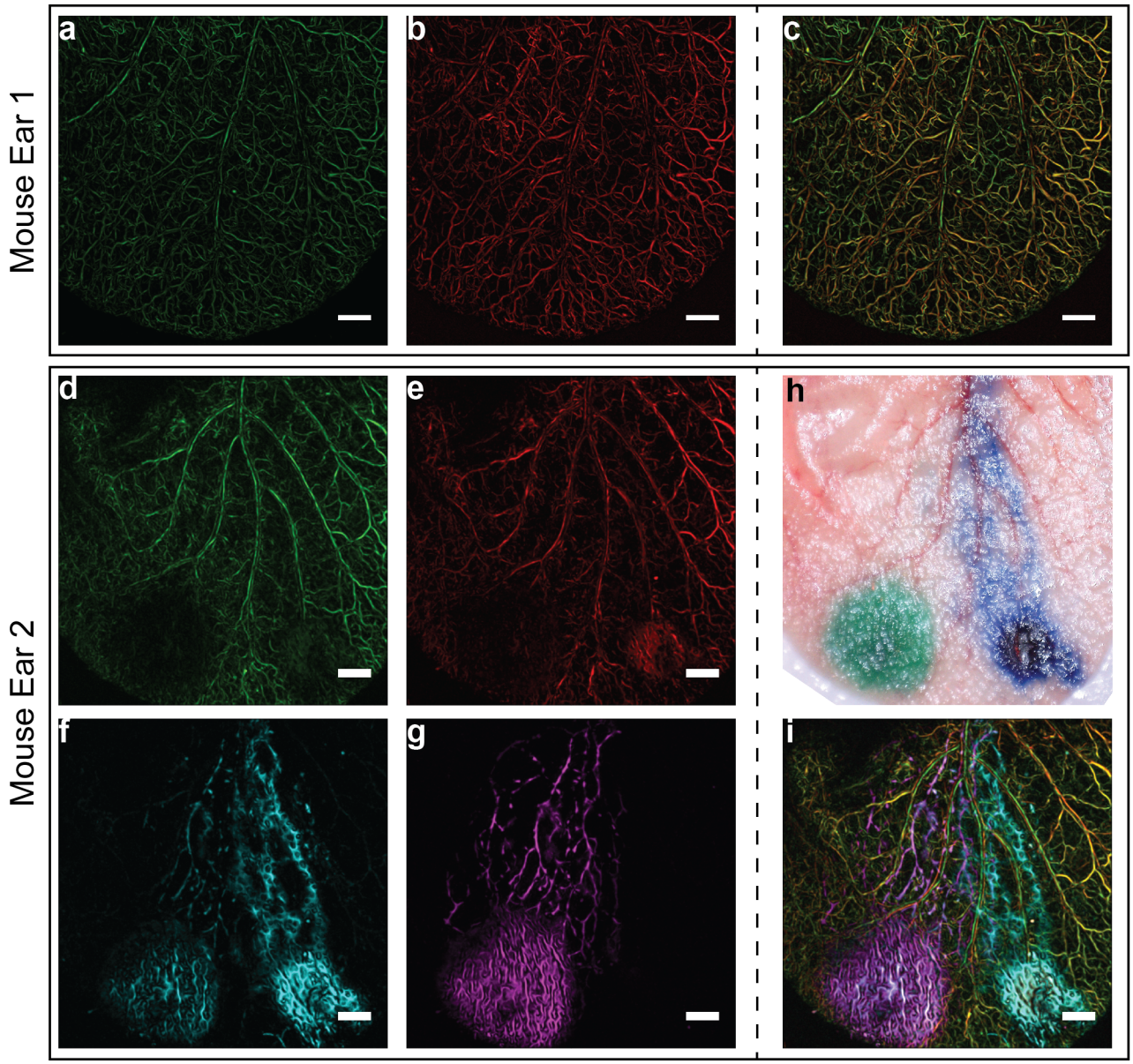

Figure 3.5: In-vivo imaging using FWMOA. **(a)** and **(b)** present a mouse ear at the 2 wavelengths with high resolution. **(c)** is showing the same mouse ear at the 2 wavelengths simultaneously. 445nm is absorbed more by de-oxygenated haemoglobin and 465nm is absorbed more by oxygenated haemoglobin, therefore more red in **(c)** presents more oxygenated areas and green less oxygenated areas. **(d)-(g)** present a second mouse ear at the 4 wavelengths. **(h)** an image of the mouse ear. We have injected Evan's Blue (absorbed in 638nm) and ICG (absorbed in 808nm) intradermal as can be seen in the images **(f)**, **(g)** and **(h)**. **(g)** and **(h)**, the dyes injected go into the lymphatic vessels that present a different structure than blood vessels. **(i)** presents the image at all 4 wavelengths simultaneously, we can observe oxygenated (red) and de-oxygenated (green) blood vessels, Evan's Blue (magenta) and ICG (cyan) in the lymphatic vessels at the same time. All images are maximum amplitude projections of reconstructed OA images. Green is 445nm, Red is 465nm, Magenta is 638nm, Cyan is 808nm, scale bar 1mm. Adapted version from [226].

The OER as a function of time (Fig.3.6c) shows a delayed drop in the OER after the two "Air" period, suggesting that not enough oxygen was available in the main artery for the cells

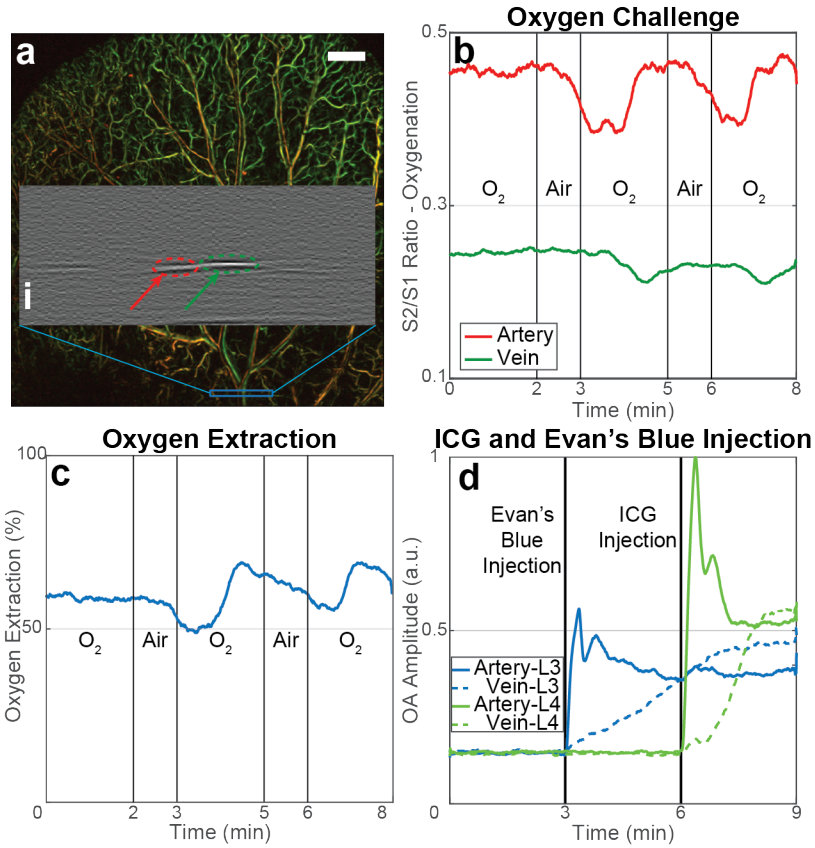

Figure 3.6: Oxygen challenge experiment and dye injection monitoring in central vein and artery in the mouse ear using FWMOA imaging. Green is 445nm, Red is 465nm, Magenta is 638nm, Cyan is 808nm, scale bar 1mm. **(a)** shows the OA images in the blue wavelengths, showing oxygenated (red) and de-oxygenated (green) vessels. We performed continuously BScans on the blue region denoted in **(a)** and **i** shows such a cross-section. The green arrow and region in **i** indicated the vessels selected as the vein and the red arrow and region the vessel selected as the artery. **(b)** demonstrates the changes in the ratio between the OA signal intensity in wavelength 2 (S_2) to that of wavelength 1 (S_1) in time during an oxygen stress test. The oxygen saturation is proportional to the ratio S_2/S_1. The oxygen saturation changes faster in the artery than in the vein, as expected. **(c)** shows the oxygen extraction during the same experiment. **(d)** presents the signal intensity at wavelengths 3 and 4 (S_3 and S_4 respectively) at the same artery and vein indicated in **(a)** during injection of the 2 dyes, Evan's Blue and ICG. In both cases the signal intensity increases first in the artery and later in the vein. Adapted version from [226].

to consume. However, following the second and third "O_2" periods, as more oxygen became available, we observe an increased OER and thus oxygen uptake that returns to the baseline values towards the end of the experiment.

Next, we injected in the tail vein the two dyes and monitored at the same point region (blue box in Fig.3.6a) the diffusion of Evan's Blue and ICG in the vascular system (Fig.3.6d). For both dyes we observe the same post-injection pattern, with two distinctive peaks before settling to a baseline value. In addition, the signal increased first and much faster in the main artery and with a small delay and slower rate to the main vein, indicative of the dye diffusion in the microvasculature network of the mouse ear.

3.4.4 Multispectral LD Mesoscopy of Skin

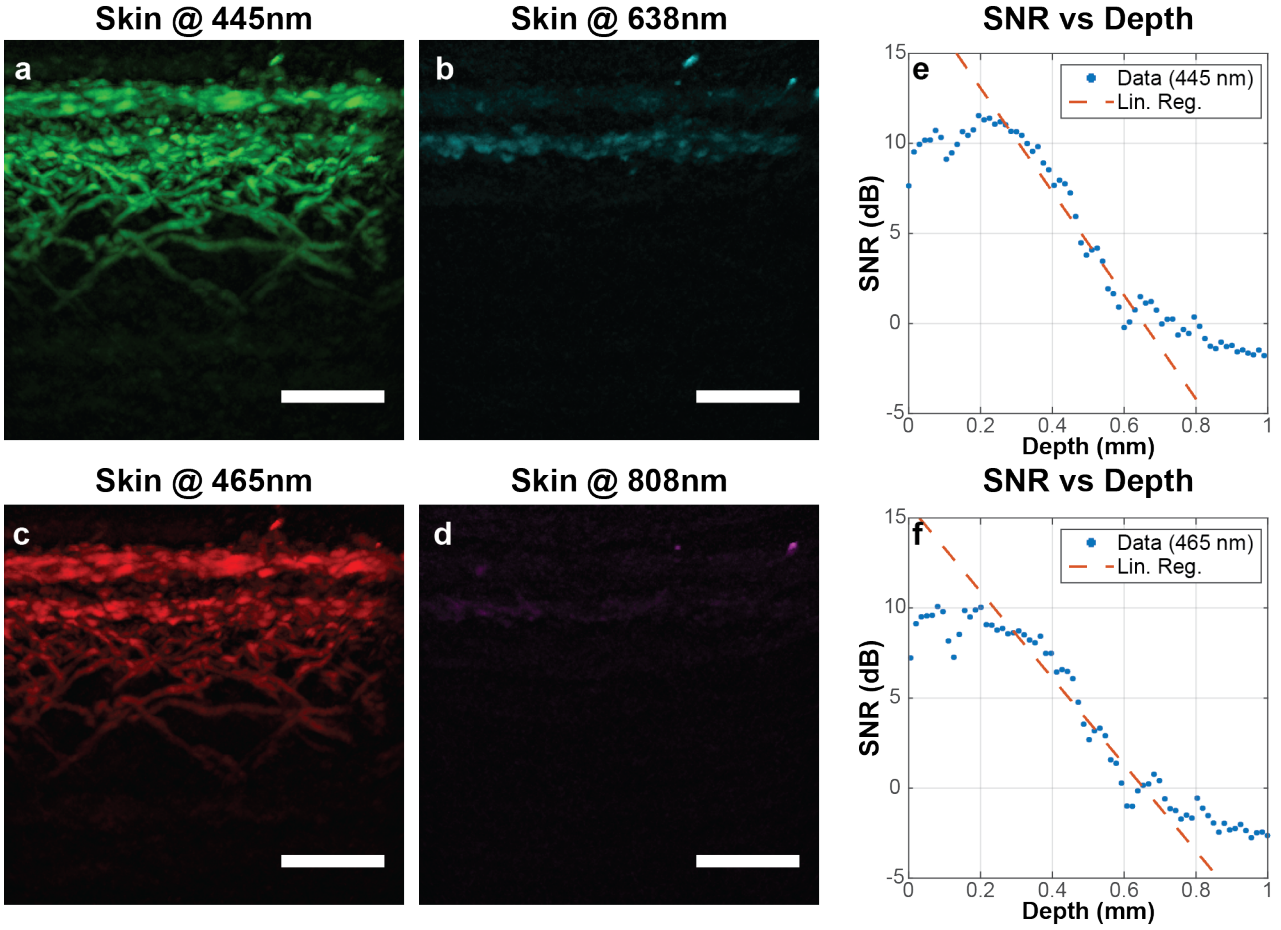

Figure 3.7: Optoacoustic imaging of skin at multiple wavelengths using the overdriven CW-LDs. **(a-d)** Maximum Intensity Projection of reconstructed optoacoustic images along a horizontal direction at 445, 465, 638 and 808 nm respectively. **(e, f)** The image SNR as a function of depth from the skin surface for images **(a)** and **(b)** respectively. Scale bar: 1mm. Adapted version from [226].

Last, we imaged a thick biological sample, the lower forearm of a healthy human volunteer. The maximum intensity projection along a horizontal direction of the reconstructed OA images are demonstrated in Fig.3.7a-d. We see that in the two blue wavelengths (445 and 465 nm, Fig.3.7 a and c) there is signal from the melanin layer of the epidermis and from the vessels that are located deeper in the tissue, in the dermis. The red laser (Fig.3.7b) has only weak signal from the melanim and the microvasculature in the upper layers of the skin. The NIR laser (Fig.3.7d) presents almost no SNR since the contrast in this wavelength is very weak to generate a detectable OA signal from such low energies per pulse that the CW-LDs provide. We also calculated the SNR of the OA images of the blue wavelengths as a function of depth (Fig.3.7e and f with the red dashed line showing a linear fit) and we notice that in both cases the image is around 10 dB for the first few hundreds of μm's and drops quickly to 0 at around 600 μm, that is the estimated penetration depth in human skin of our system. This is due to the use of blue wavelengths that are highly absorbed by the melanin and the blood vessels at the upper layers of the skin and are also highly scattered. However, it is the first time that high resolution, multi-wavelength OA images are generated by a semiconductor light source for OA imaging from human skin.

3.5 Discussion

In this chapter we presented, for the first time, a multiple wavelength Raster Scanning Optoacoustic Mesoscopy system that utilizes low-cost and miniaturized overdriven CW-LDs as the illumination source. The multispectral CW-LD RSOM offers fast multiple wavelength simultaneous illumination, by using the FWMOA algorithm, at high repetition rates. Using this system we presented high quality images from a mouse ear and the human skin in-vivo at multiple wavelengths simultaneously. We managed to reveal multiple structures, i.e. oxygenated and de-oxygenated blood vessels and lymphatic vessels simultaneously in the mouse ear and performed vessels dynamics and dye diffusion experiments *in-vivo*.

We have shown that the system can achieve high spatial resolution of 38 um in the lateral direction, the highest so far in LD AR-PAM. Previous works in OA imaging with semiconductor light sources have either focused the light in a small point to increase the energy density, and thus the SNR, and achieve high lateral resolution [210, 214, 215], in OR-PAM, or used low frequency UST [207, 212], in AR-PAM, that are more sensitive but offer low spatial resolution. In addition, previous works have mostly used long pulse widths [211,212,214] in order to increase the energy per pulse, and the SNR, in the expense of decreased spatial resolution. In this work, we managed to increase the spatial resolution of the system by achieving two things. First, by overdriving the CW-LDs we achieved the lowest pulse widths for CW-LDs, $\sim$ 7 ns, and increased the output energy per pulse, $\gtrsim$140 nJ per pulse and peak power $\gtrsim$14 W, that can provide a high SNR and spatial resolution at the same time using low-cost semiconductor light sources. Second we used a sensitive, high frequency and wide bandwidth UST that offers good SNR and high spatial resolution at the same time.

It is also the first time that an OA system achieves multiple wavelength illumination with more than 2 wavelengths in AR-PAM. Previous attempts have been limited to either sequential illumination with different wavelengths [198, 245, 246] or used a coded excitation sequence based on unipolar Golay codes [247], which is however limited to two excitation wavelengths. In this chapter we presented a system that uses the Frequency Wavelength Multiplexing algorithm to illuminate the sample with 4 wavelength. The FWMOA algorithm allows the excitation of the sample with up to 27 wavelength for the parameters used here, i.e. 200 kHz repetition rate, 100 pulses to average and an UST bandwidth between 22 and 78 MHz.

In this chapter we presented a series of improvements compared to the single wavelength system presented in Chapter 2 that provided high quality AR-PAM imaging:

- We improved the design of the custom-made pulsed laser diode driver, that is smaller in size, presents lower path inductance and achieved lower pulse widths and higher peak power. At the same time new CW-LDs became commercially available that offered new wavelengths, e.g. the LDM-465-3500 emitting at 465 nm, and higher peak power and energy per pulse, e.g. the LDM-445-6000 and the HLG63283HG.
- We found a way using of-the-shelf components to efficiently couple all CW-LDs, of any package type, into a multimode fiber of 200 μm core diameter and 0.22 NA, that allowed us to take advantage of all available CW-LD in the market. This configuration can be further miniaturized if specific optics are developed for this purpose.
- By using a fiber combiner, we found an easy and practical way of confocally aligning all the excitation sources and the UST detection field and illuminating the sample using the same path for all CW-LD.
- By illuminating the sample symmetrically from 4 sides we achieved homogeneous illumination, especially deeper in the tissue. In addition, we avoided using lenses to focus the light and relied on the small output NA of the fibers and their close proximity to the sample, as well as

the high precision of our 3D printers for good alignment with the UST sensitivity field, that achieved consistent and high quality imaging.

• We integrated in the reconstruction algorithm the electric and spatial impulse response correction for our UST that further increased the spatial resolution achieved.

• We used the Frequency Wavelength Multiplexing algorithm to illuminate the samples with multiple wavelength simultaneously and achieve a high SNR through averaging without increasing the acquisition time.

We have therefore proved that overdriven CW-LD can provide high quality multispectral AR-PAM at low-cost and with a small form factor. The system presented high performance in monitoring fast dynamic biological changes, such as oxygenation changes, dye perfusion and blood circulation. In the next chapters, we use the overdriven CW-LDs to develop miniaturized and low-cost single point sensors for biological and environmental applications. We understood that by removing the scanning stages and aiming for single point sensing the cost of the system can be drastically reduced and there is still a lot of interesting information to be recorded and processed. One possible application, that we investigate in the following chapter, is to develop a low-cost and compact OA oximeter that can detect non-invasively the local oxygen saturation of tissue microvasculature, and can provide, after proper calibration of the sensor, absolute values of the oxygen saturation and not just relative changes as presented in this chapter.

Chapter 4

Single Point Spectroscopic Optoacoustic Oximeter

The work presented herein has been separately published and the Figures have been adapted with permission from [248][1]. ©The Optical Society .

4.1 Introduction

4.1.1 Oxygenation Measurements

Blood oxygenation can be monitored at a systemic level by measuring the arterial blood oxygen saturation, that is routinely assessed by the pulse oximeter [249–251]. However, tissue oxygenation is the partial pressure of oxygen within the interstitial space of a particular tissue [252]. Each organ has its own normal oxygenation status that depends on its size and function [253]. Tissue oxygenation of specific organs or at different points in the human body may differ from the arterial blood saturation due to a multitude of conditions, including cardiovascular disease, diabetes, cancer, or metabolism [254, 255]. In particular, it is necessary to know the tissue oxygenation in critical situations, such as during surgery (anastomosis, tissue perfusion, transplantation etc.), in emergency rescue services and emergency rooms, and for patient monitoring in the Intensive Care Unit [255, 256]. Certain conditions, such as regional ischemia, are also not easily detected at a systemic level by monitoring arterial oxygenation and can cause severe complications in major trauma cases or critically ill patients [257]. It is furthermore important to monitor the tissue oxygenation and perfusion during wound healing, to estimate the healing potential [108, 258], or to know the local oxygenation of the tumor area during cancer treatment to slow or prevent its growth [255]. However, tissue oxygenation cannot be directly calculated by the arterial blood oxygenation as there is poor correlation between arterial blood oxygenation and tissue oxygenation values [252].

Invasive methods of measuring oxygen pressure (pO2) in blood or tissue are already commercially available for use in humans. The most common device is the Blood Gas Analyzer (BGA), which uses electrochemical methods to measure parameters in a sample of arterial blood, such as pO2, pCO2, and pH. The BGA is the gold standard for measuring blood parameters of

[1]Antonios Stylogiannis developed the sensor presented herein, performed the calibration and in-vivo experiments and processed the data. Dr. Lucas Riobo, Dr. Ludwig Prade, Giulia Lucidi and Dr. Martin Fuchs assisted at various stages of the sensor hardware development. Dr. Lucas Riobo, Sarah Glasl and Dr. Sabine Klein assisted with the mouse experiments. Dr. Lucas Riobo assisted in the blood phantom experiments. Dr. Dieter Saur and Dr. Vasilis Ntziachristos helped with extensive discussions and guidance in conducting this research.

patients in the clinics because of its ease of use, the diverse information it provides, and its fast operation (60 sec). However, BGAs are expensive, have a large form factor, require an arterial blood samples from patients, and cannot provide real time data [259].

OxyLite is a commercially available laboratory device that can measure tissue oxygenation (pO2) and local temperature in real time. The device detects dissolved oxygen by measuring changes in the decay rate of a fluorescence dye (using fluorescent quenching methods). The fluorescent dye is contained in a silicon matrix in the tip of a fiber that is inserted into the tissue and must remain there during the measurement period. However, despite Oxylite's advantages, it can provide real time local tissue oxygen pressure measurements, it is not suitable for use in humans, as stated in the instruments manual [260–262].

In contrast to tissue oxygenation and arterial oxygen saturation, local vascular oxygenation is calculated as the average value of the blood oxygen saturation of the arterioles and venules within a defined region. Local vascular oxygenation can be measured non-invasively by taking advantage of the different absorption spectra of oxygenated and de-oxygenated haemoglobin. Furthermore, local vascular oxygenation is organ specific and is a result of the balance between the oxygen delivery and uptake from the blood vessels to the tissue and the tissue oxygen consumption. Therefore, there is a much better correlation between local vascular oxygenation and tissue oxygenation compared to arterial oxygen saturation [252, 253].

4.1.2 Near-Infrared Spectroscopy

Local vascular oxygenation can be measured using optical methods such as Near Infrared Spectroscopy (NIRS) [257, 263, 264]. NIRS illuminates the tissue with continuous wave light at multiple wavelengths in the NIR region and, detects the back-scattered light at some distance from the illumination point. The detected light has also been attenuated by the different tissue chromophores and the different wavelength absorption by oxy- and deoxy-haemoglobin is used to calculate the local vascular oxygenation. However, due to the detection of back-scattered photons, NIRS samples a generally large volume (1.5 cm^3) which contains mixed contributions of multiple tissue components. Moreover, quantification of oxygen saturation in the tissue is affected by both scattering and absorption, making it challenging for NIRS methods [265, 266].

The pulse oximeter is a small, low-cost implementation of NIRS [249–251], that is widely used in the clinics. In order to overcome the light scattering in tissue, the pulse oximeter takes into account only the time varying part of back-scattered light that depends on the heart pulse, thus measuring only arterial blood oxygenation. However, the pulse oximeter requires a sufficient amount of blood in the measured microvasculature and a steady, strong blood pulse to measure the arterial blood oxygen saturation with accuracy. Vasoconstriction, low blood pressure, cardiac arythmia, venous congestion have been reported to influence the signal quality and the sensor's ability to measure arterial oxygen saturation [267, 268]. These limitations can limit the pulse oximeter's utility during critical situations in which these conditions are prevalent, such as during surgery or emergency rescue services.

4.1.3 Low-Cost Optoacoustic Systems

Since OA techniques rely on optical excitation, they can exploit the characteristic absorption profiles of oxy- and deoxy-haemoglobin to measure local vascular oxygenation [55, 69, 127]. Furthermore, acoustic (rather than optical) detection is not susceptible to scattering in tissues, enabling OA methods to resolve depth with higher axial and spatial resolution than NIRS and image small structures, such as microvasculature [110, 119, 160]. Oxygenation is usually

measured *in-vivo* using multispectral OA imaging systems [206,269–271], which typically employ a high energy laser source and a high bandwidth piezoelectric transducer as a detector. These systems can thus obtain high quality multispectral images, which can reveal vasculature in the skin and measure blood oxygenation in tissue [157]. However, multispectral OA imaging systems are complex, expensive, and bulky, and are therefore ill suited for point-of-care or bedside applications.

Low-cost OA imaging and sensing systems have been developed, which employ semiconductor light sources (LDs or LEDs) as illumination sources [109,137,185,198,199,272]. A commercially available system, in order to achieve the necessary power, utilizes 4 rows of 36 LED arrays (144 total elements) at different wavelengths between 470 nm and 850 nm and a 128 element US array for combined US and OA imaging [206,273]. A miniaturized OA system combines a single red laser diode and an US array to image skin melanomas [274]. However, US arrays necessitate many amplifiers and analog-to-digital converters (ADCs) to record the signals, thus increasing the cost and the complexity of the system. We have already presented OA systems that used LDs in AR- or OR-PAM with stage [214] or galvanometric [275] scanning to perform imaging. In any case, imaging increases the cost and the complexity of the OA systems for simple applications such as vascular tissue oxygenation estimation. Single point OA sensors employing bulky and expensive lasers such as dye [276] or Solid State Lasers coupled to OPOs [277] have been introduced for the determination of blood oxygenation. Spectroscopic OA sensors using low-cost LDs have been demonstrated in trace gases detection in the atmosphere [278,279] or for breath test analysis in human patients [280]. However, to-date there is no single point OA sensor for vascular tissue oxygenation estimation that uses low-cost LDs and is suitable for point-of-care or bedside applications.

4.2 Spectroscopic Portable Optoacoustic Sensor (SPOAS)

4.2.1 System Development

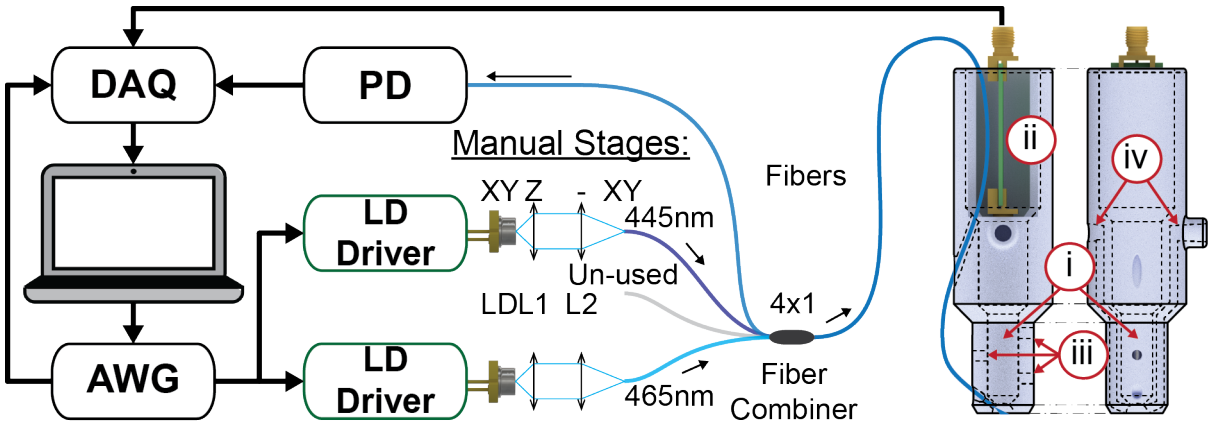

Figure 4.1: Schematic of the Spectroscopic Portable Optoacoustic Sensor (SPOAS) for assessment of local vascular tissue oxygenation. LD: Laser Diode, AWG: Arbitrary Waveform Generator, DAQ: Data Acquisition Card. Adapted with permission from [248] ©The Optical Society.

SPOAS is a simplified version of the multispectral CW-LD RSOM presented in the previous chapter. As many of the components used in this system are the same with the ones presented above (Chapter 3) we are only going to present here the new elements. The schematic of SPOAS is shown in Fig.4.1. In the absence of the stages and the stages controller, in SPOAS the AWG is

controlling the CW-LDs and the synchronization with the DAQ. For SPOAS we used a 4x1 fiber combiner (H26385704, LasFiberio, China) with four 200 μm fiber core, 0.22 NA input fibers and a single 400 μm fiber core with 0.22 NA as the output. Only the two blue laser diodes were used here, emitting at 445 nm (LDM-448-3500, LaserTack, Germany) and at 465 nm (LDM-465-3500, LaserTack, Germany) using the updated pulsed laser diode driver from Chapter 3. Only two of the fiber inputs were used and we utilized the small amount of back-scattered light (present in all input fibers) of the third fiber to use it as an input to the Photodiode (DET10A2, Thorlabs, USA) and correct for the pulse per pulse energy variation and the time-jitter. The four input was left empty and available for future updates.

The SPOAS probe was a custom-made 3D-printed holder that hosted the UST (**i** in Fig.4.1, HFM29, Sonaxis, France). The use of lower central frequency UST increases the sensitivity (as lower frequencies attenuate less and lower frequency UST as usually more sensitive) and reduces the spatial resolution. Since no imaging is performed the acquisition of OA signal from a larger area can further increase the SNR. A low-cost and miniaturized low noise amplifier (**ii**) has also been developed using two monolithic voltage amplifiers (ERA-8SM+, Minicircuits, USA) that is connected directly to the UST. The holder also utilizes retaining screws (**iii**) to secure the position of the UST and water tubes (**iv**) to allow for easy water coupling of the UST. The output fiber is aligned to illuminate the same point as the UST detection focal spot for optimal OA signal detection. As it was demonstrated in Chapter 3, no focusing lens was used and the sample was illuminated from the side, at an angle of $\sim 50^o$.

The size of the illumination spot on the sample was measured with a CCD camera (daA1920-30um; Basler AG, Germany) and it was circular with a diameter of ~ 1 mm. The energy per pulse of the overdriven CW-LDs was measured with the stabilized thermal power meter (PM160T, Thorlabs, USA) and it was 120 and 140 nJ for the 445 and 465 nm CW-LDs respectively. For all OA measurements, we used a repetition rate of 250 kHz and 700 averages for both LDs that resulted in an acquisition rate of 15 Hz, including signal acquisition and processing. Using these values, the total skin exposure was calculated as 8.3 μJ/cm^2 and 2.07 W/cm^2 far less than the MPE limits of 20 mJ/cm^2 and 8 W/cm^2 imposed by the American National Standards Institute (ANSI) [220].

4.2.2 Blood Phantom Calibration

In order to characterize the system and calibrate it to provide absolute values of blood oxygen saturation we developed the setup shown in Fig.4.2a. A volume of 50 mL of heparinized pig blood (Fiebig-Naehrstofftechnik, Germany) was placed in a blood receptacle and was continuously stirred with a magnetic stirrer. The pig blood was mixed with air to increase its oxygen saturation to the maximum. Next, in order to reduce its oxygenation in a controlled fashion we injected in the blood a de-oxygenation agent (DOA) that was a solution of phosphate buffered saline (PBS) and sodium dithionite (Merck KGaG, Germany). The blood recepticle was connected with tubes to a microfluidic chip (01-0173-0156-02, Microfluidics ChipShop, Germany) on top of which SPOAS was placed to monitor the blood oxygenation. After measuring the blood oxygenation on the microfluidic chip the blood was drawn into a syringe and its oxygenation status was measured with the gold standard instrument in the clinics, the Blood Gas Analyzer (BGA, Combiline, Medizintechnik Hadler & Braun GmbH, Germany).

Fig.4.2b shows the correlation of the blood phantom oxygen saturation as measured by SPOAS and the gold standard instrumentation, the BGA, that also serves as the calibration curve. The power of the signal at both wavelengths, S_{445} and S_{465}, was used to calculate the

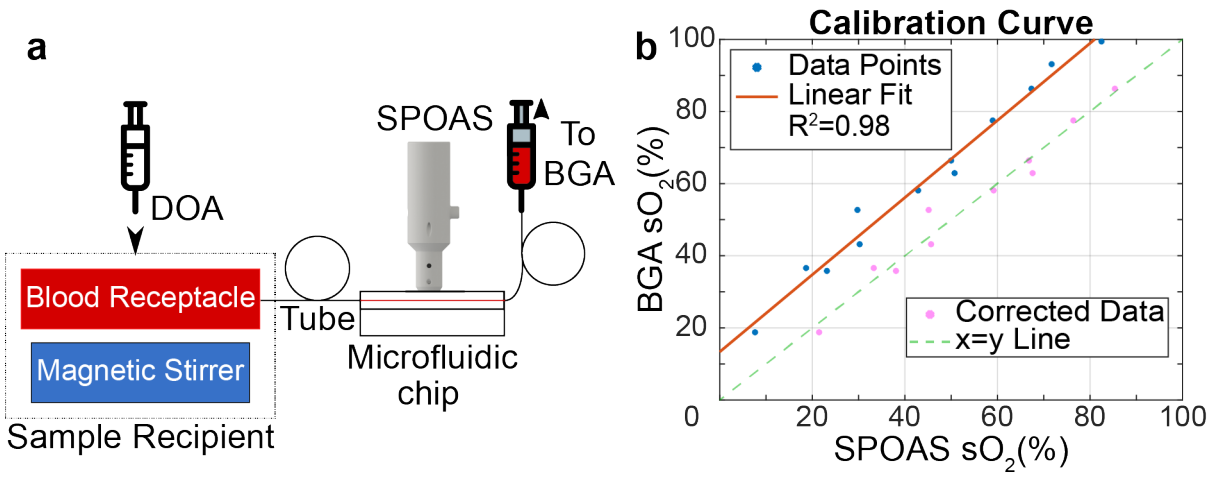

Figure 4.2: System characterization and calibration. **(a)** Experimental setup for assessment of blood phantom oxygenation. DOA: Deoxygenation Agent, BGA: Blood Gas Analzyer. **(b)** SPOAS calibration curve showing strong linear correlation between the values of SPOAS and BGA; the same data corrected to fit the $x = y$ line fit. Adapted with permission from [248] ©The Optical Society.

blood oxygen saturation of the blood phantom using the following formula [270]

$$SO_2 = \frac{\varepsilon^d_{445} S_{465} - \varepsilon^d_{465} S_{445}}{(\varepsilon^d_{445} - \varepsilon^o_{445}) S_{465} - (\varepsilon^d_{465} - \varepsilon^o_{465}) S_{445}}, \tag{4.1}$$

where, ε^o_{445} and ε^d_{445} are the absorption coefficient of oxy and de-oxy hemoglobin at 445 nm, respctively, and ε^o_{465} and ε^d_{465} the respective coefficients for 465 nm.

We measured the blood oxygenation at various levels of DOA concentration in the blood and the data are presented in Fig.4.2b with the blue dots. The linear fit (orange line) shows a strong linear correlation ($R^2 = 0.98$) between the blood oxygenation as measured by SPOAS and the BGA, with an offset of 13% and a slope of 1.07, values very close to the expected 0 and 1. The same data were corrected, using these calibration values, to the $x = y$ line and are also presented in Fig.4.2b (pink dots and green dashed line). In the following, we use the values of the linear fit (both the offset and the slope) to correct the raw values of SPOAS to the BGA for the *in-vivo* experiments.

4.2.3 In-vivo Results

We validated the ability of SPOAS to assess the vascular tissue oxygenation in living mice by performing an oxygen stress test *in-vivo* and the results are shown in Fig.4.3. All procedures with animals were approved by the District Government of Upper Bavaria. SPOAS was used to measure the local vascular tissue oxygenation above the mouse skin non-invasively at three different points as shown in Fig.4.3a, one in the belly region, one in the left and one in the right mouse thigh. As a control instrument we could not use the BGA in this case, as it is calibrated for human blood and not for mouse blood that has much smaller red blood cells (pig has similar size red blood cells to human and we were able to use for calibration). Therefore, as a control instrument we used the Oxylite Pro (Oxford Optronix, UK) that measures the local value of oxygen partial pressure (pO_2) and the temperature. The OxyLite Pro probing fiber was inserted in the mouse tail vein using a 22 G catheter to monitor the overall oxygenation

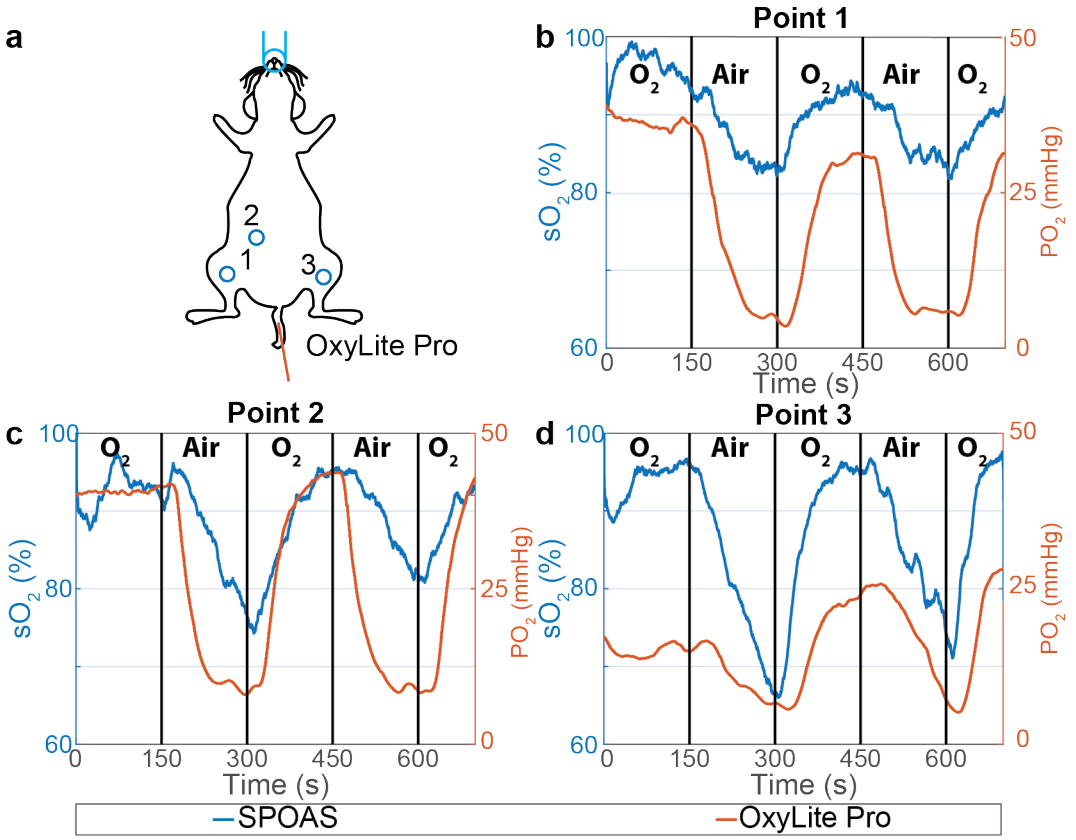

Figure 4.3: Vascular Tissue Oxygenation assessment of a mouse *in-vivo*. **(a)** Mouse schematic showing the measurement location points. **(b)-(d)** Blood oxygen saturation from SPOAS and pressure of Oxygen from OxyLite Pro obtained at point 1,2 and 3 during an oxygen stress test. Adapted with permission from [248] ©The Optical Society.

changes. The nude mouse (Athymic Fox-N1) was positioned on its back and it was breathing a mix of isoflurane for anesthesia and two different concentrations of oxygen for 150 second alternatively for five cycles: 0.9 lpm of 100% oxygen (indicated by "O_2") and 0.9 lpm of 20% oxygen (indicated by "Air").

The results of the experiments are presented in Fig.4.3b-d for point 1,2 and 3 respectively. The is a relationship between the pressure of oxygen (pO_2, the value provided by the OxyLite Pro) and the blood oxygen saturation [281](sO_2, the value provided by SPOAS) but it requires the values of pressure of carbon dioxide (pCO_2) and the pH, which are not provided by the reference instrument. Therefore, for the tail vein oxygenation we plot only the pO_2 value and do not convert it into sO_2, as we would have to assume the values of pCO_2 and pH from the literature.

We observe that in all three point the oxygenation changes are in agreement with the oxygen stress test expectations, it drops to lower values during the "Air" periods and recovers to the baseline values during the "O_2" periods. In addition, we observe a similar behavior of the OxyLite Pro probe values that strengthen the validity of SPOAS. According to the literature, arteries and arterioles present a normal oxygen saturation of over 95% and veins and venules a normal oxygen saturation value between 65 and 75 % [256]. During the "O_2" periods the local vascular oxygenation is always around 95%, that fits the theoretical expectations, the mouse is breathing 100% oxygen and an increased oxygenation is to be expected also in the veins and venules. During the "Air" periods the vascular tissue oxygenation drops to values higher than

80, 70 and 65 % for the measurement Points 1,2 and 3 respectively. As the local vascular tissue oxygenation is expected to be a mean value of the oxygenation of the arterioles and the venules in the interrogation volume, the values provided by SPOAS are also reasonable. As there is no other instrument that can calculate the local vascular tissue oxygenation and can serve as a reference measurement, we can infer that SPOAS is well calibrated and can provide accurately measurements of vascular tissue oxygenation in tissue, for the first time for an OA system.

4.3 Discussion

In this chapter, we developed a single point OA sensor that utilized two small and low-cost overdriven CW-LDs in the blue wavelength that is simple to use, non-invasive, handheld and can accurately measure the local vascular tissue oxygenation. SPOAS has been benchmarked against two reference instruments in blood phantoms and in mouse skin measurements *in-vivo* and achieved excellent linear correlation with those.

Vascular tissue oxygenation images have been provided by OA imaging devices in the past, however all these devices are complex, bulky and expensive to be routinely used in the clinics for non-invasive, *in-vivo* measurements of oxygenation. SPOAS is the first single point OA sensor developed to monitor the vascular tissue oxygen saturation. SPOAS has been made significantly simpler than other OA imaging devices by getting rid off galvanometric or stage scanning and using two low-cost CW-LDs. SPOAS proves that by there are a lot of information to be acquired even if signal at a single point is recorded, in comparison to imaging, thus reducing the cost and complexity of the system. In addition, SPOAS employed overdriven CW-LDs that require averaging over multiple pulses in order to increase the SNR and the systems sensitivity. However, by using the high repetition rate the overdriven CW-LDs can achieve, SPOAS provided measurements with a frame rate of ∼15 Hz (including signal processing), that is fast enough to detect oxygenation changes in real-time since these changes happen in the range of tens of seconds.

SPOAS presented excellent linear correlation with the gold standard blood analysis device in the clinics, the BGA, in blood phantom experiments ($R^2 = 0.98$). By using these data to calibrate SPOAS we proved in *in-vivo* experiments that SPOAS can provide accurately absolute values of vascular tissue oxygenation, rather than relative values (as was done for example in the previous chapter) that has challenged many OA devices so far [109]. In the future, many techniques that have been developed to correct for spectral coloring can be used to increase the sensitivity and specificity of the measurements [109].

SPOAS is the first step towards a dedicated OA oximeter. It proved that OA can be miniaturized by using the inexpensive overdriven CW-LDs. However, due to the use of CW-LDs that emit in the blue region limits the depth penetration in the skin, due to the heavy scattering of blue wavelengths by the tissue and the strong absorption of blue light by the upper skin layers that contain melanin and blood. At the moment, there are no strong CW-LDs that emit in the green region that would enable deeper imaging with a high SNR, due to the reduced scattering of green light by the tissue and the reduced melanin absorption of green compared to the blue [282]. In the future, the entrance in the market of high power green LD will overcome this limitation.

SPOAS can be further miniaturized by using low-cost and miniaturized US detection devices such as fiber optical US sensors [283–285]. Another alternative could be the use of a simple microphone or a Quartz Tuning Fork (QTF) [286] that are also air coupled devices and could also simplify the US coupling without necessitating water or ultrasound gel coupling. However, it remains to be investigated whether the low frequency US detectors can detect the broadband

OA signal from skin that contains absorbers of various sizes. Furthermore, development of dedicated electronics for excitation, detection and signal processing can reduce the size, cost and complexity of the system.

Last but not least, clinical translation of SPOAS necessitates the calibration of the system for use in humans, taking into account many other absorbers in the human tissue, such as methemoglobin, myoglobin, carboxyhemoglobin etc [264], as was previously done in the development of the pulse oximeter. Additionally, the transition from laboratory mouse measurements to *in-vivo* measurements in humans required increased energy per pulse to overcome the absorption of light by the melanin that is located at the upper part of the human skin and was not present in the nude albino mice used herein.

In this chapter, we used the miniaturized and low-cost overdriven CW-LDs to develop a single point OA oximeter, a device not previously available. Such a device can be used in the clinics, alongside the common pulse oximeter, to provide additional and complementary information that are extremely useful and valuable during surgery, emergency rescue and other critical information and help to improve treatment decisions.

We have also demonstrated that sensing, in comparison to imaging, is an area that the overdriven CW-LDs can be effectively used. We have proven herein that single point sensing can provide many valuable information with a much simpler, smaller and lower cost implementation. In addition, LD that usually require many averages to achieve a good SNR, slowing down the image acquisition, can still achieve real time sensing in situations like oxygenation changes. Another single point sensing application that overdriven CW-LDs can serve as a valuable alternative is sensing of particulates and gases in the atmosphere or at the exhaust of Internal Combustion Engines (ICEs) [287, 288]. Such a sensor is developed and presented in the next chapter.

Chapter 5

Environmental Optoacsoutic Soot Sensor

The work presented in this chapter has been published as a separate research article and the Figures and Tables are adapted versions from [289][1] with permission from the Journal. A patent application has also been filed for the OA soot sensor presented herein [290].

5.1 Introduction

Clean air is pivotal for public health as poor air quality is associated with a series of diseases, especially of the respiratory system, including asthma, lung cancer etc. The spectrum of pollutants is broad and includes greenhouse gases (CO_2, CH_4), nitric and sulphuric oxides (NO_x, SO_x) as well as particulates (including black carbon or soot). Black Carbon (BC) has been recently attracted a lot of attention due to its severe effects on human health and the environment [291, 292].

BC consists of carbonaceous micro-particles that can infiltrate the respiratory system. BC also has the ability to carry toxic chemicals with it and is especially harmful for human health [293,294]. Moreover, BC has been associated with many respiratory as well as cardiovascular diseases, contains very fine carcinogens [295] and it is estimated that a lot of human lives could be saved if BC emissions are mitigated or reduced [296]. BC significantly affects the climate, especially due to its ability to strongly absorb light and perturb the environment's albedo, most importantly in remote, snow-covered areas, like the Arctic region, the Himalayas etc [297, 298], contributing to Global Warming. Soot is also considered the second most important contributor to climate change after CO_2 [291, 299]. However, soot is considered a short-lived climate-altering agent, with a lifetime of weeks when CO_2 has a lifetime of more than 100 years [299]. Therefore, regulation of BC can immediately lead to fast climate recovery [292].

Black Carbon or Soot consists of very fine micro-particles in the range of 10-200 nm, which are products of incomplete combustion of carbon-containing fuels, such as fossil fuels, biofuels and biomass [300, 301]. The difficulty in defining BC arises from the fact that its physical and chemical properties constantly change due to atmospheric aging, different combustion temperature and pressure conditions etc. However, the most complete definition of BC is given by the International Maritime Organization [302] and is based in its carbonaceous nature, its

[1] Antonios Stylogiannis developed the optoacoustic sensor. Nikos Kousias developed the soot generation and conditioning system with the help of Anastastios Kontses. Antonios Stylogiannis and Nikos Kousias performed the soot sensor experiments together and processed the data. Dr. Leonidas and Dr. Vasilis Ntziachristos helped with extensive discussions and guidance in conducting this research.

composition of more than 80% carbon by mass and its strong light absorption across all visible wavelengths, thus the name Black Carbon. However, many other species, such as micro-particles that are products of material wear such as tar or tire rubber, also contribute to what is measured as BC.

The main source of BC today is considered to be Internal Combustion Engines (ICE) that are widely used in the Transport section (cars, buses, airplanes, trains, vessels etc) and the Industrial sector, energy generation etc. Therefore, it becomes increasingly more important to continuously monitor the BC production of the ICEs, with miniaturized and low-cost BC sensors on-board, that can help regulate and reduce the BC emissions and its impact on the environment. In addition, such sensors can be used in wide-spread sensor networks [303, 304] that can monitor the air quality in the environment. However, no such low-cost and miniaturized sensor exists that can detect a big range of particle diameters, with good accuracy [305] and preferable monitor multiple other gaseous atmospheric pollutants, such as CO_2, CO, NO_x, SO_x, HC, at the same time.

BC and other particulate matter components are measured with a wide variety of techniques. The Condensation Particle Counter (CPC) [306] enlarges the particles by using n-butanol or water to create droplets in a supersaturated gas where the particles are used as nucleation centres. The CPC detects the amount of light that is scattered by the enlarged particles and depends on their number. Therefore, the particle number of the sample can be estimated [307]. Another very common technique for measuring the particle number is the electric discharge. A device that uses this technique is the Pegasor Particle Sensor (PPS) [308, 309] which uses a corona discharge to ionize the air inflow and the particles. An ion trap removes ions that are not attached to particles and then the current of the air flow with the ionized particles is measured. However, this system requires a pressurized clean air intake to properly work that is not possible for every day on-board use. The nephelometer [310] illuminates the air suspended particles with a light source, and as particle heavily scatter photons the device quantifies the particle concentration by measuring the scattered light at 90^o. However, the nephelometer cannot measure small particles. A common disadvantage of the above mentioned techniques is that they all measure particulates in general and cannot distinguish BC from other particulate species.

As the BC definition is based on its almost flat absorption spectrum, methods based on the measurement of optical absorption are commonly used to monitor BC emissions. The opacimeter [311–313] illuminates the gaseous sample with a light source and measures the light extinction through the sample, that is affected by both absorption and scattering, and leads to low sensitivity ($\sim 300 \mu g/m^3$) even for raw exhaust concentrations and direct exhaust measurements. The aethalometer [311, 314, 315] uses a filter to trap the BC particles and then measures the light attenuation through the dirty filter at different time points. These drawbacks of this technique include slow measurement intervals, frequent change of the filter, scattering also affects the measurements and the BC properties are also affected by the particle deposition on the filter. A miniaturized aethalometer has been proposed [316] but it overestimates BC concentrations, probably due to accumulation of large amounts of BC on the filter that is used for several days that leads to artifacts. Laser Induced Incadescence (LII) [317] systems use a high energy light source to heat the particles at $\sim$4000 K and measure the black body radiation they emit to estimate the particle concentration. These systems require a very high energy light source to operate and are thus unsuitable for miniaturization.

OA (also called OptA here) signal strength is based only on light absorption and is not effected by light scattering [318, 319]. This makes OA an attractive alternative for measuring BC based on its definition of absorbing light at all wavelengths. OA sensors for the detection

and measurement of various trace gas concentration have already been developed [318, 319]. This OA technique is called Quartz Enhanced Photoacoustic Spectroscopy (QEPAS) since it uses a Quartz detector, usually a Quartz Tuning Fork (QTF), as an air coupled UST with a very high quality (Q) factor, and thus high sensitivity. QEPAS uses light sources at a wide range of wavelengths to detect a various trace gases. QEPAS is used in environmental studies to detect Green House Gases and ozone, in breath diagnosis of patients and to monitor substances such as nitric oxide, ethane, ammonia and other biomarkers [280, 318, 319].

An OA soot sensor is commercially available [320], the AVL Micro Soot Sensor (MSS), but it is only suitable for laboratory use due to its cost and size. The need for a complex flow path in order to protect the acoustic detector and the optical components from contamination from the exhaust gas, makes the device bulky and complex. Recently a low-cost soot sensor was proposed [279] that used a QTF and a LD to lower the cost and size of the device. However, the QTF stands in the exhaust gas flow to maximize its sound detection sensitivity making it prone to contamination from the measurement target gas. In addition, the laser beam needs to be focused in between the QTF legs to achieve maximum SNR that makes the sensor sensitive to small vibrations, and allows no flexibility in investigating the optimal beam size and shape to achieve maximum sensor sensitivity.

In this chapter, we developed an OA soot sensor that uses the overdriven CW-LDs together with a sensitive QTF. We introduced a novel sensor chamber design that decouples the air flow path from the US detector minimizing QTF contamination and allows for sound refocusing at the same time for maximal SNR and sensor sensitivity. The OA soot sensor developed herein, was able to detect black carbon and nitrogen dioxide (NO_2) using a single overdriven CW-LD and offered fast response to BC changes when benchmarked against a reference instrument. This sensor offers an alternative design path for an OA soot sensor that can be miniaturized and mass produced with low-cost. Such a sensor, suitable for on-board measurements, or in a large scale sensor network, will be able to monitor soot emissions in real time and help in enforcing the regulations, in order to improve air quality in the urban areas.

5.2 System Development

5.2.1 Sensor Design

There are two major design choices for the geometry of the sensor chamber that determine the sensor's characteristics and sensitivity, the off-beam and the on-beam. The off-beam sensor has a cylindrical resonator that amplifies the generated ultrasound of a specific frequency in order to increase the sensitivity [319, 321, 322]. A small hole on the cylindrical resonator allow the sound to be recorded by the UST, usually a QTF or a normal microphone. This configuration allows for a high SNR and the optical components and the ultrasound detector are not in contact with the sample gas flow and can therefore stay clean for longer periods. However, the dimensions of the cylinder, the dimensions and the position of the hole, the speed of sound that depends on the temperature and the pressure in the chamber, affect the resonant frequency and can cause major fluctuations on the sensor's sensitivity [323]. The AVL MSS system uses this design and to counter these problems a conditioning unit is necessary to control the temperature and the pressure of the sample, that increases the size and complexity of the product [320]. Another solution that has been proposed is to use multiple mirrors for the light to bounce between and increase the light path and therefore the light absorption. The use of mirrors leads to more frequent need of cleaning and maintaining the optics that are positioned in the chamber and are in contact with the gas flow [324].

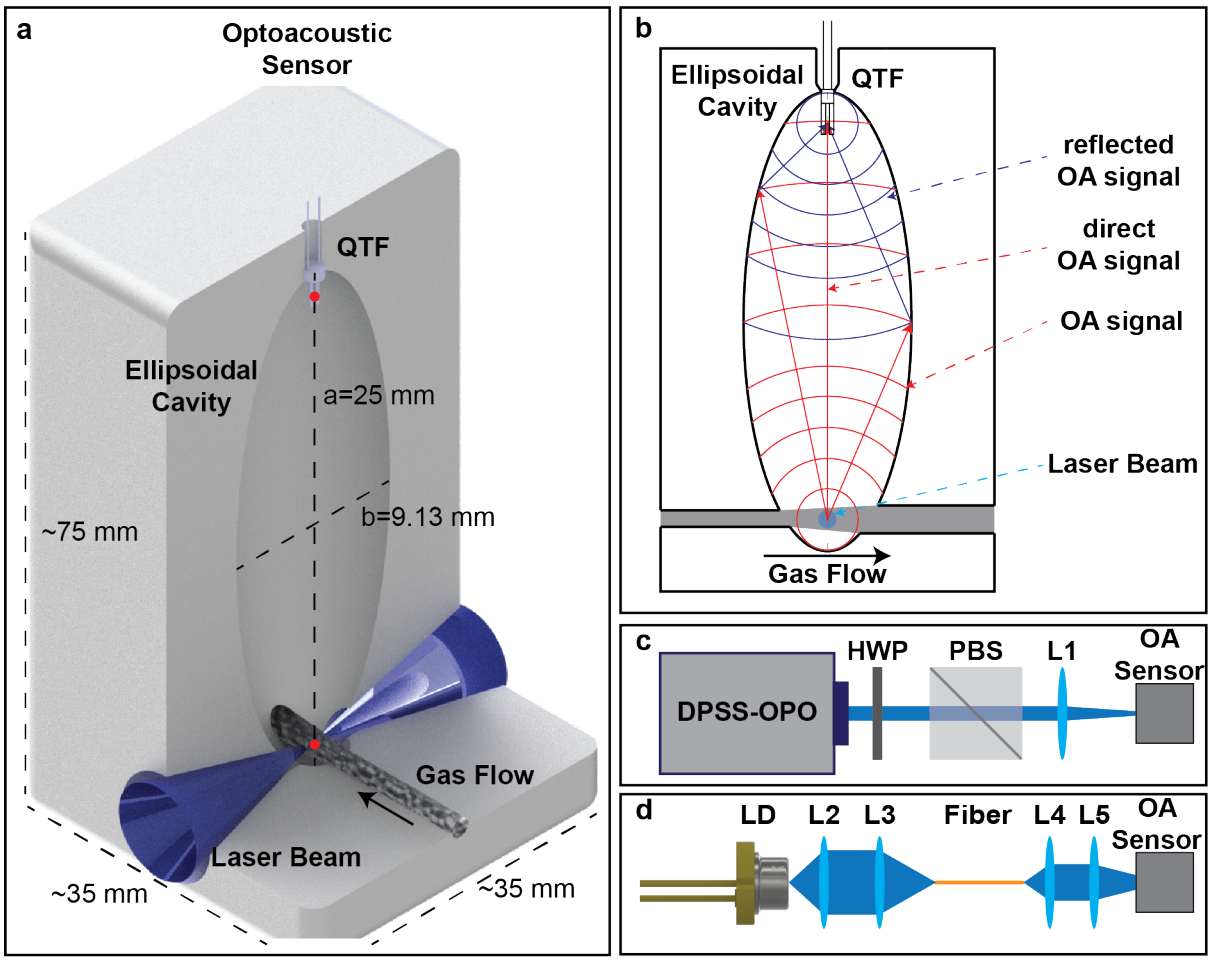

Figure 5.1: The prototype optoacoustic sensor. **(a)** 3D render across the light path cross-section of the OA sensor; QTF, Quartz Tuning Fork. **(b)** 2D cross-section of the OA sensor across the gas flow and the propagation, reflection and interference of the OA waves. **(c)** The laser source used to measure the absorption spectra of the exhaust gas; DPSS-OPO, Diode Pumped Solid State - Optical Parametric Oscillator, HWP, Half-Wave Plate, PBS, Polarizing Beam Splitter, L, Lens. **(d)** The overdriven CW-LD source used to detect the soot; LD, Laser Diode, L1, L2, L3 and L4, Lens 1,2,3 and 4. Adapted version with permission from [289].

The alternative configuration is the on-beam [279, 318, 319, 325–328], that uses a light beam tightly focused between the QTF prongs, that usually have a space of 300 μm between them. The on-beam design brings the sound source as close as possible to the US detector to increase the SNR. Moreover, since it is not using a resonator, the system is not so sensitive to the exact dimensions and speed of sound [327, 328]. There are some systems that use two identical cylindrical resonators, each at either side of the QTF, to achieve resonance, amplify the US of a specific frequency and increase the SNR; but these advantages come with all the drawback of using a resonator that were discussed above. The main drawback of the on-beam designs is that it is very sensitive to the exact positioning of the light beam that needs to be between the QTF prongs to provide a good SNR. Therefore, the whole system is prone to mechanical vibrations. Moreover, the QTF stands in the sample flow rendering the QTF vulnerable to contamination

that can alter its resonant frequency and reduce the sensor's sensitivity as well.

In this chapter we propose a fundamentally different and novel design of the sensor's resonant cavity [329], that provides a high SNR and is expected to not have many of the drawbacks discussed above. Fig.5.1 presents the OA sensor and the experimental setup used. The OA sensor consist of a hollow ellipsoidal cavity (Fig.5.1a) with openings to host the US detector, a QTF, and to enable the gas flow and the laser beam to cross at the same point. Fig.5.1a shows a 3D render of the sensor across the light path cross-section and the dimension of the sensor. The ellipsoid has two focal points, indicated with red dots in Fig.5.1a; the QTF is positioned at the first, the sample gas and the laser beam cross each other at the second. This design takes advantage of the special property of the ellipsoid, according to which every path between the two focal spots, expect the direct one, has exactly the same distance. This allows the US wave, that is generated at the second focal spot, to bounce off of the walls of the ellipsoidal cavity and refocus at the first focal spot, where the QTF is positioned. All of the US waves, that have been reflected at different points of the ellipsoid, interfere constructively, essentially generating a mirror image of the US source at a distant point, as presented in Fig.5.1b. In addition, the size of the ellipsoid has been designed so that, for the QTF's central frequency, the direct US wave will also interfere in phase on the QTF with all the reflected US waves, to further increase the SNR.

This design offers specific advantages; the QTF and the optical components are positioned away from the gas flow and this is expected to protect them from contamination. The gas enters the chamber through a 2 mm diameter tube and exits through a 3 mm diameter tube that is located ∼6 mm away. The particles remain in the sensor's chamber ∼ 1 ms and for 10 nm particles the diffusion coefficient is $5.4{\cdot}10^{-8}\mathrm{m}^2/\mathrm{s}$, that results in particle losses because of diffusion in the chamber of less than 0.2% [330]. The ellipsoidal cavity is not as sensitive to exact dimensions, temperature or pressure fluctuations to amplify a specific frequency; this is not a resonance chamber. As the vast majority of the interfering waves on the QTF are reflected from the ellipsoid walls, they will travel the exact same distance regardless of the speed of sound or the slight changes in the dimensions of the chamber due to temperature. The direct wave will be slightly out of phase when the speed of sound changes, but it is only one of the many interfering waves and it will not interfere destructively if the changes in the speed of sound are small. In addition, the light beam does not need to be focused in between the QTF prongs for maximal SNR, that allows for optimization of the SNR by changing the beam shape and the sensor is expected to be less susceptible to mechanical vibrations.

Two different laser illumination systems were used to characterize the sensor and detect soot with low-cost devices. To measure the OA absorption spectra of the exhaust gas a multiple wavelength excitation system was used. A Diode Pumped Solid State (DPSS) laser equipped with an OPO (Spitlight-DPSS-250 ZHGOPO, InnoLas, Germany) provided 10 ns pulses at a repetition rate of 50 Hz at wavelengths between 420 and 700 nm. To maintain constant energy per pulse, 2 mJ, across all wavelengths a Half-Wave-Plate was installed on a motorized rotational stage (PRM1Z8, Thorlabs, USA), a Polarizing Beam Splitter (PBS) was used before the 75 mm plano-convex focusing lens (L1, LA1608-A, Thorlabs, USA). L1 was focusing the laser light into the sensor that was mounted on a manual three dimensional translation stage (M-460A-XYZ, Newport, USA) for precise positioning of the sensor. This illumination system is demonstrated in Fig.5.1c.

We also used the overdriven CW-LDs as the illumination source to examine if we could achieve a good SNR with a low-cost and miniaturized semiconductor light source. The CW-LD (L462P1400MM, Thorlabs, USA) emitting at 462 nm was pulsed with the updated pulsed laser diode driver presented in Chapter 3, providing ∼140 nJ per pulse and 7 ns pulse width at a

repetition rate matching the QTF's central frequency (∼ 100 kHz). The blue wavelength was chosen for two reasons. First, the most powerful overdriven CW-LDs emit at this wavelength range and second the soot absorption is slightly stronger towards the shorter wavelengths. The CW-LD was focused in a multimode fiber (M92L02, Thorlabs, USA) with a 2 lens system (L1 and L2, C340TMD-A and C560TME-A, Thorlabs, USA). After the multimode fiber a second two lens system (L3 and L4, 15mmD., 0.33NA and 18mm D.x8mm FL, Edmund Optics, USA) was used to focus the light in the sensor, crossing the gas flow. This system is presented in Fig.5.1d.

The OA sensor and the holder for the two lenses (L3 and L4) were all designed and 3D printed using an inverted stereo-lithography 3D printer (Form2, Formlabs, USA).

The OA signal was detected by a 100 kHz QTF (100 kHz, Type TC-26, Conrad, Germany), amplified by a custom-made amplifier utilizing a dual operational amplifier (AD712D, Analog Devices, USA). The signal was digitized by a high speed digitizer (CSE1222, Dynamic Signals, USA) with a sampling rate of 500 kS/s for an acquisition time of 1 second. The recorded signal was processed in Matlab (Matlab 2016b, Mathworks, USA) by performing the Fourier Transform and recording the amplitude of the frequency component at the QTF's central frequency.

5.2.2 Burner Exhaust Gas Characterization

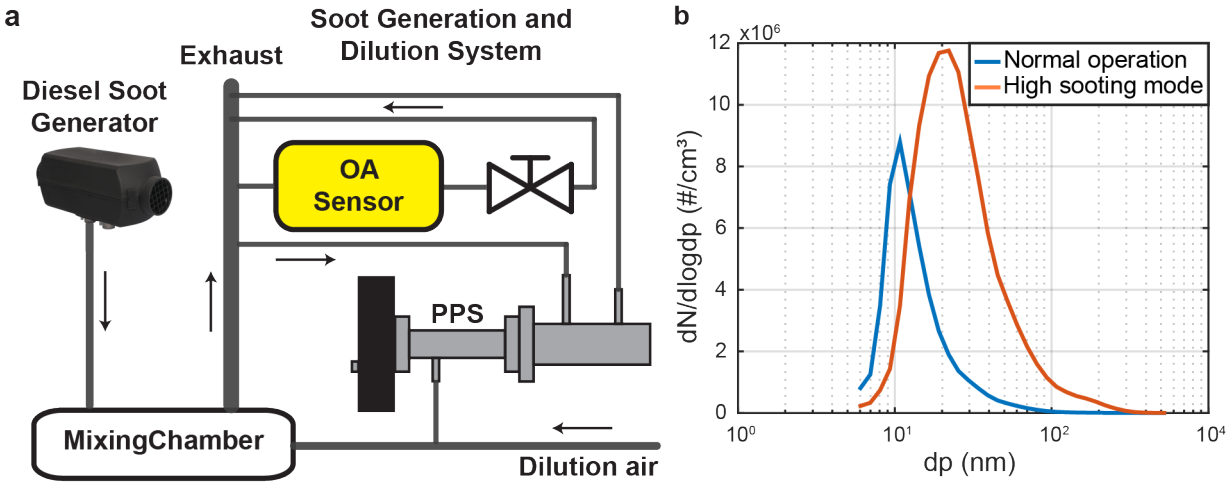

Figure 5.2: Soot generation system and particle size distribution. **(a)** Schematic of the soot generation and dilution system; PPS: Pegasor Particle Sensor. **(b)** The size distribution of the particle number; dp: particle diameter, dN/dlogdp: number fo particles in a specific tange of particle diameters. Adapted version with permission from [289].

A Planar 2D burner that operates on diesel was used to produce soot particles. After the burner, a dilution chamber was used, which was mixing the burner exhaust gas with clean and dry air (with a variable flow rate between 20 and 100 lpm) that achieved a dilution ratio between 1.2 and 2.5. The dilution chamber helped with reducing the temperature and humidity of the exhaust gas while maintaining a high particle mass concentration. Conductive tubes were carrying the gas to the OA Sensor and the reference instrument, the PPS. The PPS was chosen as it offers very fast response to changes in the particle mass concentration. The PPS also required a constant 1.5 bar pressure of clean and dry air as well. After the OA sensor a flow control unit was installed followed by a pump to force a controlled flow (0-5 lpm) of the sample gas through the sensor by creating a negative pressure in the sensor's chamber. The schematic of the soot generation and dilution system is shown in Fig.5.2a.

The burner at maximum power operates with lean combustion at a lambda value of 1.9. It is possible to reduce the lambda to 1.6 that leads to an increase in the particle number and the mean particle size, i.e. a big increase in the BC concentration in the exhaust gas. Such high BC outputs can cause buildup of BC deposits in the burner and damage it. Therefore such low lambda values are only used for a few minutes each time. Operation with a lambda ratio of 1.9 is called Normal Operation and a lambda ratio of 1.6 High Sooting Mode in the following.

In order to characterize the content of the exhaust gas of the burner we used several high-end devices. A HORIBA Portable Emission Measurement System (PEMS) was used to estimate the gaseous content and their concentrations as well as the particle number (PN), an Engine Exhaust Particle Sizer (EEPS) was used to monitor the particle size distribution and an AVL MSS to measure the soot mass concentration.

The results of the exhaust gas characterization in Normal Operation ($\lambda = 1.9$) and High Sooting Mode ($\lambda = 1.6$) are presented in Table 5.1. Some of the most important pollutant gaseous emissions are characterized, including carbon dioxide and monoxide, nitric dioxide and moxide, un-burnt hydrocarbons as well as the particle number and the BC mass. We observe that the NO_2 emissions only slightly increases in High Sooting Mode compared to Normal Operation, from 7.6 to 9 parts per million (ppm). However, we observe a big increase in the particle number as well as the soot mass concentration, from $2.1 \cdot 10^6$ to $1.3 \cdot 10^7$ particle per cubic centimeter and from 0.1 to 1.7 mg/m^3. The particle size distribution is also presented in Fig.5.2b and shows an increase in the particle number and the particle size during High Sooting Mode.

In the following experiment we used two different kinds of filters to remove gaseous and particulates from the exhaust sample. A HEPA filter is used to remove particles with an efficiency of $\sim 99\%$, including soot, but allows gaseous components to pass. An activated carbon filter is in contrary used to remove the gaseous content without capturing the particles. These two filterd can be used in series and are expected to filter out both gases and particulates from the exhaust stream, leaving clean air to be measured.

5.3 Results

5.3.1 Sample Absorption Spectra

To examine the novel chamber's ability to refocus the sound and detect a good signal as well as to measure the sample's OA absorption spectra we used the powerful and wavelength tunable

Table 5.1: Exhaust gas pollutants content in Normal and High Sooting Mode. Adapted version with permission from [289].

Pollutant	Normal Operation $\lambda = 1.9$	High Sooting Mode $\lambda = 1.6$
CO_2 (%)	7.2	9.8
CO (ppm)	84	475
NO_2 (ppm)	7.6	9
NO (ppm)	44	57
HC (ppm C)	0	2.2
PN [CPC] (#/cm^3)	$2.1 \cdot 10^6$	$1.3 \cdot 10^7$
BC [MSS] (mg/m^3)	0.1	1.7

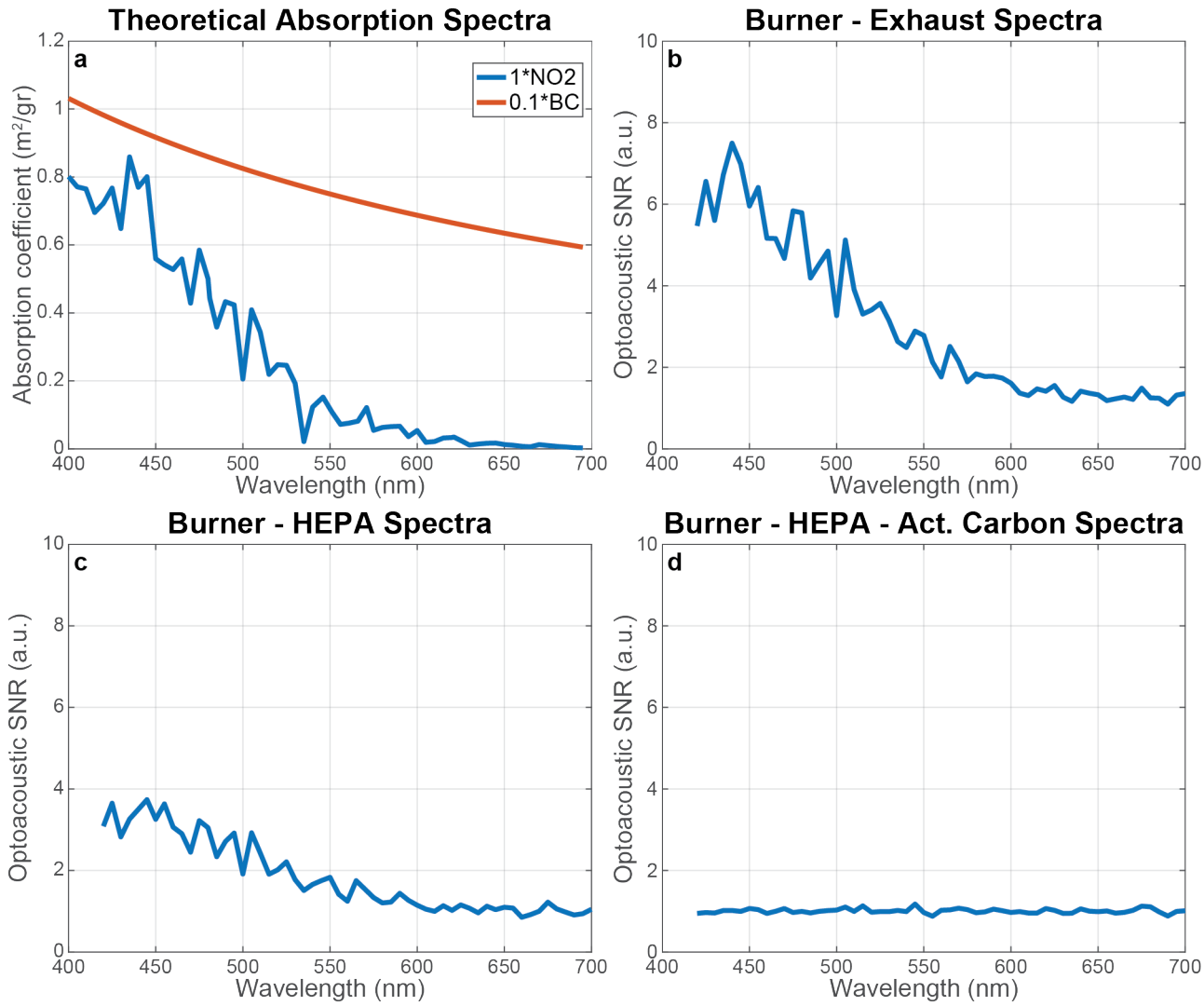

Figure 5.3: Theoretical and detected optical absorption spectra of the exhaust gas across the visible optical range. **(a)** The theoretical absorption spectra of NO_2 (orange line) and soot (blue line). **(b)** Optical absorption spectra of the raw exhaust gas,**(c)** the exhaust gas filtered with HEPA filter to remove soot and **(d)** the exhaust gas filtered with HEPA and an activated carbon filter to remove all gas components and particulates. Adapted version with permission from [289].

DPSS-OPO laser presented in Fig.5.1c. The burner was operating at Normal Operation, $\lambda = 1.9$. The results are shown in Fig.5.3. From the pollutant gases in the sample, that were presented in Table 5.1, only NO_2 absorbs light at the visible range. The theoretical absorption spectra of BC and NO_2 [315, 331] are plotted in Fig.5.3a. We see that BC strongly absorbs light at all wavelengths in this range while the NO_2 absorption is dropping fast and almost reaches zero around 600 nm. Our sensor was able to recover these absorption spectra as presented in Fig.5.3b-d, where the absorption spectra of the raw exhaust gas, filtered with a High Efficiency Particle Absorption (HEPA) filter and with both filters were measured, respectively. It is apparent (Fig.5.3b) that we measured a very similar shape of the absorption spectra when both NO_2 and BC are present. By removing BC from the sample using the HEPA filter the measured OA spectra presented lower signal intensity and a similar shape to the previous two cases (Fig.5.3a and b), confirming that our sensor detects NO_2 as well. Last, when both filters

were used to remove all absorbing components our sensor measured no spectra at all, confirming that there is no parasitic signal in our measurements.

These spectra were measured for a second time after developing and assembling a second OA sensor with a new QTF. Both times the assembly was performed by hand, without using any micro-positioning stages. The results were similar (data not shown here) and they confirmed that, as suspected, our sensor is not sensitive to the exact positioning of the QTF in the ellipsoidal cavity. This can be explained from the fact that sound at such low frequencies, 20-100 kHz, traveling in air (c=330m/s), has a big wavelength, 3-16 mm. Therefore, as long as the QTF is the US focal zone, that is also of the same order of magnitude in size, the detection efficiency is not significantly affected.

These results indicate that the blue CW-LD chosen will be able to generate an OA signal from both NO_2 and BC. A LD emitting at the red ($\sim$ 640 nm) or NIR ($\sim$ 800 nm) would be a better wavelength choice since none of the existing gaseous pollutant components absorb at these wavelengths. However, as we can see in Fig.5.3a the soot absorption also drops with increasing wavelength. In addition, the LDs commercially available at the time of performing the experiments were not as strong as the blue LD. Therefore, we will have to use filters to separate the soot from NO_2 in the following experiments.

5.3.2 Soot Detection Characterization

Next, we investigated whether the overdriven CW-LD emitting at 462 nm can provide enough energy to generate a detectable OA signal from soot, NO_2 or both at the same time. First, we measured the frequency response of our sensor by varying the repetition rate of the excitation laser pulse train with a step of 1 Hz between 99.7 and 100.3 kHz. The experiments were performed twice, once with clean and dry air, to serve as the measurement of the background noise signal, and once with the raw burner exhaust gas. The sensor's SNR was calculated as the signal intensity at the QTF's central frequency over the 1σ of the noise standard deviation. The burner was operated in Normal Operation. The sensor presented a frequency response (Fig.5.4a) of zero outside the QTF sensitivity frequency range that had a central frequency of 99.974 kHz and a quality factor Q=3477. This value is $\sim$ 2-3 times lower than expected for QEPAS systems [318]. This is due to the relatively large bandwidth, Δf $\sim$29 Hz because the proposed sensor is not a resonator. The value of the central frequency is expected to be lower than its nominal value, 100 kHz, as the QTF was operating in air and not in vacuum.

In order to test the performance of the sensor in detecting fast changes in the soot concentration we operated the burner in Normal Operation, followed by one minute in High Sooting Mode and back to Normal Operation and monitored the particle concentration with the PPS and the OA sensor. As mentioned above (Table 5.1) during the burner operation at High Sooting Mode the changes in the BC concentration are significant and fast while the NO_2 concentration only increase slightly and remains stable during that time.

The OA sensor was able to detect the fast changes in soot concentration and the OA signal appeared the same shape as the reference instrument (PPS) when the exhaust gas was filtered with an Activated Carbon filter (removing NO_2) as presented in Fig.5.4b. When the burner exhaust was filtered with a HEPA filter (soot was blocked) then the sensor responded with a non-zero and non-time-varying signal (Fig.5.4c), as expected since the NO_2 is not time-varying during High Sooting Mode operation. When the sensor detected the raw exhaust gas, its response was also following the reference instrument's shape (Fig.5.4d) only now with increased signal intensity compared to Fig.5.4b, since both soot and NO_2 are present. Last, when the exhaust gas was filtered with both filters, the sensor returned, once more, a very low, almost

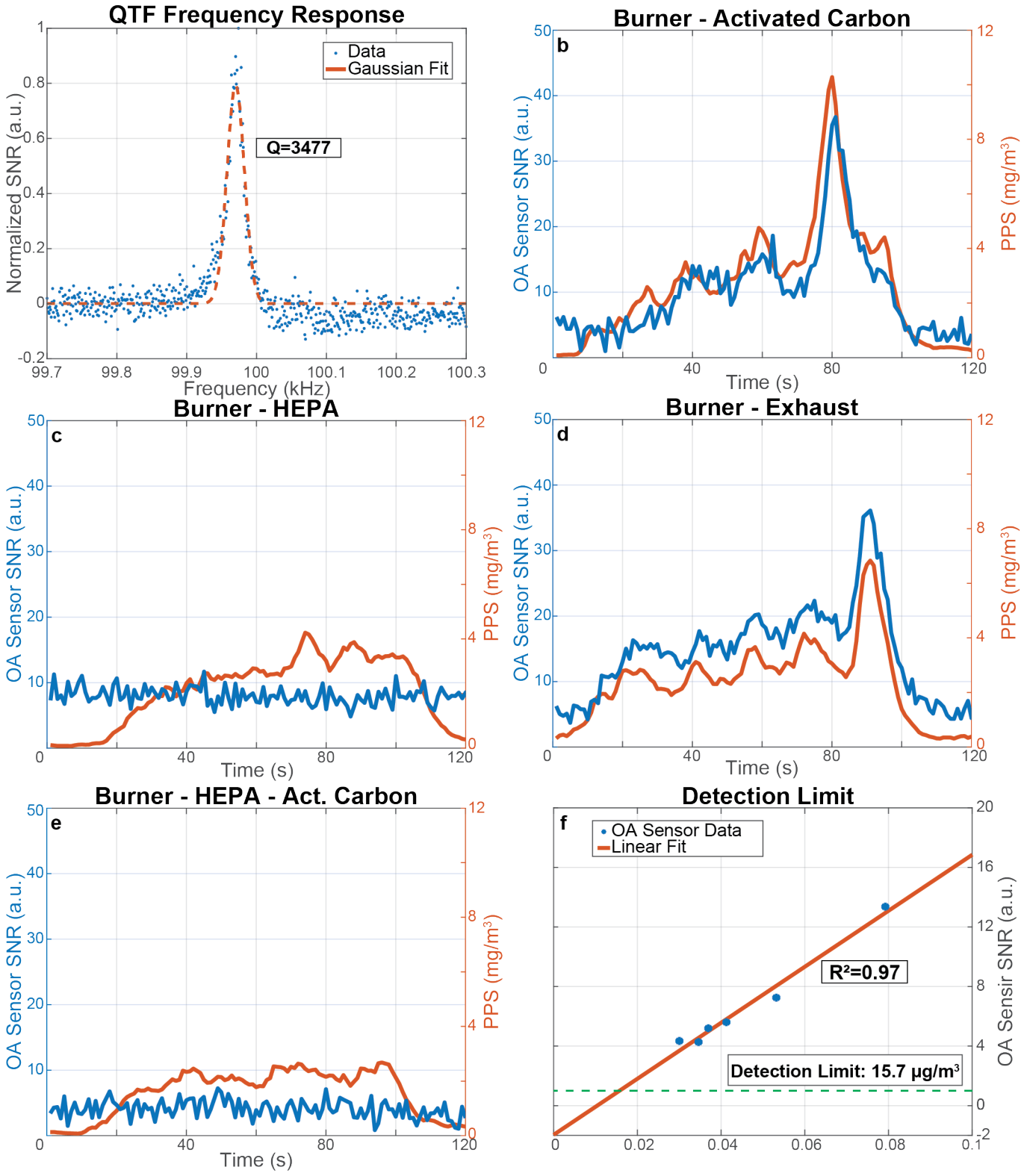

Figure 5.4: OA sensor characterization. **(a)** The frequency response of the QTF results in a Q factor of 3477. **(b)-(e)** OA sensor SNR as a function of time in high sooting mode with different exhaust gas treatment. **(b)** The exhaust gas after an activated carbon filter, **(c)** the exhaust gas after a HEPA filter, **(d)** the raw exhaust gas and **(e)** the exhaust gas after an activated carbon and a HEPA filter is detected. **(f)** the OA sensor SNR under different sample dilution ratios as a function of the PPS signal results in a detection limit of 15.7 μg/m^3. Adapted version with permission from [289].

zero signal since no absorbing gases or particulates were present to absorb the light.

Last, we set to estimate the soot detection limit of our sensor. The sensor as well as the PPS that measures only particulates were monitoring the raw exhaust gas at different dilution levels. The different dilution was achieved by varying the dry and clean air input of the dilution box (Fig.5.1b) between 0 and 100 lpm, achieving, according to the PPS, a BC concentration between 30 and 80 μ g/m^3. As the OA signal contains mixed contribution from soot and NO_2 we used the previous results (Fig.5.3b and c) to calculate that the contribution of soot in the total SNR is $\sim$44%. In addition, according to the exhaust gas characterization, the PPS overestimates the soot concentration compared to the MSS by a factor of 4. Both these parameters have been taken into account. The estimated OA SNR only from soot is plotted against the PPS signal (Fig.5.4f). A good linear correlation ($R^2 = 0.97$) was observed and the linear fit (orange line) yielded a non-zero offset ($\sim$-2 a.u.). This indicates that additional noise from multiple sources reduces the sensor's SNR and increases the detection limit. The Normalized Noise Equivalent Absorption Coefficient (NNEA) [332] has be calculated to be $7.39{\cdot}10^{-9}$ Wcm^{-1}Hz$^{-1/2}$ with a Noise Equivalent Concentration for soot of 15.7 μ g/m^3, that is the estimated detection limit of our sensor at the moment.

5.4 Discussion

Regulation of soot emissions becomes increasingly important due to the adverse effects of soot to air quality, human health and climate change. However, regulation of soot emissions is extremely difficult without devices that can continuously monitor soot emissions from ICEs or as a distributed sensor network in the environment. At the moment there is no commercially available device suitable for on-board detection of soot. In this chapter, we used the overdriven CW-LDs to develop miniaturized and low-cost OA soot sensor with a novel chamber design that offers many advantages to existing laboratory OA sensors.

The novelty of our sensor arises from the ellipsoidal geometry of the acoustic chamber that allows the sound to be generated at the first focal point and be refocused at the second focal point that is located at a distance from the fist. This geometry overcomes the drawbacks of the on-beam and the off-beam chamber designs that have been used up to now. First, the US detector and the optical components are located away from the gas flow path and are less prone to contamination. After using the sensor for many weeks no obvious signal strength or shift in the QTF's central frequency was observed, that would indicate contamination. However, a more precise evaluation of the sensors longevity needs to be performed. Second, the sensor is not sensitive to the exact positioning of the QTF in the ellipsoidal cavity, or mechanical vibrations, as was confirmed by the development of two identical sensors that offered the same performance. Third, as the proposed sensor chamber does not amplify the US at a specific frequency, it is not a resonator, the sensor is expected to be more stable to changes in the temperature or the pressure. This remains to be investigated in the future.

To maintain the small size and the low-cost of the sensor the overdriven CW-LDs and a very sensitive QTF have been used. The sensor offered good sensitivity and fast response to changes in soot concentration. However, the use of the blue wavelength is not ideal for soot detection as NO_2, present in most ICE exhaust stream, also absorbs in this wavelength. We showed that it is possible to filter out any gaseous pollutants with the use of activated carbon filters, that would complicate the system. The use of powerful LD that emit in the red or NIR region would enable the detection of only soot in the exhaust gas without the use of filters. Moreover, the use of multiple wavelengths simultaneously, most likely by using fiber combiners as done in Chapters 3

and 4, will allow detection of multiple particulate and gaseous pollutant simultaneously. Sodium dioxide (SO_2) absorbs light at the UV region, methane (CH_4) at the NIR ($\sim$ 890 nm) and carbon dioxide (CO_2) has an absorption line at the NIR region as well ($\sim$ 1370 nm). LDs that emit at these wavelength are already commercially available. However, different multiplexing techniques will have to be developed in order not to increase the acquisition time when multiple wavelengths are added to the system. The use of Golay code can be such an alternative [247].

Currently the sensor's soot detection limit has been estimated to be $\sim$15.7 μ g/m^3. However, the use of the PPS as the reference instrument and the mixed contribution of NO_2 in the measurement and the limited range of the dilution system increase the uncertainty in the calculation of this limit. However, the soot detection limit that was calculated is expected to be enough for evaluation of proper function of exhaust post-treatment systems, which require a detection limit of 100 μ g/m^3. The NNEA is a figure of merit of the sensor's sensitivity, was calculated to be $7.39{\cdot}10^{-9}$ Wcm^{-1}Hz$^{-1/2}$ and is comparable with other QEPAS sensors that usually have an NNEA in the order of 10^{-8} to 10^{-10} Wcm^{-1}Hz$^{-1/2}$ [332]. The measured value of the NNEA indicates that the proposed sensor is already sensitive enough for a newly developed prototype.

However, for the sensor to be used in atmospheric measurements the desired detection limit is 1 μ g/m^3 or less. Therefore, the sensor sensitivity needs to be improved in the future. The development of a metal sensor is expected to improve the sensor SNR due to better sound reflection on the sensor's walls. Optimization of the laser's excitation pulse width and the laser beam shape can also lead to improvements in the detection limit. The novel sensor chamber design also allows for easy and straightforward implementation of pure optical absorption methods. Correlation of the OA signal and the optical attenuation can improve the sensor's sensitivity. In addition, measuring the intensity of the scattered photons by the soot particles at different angles can give information on the particle size distribution of the soot.

Concluding, the CW-LDs in combination with the novel sensor chamber design can be used to develop a low-cost and miniaturized soot sensor for continuous on-board detection of soot, that today is not possible with existing devices. The proposed sensor offers a promising potential for such a sensor that will help regulate and reduce the BC emission and improve the air quality, human health and achieve fast climate recovery.

Chapter 6

Conclusion and Discussion

Optoacoustic imaging and sensing has many advantages over traditional optical imaging modalities. OA offers optical contrast and handles light scattering by tissue better than optical methods since it detects generated ultrasound waves. Ultrasound waves experience much less scattering as they propagate in the tissue, achieving higher penetration depth and with a spatial resolution that exceeds the optical spatial resolution at the same depth in diffusive media.

However, OA requires a strong light energy transient for efficient OA signal generation; the initial pressure rise is proportional to Φ (eq.1.24), the excitation light fluence on the sample. This means that a CW, non-varying light source does not generate an OA signal at all, and a strong output peak power is required for signal generation in OA imaging and sensing.

Therefore, the light sources used in OA are usually Q-Switched Solid State lasers equipped with an Optical Parametric Oscillator that provide strong, high peak power and short light pulses at multiple wavelengths. However, these lasers are bulky, complex, require frequent maintenance, are expensive and majorly contribute to the overall OA system's cost and size.

In the past decade there has been a lot of interest in developing low-cost and miniaturized light sources for OA imaging [198, 199, 202], focusing on semiconductor light sources, such as laser diodes and LEDs. Semiconductor light sources are much more cost-effective and smaller in size than traditional OA lasers, but they suffer from low output peak power. Up to now the focus has been on investigating whether existing laser diodes can generate an OA signal from various samples.

As discussed in Chapter 2 in more detail, P-LDs have been used for PAT applications due to their high peak power output, relatively long pulse width and output beam characteristics that suit the illumination of a large area. P-LDs have also been used in OR-PAM applications. However, P-LDs found limited success due to their emission in the NIR where hemoglobin, the most important endogenous biological absorber, absorbs light weakly. LEDs have also been considered only for PAT applications due to their long pulse width and broad area illumination, but the output energy of single LED, even when overdriven, is too low for real world applications. A commercial PAT system uses multiple LEDs in a row to achieve a high enough peak power to generate a high SNR OA signal, increasing the cost and complexity of the system. All OA systems that utilize semiconductor light sources require a lot of averaging, up to 5000 pulses [205, 207, 213], to achieve the necessary SNR. However, the laser repetition rate of these light sources has not exceeded $\sim$50 kHz [215, 333], increasing the signal acquisition time significantly.

In this thesis, we investigated how to operate the laser diodes at and above their limits in order to generate higher peak power and energy per pulse than previously achieved. Chapter 2 illustrates, that it is possible to drive the CW-LDs with an up to 45-fold higher peak current

than their nominal values and the CW-LDs can provide up to 27-fold higher peak power than the nominal value, without getting damaged or destroyed. Moreover, it is also possible to drive the CW-LDs with much higher repetition rates than previously achieved, up to 6-fold faster, which allows for faster averaging and increases the SNR at the same acquisition time.

CW-LDs offer certain advantages compared to P-LDs that were the go-to choice for LD OA imaging up to now. CW-LDs are available in many more wavelengths compared to P-LDs that only emit at the NIR, including the visible range, which enables more OA applications and a higher SNR for specific absorbers such as blood. CW-LDs feature smaller emitting areas and are designed to manage and remove heat more efficiently than P-LDs that are designed for low pulse repetition rates. Therefore, it is more efficient to focus the output of CW-LDs in a smaller area and increase the SNR through higher energy density on the sample. Additionally, CW-LDs can be pulsed faster than P-LDs, without overheating and getting damaged, further increasing the SNR. CW-LDs offer 20-fold lower peak power compared to P-LDs [197], but their aforementioned advantages compensate for it, rendering them a more attractive alternative for compact and low-cost OA devices. Overdriven CW-LDs are more suitable for AR-PAM applications due to their characteristics, such as the achieved peak power, emitting wavelength, output beam characteristics and pulse repetition rate.

In this thesis, we have also shown that overdriven CW-LDs can be effectively used in OA applications by developing three OA systems for different applications, a multispectral RSOM, a single point OA oximeter and a low-cost and miniaturized soot sensor for environmental applications. These three developed systems demonstrate that OA imaging and sensing is possible with miniaturized and low-cost sources, even with an output power that is up to $\sim$5 orders of magnitude lower than conventional OA light sources [69].

Developing an OA system with a LD excitation source requires optimization of every component used to achieve the maximum possible SNR. During this thesis, we had to discover multiple solutions to various challenges faced in the development process of each OA system. The various optimization steps and possible solutions to them that require further investigation will also be discussed in this chapter.

6.1 Suitable OA applications for overdriven CW-LDs

Chapter 1 discussed that OA can be implemented in three modalities: tomography, mesoscopy and microscopy. Tomography offers high penetration depth and low spatial resolution, microscopy (also referred as Optical Resolution Photoacoustic Microscopy) achieves very high spatial resolution but only at shallow penetration depths, while mesoscopy (Acoustic Resolution Photoacoustic Microscopy) offers penetration depth and spatial resolution in the range between tomography and microscopy setups. For all modalities, a larger ratio of penetration depth to spatial resolution improves the system's performance [69].

Developing miniaturized and low-cost light sources for OA imaging and sensing requires the right choice of the OA modality. This section outlines which OA modality -tomography, mesoscopy or microscopy- the overdriven CW-LDs are most suitable for.

6.1.1 Optoacoustic Tomography

OA Tomography systems require a lot of energy per pulse ($\gtrsim$ 10 mJ per pulse) to illuminate a large area on the sample and detect the generated US wave with an US array to generate one volumetric image per excitation pulse. PACT systems often use excitation wavelengths at the

NIR range to achieve a high penetration depth and maintain a high penetration-to-resolution ratio.

Therefore, the overdriven CW-LDs are not the optimal choice for a PACT setup. Their energy output is very low ($\gtrsim$ 200 nJ) and would require an array of $\sim$ 5000 CW-LDs to reach the necessary energy per pulse, which would be impractical. Moreover, the CW-LDs offer more advantages compared to P-LDs due to their emission wavelength in the visible range, which is not as attractive for PACT applications.

Pulsed LD, however, offer much higher peak powers, up to 650W, in the NIR range (mainly 905 nm) and are thus more attractive for PACT setups. In addition, the output beam characteristics of P-LDs fit the illumination scheme of PACT systems and P-LDs are easy to implement in such setups. PACT systems that utilize P-LD have already been developed and characterized in phantoms and in-vivo samples [207–209]. However, their energy per pulse is still low compared to conventional OA laser sources, requiring extensive averaging to increase the SNR which reduces the imaging speed [207].

LEDs are also another attractive alternative choice for PACT systems due to their high energy output, beam characteristics and low cost. PACT systems with multiple rows of LEDs are already commercially available [206, 273] but suffer from low penetration depth, $\sim$ 5 mm [206] due to the excitation wavelength in the visible range and the lower energy per pulse compared to conventional OA lasers.

6.1.2 Optoacoustic Microscopy

Optoacoustic Microcopy (OR-PAM) has been extensively investigated with LDs, CW and Pulsed LDs [210–215]. By tightly focusing the laser beam in a small area the energy density (energy per area) increases and thus the SNR increases as well. Therefore, using LDs in OR-PAM was the method of choice for the early LD OR-PAM systems. Moreover, OR-PAM systems can use lower frequency UST that are more sensitive to achieve a good SNR [55], as the spatial resolution is determined by the size of the optical beam spot.

However, OR-PAM is not the optimal OA modality for LDs because there is a trade-off between the SNR and the spatial resolution. The LDs that offer the most energy per pulse and the highest peak power are multi-mode LDs. This means that it is not possible to focus them in a diffraction limited spot without blocking all higher modes [174], except the TEM_{00}, that results in a drastic energy loss, usually $\gtrsim$ 90%.

Moreover, OR-PAM systems require dedicated and sophisticated optical setups in order to focus the light in a diffraction-limited spot which are very sensitive to exact positioning and vibrations. For this reason OR-PAM systems are often used in the laboratory and are not as common in clinics. Therefore, although the use of low-cost and compact light sources in such a system can be advantageous, it will not necessarily lead to wide-spread use of OR-PAM systems in the clinic where they can be used to monitor and diagnose patients.

On the other hand, using LDs in OR-PAM has some advantages as well. LDs offer very high repetition rates which, if combined with the common use of galvanometric beam scanning to form the image, can achieve high frame rates. Taking advantage of this fact, we integrated three CW-LDs in an OR-PAM [334][1], emitting in the blue, green and red wavelengths for the

[1]These results are part of the PhD Thesis of Markus Seeger, citation is pending as the Thesis is still not available online. Antonios Stylogiannis developed the laser diode excitation source. Markus Seeger integrated, focused and aligned the laser diodes into the Optoacoustic Microscope. Antonios Stylogiannis, Markus Seeger and Sarah Glasl performed the mouse experiments. Antonios Stylogiannis and Markus Seeger processed the data. Ludwig Prade and Dr. Vasilis Ntziachristos helped with extensive discussions and guidance in conducting this research.

first time for an LD OR-PAM system. We achieved high spatial resolution of ∼2 μm at all wavelengths and measured relative oxygenation changes in the mouse ear vasculature at a high imaging frame rate and detected single circulating tumor cells in the mouse blood flow *in-vivo*.

It would be interesting, as a next step, to overdrive single mode laser diodes in order to investigate whether they can provide enough energy to be used in OR-PAM systems and provide better performance compared to what multi-mode LDs have achieved so far.

6.1.3 Optoacoustic Mesoscopy

AR-PAM covers the ground between microscopy and tomography [69], commonly using wavelengths in the visible spectrum and offering penetration depths of $\lesssim$ 2 mm in human skin with acoustic spatial resolution of tens of μm's. It therefore seems as the most suitable OA modality for the overdriven CW-LDs developed herein.

In AR-PAM the spatial resolution is provided by the acoustic focusing and thus the laser beam can be only loosely focused on the sample, which is much more efficient taking into account the low quality output beam characteristic of a LD. Overdriving CW-LDs provided new light sources that can be used to excite the tissue. The overdriven CW-LDs offered high peak power ($\lesssim$30 W) at low pulse widths ($\sim$ 7 ns) that, in combination with the high frequency and sensitive UST, achieved spatial resolution of 38 μm at all excitation wavelengths.

We were the first to develop an AR-PAM system that excites the tissue with 4 wavelengths at the same time. That was due to the innovative Frequency Wavelength Multiplexing algorithm developed in our institute [200, 226] which offers a high SNR from multiple wavelengths without increasing the acquisition time. The multi-wavelength LD RSOM showed excellent performance and acquired high resolution images of a mouse ear at four wavelengths. Using the overdriven CW-LD we revealed relative oxygenation levels in the blood micro-vasculature and detected two external contrast agent in the lymphatic vessels of the mouse ear in a single image. Moreover, taking advantage of the high repetition rate of the laser diodes as well as the innovative Frequency Wavelength Multiplexing algorithm, we performed vessels dynamics by monitoring changes of the relative blood oxygenation of the main artery and the main vein of the mouse ear during an oxygen stress test and the diffusion of exogenous contrast agent.

Nevertheless, the penetration depth achieved by measuring human skin was low, only 600 μm, compared to other RSOM system that use high-end lasers. The limiting factor is the use of the blue wavelengths to excite the tissue, which are heavily scattered by the tissue and heavily absorbed by the biological components in upper skin layers. More powerful LDs that emit in the green region might become available in the ear future and will help pushing the imaging depth in human skin.

6.1.4 Biological Single Point Sensing

Single point measurements can still provide valuable information about the human tissue in a smaller and more compact package. Therefore, in order to capitalize on the small size and low-cost of the CW-LDs in an AR-PAM system, we further simplified the OA system by developing a single point OA sensor that utilizes two wavelengths in the blue that is able to precisely measure the local tissue vascular oxygenation- the first example of a dedicated and simple OA oximeter.

Overdriven CW-LDs are a perfect match for such applications as it is still a simpler and smaller AR-PAM-like system. The output energy, emitting wavelength and repetition rate fit the corresponding application as a large penetration depth is not necessary here, nor the very

high signal acquisition rate, which allows for more averaging to further increase the SNR. We calibrated the OA sensor using blood phantoms and validated its ability to accurately measure the blood oxygen saturation in tissues in-vivo. The single point sensor presented in this Thesis addresses the need to measure the local vascular tissue oxygenation with a compact and low-cost device. Using single point sensing in applications where spatial information is not necessary proves advantageous. Moreover, further investigations of single point sensing can reveal that even more biological informations can be retrieved from the tissue in addition to local vascular tissue oxygenation.

There is no other single point OA oximeter available today. Currently, in the clinics it is possible to measure arterial blood oxygenation that does not correlate with the local vascular tissue oxygenation. NIRS sensors are used for this purpose but they do not handle scattering effectively and usually sample a large volume that contains mixed contributions from multiple absorbers. Alternatively, tissue or arterial oxygenation can be measured by various invasive methods which are not practical or comfortable for the patient.

An OA oximeter can fill this gap and easily and accurately measure local vascular oxygenation, which more closely relates with tissue oxygenation, and help clinicians with diagnosis and decision making in critical situations and various disease monitoring in patients. However, further miniaturization of the sensor and proper calibration of such a system for use in humans is required.

6.1.5 Environmental Sensing

We developed a second single point OA sensor, this time for detection of soot and gaseous pollutants for environmental applications. This sensor utilized the low-cost overdriven CW-LDs as the light source which offer high peak power and a miniaturized QTF as the sound detector, which is very cheap and sensitive. The novel design of the sensor's acoustic chamber allows for sound refocusing away from the US generation point and gas flow, thus protecting the QTF and the optical components from contamination. Furthermore, the novel design makes the sensor less sensitive to the exact positioning of the QTF and to vibrations, rendering the sensor suitable for on-board measurements or in a distributed network for soot monitoring.

The overdriven CW-LD are shown to be a valuable tool for the development of low-cost and compact sensors and the measurement of soot even at low concentrations. The first developed laboratory prototype achieved a detection limit of 15.7 $\mu g/m^3$ that is already good enough for the on-board detection of proper function of exhaust post-treatment systems in vehicles. Future versions of the developed prototype can achieve higher sensitivity and soot detection limit making the sensor suitable even for environmental measurements. Future developments can also enable the sensor to detect multiple pollutants, such as particulates and gaseous pollutants, simultaneously. Currently there is no sensor that can offer such versatility in a low-cost and compact package. Such as sensor can help in monitoring and regulation of soot emissions that can result in improvements in the air quality, human health and fast climate recovery.

6.2 Optimization of an OA system utilizing LDs

The overdriven CW-LDs have shown their potential in generating a strong SNR from biological and environmental applications and can play a central role in the miniaturization and cost reduction of OA systems in the near future. Nevertheless, the low output peak power of the LDs makes it more challenging for developing an OA system compared to using conventional strong laser sources. When using LDs every design choice needs to be optimized in order to maximize

the SNR, from the LD wavelength choice, the pulsed laser diode driver design, the optical path for light delivery to the sample, the multiplexing scheme, the detection and digitization electronics and the signal processing techniques and algorithms. Any sub-optimal choice in the design of the system will reduce the already low SNR, resulting in an OA system that cannot be used for real-world applications. Therefore, it is critical that all design elements are well optimized to develop an OA system that utilizes these low-cost and compact light sources.

This section, discusses many of the optimization steps that have been achieved in this thesis in order to develop the three OA systems for different OA applications, and the possible next steps that can further improve these systems in the near future.

6.2.1 Wavelength Selection

The emission wavelength of semiconductor light sources depends on the p-n junction materials and its band-gap energy separation. Market introduction of semiconductor light sources that emit new wavelengths requires extensive research and development in semiconductor and solid state physics, as well as new material growth an processing techniques. The introduction of stronger laser diodes in existing wavelengths to the market, e.g. laser diodes emitting at 510 nm, still requires more research in these fields, since LDs emitting at certain wavelengths only appeared a few years ago and knowledge is still limited on how to increase their output power. However, laser diode technology is progressing fast and new developments is this field will result in new emitting wavelengths and in stronger LD in existing wavelengths [193].

Semiconductor light sources, LEDs, PLDs and CW-LDs are available in a wide range of wavelengths, covering the entire range between the UV to the NIR. However, only certain wavelengths are available with limited wavelength tuning ability. Some of the most common emitting wavelengths for LDs are 375, 405, 445, 465, 480, 510, 635, 780, 808, 830, 905, 940, 1064, 1310, 1550 and other wavelengths up to 3330 nm [193]. Many of these wavelengths are of interest for applications in biology or the environment.

Some of the most important absorbers for biological applications and the relevant wavelength absorption range are blood (from UV up to $\sim$ 600 nm), melanin (200 to $\sim$900 nm), fat (absorption peak at 760, 930, 1040 nm), connective tissue and collagen (strong absorption at UV), Green Fluorescent Protein (peak at 480 nm), ICG (peak absorption at $\sim$ 800 nm), Evan's Blue ($\sim$ 600 nm) and many proteins (Near and Middle IR). For environmental applications, SO_2 absorbs wavelengths below $\sim$ 300 nm, NO_2 below $\sim$ 500 nm, soot across UV and visible range, methane $\sim$ 890 nm and CO_2 has its first absorption peak at $\sim$ 1370 nm.

However, the existing LD emitting wavelengths do not always match the peak absorption of specific targets that would help to achieve a maximum SNR and better selectivity. For example, the existing wavelengths for fat detection are always close, $\pm$ 25 nm, but not exactly at the peak absorption. Another challenge that LD OA faces is that, although certain wavelengths are available, the LDs are not strong enough yet to generate the necessary SNR. Stronger LDs at $\sim$510 nm would be better suited for LD RSOM applications for skin imaging [282]. Melanin still absorbs strongly, but less compared to the blue; blood presents a local peak at these wavelengths that would also result in a good SNR. Green light is also less scattered in tissue compared to blue light which would result in better penetration depth in skin. LDs that emit in 2 different wavelengths in the green region would help OA imaging of skin to further advance and achieve same imaging quality with low-cost light sources.

It becomes evident that a more fine-tuned selection of wavelengths would benefit OA LD systems as it would improve the SNR for specific biological and environmental targets. Moreover, there are some considerable gaps in the emitting wavelengths, namely at $\sim$ 420 and 550-610

nm, that further challenge the wavelength choice for LD OA systems. Using an OPO with LDs to make certain wavelengths available is not possible due to the drastic energy loss in the wavelength conversion with an OPO and the complexity an OPO would add to a simple LD light source.

Another important point that to mention is that current P-LDs are only available in the NIR region, due to the market demand of such LDs for LIDAR applications. P-LDs that emit in the visible range do not exist yet, since there was no market for them, up to now. However, we hope that the work done during this thesis will push the development of such LDs that could in turn help the fast development of low-cost OA systems using semiconductor light sources.

6.2.2 Improved pulsed laser diode driver

In order to generate a short and strong current pulse to driver the CW-LDs we developed a custom made pulse laser diode driver, described in Chapter 2, that was an updated and adopted version of a commercially available driver for radar or lidar applications [217]. The custom made driver consists of components such as, resistors, capacitors and transistors, of which the limits in terms of voltage and power consumption are well known. This allowed us to achieve higher peak current than the already available drivers and most importantly to achieve much higher pulse repetition rates than before.

The maximum peak power a LD can provide before getting destroyed is inversely proportional to the square root of the pulse width [221–223]. The fact that all the overdriven CW-LDs used in this thesis have been safely driven with the existing driver for about 5 years, while conducting this thesis, suggests that the limits of the CW-LDs have not yet been reached. We could still increase the peak current, with the existing pulse width, and gain more output peak power without destroying the LDs. At the moment we do not know the limits of each LD, as this way of driving them is out of the scope of their intended use and this information is thus not provided in their datasheet.

In order to find the limits of each LD it would require a better pulsed laser diode driver and to drive one LD of each kind at and above its limits and destroying it. However, the current limit is that the pulsed laser diode driver cannot provide shorter pulses nor a higher peak current. The main reason for this is the circuit's and the LD's inductance that impedes the fast rise of the current through the LD, as the voltage across any inductor is given by $V_L = -LdI/dt$, where L is the self-inductance. At such high and fast current changes, $dI \simeq 60$ A at $dt \simeq 3$ ns, even the smallest inductance plays a major role, drastically impeding the peak current and the pulse width.

Possible next steps in improving the laser diode excitation system include:

- Removal of the current limiting resistor, R_{CL} in Fig.2.1a, to increase the peak current.
- Improved PCB design for reduced inductance at the LD current path.
- Impedance matching between the pulsed laser diode driver output and the specific CW-LD used.
- Use of a current source instead of a voltage source to charge the capacitor bank, which will enable removing the charging resistors, R_C, and reducing the heat generation and management of the driver.
- Attaching the CW-LD p-n junction directly on the pulsed laser diode PCB will drastically help reducing the circuits inductance, as the CW-LD in its TO-Can package (~ 7 nH) contributes the most significant part of the overall inductance of the circuit [335].

However, it is important to mention that the minimum optical pulse width depends on the current pulse width and the round trip time of the laser field in the active region and the laser

resonator. Therefore, a minimum of $\sim$ 3-5 ns optical pulse width, depending on the specific CW-LD under use, is expected. This would be a major improvement compared to the 7 ns pulse width achieved so far. Taking for example the maximum peak power achieved so far, 28.2 W at 6.7 ns for the LDM-445-6000 in Chapter3, the inverse square root law suggests that by reducing the pulse width to 4 ns a maximum peak power of 36.5 W could be achieved, which is a 29% increase in peak power. This increase could be even bigger since the 28.2 W peak power is not the maximum that the CW-LD can provide, but rather the limit of the pulsed laser diode driver.

6.2.3 High quality and miniaturized optics and fiber combiners

LDs need to soldered very close to, or even on, the pulsed laser diode driver circuit to optimize its performance. Due to the dimensions of the driver and those of the off-the-shelf optics the resulting illumination system becomes bulky in order to use it to illuminate the sample directly. Taking into account that the UST also needs to be very close to the sample and co-aligned with the illumination spot and water, or with an ultrasound gel, coupling to detect the sound, this task becomes even harder. The difficulty increases even further if multi-wavelengths illumination is required.

To solve the above mentioned challenge we opted for focusing the light into multi-mode fibers and delivering the light on the sample that is at a distance away from the pulse laser diode driver. This also allowed miniaturization of the scanning head and ease of use of the whole system.

Using four different fibers for illuminating the sample with four different wavelengths would create the problem of not illuminating the sample in the same way for each wavelength, and introducing additional parameters in the OA signal generation for each laser that would have to be later corrected to get the equivalent OA signal for each laser. The use of custom made multi-mode fiber combiners, which achieved a very high coupling efficiency ($\gtrsim 90\%$), allowed us to efficiently couple all wavelengths into the same optical path and illuminate the same area on the sample with all the wavelengths.

Coupling the output of the CW-LDs into multi-mode fibers appeared to be a new challenge. Coupling efficiency was the top priority, since there is simply not enough power generated by the LDs to waste. Second, coupling the light into a small core and low NA fiber was preferable because it is easier to focus the light after the fiber into a smaller spot and increase the energy density and the SNR, compared to coupling the light into a large core and high NA fiber. Therefore, we had to investigate the trade-off between the coupling efficiency into the fiber and the focusing of the light on the sample after the fiber.

The most common, simple and cost-effective way was to use a two lens setup between the LD and the fiber. The first lens, L1, needs to have a high NA to effectively collect and collimate the laser beam. The NA of a lens is given by

$$NA \approx n\frac{D}{2f}, \tag{6.1}$$

where n is the refractive index of the medium, air in our case, D the clear aperture of the lens and f its focal distance. The magnification ratio of the lens pair is given by f_2/f_1. This means that the second lens, L2 the focusing lens, requires a small NA to focus the light into a low NA fiber and a small focal distance to focus the light into a small core fiber. This is very hard to achieve since the lens' NA is inversely proportional to its focal distance, eq.(6.1). We found only one lens pair with the correct value combinations ($f_1 = 4.03$ mm, NA_1=0.64 and $f_2 = 13.86$

mm, NA_2=0.18) to efficiently ($\gtrsim$ 90 %) couple the LD output into a relatively small core fiber (200 μm core diameter and 0.22 NA).

Despite all the progress made here, the system with off-the shelf components (optics and optomechanical components, lens holders and stages) still retains a relatively big form factor. A possible solution to this is the development of dedicated miniaturized optics for each CW-LD that can more efficiently focus the light into fibers, possibly with a smaller core diameter and NA as well. In this way, not only a higher energy output can be achieved but also further miniaturization of the illumination source.

In this thesis, we have demonstrated the concept that overdriven CW-LDs can be coupled into small core fibers and be used as OA light sources for various applications.

6.2.4 Optimal sample illumination

Proper distribution of the available light energy on the sample appears to be important in maximizing the SNR and the spatial resolution in AR-PAM applications.

Chapter 2 describes a single wavelength LD RSOM that used a lens pair on a tip-tilt mount to illuminate the sample under a big angle compared to the UST axis. The UST was positioned in the water for optimal US coupling, while the lenses were out of the water, as these lenses were designed for operation in air. This choice raised questions regarding sensitivity and practicality of the system.

The fact that the lens pair was out of the water meant that we had to re-align the optical illumination spot with the acoustic focal spot for every measurement. In addition, if the water surface level was changed due to evaporation for example, the SNR would be reduced and re-alignment was necessary.

Moreover, due to the steep illumination angle sample illumination was not homogeneous deeper in the tissue, despite light diffusion. This resulted in a lower SNR and spatial resolution after image reconstruction. This is because the back-projection algorithm was developed for the RSOM system that was using a high-end laser and a fiber bundle to illuminate the sample, achieving homogeneous and strong light field at all depth.

This challenge was solved for the LD system by using a custom-made 4x4 fiber combiner that could efficiently combine and split the light field of 4 LDs. Each output fiber contained $\sim$ 25% of the energy of each input fiber. By positioning them into the US coupling medium, water, without any lenses, in a circular pattern and very close to the UST and the sample surface, we achieved more homogeneous light distribution, even at higher depths. This drastically helped in increasing the SNR and the penetration depth as well as the spatial resolution after image reconstruction, since the reconstructions code assumption were now met.

6.2.5 Multiplexing techniques

Multi-wavelength illumination in OA can be used to detect and separate the signal from multiple absorbers. In multi-wavelength illumination it is desirable to illuminate the sample with all the wavelengths at the same time in order to save time compared to sequential illumination. However, it is not practical, or even impossible, with high-end lasers due to their size and cost. A DPSS-OPO laser can generate many wavelengths but only in a sequential matter.

Simultaneous excitation with multiple wavelengths requires multiple discrete light sources emitting at different wavelengths. The development of low-cost and compact light sources for OA imaging and sensing, such as the overdriven CW-LDs, enables the illumination and excitation with many wavelengths at the same time. However, proper signal multiplexing techniques need

to be developed and used in order to be able to recover the signal from each light sources after signal acquisition.

Frequency Domain Optoacoustics (FD-OA) excites the sample with a laser modulated at a single frequency and detects the OA signal at the same frequency [238, 243]. This allows for very easy wavelength multiplexing by frequency sharing, i.e. each laser is assigned to a different modulation frequency. However, FD-OA offers no axial resolution, due to the use of a sinusoidal wave excitation, and inherently low SNR, due to the low energy transient of a sine wave.

Multiplexing in Time Domain Optoacoustics [127], requires sequential illumination of the sample with all the wavelengths. This comes at the cost of reduced depth of view for each wavelength, lower SNR or increased acquisition time.

Signal multiplexing with mutual orthogonal uni-polar Golay Codes has already been proposed and demonstrated for 2 wavelength illumination [247]. However, adding more than two wavelengths causes the appearance of non-zero cross-correlation artefacts, limiting the potential of this multiplexing technique.

We developed a novel multiplexing scheme and algorithm to recover the OA from each excitation wavelength, termed Frequency Wavelength Multiplexed Optoacoustics (FWMOA) [200, 226]. FWMOA uses a pulse train at a different pulse repetition rate for each wavelength and recovers the signal by processing it in the Fourier Domain. FWMOA identifies the correct set of harmonics (that resembles an optical frequency comb) for each laser depending on its repetition rate and performs an inverse Fourier Transform at only those frequencies to recover the OA signal of each wavelength as a function of time. Thus, FWMOA achieved similar performance to TD-OA at single wavelength illumination. However, when multiple wavelengths are used, FWMOA showed improved performance and provided the same SNR for each wavelength compared to the single wavelength case, without sacrificing the depth of view or the acquisition time.

6.2.6 Noise reduction methods

Thermal, white gaussian, noise is always present in analog electronics and many techniques have been developed to reduce it. Noise reduction is even more important in LD OA imaging and sensing due to the inherently low SNR offered by the LDs.

Using low noise co-axial cables, impedance matching of all connections, proper shielding and grounding can drastically help in transmitting the OA signal. The use of low-noise amplifiers and digitization electronics is critical in order to achieve a high SNR. In the course of this thesis, we tried to use a lower-end, cost and size, portable USB oscilloscope [336], to further reduce the size of the system, but the SNR was severely reduced. Therefore, we used a high-end DAQ system that offers digitization with high vertical resolution (14-bit) and low input noise to record the high quality images presented herein. Future developments should also focus on miniaturizing the cost and size of the amplification and acquisition electronics without sacrificing the SNR.

Moreover, the pulsed laser diode driver used in this thesis was generating a lot of electromagnetic interference, due to the very high dI/dt it offers, which affects the OA signal and possibly other electronic devices in the lab. Therefore, effort should be put on reducing or removing the interference or shielding properly, before an overdriven CW-LD system can make its way into the clinics. We have already seen that this interference is detected and recorded along with the OA signal. However, it is possible to remove it during signal post-processing, by applying a time-gate filter, since the laser trigger interference appears when the laser diode driver is triggered and the OA signal a few microseconds later, as it needs time to travel from the source

to the UST. In addition, analog or even digital band-pass filtering of the OA signal helps in reducing the noise power at frequencies where the OA is not present.

6.3 Conclusion

Only in the last few years have Optoacoustic imaging and sensing systems started exiting the research laboratories and becoming available in the market. However, their potential for widespread use in the clinics or for other real-world applications is held back by the requirement for strong energy transients and the need for expensive, bulky and complicated lasers.

In this thesis, we investigated whether the development of low-cost and compact optoacoustic excitation sources by using Continuous Wave Laser Diodes to generate an Optoacoustic signal. Driving CW-LDs with much higher current, >40-fold higher than the CW absolute maximum value for a very short time of ∼5 ns, can provide up to ∼ 27 fold higher peak power than the absolute maximum CW value without getting damaged. Therefore, overdriven CW-LDs offer an excellent and attractive alternative for OA mesoscopy.

Furthermore, we also demonstrated that it is possible to develop multiple systems that utilize the overdriven CW-LDs for various applications. We developed a four wavelengths low cost RSOM system that generated high quality images from a mouse ear and human skin. We also developed two single point sensors, one for biological applications such as non-invasive measurements of local vascular oxygen saturation and one for environmental applications of soot monitoring.

Overdriven CW-LDs can play a central role in the near future for the development of compact and low-cost OA systems for biological and environmental applications. We hope that the work done in this thesis can help OA, a still expanding research field, in making its way into the market and mark the beginning of a new era in OA light sources.

Chapter 7

Appendix

In this section I included a small collection of photos that I took over the course of the last five years working on this thesis. I am presenting them here, with only a small explanation, to show, in a more graphical and vivid way, the progress of all the projects that I was involved in during these years and the different stages the developed systems went through. I hope that in this way the reader will get a more complete picture of the different development phases and the struggles that I faced that were otherwise hard to present in the thesis main text.

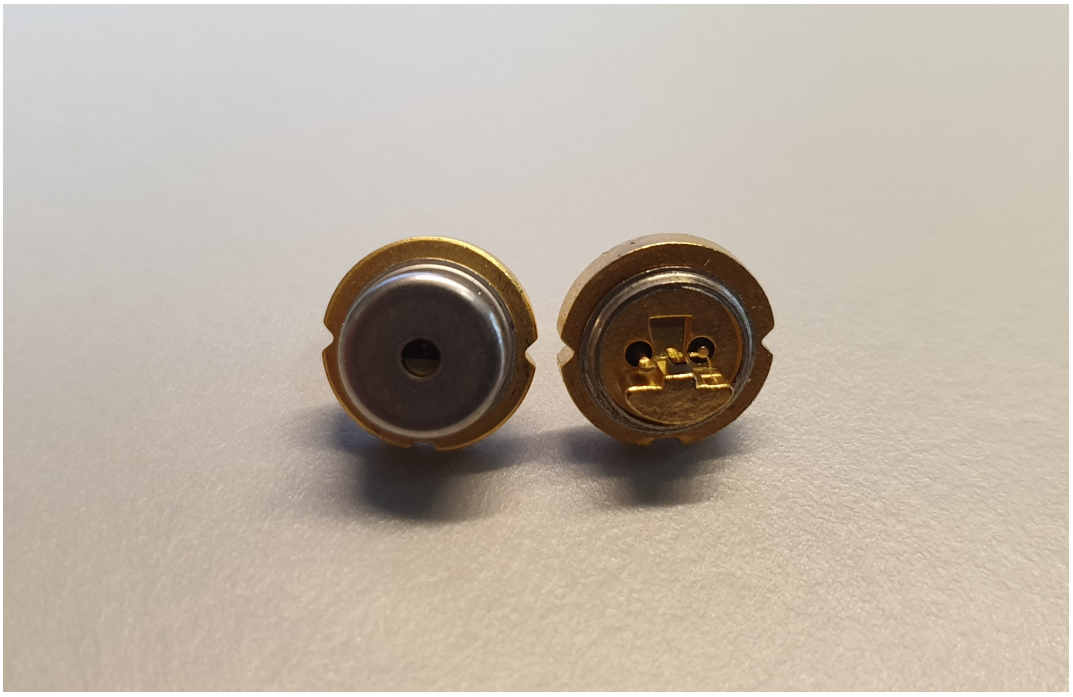

Figure 7.1: Two Continuous Wave Laser Diodes in TO-Can packages, one of which has its cap removed.

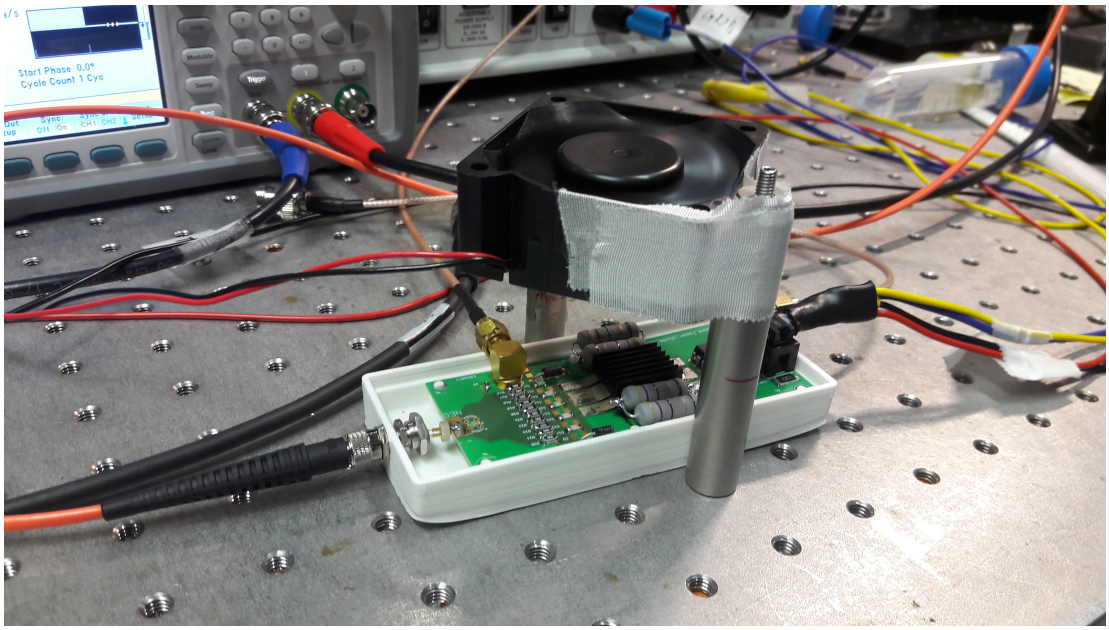

Figure 7.2: The first version of the pulsed laser diode driver that was developed, in use while characterizing the CW-LDs for the measurements in Chapter 1.

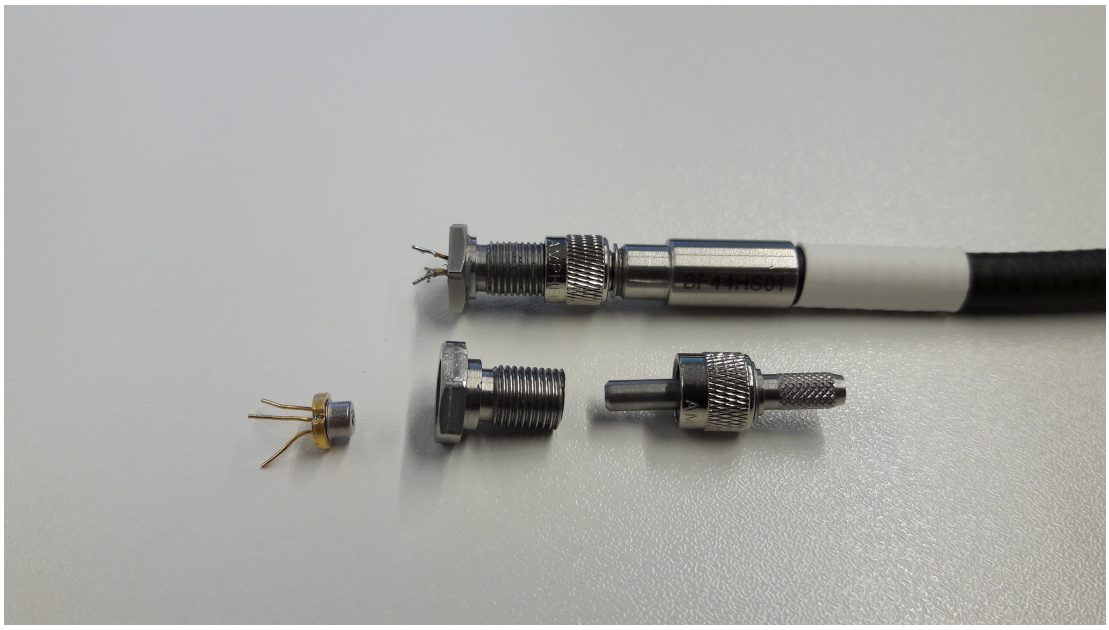

Figure 7.3: The way we first coupled the CW-LDs into a large core multi-mode fiber for the measurements in Chapter 1.

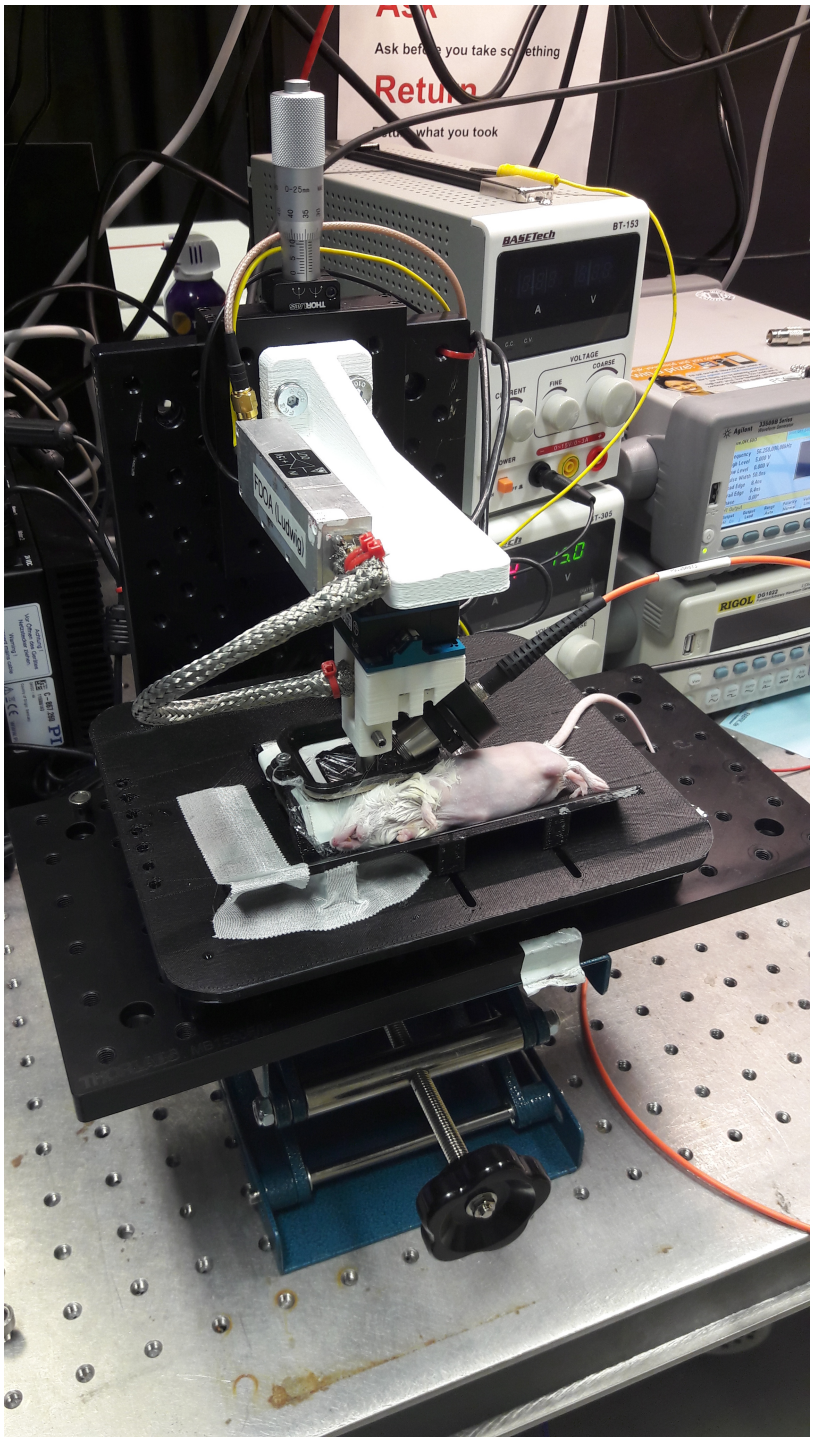

Figure 7.4: The single wavelength LD RSOM, with the focusing lens pair out of the water while measuring a mouse ear.

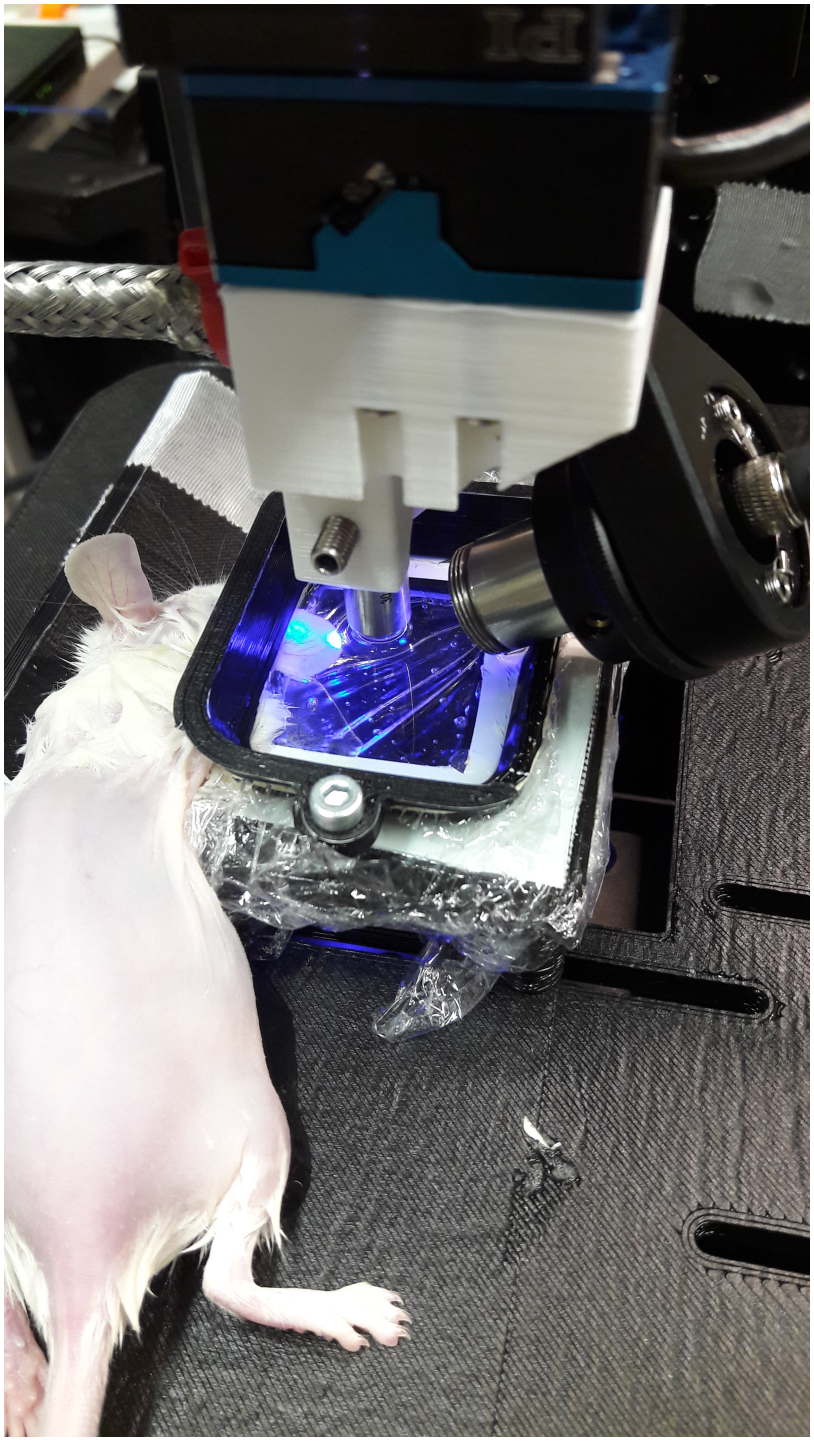

Figure 7.5: A close up look of the same system as before.

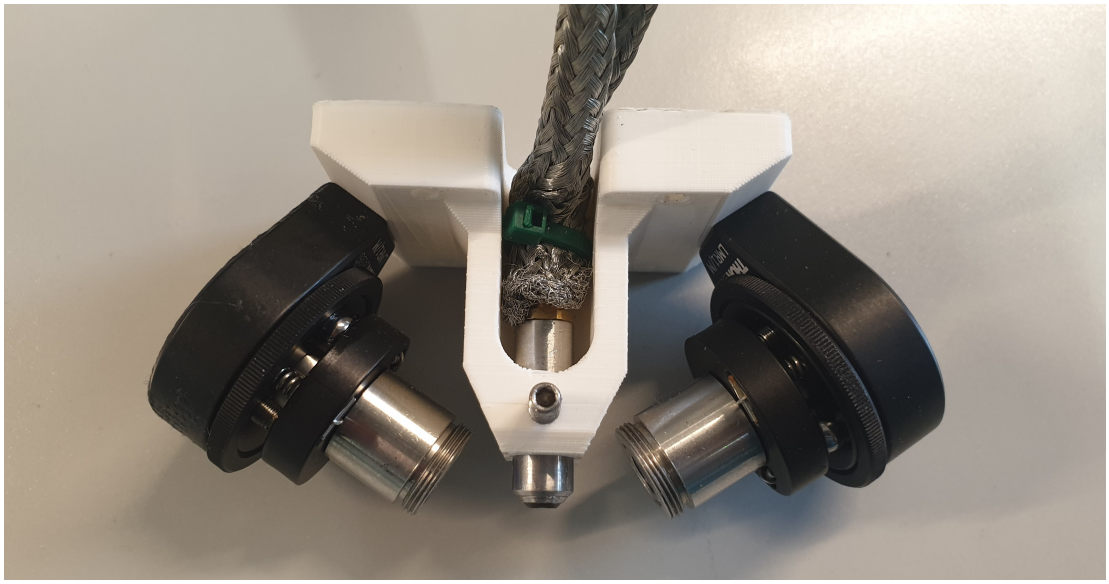

Figure 7.6: A intermediate version of the the multi-wavelength RSOM. It has two wavelength, both illuminating the sample with a separate lens pair that is out of the water.

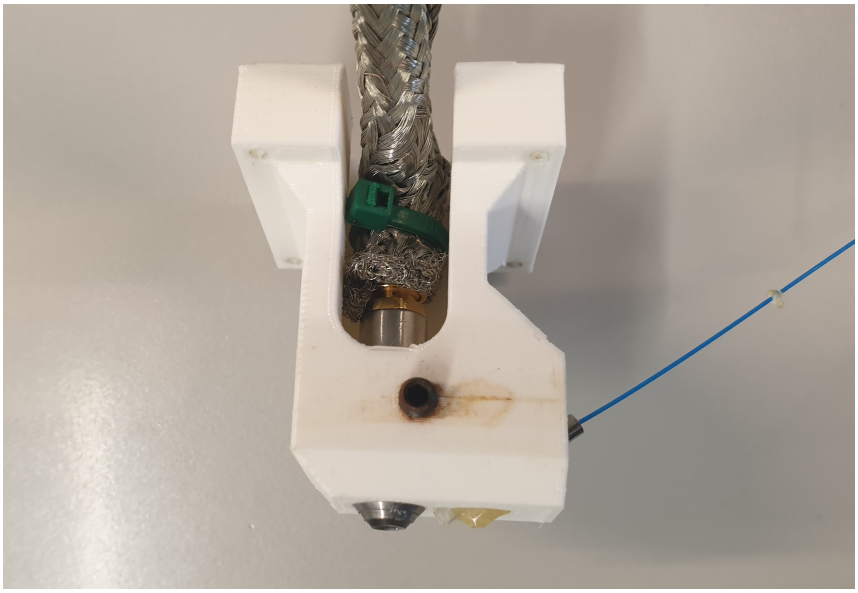

Figure 7.7: Another intermediate version of the the LD RSOM. Trying to use something else rather than the lens pair that was out of the water, we tried to use a Graded Index (GRIN) lens to focus the light of the single fiber. The GRIN lens is now positioned in the water and it alignment is much easier. Illumination is still, though, from one side with a steep angle.

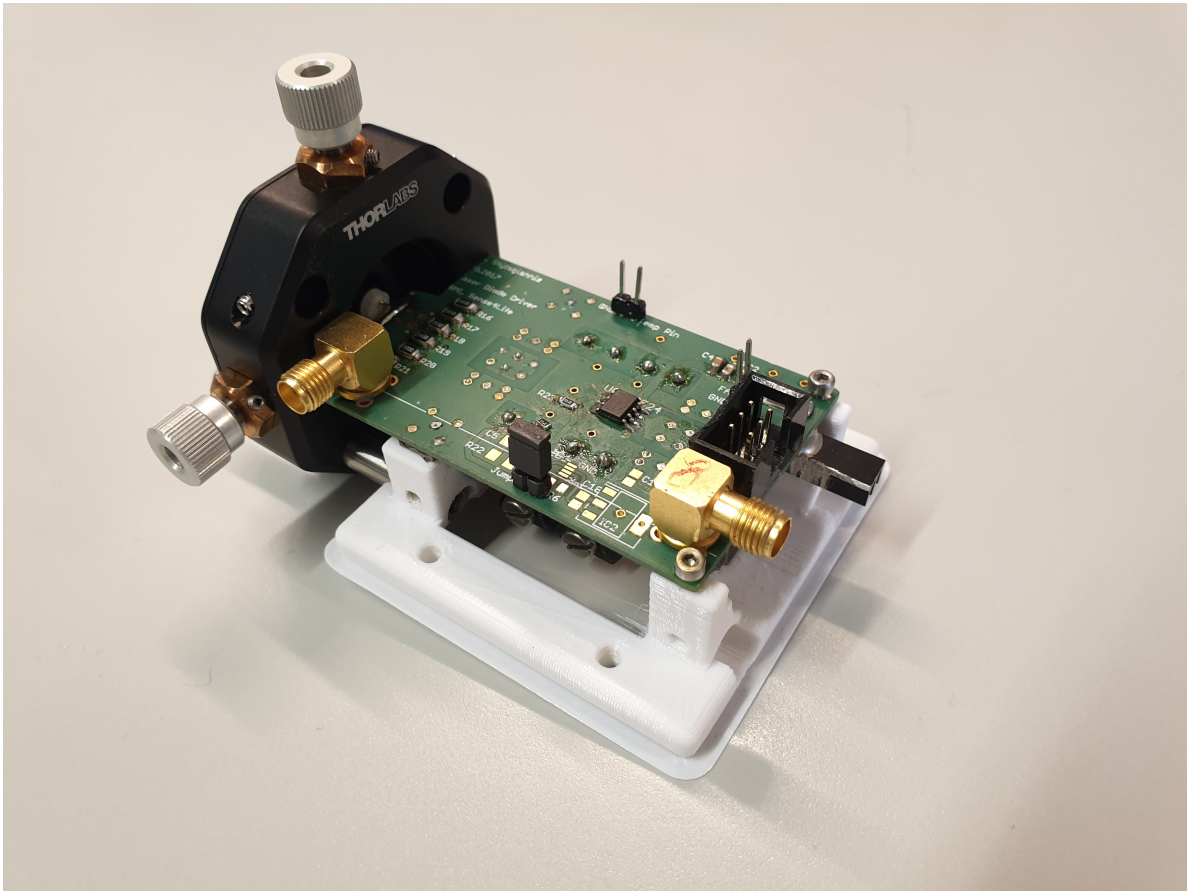

Figure 7.8: The final, updated, version of the pulsed laser diode driver that was used for all the experiments of Chapters 3-5.

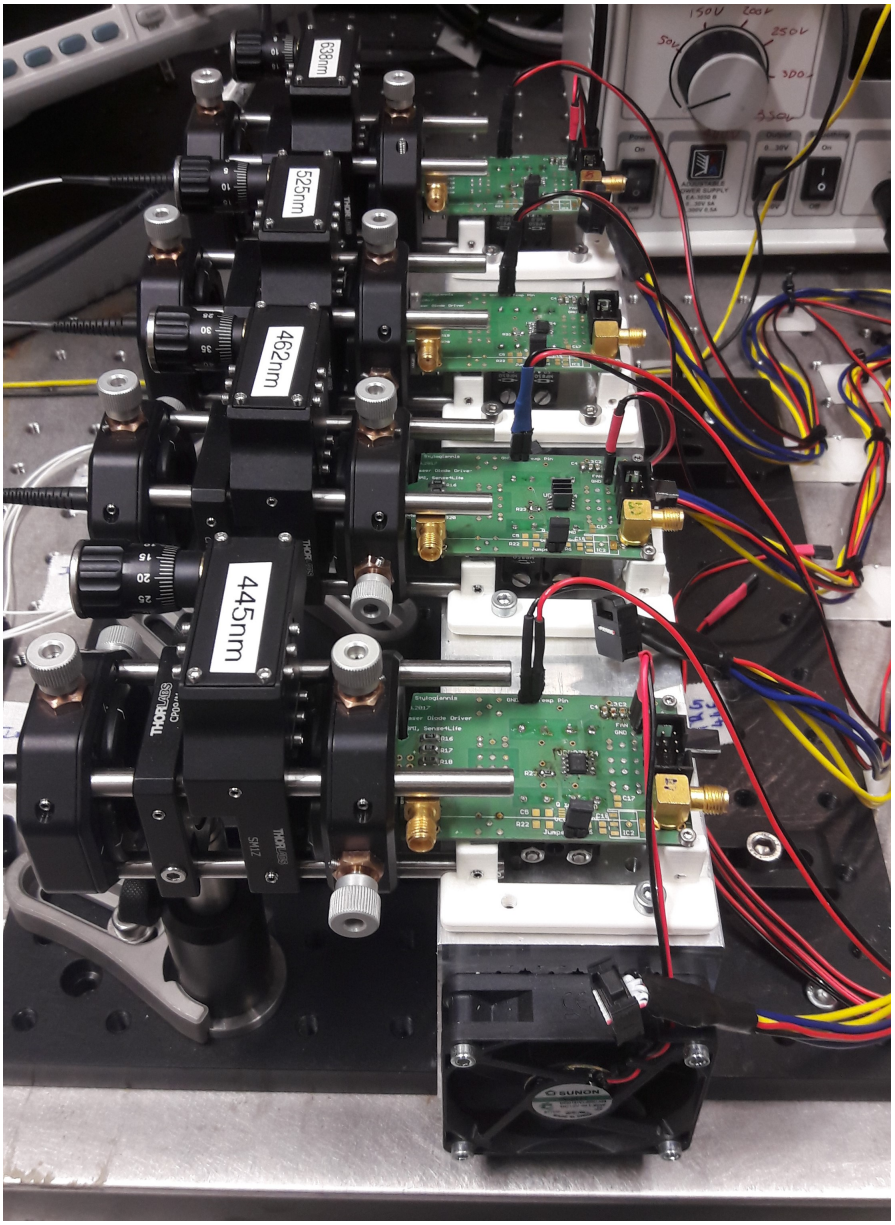

Figure 7.9: The four wavelength overdriven CW-LD illumination source.

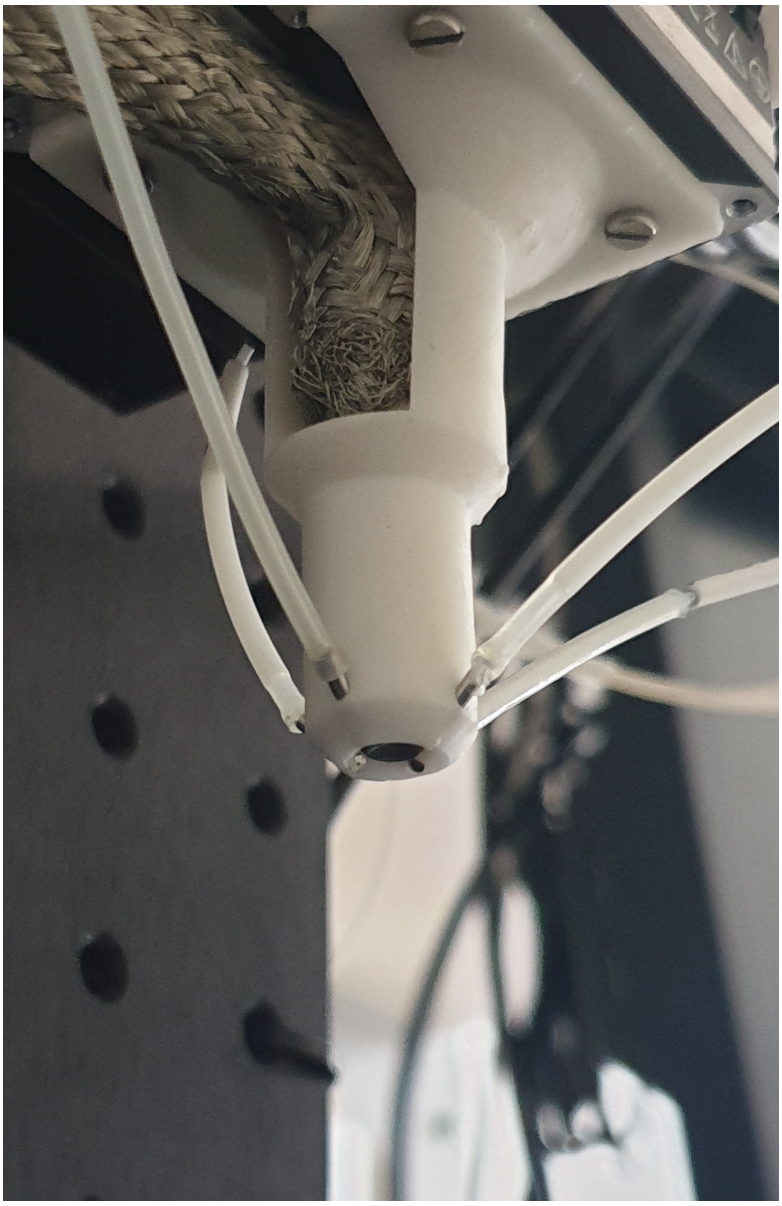

Figure 7.10: The scanning head of the four wavelength LD RSOM where the sample is illuminated from four side and the output of the fibers is not focused with a lens. All fibers and the UST are submerged into water.

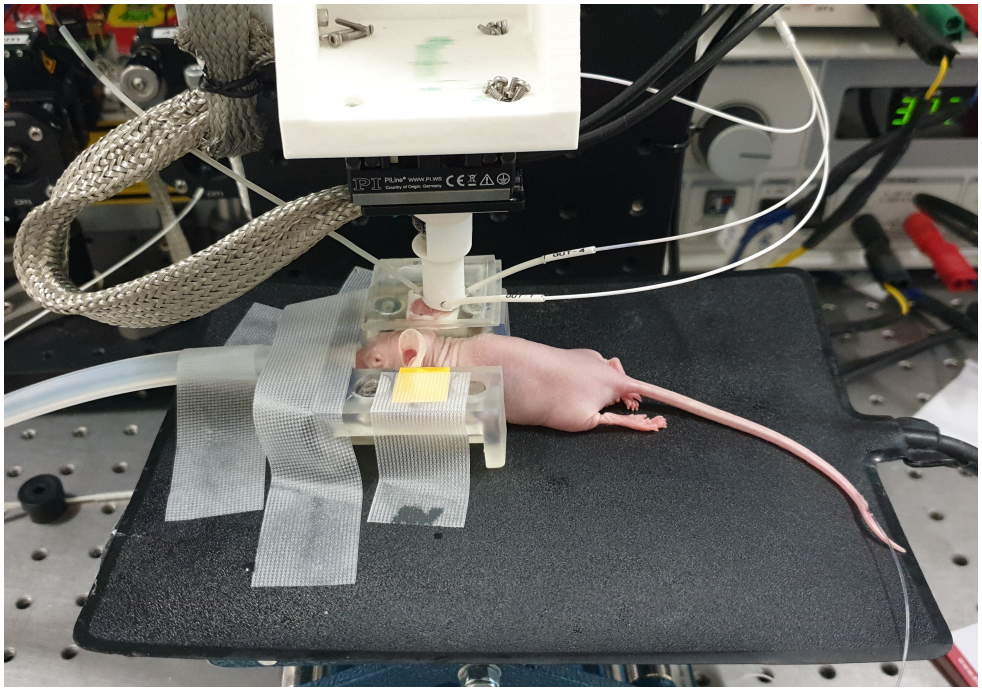

Figure 7.11: The multi-wavelength LD RSOM while it is measuring a mouse ear with the LDs momentarily off.

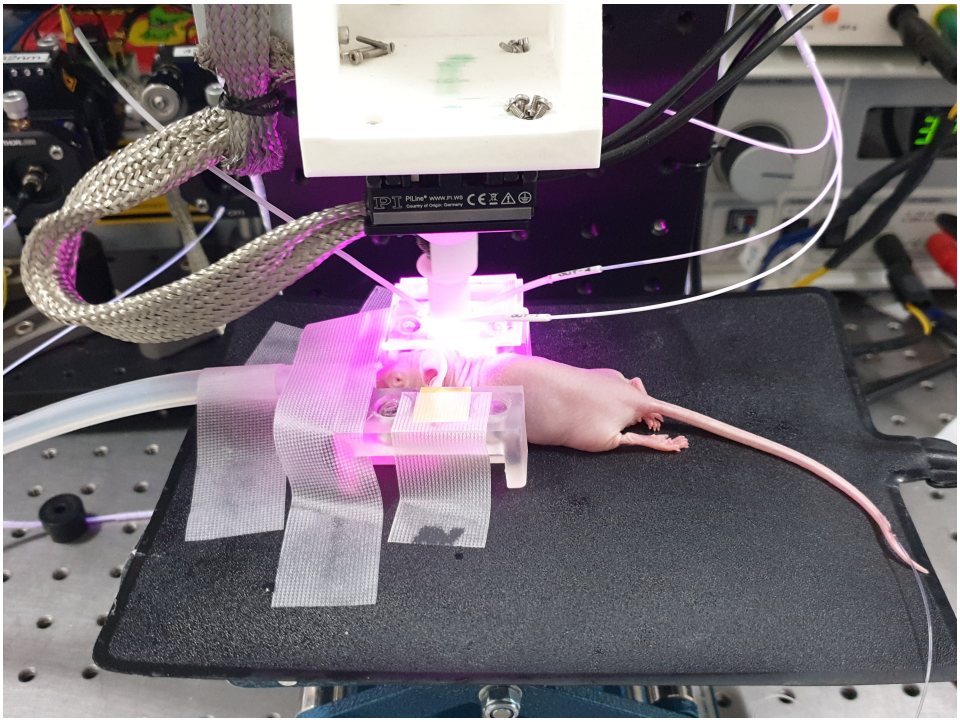

Figure 7.12: The multi-wavelength LD RSOM while it is measuring a mouse ear with the LDs on.

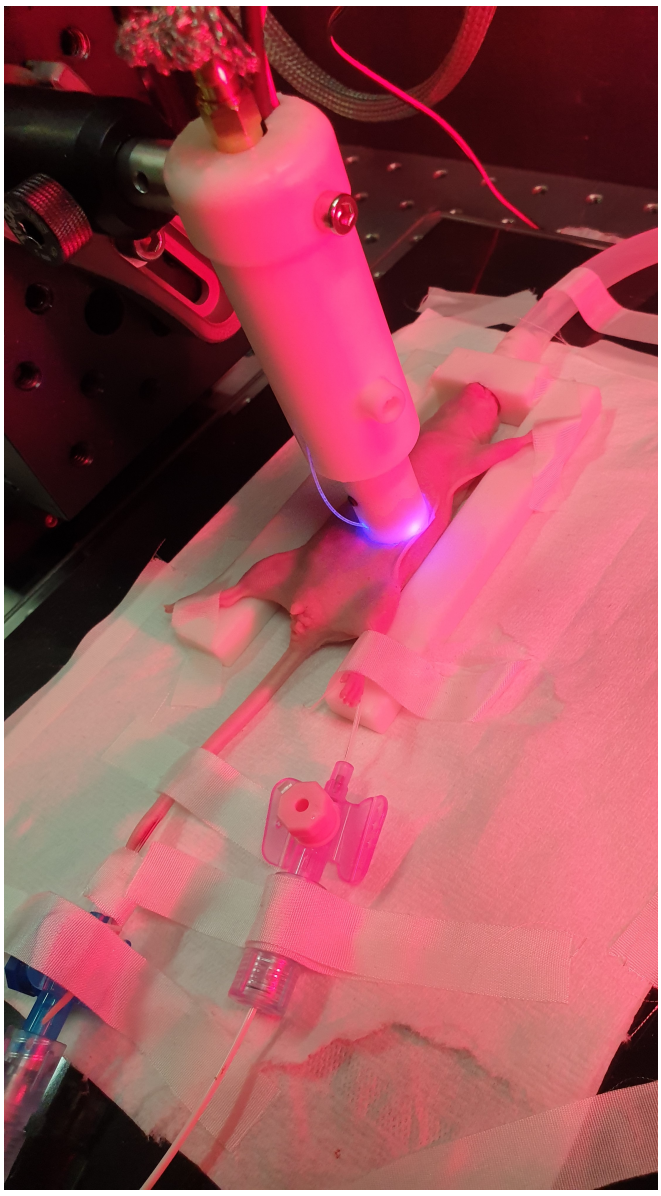

Figure 7.13: The single point OA sensor (SPOAS) while it is measuring the local vascular tissue oxygenation of a mouse.

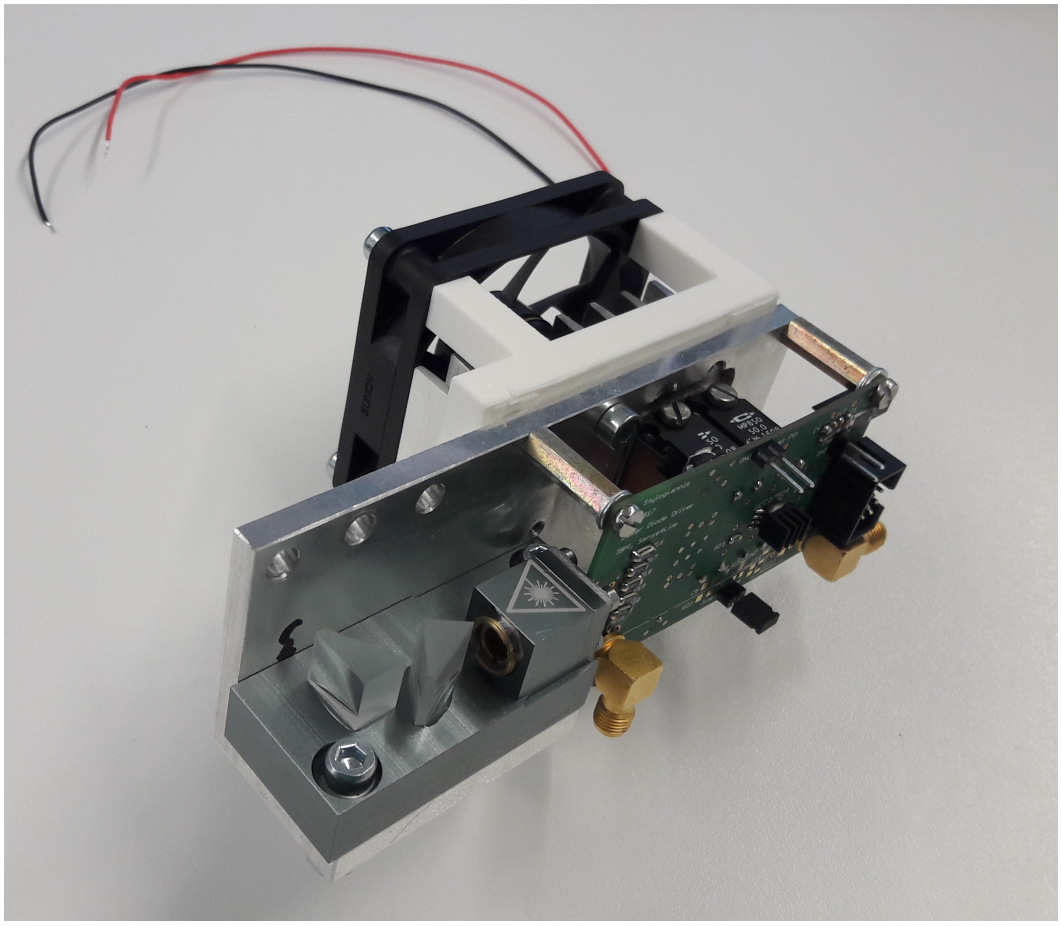

Figure 7.14: One of the three overdriven CW-LD illumination sources developed to be integrated in the OA microscope. The output of the CW-LD is collimated with a lens and a pair of anamorthic prisms is correctic the cylindrical output of the LD. This system and the results it produced has been presented in [334].

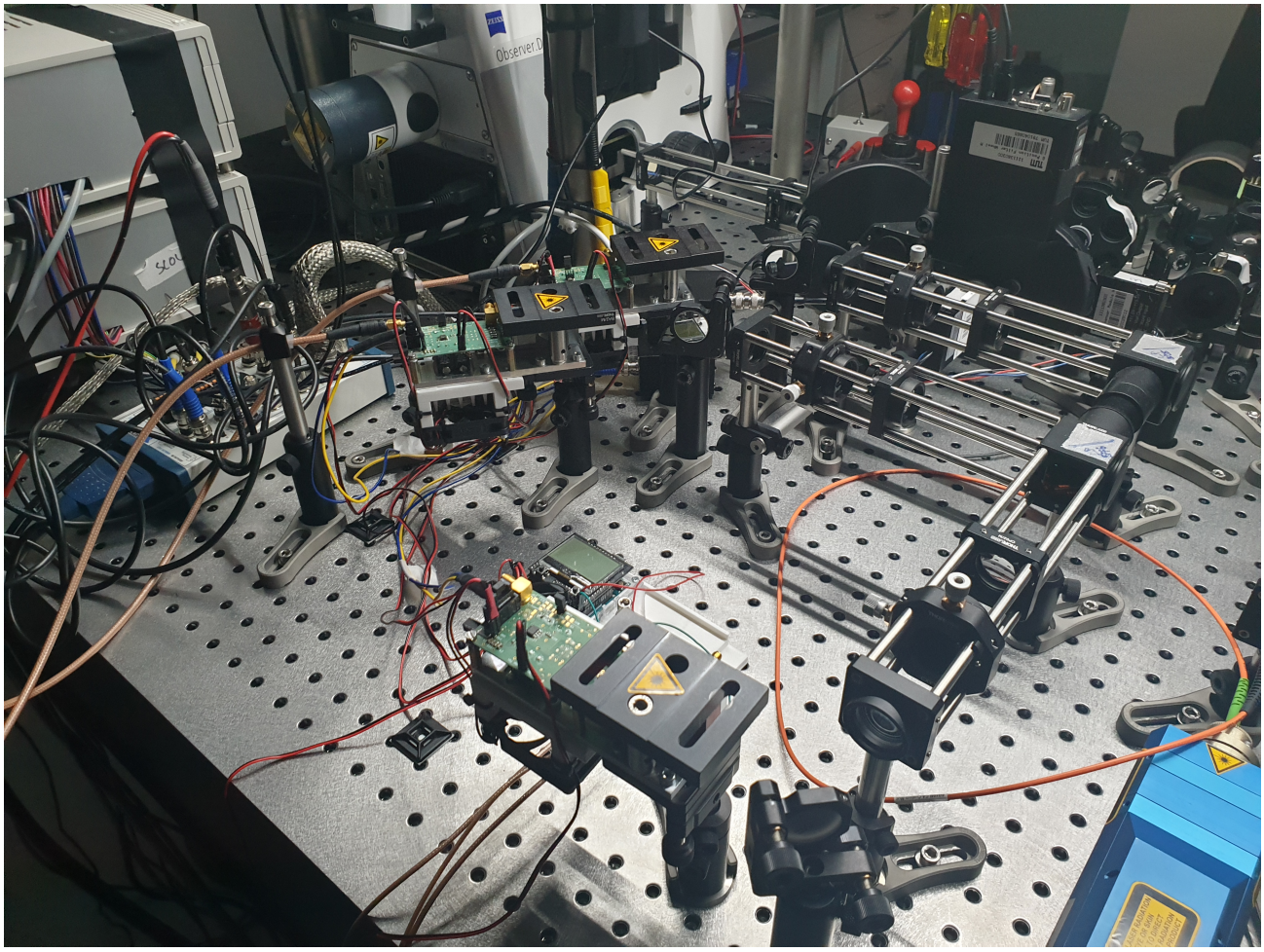

Figure 7.15: The microscopy setup that has three different overdriven CW-LDs, emitting at 450, 520 and 638 nm, integrated in it.

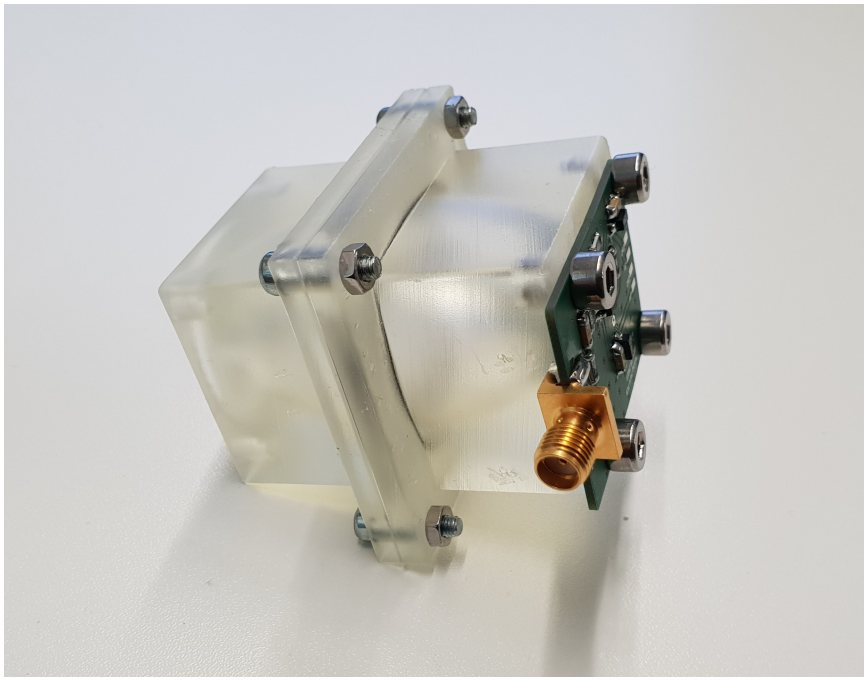

Figure 7.16: The 3D printed OA soot sensor that was developed featuring a hollow ellipsoidal chamber.

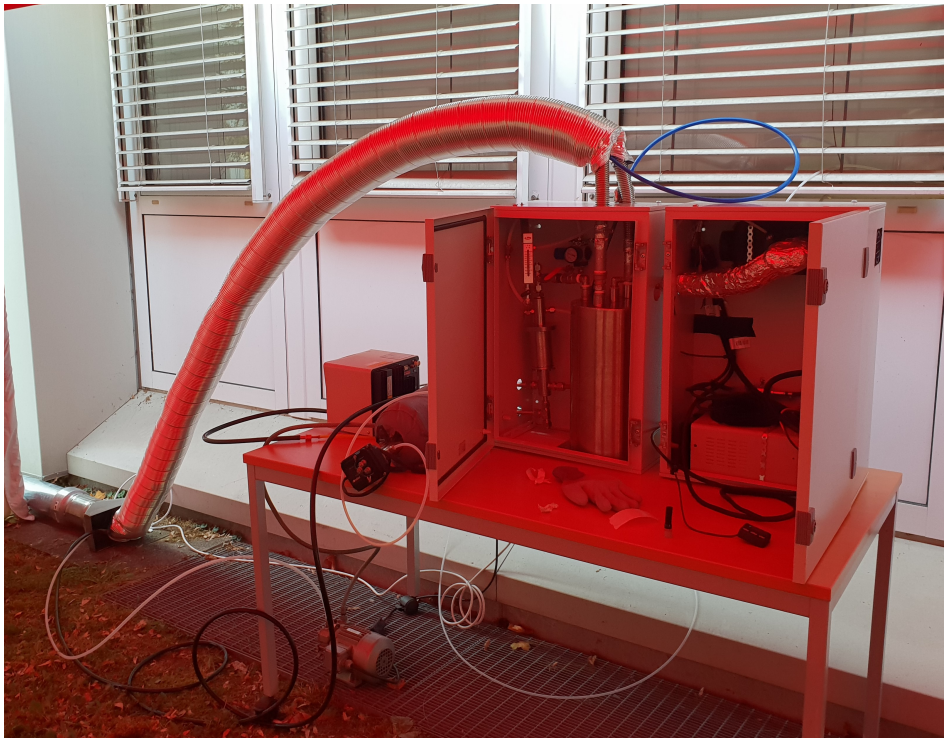

Figure 7.17: The soot generation and dilution system that was temporarily installed in the Helmholtz-Zentrum Muenchen (HMGU) facilities.

Figure 7.18: The soot generator could not be installed in the building and the biological labs. The solution we provided was this tent that we installed to protect the soot generator from the weather.

Figure 7.19: The permanent solution we found to host the soot generator outside of the main building, right next to the lab that we perform the experiments.

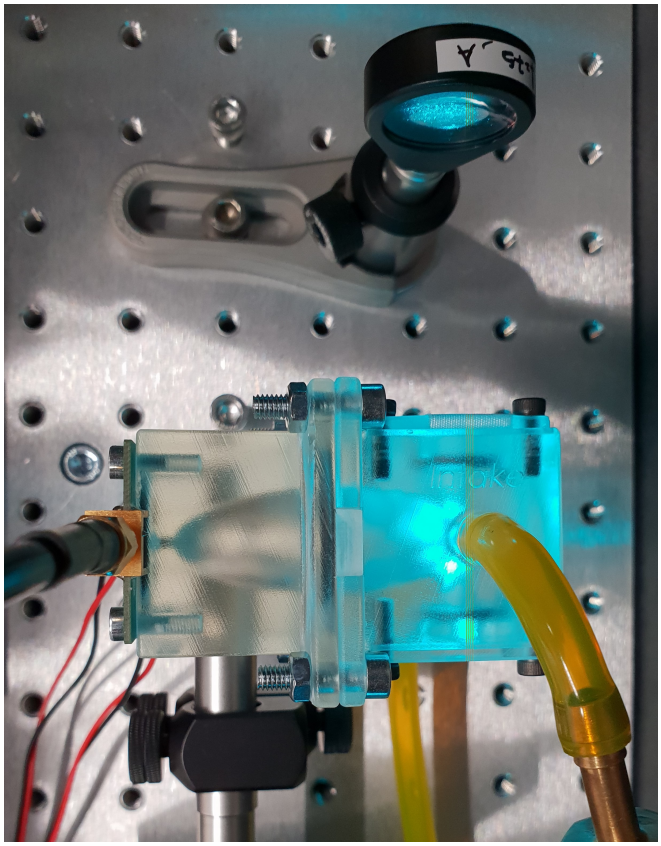

Figure 7.20: The OA soot sensor while it is characterized with the DPSS-OPO laser. The hollow ellipsoidal cavity is clearly visible.

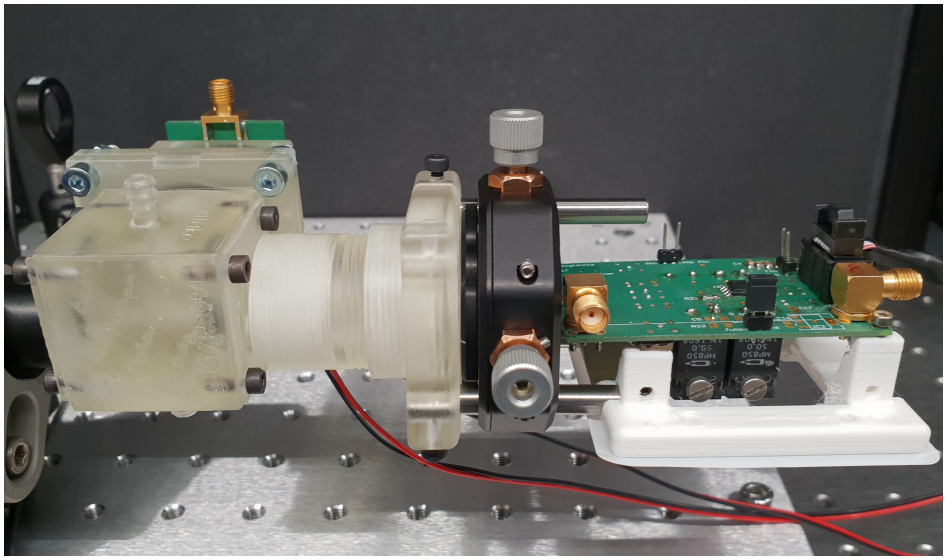

Figure 7.21: The first version of the OA soot sensor with the CW-LD and the pulsed laser diode driver directly attached on the sensor.

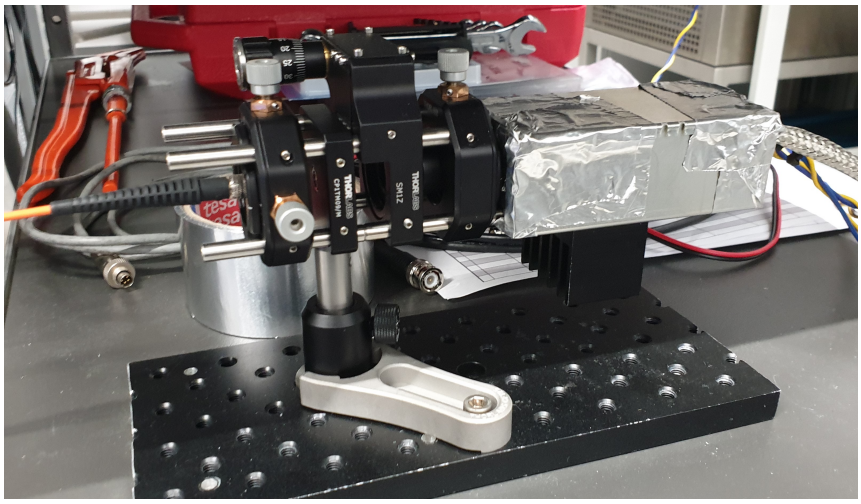

Figure 7.22: The pulsed laser diode driver enclosed in a metal box to reduce the electromagnetic interference during soot measurements. The output of the CW-LD is coupled into a fiber.

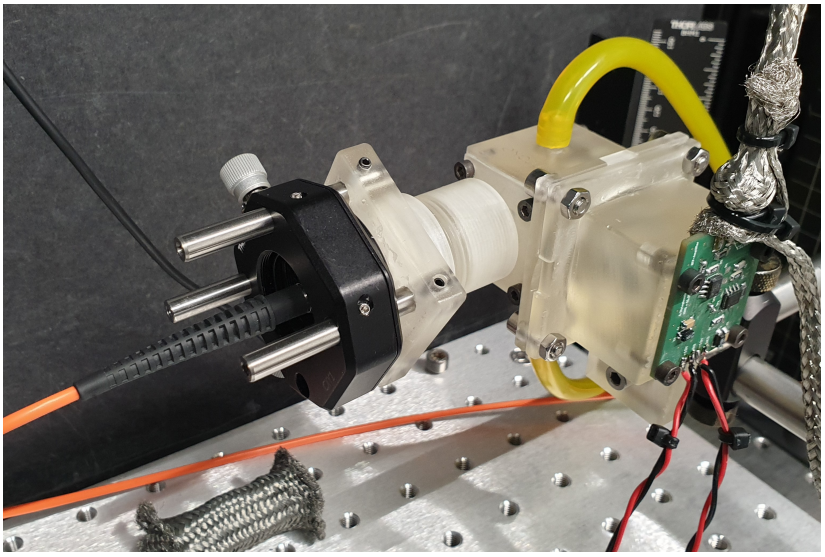

Figure 7.23: The OA soot sensor with the fiber coming from the CW-LD as the illumination source.

List of Publications

Patent Submissions

1. Vasilis Ntziachristos, Leonidas Ntziachristos, **Antonios Stylogiannis**, Nikolaos Kousias, Anastasios Kontses, *An apparatus with a high sensitivity optical absorption sensor and a method of use thereof for environmental applications*, Patent application no. GR20200100657.

First author Publications

1. **Antonios Stylogiannis***, Ludwig Prade*, Andreas Buehler, Juan Aguirre, George Sergiadis, Vasilis Ntziachristos, *Continuous wave laser diodes enable fast optoacoustic imaging*, Photoacoustics, Volume 9, 2018, Pages 31-38.

2. **Antonios Stylogiannis**, Lucas Riobo, Ludwig Prade, Sarah Glasl, Sabine Klein, Giulia Lucidi, Martin Fuchs, Dieter Saur, Vasilis Ntziachristos, *Low-cost single-point optoacoustic sensor for spectroscopic measurement of local vascular oxygenation*, Opt. Lett. 45, 6579-6582 (2020).

3. **Antonios Stylogiannis***, Nikolaos Kousias*, Anastasios Kontses, Leonidas Ntziachristos, Vasilis Ntziachristos, *A Low – Cost Optoacoustic Sensor for Environmental Monitoring*, MDPI Sensors 21, no. 4: 1379.

4. **Antonios Stylogiannis**, Ludwig Prade, Sarah Glasl, Mustafa Qutaiba, Christian Zakian, Vasilis Ntziachristos, *Frequency Wavelength Multiplexed Optoacoustic Tomography*, accepted in Nature Communications (20/05/2022).

5. **Antonios Stylogiannis***, Markus Seeger*, Ludwig Prade, Sarah Glasl, Vasilis Ntziachristos, *Optoacoustic microscopy with over-driven continuous wave laser diodes*, under preparation.

Other Publications

1. Hailong He, **Antonios Stylogiannis**, Parastoo Afshari, Tobias Wiedemann, Katia Steiger, Andreas Buehler, Christian Zakian, Vasilis Ntziachristos, *Capsule optoacoustic endoscopy for esophageal imaging*. J Biophotonics. 2019 Oct 12(10).

2. Chen Yang, Xiaohua Jian, Xinle Zhu, Jiabing Lv, Yang Jiao, Zhile Han, **Antonios Stylogiannis**, Vasilis Ntziachristos, George Sergiadis, YaoYao Cui, *Sensitivity Enhanced Photoacoustic Imaging Using a High-Frequency PZT Transducer with an Integrated Front-End Amplifier*, Sensors 2020, 20, 766.

3. Mustafa Qutaiba*, Murad Omar*, Pouyan Mohajerani, Ludwig Prade, **Antonios Stylogiannis** and Vasilis Ntziachristos, *In-vivo three-dimensional Raster Scan Optoacoustic Mesoscopy using Frequency Domain Inversion*, IEEE Trans Med Imaging. 2021 Dec;40(12):3349-3357.

Conferences Presentations and Posters

1. **Antonios Stylogiannis***, Ludwig Prade*, Andreas Buehler, Juan Aguirre, George Sergiadis, Vasilis Ntziachristos, *Continuous Wave Laser Diodes Enable Fast Optoacsoutic Imaging*, Photonics West 2018, poster presentation.

(* These authors contributed equally)

List of Figures

List of Tables

Bibliography

[1] W. G. Bradley, "History of medical imaging," *Proceedings of the American Philosophical Society*, vol. 152, p. 349—361, September 2008.

[2] W. R. Hendee and E. R. Ritenour, *Medical Imaging Physics*. Wiley-Liss, Inc., 2002.

[3] N. B. Smith and A. Webb, *Introduction to Medical Imaging: Physics, Engineering and Clinical Applications*. Cambridge Texts in Biomedical Engineering, Cambridge University Press, 2010.

[4] A. Haga, S. Senda, Y. Sakai, Y. Mizuta, S. Kita, and F. Okuyama, "A miniature x-ray tube," *Applied Physics Letters*, vol. 84, no. 12, pp. 2208–2210, 2004.

[5] H. Ebel, "X-ray tube spectra," *X-Ray Spectrometry*, vol. 28, no. 4, pp. 255–266, 1999.

[6] G. G. Poludniowski, "Calculation of x-ray spectra emerging from an x-ray tube. Part II. X-ray production and filtration in x-ray targets," *Medical Physics*, vol. 34, no. 6, pp. 2175–2186, 2007.

[7] B. K. Ridley and B. K. Ridley, "Compton scattering of x rays from bound electrons," *Hybrid Phonons in Nanostructures*, vol. 2, pp. 124–128, 2017.

[8] A. R. Cowen, A. G. Davies, and M. U. Sivananthan, "The design and imaging characteristics of dynamic, solid-state, flat-panel x-ray image detectors for digital fluoroscopy and fluorography," *Clinical Radiology*, vol. 63, no. 10, pp. 1073–1085, 2008.

[9] G. R. Davis and F. S. L. Wong, "X-ray microtomography of bones and teeth," *Physiological Measurement*, vol. 17, pp. 121–146, aug 1996.

[10] W. Hendee, "History and status of x-ray mammography," *Health physics*, vol. 69, p. 636—648, November 1995.

[11] C. Cole-Beuglet, R. Soriano, A. B. Kurtz, J. E. Meyer, D. B. Kopans, and B. B. Goldberg, "Ultrasound, x-ray mammography, and histopathology of cystosarcoma phylloides.," *Radiology*, vol. 146, no. 2, pp. 481–486, 1983. PMID: 6294737.

[12] J. F. Hainfeld, S. M. Ridwan, Y. Stanishevskiy, N. R. Smilowitz, J. Davis, and H. M. Smilowitz, "Small, Long Blood Half-Life Iodine Nanoparticle for Vascular and Tumor Imaging," *Scientific Reports*, vol. 8, no. 1, p. 13803, 2018.

[13] H. Abrahamsson, S. Antov, and I. Bosaeus, "Gastrointestinal and colonic segmental transit time evaluated by a single abdominal x-ray in healthy subjects and constipated patients," *Scandinavian Journal of Gastroenterology*, vol. 23, no. sup152, pp. 72–80, 1988.

[14] T. G. Flohr, H. Bruder, K. Stierstorfer, M. Petersilka, B. Schmidt, and C. H. McCollough, "Image reconstruction and image quality evaluation for a dual source CT scanner," *Medical Physics*, vol. 35, no. 12, pp. 5882–5897, 2008.

[15] M. E. Raichle, "Functional brain imaging and human brain function," *Journal of Neuroscience*, vol. 23, no. 10, pp. 3959–3962, 2003.

[16] X. Zhang, X.-R. Yang, Y. Chen, H.-Q. Li, R.-M. Li, Q.-X. Yuan, P.-P. Zhu, W.-X. Huang, and W.-j. Peng, "Visualising liver fibrosis by phase-contrast X-ray imaging in common bile duct ligated mice," *European Radiology*, vol. 23, no. 2, pp. 417–423, 2013.

[17] W. Huda and R. Brad Abrahams, "X-ray-based medical imaging and resolution," *American Journal of Roentgenology*, vol. 204, no. 4, pp. W393–W397, 2015.

[18] B. F. Wall and D. Hart, "Revised radiation doses for typical X-ray examinations: Report on a recent review of doses to patients from medical X-ray examinations in the UK by NRPB," *British Journal of Radiology*, vol. 70, no. MAY, pp. 437–439, 1997.

[19] K. R. Brown and E. Rzucidlo, "Acute and chronic radiation injury," *Journal of Vascular Surgery*, vol. 53, no. 1 SUPPL., pp. 15S–21S, 2011.

[20] A. Safwat, S. M. Bentzen, I. Turesson, and J. H. Hendry, "Deterministic rather than stochastic factors explain most of the variation in the expression of skin telangiectasia after radiotherapy," *International Journal of Radiation Oncology Biology Physics*, vol. 52, no. 1, pp. 198–204, 2002.

[21] J. K. Seo, D. H. Kim, J. Lee, O. I. Kwon, S. Z. Sajib, and E. J. Woo, "Electrical tissue property imaging using MRI at dc and Larmor frequency," *Inverse Problems*, vol. 28, no. 8, 2012.

[22] H. Ammari, H. Kwon, Y. Lee, K. Kang, and J. K. Seo, "Magnetic resonance-based reconstruction method of conductivity and permittivity distributions at the Larmor frequency," *Inverse Problems*, vol. 31, no. 10, pp. 0–24, 2015.

[23] D. I. Hoult and N. S. Ginsberg, "The quantum origins of the free induction decay signal and spin noise," *Journal of Magnetic Resonance*, vol. 148, no. 1, pp. 182–199, 2001.

[24] G. E. Gold, E. Han, J. Stainsby, G. Wright, J. Brittain, and C. Beaulieu, "Musculoskeletal MRI at 3.0 T: Relaxation times and image contrast," *American Journal of Roentgenology*, vol. 183, no. 2, pp. 343–351, 2004.

[25] J. Z. Bojorquez, S. Bricq, C. Acquitter, F. Brunotte, P. M. Walker, and A. Lalande, "What are normal relaxation times of tissues at 3 T?," *Magnetic Resonance Imaging*, vol. 35, pp. 69–80, 2017.

[26] A. Parry, S. Clare, M. Jenkinson, S. Smith, J. Palace, and P. M. Matthews, "MRI brain T1 relaxation time changes in MS patients increase over time in both the white matter and the cortex," *Journal of Neuroimaging*, vol. 13, no. 3, pp. 234–239, 2003.

[27] R. A. Edden, S. A. Smith, and P. B. Barker, "Longitudinal and multi-echo transverse relaxation times of normal breast tissue at 3 Tesla.," *Journal of magnetic resonance imaging : JMRI*, vol. 32, no. 4, pp. 982–987, 2010.

[28] E. David-Vaudey, S. Ghosh, M. Ries, and S. Majumdar, "T2 relaxation time measurements in osteoarthritis," *Magnetic Resonance Imaging*, vol. 22, no. 5, pp. 673–682, 2004.

[29] R. M. Henkelman, G. J. Stanisz, and S. J. Graham, "Magnetization transfer in MRI: A review," *NMR in Biomedicine*, vol. 14, no. 2, pp. 57–64, 2001.

[30] D. A. Feinberg and K. Setsompop, "Ultra-fast MRI of the human brain with simultaneous multi-slice imaging," *Journal of Magnetic Resonance*, vol. 229, pp. 90–100, 2013.

[31] S. Schmitter, S. Moeller, X. Wu, E. J. Auerbach, G. J. Metzger, P. F. Van de Moortele, and K. Uğurbil, "Simultaneous multislice imaging in dynamic cardiac MRI at 7T using parallel transmission," *Magnetic Resonance in Medicine*, vol. 77, no. 3, pp. 1010–1020, 2017.

[32] A. Filler, "The History, Development and Impact of Computed Imaging in Neurological Diagnosis and Neurosurgery: CT, MRI, and DTI," *Nature Precedings*, 2009.

[33] J. Alvarez-Linera, "3t mri: Advances in brain imaging," *European Journal of Radiology*, vol. 67, no. 3, pp. 415–426, 2008. Spanish Radiology - Spanish Researchers Open MR to Clinical Applications.

[34] M. R. Oliva and S. Saini, "Liver cancer imaging: Role of CT, MRI, US and PET," *Cancer Imaging*, vol. 4, pp. S42–S46, 2004.

[35] S. Namasivayam, D. R. Martin, and S. Saini, "Imaging of liver metastases: MRI," *Cancer Imaging*, vol. 7, no. 1, pp. 2–9, 2007.

[36] D. Jackson, L. Jennings, R. Maywood, and P. Berger, "Magnetic resonance imaging of the knee," *The American Journal of Sports Medicine*, vol. 16, no. 1, pp. 29–38, 1988. PMID: 3344877.

[37] S. Geethanath and J. T. Vaughan, "Accessible magnetic resonance imaging: A review," *Journal of Magnetic Resonance Imaging*, vol. 49, no. 7, pp. e65–e77, 2019.

[38] J. Hli, K. R. Erikson, F. J. Fry, and J. P. Jones, "Ultrasound in medicine-a review," *Transactions on sonics and ultrasonics*, no. 3, pp. 144–170, 1974.

[39] F. D'Astous and F. Foster, "Frequency dependence of ultrasound attenuation and backscatter in breast tissue," *Ultrasound in Medicine and Biology*, vol. 12, no. 10, pp. 795 – 808, 1986.

[40] D. C. Bauer, C. C. Glüer, J. A. Cauley, T. M. Vogt, K. E. Ensrud, H. K. Genant, and D. M. Black, "Broadband Ultrasound Attenuation Predicts Fractures Strongly and Independently of Densitometry in Older Women: A Prospective Study," *Archives of Internal Medicine*, vol. 157, pp. 629–634, 03 1997.

[41] A. Fenster and D. B. Downey, "3-d ultrasound imaging: a review," *IEEE Engineering in Medicine and Biology Magazine*, vol. 15, no. 6, pp. 41–51, 1996.

[42] B. Ward, A. C. Baker, and V. F. Humphrey, "Nonlinear propagation applied to the improvement of resolution in diagnostic medical ultrasound," *The Journal of the Acoustical Society of America*, vol. 101, no. 1, pp. 143–154, 1997.

[43] O. V. Solberg, F. Lindseth, H. Torp, R. E. Blake, and T. A. Nagelhus Hernes, "Freehand 3D Ultrasound Reconstruction Algorithms-A Review," *Ultrasound in Medicine and Biology*, vol. 33, no. 7, pp. 991–1009, 2007.

[44] J. A. Jensen, *Estimation of Blood Velocities Using Ultrasound, A signal Processing Approach*. Cambridge University Press, 1996.

[45] C. Errico, J. Pierre, S. Pezet, Y. Desailly, Z. Lenkei, O. Couture, and M. Tanter, "Ultrafast ultrasound localization microscopy for deep super-resolution vascular imaging," *Nature*, vol. 527, no. 7579, pp. 499–502, 2015.

[46] Y. Takeda, "Velocity profile measurement by ultrasound doppler shift method," *International Journal of Heat and Fluid Flow*, vol. 7, no. 4, pp. 313 – 318, 1986.

[47] L. Hatle, B. A. Angelsen, and A. Tromsdal, "Non-invasive assessment of aortic stenosis by doppler ultrasound.," *Heart*, vol. 43, no. 3, pp. 284–292, 1980.

[48] W. L. Nyborg, "Biological effects of ultrasound: Development of safety guidelines. Part II: General review," *Ultrasound in Medicine and Biology*, vol. 27, no. 3, pp. 301–333, 2001.

[49] S. Barnett, G. Ter Haar, M. Ziskin, H. Rott, F. Duck, and K. Maeda, "International recommendations and guidelines for the safe use of diagnostic ultrasound in medicine," *Ultrasound Med Biol*, 2000.

[50] T. Marwick, "The future of echocardiography," *Eur J Echocardiogr*, 2009.

[51] R. M. Sigrist, J. Liau, A. E. Kaffas, M. C. Chammas, and J. K. Willmann, "Ultrasound elastography: Review of techniques and clinical applications," *Theranostics*, vol. 7, no. 5, pp. 1303–1329, 2017.

[52] R. H. Silverman, "High-resolution ultrasound imaging of the eye - A review," *Clinical and Experimental Ophthalmology*, vol. 37, no. 1, pp. 54–67, 2009.

[53] A. Klauser and P. Peetrons, "Developments in musculoskeletal ultrasound and clinical applications.," *Skeletal Radiol.*, 2010.

[54] L. Wang and H. Wu, *Biomedical Optics, Principles and Imaging*, ch. 1, pp. 1–15. John Wiley and Sons, Ltd, 2012.

[55] V. Ntziachristos, "Going deeper than microscopy: the optical imaging frontier in biology," *Nat Meth*, vol. 7, pp. 603–614, aug 2010.

[56] L. Wang and H. Wu, *Biomedical Optics, Principles and Imaging*, ch. 8, pp. 153–179. John Wiley and Sons, Ltd, 2012.

[57] K. Ng and S. Number, "Technology review of charge-coupled device and cmos based electronic imagers."

[58] J. Kaluzny, H. Li, W. Liu, P. Nesper, J. Park, H. F. Zhang, and A. A. Fawzi, "Bayer filter snapshot hyperspectral fundus camera for human retinal imaging," *Current Eye Research*, vol. 42, no. 4, pp. 629–635, 2017. PMID: 27767345.

[59] P. A. Cheremkhin, V. V. Lesnichii, and N. V. Petrov, "Use of spectral characteristics of DSLR cameras with bayer filter sensors," *Journal of Physics: Conference Series*, vol. 536, p. 012021, sep 2014.

[60] J. Zhao and H. Zeng, *Biomadical Optical Imaging Technologies, Design and Applications*, ch. 1, pp. 1–54. Springer-Verlag Berlin Heidelberg, 2013.

[61] T. Bernas, "Basics of digital microscopy.," *Current protocols in cytometry / editorial board, J. Paul Robinson, managing editor ... [et al.]*, vol. Chapter 12, 2005.

[62] A. Holik, "Optical microscopy," in *Encyclopedia of Materials: Science and Technology* (K. J. Buschow, R. W. Cahn, M. C. Flemings, B. Ilschner, E. J. Kramer, S. Mahajan, and P. Veyssière, eds.), pp. 6458 – 6463, Oxford: Elsevier, 2001.

[63] T. Wilson, "Scanning optical microscopy," *Scanning*, vol. 7, no. 2, pp. 79–87, 1985.

[64] R. R. Alfano, X. Liang, L. Wang, and P. P. Ho, "Time-resolved imaging of translucent droplets in highly scattering turbid media," *Science*, vol. 264, no. 5167, pp. 1913–1915, 1994.

[65] B. B. Das, K. M. Yoo, and R. R. Alfano, "Ultrafast time-gated imaging in thick tissues: a step toward optical mammography," *Opt. Lett.*, vol. 18, pp. 1092–1094, Jul 1993.

[66] L. Florack, "A spatio-frequency trade-off scale for scale-space filtering," *IEEE Transactions on Pattern Analysis and Machine Intelligence*, vol. 22, no. 9, pp. 1050–1055, 2000.

[67] T. Wilson and B. R. Masters, "Confocal microscopy," *Appl. Opt.*, vol. 33, pp. 565–566, Feb 1994.

[68] T. WILSON, "Resolution and optical sectioning in the confocal microscope," *Journal of Microscopy*, vol. 244, no. 2, pp. 113–121, 2011.

[69] L. V. Wang and J. Yao, "A practical guide to photoacoustic tomography in the life sciences," *Nat Meth*, vol. 13, pp. 627–638, aug 2016.

[70] Y. Sun and A. Periasamy, *Biomadical Optical Imaging Technologies, Design and Applications*, ch. 3, pp. 79–110. Springer-Verlag Berlin Heidelberg, 2013.

[71] C. Würth, M. Grabolle, J. Pauli, M. Spieles, and U. Resch-Genger, "Relative and absolute determination of fluorescence quantum yields of transparent samples," *Nature Protocols*, vol. 8, no. 8, pp. 1535–1550, 2013.

[72] R. Datta, T. M. Heaster, J. T. Sharick, A. A. Gillette, and M. C. Skala, "Fluorescence lifetime imaging microscopy: fundamentals and advances in instrumentation, analysis, and applications," *Journal of Biomedical Optics*, vol. 25, no. 07, p. 1, 2020.

[73] C. N. Pace, F. Vajdos, L. Fee, G. Grimsley, and T. Gray, "How to measure and predict the molar absorption coefficient of a protein," *Protein Science*, vol. 4, no. 11, pp. 2411–2423, 1995.

[74] L. Wang and H. Wu, *Biomedical Optics, Principles and Imaging*, ch. 7, pp. 135–151. John Wiley and Sons, Ltd, 2012.

[75] F. Stuker, J. Ripoll, and M. Rudin, "Fluorescence molecular tomography: Principles and potential for pharmaceutical research," *Pharmaceutics*, vol. 3, no. 2, pp. 229–274, 2011.

[76] V. Ntziachristos, C. H. Tung, C. Bremer, and R. Weissleder, "Fluorescence molecular tomography resolves protease activity in vivo," *Nature Medicine*, vol. 8, no. 7, pp. 757–760, 2002.

[77] X. Ma, J. Prakash, F. Ruscitti, S. Glasl, F. F. Stellari, G. Villetti, and V. Ntziachristos, "Assessment of asthmatic inflammation using hybrid fluorescence molecular tomography–x-ray computed tomography," *Journal of Biomedical Optics*, vol. 21, no. 1, pp. 1 – 9, 2016.

[78] A. Ale, V. Ermolayev, E. Herzog, C. Cohrs, M. H. De Angelis, and V. Ntziachristos, "FMT-XCT: In vivo animal studies with hybrid fluorescence molecular tomography-X-ray computed tomography," *Nature Methods*, vol. 9, no. 6, pp. 615–620, 2012.

[79] C. Vinegoni, C. Pitsouli, D. Razansky, N. Perrimon, and V. Ntziachristos, "In vivo imaging of Drosophila melanogaster pupae with mesoscopic fluorescence tomography," *Nature Methods*, vol. 5, no. 1, pp. 45–47, 2008.

[80] J. R. Swedlow and M. Platani, "Live cell imaging using wide-field microscopy and deconvolution," *Cell Structure and Function*, vol. 27, no. 5, pp. 335–341, 2002.

[81] P. G. Bush, D. L. Wokosin, and A. C. Hall, "Two-versus one photon excitation laser scanning microscopy: critical importance of excitation wavelength," *Frontiers in bioscience : a journal and virtual library*, vol. 12, pp. 2646–2657, jan 2007.

[82] P. T. C. So, C. Y. Dong, B. R. Masters, and K. M. Berland, "Two-photon excitation fluorescence microscopy," *Annual Review of Biomedical Engineering*, vol. 2, no. 1, pp. 399–429, 2000. PMID: 11701518.

[83] A. USTIONE and D. PISTON, "A simple introduction to multiphoton microscopy," *Journal of Microscopy*, vol. 243, no. 3, pp. 221–226, 2011.

[84] X. Liu, D. Lin, W. Becker, J. Niu, B. Yu, L. Liu, and J. Qu, "Fast fluorescence lifetime imaging techniques: A review on challenge and development," *Journal of Innovative Optical Health Sciences*, vol. 12, no. 05, p. 1930003, 2019.

[85] W. BECKER, "Fluorescence lifetime imaging – techniques and applications," *Journal of Microscopy*, vol. 247, no. 2, pp. 119–136, 2012.

[86] L. Wang and H. Wu, *Biomedical Optics, Principles and Imaging*, ch. 9, pp. 181–218. John Wiley and Sons, Ltd, 2012.

[87] H. M. Subhash and R. K. Wang, *Biomadical Optical Imaging Technologies, Design and Applications*, ch. 5, pp. 163–212. Springer-Verlag Berlin Heidelberg, 2013.

[88] N. A. Kharousi, U. K. Wali, and S. Azeem, "Current applications of optical coherence tomography in ophthalmology," in *Optical Coherence Tomography* (M. Kawasaki, ed.), ch. 1, Rijeka: IntechOpen, 2013.

[89] M. Adhi and J. S. Duker, "Optical coherence tomography – current and future applications," *Current Opinion in Ophthalmology*, vol. 24, no. 3, 2013.

[90] T. Mitsuyasu, K. Hideaki, and S. Takahiko, "The role of optical coherence tomography in coronary intervention," *Korean J Intern Med*, vol. 27, no. 1, pp. 1–12, 2012.

[91] N. Burris, K. Schwartz, C.-M. Tang, M. S. Jafri, J. Schmitt, M. H. Kwon, O. Toshinaga, J. Gu, J. Brown, E. Brown, R. Pierson III, and R. Poston, "Catheter-based infrared light scanner as a tool to assess conduit quality in coronary artery bypass surgery," *The Journal of Thoracic and Cardiovascular Surgery*, vol. 133, pp. 419–427, feb 2007.

[92] T.-H. Tsai, J. G. Fujimoto, and H. Mashimo, "Endoscopic Optical Coherence Tomography for Clinical Gastroenterology," *Diagnostics (Basel, Switzerland)*, vol. 4, pp. 57–93, may 2014.

[93] T.-H. Tsai, C. L. Leggett, A. J. Trindade, A. Sethi, A.-F. Swager, V. Joshi, J. J. Bergman, H. Mashimo, N. S. Nishioka, and E. Namati, "Optical coherence tomography in gastroenterology: a review and future outlook," *Journal of Biomedical Optics*, vol. 22, no. 12, pp. 1 – 17, 2017.

[94] H.-W. Wang and Y. Chen, "Clinical applications of optical coherence tomography in urology," *Intravital*, vol. 3, pp. e28770–e28770, apr 2014.

[95] J. E. Freund, M. Buijs, C. D. Savci-Heijink, D. M. de Bruin, J. J. M. C. H. de la Rosette, T. G. van Leeuwen, and M. P. Laguna, "Optical Coherence Tomography in Urologic Oncology: a Comprehensive Review," *SN Comprehensive Clinical Medicine*, vol. 1, no. 2, pp. 67–84, 2019.

[96] M. Ibne Mokbul, "Optical Coherence Tomography: Basic Concepts and Applications in Neuroscience Research," *Journal of Medical Engineering*, vol. 2017, p. 3409327, 2017.

[97] D. M. Heiferman, M. J. Heiferman, B. N. Africk, L. K. Ghadiali, E. B. Price, S. Pappu, J. C. Serrone, J. U. Kang, and V. C. Prabhu, "Optical Coherence Tomography and Its Relevance to Neurosurgical Practice," *Contemporary Neurosurgery*, vol. 41, no. 11, 2019.

[98] A. G. Bell, "The photophone," *Science*, vol. 1, no. 11, pp. 130–134, 1880.

[99] L. Wang and H. Wu, *Biomedical Optics, Principles and Imaging*, ch. 12, pp. 283–321. John Wiley and Sons, Ltd, 2012.

[100] Y. Zhou, J. Yao, and L. V. Wang, "Tutorial on photoacoustic tomography," *Journal of Biomedical Optics*, vol. 21, no. 6, pp. 1 – 14, 2016.

[101] G. J. Diebold, T. Sun, and M. I. Khan, "Photoacoustic monopole radiation in one, two, and three dimensions," *Phys. Rev. Lett.*, vol. 67, pp. 3384–3387, Dec 1991.

[102] I. G. Calasso, W. Craig, and G. J. Diebold, "Photoacoustic point source," *Phys. Rev. Lett.*, vol. 86, pp. 3550–3553, Apr 2001.

[103] G. Langer, B. Buchegger, J. Jacak, T. A. Klar, and T. Berer, "Frequency domain photoacoustic and fluorescence microscopy," *Biomedical Optics Express*, vol. 7, no. 7, p. 2692, 2016.

[104] J. Aguirre, M. Schwarz, D. Soliman, A. Buehler, M. Omar, and V. Ntziachristos, "Broadband mesoscopic optoacoustic tomography reveals skin layers," *Opt. Lett.*, vol. 39, pp. 6297–6300, Nov 2014.

[105] J.-P. Ortonne, "Photoprotective properties of skin melanin," *British Journal of Dermatology*, vol. 146, no. s61, pp. 7–10, 2002.

[106] A. N. Bashkatov, E. V. Koblova, V. V. Bakutkin, E. A. Genina, E. P. Savchenko, and V. V. Tuchin, "Estimation of melanin content in iris of human eye," in *Ophthalmic Technologies XV* (F. Manns, P. G. Söderberg, A. Ho, B. E. Stuck, and M. B. M.D., eds.), vol. 5688, pp. 302 – 311, International Society for Optics and Photonics, SPIE, 2005.

[107] A. B. E. Attia, G. Balasundaram, M. Moothanchery, U. Dinish, R. Bi, V. Ntziachristos, and M. Olivo, "A review of clinical photoacoustic imaging: Current and future trends," *Photoacoustics*, vol. 16, p. 100144, 2019.

[108] F. Cao, Z. Qiu, H. Li, and P. Lai, "Photoacoustic imaging in oxygen detection," *Applied Sciences*, vol. 7, no. 12, 2017.

[109] M. Li, Y. Tang, and J. Yao, "Photoacoustic tomography of blood oxygenation: A mini review," *Photoacoustics*, vol. 10, pp. 65 – 73, 2018.

[110] M. Omar, M. Schwarz, D. Soliman, P. Symvoulidis, and V. Ntziachristos, "Pushing the optical imaging limits of cancer with multi-frequency-band raster-scan optoacoustic mesoscopy (rsom)," *Neoplasia*, vol. 17, no. 2, pp. 208 – 214, 2015.

[111] J. Li, A. Chekkoury, J. Prakash, S. Glasl, P. Vetschera, B. Koberstein-Schwarz, I. Olefir, V. Gujrati, M. Omar, and V. Ntziachristos, "Spatial heterogeneity of oxygenation and haemodynamics in breast cancer resolved in vivo by conical multispectral optoacoustic mesoscopy," *Light: Science and Applications*, vol. 9, no. 1, 2020.

[112] A. Berezhnoi, J. Aguirre, B. Hindelang, N. Garzorz-Stark, M. Omar, U. Darsow, K. Eyerich, and V. Ntziachristos, "Optical features of human skin revealed by optoacoustic mesoscopy inthe visible and short-wave infrared regions," *Opt. Lett.*, vol. 44, pp. 4119–4122, Sep 2019.

[113] K. H. Liu, Y. L. Chan, W. B. Chan, W. L. Kong, M. O. Kong, and J. C. Chan, "Sonographic measurement of mesenteric fat thickness is a good correlate with cardiovascular risk factors: Comparison with subcutaneous and preperitoneal fat thickness, magnetic resonance imaging and anthropometric indexes," *International Journal of Obesity*, vol. 27, no. 10, pp. 1267–1273, 2003.

[114] J. Laufer, C. Elwell, D. Delpy, and P. Beard, "In vitromeasurements of absolute blood oxygen saturation using pulsed near-infrared photoacoustic spectroscopy: accuracy and resolution," *Physics in Medicine and Biology*, vol. 50, pp. 4409–4428, sep 2005.

[115] B. T. Cox, J. G. Laufer, P. C. Beard, and S. R. Arridge, "Quantitative spectroscopic photoacoustic imaging: a review," *Journal of Biomedical Optics*, vol. 17, no. 6, pp. 1 – 23, 2012.

[116] S. Kim, Y.-S. Chen, G. P. Luke, and S. Y. Emelianov, "In vivo three-dimensional spectroscopic photoacoustic imaging for monitoring nanoparticle delivery," *Biomed. Opt. Express*, vol. 2, pp. 2540–2550, Sep 2011.

[117] Z. Guo, S. Hu, and L. V. Wang, "Calibration-free absolute quantification of optical absorption coefficients using acoustic spectra in 3d photoacoustic microscopy of biological tissue," *Opt. Lett.*, vol. 35, pp. 2067–2069, Jun 2010.

[118] Z. Guo, C. P. Favazza, A. Garcia-Uribe, and L. V. Wang, "Quantitative photoacoustic microscopy of optical absorption coefficients from acoustic spectra in the optical diffusive regime," *Journal of Biomedical Optics*, vol. 17, no. 6, pp. 1 – 6, 2012.

[119] S. Tzoumas, A. Nunes, I. Olefir, S. Stangl, P. Symvoulidis, S. Glasl, C. Bayer, G. Multhoff, and V. Ntziachristos, "Eigenspectra optoacoustic tomography achieves quantitative blood oxygenation imaging deep in tissues," *Nature Communications*, vol. 7, no. 1, p. 12121, 2016.

[120] P. Liu, "Image reconstruction from photoacoustic pressure signals," in *Laser-Tissue Interaction VII* (S. L. Jacques, ed.), vol. 2681, pp. 285 – 296, International Society for Optics and Photonics, SPIE, 1996.

[121] C. G. A. Hoelen and F. F. M. de Mul, "Image reconstruction for photoacoustic scanning of tissue structures," *Appl. Opt.*, vol. 39, pp. 5872–5883, Nov 2000.

[122] M. Xu and L. V. Wang, "Universal back-projection algorithm for photoacoustic computed tomography," *Phys. Rev. E*, vol. 71, p. 016706, Jan 2005.

[123] X. L. Dean-Ben, A. Buehler, V. Ntziachristos, and D. Razansky, "Accurate model-based reconstruction algorithm for three-dimensional optoacoustic tomography," *IEEE Transactions on Medical Imaging*, vol. 31, no. 10, pp. 1922–1928, 2012.

[124] H. Huang, G. Bustamante, R. Peterson, and J. Y. Ye, "An adaptive filtered back-projection for photoacoustic image reconstruction," *Medical Physics*, vol. 42, no. 5, pp. 2169–2178, 2015.

[125] M. Pramanik, "Improving tangential resolution with a modified delay-and-sum reconstruction algorithm in photoacoustic and thermoacoustic tomography," *J. Opt. Soc. Am. A*, vol. 31, pp. 621–627, Mar 2014.

[126] M. Omar, J. Gateau, and V. Ntziachristos, "Raster-scan optoacoustic mesoscopy in the 25-125 mhz range," *Opt. Lett.*, vol. 38, pp. 2472–2474, Jul 2013.

[127] V. Ntziachristos and D. Razansky, "Molecular imaging by means of multispectral optoacoustic tomography (msot)," *Chemical Reviews*, vol. 110, no. 5, pp. 2783–2794, 2010. PMID: 20387910.

[128] R. Ma, A. Taruttis, V. Ntziachristos, and D. Razansky, "Multispectral optoacoustic tomography (msot) scanner for whole-body small animal imaging," *Opt. Express*, vol. 17, pp. 21414–21426, Nov 2009.

[129] D. Razansky, J. Baeten, and V. Ntziachristos, "Sensitivity of molecular target detection by multispectral optoacoustic tomography (msot)," *Medical Physics*, vol. 36, no. 3, pp. 939–945, 2009.

[130] A. Shah, N. Bush, G. Box, S. Eccles, and J. Bamber, "Value of combining dynamic contrast enhanced ultrasound and optoacoustic tomography for hypoxia imaging," *Photoacoustics*, vol. 8, pp. 15 – 27, 2017.

[131] E. Merčep, X. L. Deán-Ben, and D. Razansky, "Combined pulse-echo ultrasound and multispectral optoacoustic tomography with a multi-segment detector array," *IEEE Transactions on Medical Imaging*, vol. 36, no. 10, pp. 2129–2137, 2017.

[132] S. Zackrisson, S. van de Ven, and S. Gambhir, "Light in and sound out: Emerging translational strategies for photoacoustic imaging," *Cancer Research*, vol. 74, no. 4, pp. 979–1004, 2014.

[133] K. E. Wilson, T. Y. Wang, and J. K. Willmann, "Acoustic and photoacoustic molecular imaging of cancer," *Journal of nuclear medicine : official publication, Society of Nuclear Medicine*, vol. 54, pp. 1851–1854, nov 2013.

[134] J. G. Laufer, E. Z. Zhang, B. E. Treeby, B. T. Cox, P. C. Beard, P. Johnson, and B. Pedley, "In vivo preclinical photoacoustic imaging of tumor vasculature development and therapy," *Journal of Biomedical Optics*, vol. 17, no. 5, pp. 1 – 9, 2012.

[135] G. Diot, S. Metz, A. Noske, E. Liapis, B. Schroeder, S. V. Ovsepian, R. Meier, E. Rummeny, and V. Ntziachristos, "Multispectral Optoacoustic Tomography (MSOT) of human breast cancer," *Clinical Cancer Research*, vol. 23, no. 22, pp. 6912–6922, 2017.

[136] E. Liapis, U. Klemm, A. Karlas, J. Reber, and V. Ntziachristos, "Resolution of spatial and temporal heterogeneity in bevacizumab-treated breast tumors by eigenspectra multispectral optoacoustic tomography," *Cancer Research*, 2020.

[137] A. Karlas, N. A. Fasoula, K. Paul-Yuan, J. Reber, M. Kallmayer, D. Bozhko, M. Seeger, H. H. Eckstein, M. Wildgruber, and V. Ntziachristos, "Cardiovascular optoacoustics: From mice to men – A review," *Photoacoustics*, vol. 14, no. March, pp. 19–30, 2019.

[138] A. Karlas, M. Kallmayer, N. A. Fasoula, E. Liapis, M. Bariotakis, M. Krönke, M. Anastasopoulou, J. Reber, H. H. Eckstein, and V. Ntziachristos, "Multispectral optoacoustic tomography of muscle perfusion and oxygenation under arterial and venous occlusion: A human pilot study," *Journal of Biophotonics*, vol. 13, no. 6, pp. 1–9, 2020.

[139] W. Roll, N. A. Markwardt, M. Masthoff, A. Helfen, J. Claussen, M. Eisenblätter, A. Hasenbach, S. Hermann, A. Karlas, M. Wildgruber, V. Ntziachristos, and M. Schäfers, "Multispectral Optoacoustic Tomography of Benign and Malignant Thyroid Disorders: A Pilot Study," *Journal of nuclear medicine : official publication, Society of Nuclear Medicine*, vol. 60, pp. 1461–1466, oct 2019.

[140] M. Masthoff, A. Helfen, J. Claussen, W. Roll, A. Karlas, H. Becker, G. Gabriëls, J. Riess, W. Heindel, M. Schäfers, V. Ntziachristos, M. Eisenblätter, U. Gerth, and M. Wildgruber, "Multispectral optoacoustic tomography of systemic sclerosis," *Journal of Biophotonics*, vol. 11, no. 11, pp. 1–7, 2018.

[141] M. Seeger, D. Soliman, J. Aguirre, G. Diot, J. Wierzbowski, and V. Ntziachristos, "Pushing the boundaries of optoacoustic microscopy by total impulse response characterization," *Nature Communications*, vol. 11, no. 1, p. 2910, 2020.

[142] L. V. Wang and S. Hu, "Photoacoustic tomography: In vivo imaging from organelles to organs," *Science*, vol. 335, no. 6075, pp. 1458–1462, 2012.

[143] E. M. Strohm, E. S. L. Berndl, and M. C. Kolios, "Probing red blood cell morphology using high-frequency photoacoustics," *Biophysical journal*, vol. 105, pp. 59–67, jul 2013.

[144] D. Soliman, G. J. Tserevelakis, M. Omar, and V. Ntziachristos, "Combining microscopy with mesoscopy using optical and optoacoustic label-free modes," *Scientific Reports*, vol. 5, no. 1, p. 12902, 2015.

[145] E. M. Strohm, M. J. Moore, and M. C. Kolios, "Single cell photoacoustic microscopy: A review," *IEEE Journal of Selected Topics in Quantum Electronics*, vol. 22, no. 3, pp. 137–151, 2016.

[146] E. M. Strohm, E. S. Berndl, and M. C. Kolios, "High frequency label-free photoacoustic microscopy of single cells," *Photoacoustics*, vol. 1, no. 3, pp. 49 – 53, 2013.

[147] E. I. Galanzha, E. V. Shashkov, P. M. Spring, J. Y. Suen, and V. P. Zharov, "In vivo, noninvasive, label-free detection and eradication of circulating metastatic melanoma cells using two-color photoacoustic flow cytometry with a diode laser," *Cancer Research*, vol. 69, no. 20, pp. 7926–7934, 2009.

[148] G. He, D. Xu, H. Qin, S. Yang, and D. Xing, "In vivo cell characteristic extraction and identification by photoacoustic flow cytography," *Biomed. Opt. Express*, vol. 6, pp. 3748–3756, Oct 2015.

[149] E. I. Galanzha, Y. A. Menyaev, A. C. Yadem, M. Sarimollaoglu, M. A. Juratli, D. A. Nedosekin, S. R. Foster, A. Jamshidi-Parsian, E. R. Siegel, I. Makhoul, L. F. Hutchins, J. Y. Suen, and V. P. Zharov, "In vivo liquid biopsy using cytophone platform for photoacoustic detection of circulating tumor cells in patients with melanoma," *Science Translational Medicine*, vol. 11, no. 496, 2019.

[150] L. Wang, K. Maslov, and L. V. Wang, "Single-cell label-free photoacoustic flowoxigraphy in vivo," *Proceedings of the National Academy of Sciences*, vol. 110, no. 15, pp. 5759–5764, 2013.

[151] M. Schwarz, M. Omar, A. Buehler, J. Aguirre, and V. Ntziachristos, "Implications of ultrasound frequency in optoacoustic mesoscopy of the skin," *IEEE Transactions on Medical Imaging*, vol. 34, no. 2, pp. 672–677, 2015.

[152] M. Schwarz, D. Soliman, M. Omar, A. Buehler, S. V. Ovsepian, J. Aguirre, and V. Ntziachristos, "Optoacoustic Dermoscopy of the Human Skin: Tuning Excitation Energy for Optimal Detection Bandwidth with Fast and Deep Imaging in vivo," *IEEE Transactions on Medical Imaging*, vol. 36, no. 6, pp. 1287–1296, 2017.

[153] M. Omar, J. Aguirre, and V. Ntziachristos, "Optoacoustic mesoscopy for biomedicine," *Nature Biomedical Engineering*, vol. 3, no. 5, pp. 354–370, 2019.

[154] M. Schwarz, N. Garzorz-Stark, K. Eyerich, J. Aguirre, and V. Ntziachristos, "Motion correction in optoacoustic mesoscopy," *Scientific Reports*, vol. 7, no. 1, pp. 1–9, 2017.

[155] J. Aguirre, A. Berezhnoi, H. He, M. Schwarz, B. Hindelang, M. Omar, and V. Ntziachristos, "Motion quantification and automated correction in clinical RSOM," *IEEE Transactions on Medical Imaging*, vol. 38, no. 6, pp. 1340–1346, 2019.

[156] B. Hindelang, J. Aguirre, M. Schwarz, A. Berezhnoi, K. Eyerich, V. Ntziachristos, T. Biedermann, and U. Darsow, "Non-invasive imaging in dermatology and the unique potential of raster-scan optoacoustic mesoscopy," *Journal of the European Academy of Dermatology and Venereology*, vol. 33, no. 6, pp. 1051–1061, 2019.

[157] M. Schwarz, A. Buehler, J. Aguirre, and V. Ntziachristos, "Three-dimensional multispectral optoacoustic mesoscopy reveals melanin and blood oxygenation in human skin in vivo," *Journal of Biophotonics*, vol. 9, no. 1-2, pp. 55–60, 2016.

[158] S. Moustakidis, M. Omar, J. Aguirre, P. Mohajerani, and V. Ntziachristos, "Fully automated identification of skin morphology in raster-scan optoacoustic mesoscopy using artificial intelligence," *Medical Physics*, vol. 46, no. 9, pp. 4046–4056, 2019.

[159] J. Staley, P. Grogan, A. K. Samadi, H. Cui, M. S. Cohen, and X. Yang, "Growth of melanoma brain tumors monitored by photoacoustic microscopy," *Journal of Biomedical Optics*, vol. 15, no. 4, pp. 1 – 3, 2010.

[160] J. Aguirre, M. Schwarz, N. Garzorz, M. Omar, A. Buehler, K. Eyerich, and V. Ntziachristos, "Precision assessment of label-free psoriasis biomarkers with ultra-broadband optoacoustic mesoscopy," *Nature Biomedical Engineering*, vol. 1, no. 5, pp. 1–8, 2017.

[161] B. Hindelang, J. Aguirre, A. Berezhnoi, H. He, K. Eyerich, V. Ntziachristos, T. Biedermann, and U. Darsow, "Optoacoustic mesoscopy shows potential to increase accuracy of allergy patch testing," *Contact Dermatitis*, vol. 83, no. 3, pp. 206–214, 2020.

[162] A. Berezhnoi, M. Schwarz, A. Buehler, S. V. Ovsepian, J. Aguirre, and V. Ntziachristos, "Assessing hyperthermia-induced vasodilation in human skin in vivo using optoacoustic mesoscopy," *Journal of Biophotonics*, vol. 11, no. 11, pp. 1–8, 2018.

[163] B. Hindelang, J. Aguirre, A. Berezhnoi, T. Biedermann, U. Darsow, B. Eberlein, and V. Ntziachristos, "Quantification of skin sensitivity to ultraviolet radiation using ultra-wideband optoacoustic mesoscopy," *British Journal of Dermatology*, 2020.

[164] B. Hitz, J. Ewing, and J. Hecht, *Laser Light*, ch. 5, pp. 55–62. John Wiley and Sons, Ltd, 2012.

[165] K. F. Renk, *Gas Lasers*, pp. 271–289. Cham: Springer International Publishing, 2017.

[166] B. Hitz, J. Ewing, and J. Hecht, *Gas Lasers: Helium-Neon and Ion*, ch. 17, pp. 225–238. John Wiley and Sons, Ltd, 2012.

[167] K. F. Renk, *Laser Principle*, pp. 17–42. Cham: Springer International Publishing, 2017.

[168] B. Hitz, J. Ewing, and J. Hecht, *Atoms, Molecules, and Energy Levels*, ch. 6, pp. 63–72. John Wiley and Sons, Ltd, 2012.

[169] K. F. Renk, *Basis of the Theory of the Laser: The Einstein Coefficients*, pp. 85–96. Cham: Springer International Publishing, 2017.

[170] B. Hitz, J. Ewing, and J. Hecht, *Energy Distributions and Laser Action*, ch. 7, pp. 73–86. John Wiley and Sons, Ltd, 2012.

[171] K. F. Renk, *A Laser Theory*, pp. 119–136. Cham: Springer International Publishing, 2017.

[172] K. F. Renk, *The Active Medium: Energy Levels and Lineshape Functions*, pp. 57–76. Cham: Springer International Publishing, 2017.

[173] B. Hitz, J. Ewing, and J. Hecht, *Laser Resonators*, ch. 8, pp. 87–97. John Wiley and Sons, Ltd, 2012.

[174] B. Hitz, J. Ewing, and J. Hecht, *Resonator Modes*, ch. 9, pp. 99–112. John Wiley and Sons, Ltd, 2012.

[175] K. F. Renk, *Cavity Resonator*, pp. 181–193. Cham: Springer International Publishing, 2017.

[176] B. Hitz, J. Ewing, and J. Hecht, *Reducing Laser Bandwidth*, ch. 10, pp. 113–127. John Wiley and Sons, Ltd, 2012.

[177] B. Hitz, J. Ewing, and J. Hecht, *Q-Switching*, ch. 11, pp. 129–142. John Wiley and Sons, Ltd, 2012.

[178] K. F. Renk, *Different Ways of Operating a Laser*, pp. 235–244. Cham: Springer International Publishing, 2017.

[179] B. Hitz, J. Ewing, and J. Hecht, *Cavity Dumping and Modelocking*, ch. 12, pp. 143–153. John Wiley and Sons, Ltd, 2012.

[180] K. F. Renk, *Femtosecond Laser*, pp. 245–267. Cham: Springer International Publishing, 2017.

[181] J. W. Evans, "The birefringent filter," *J. Opt. Soc. Am.*, vol. 39, pp. 229–242, Mar 1949.

[182] B. Hitz, J. Ewing, and J. Hecht, *Nonlinear Optics*, ch. 13, pp. 155–173. John Wiley and Sons, Ltd, 2012.

[183] K. F. Renk, *Nonlinear Optics*, pp. 635–644. Cham: Springer International Publishing, 2017.

[184] B. Hitz, J. Ewing, and J. Hecht, *Tunable and Ultrafast Lasers*, ch. 20, pp. 263–281. John Wiley and Sons, Ltd, 2012.

[185] A. Fatima, K. Kratkiewicz, R. Manwar, M. Zafar, R. Zhang, B. Huang, N. Dadashzadeh, J. Xia, and K. M. Avanaki, "Review of cost reduction methods in photoacoustic computed tomography," *Photoacoustics*, vol. 15, p. 100137, 2019.

[186] B. Hitz, J. Ewing, and J. Hecht, *Solid-State Lasers*, ch. 15, pp. 191–213. John Wiley and Sons, Ltd, 2012.

[187] K. F. Renk, *Solid State Lasers*, pp. 291–308. Cham: Springer International Publishing, 2017.

[188] K. F. Renk, *Some Other Lasers and Laser Amplifiers*, pp. 309–316. Cham: Springer International Publishing, 2017.

[189] K. F. Renk, *An Introduction to Semiconductor Lasers*, pp. 415–426. Cham: Springer International Publishing, 2017.

[190] A. Müller, S. Marschall, O. B. Jensen, J. Fricke, H. Wenzel, B. Sumpf, and P. E. Andersen, "Diode laser based light sources for biomedical applications," *Laser & Photonics Reviews*, vol. 7, no. 5, pp. 605–627, 2013.

[191] B. Hitz, J. Ewing, and J. Hecht, *Semiconductor Lasers*, ch. 14, pp. 175–190. John Wiley and Sons, Ltd, 2012.

[192] P. Unger, *Introduction to Power Diode Lasers*, pp. 1–54. Berlin, Heidelberg: Springer Berlin Heidelberg, 2000.

[193] H. Sun, *Laser Diode Basics*, pp. 1–26. Dordrecht: Springer Netherlands, 2015.

[194] H. Sun, *Laser Diode Beam Basics*, pp. 27–51. Dordrecht: Springer Netherlands, 2015.

[195] H. Sun, *Laser Diode Beam Manipulations*, pp. 53–104. Dordrecht: Springer Netherlands, 2015.

[196] P. Rainbow, "High-power pulsed laser diodes take on new industrial and commercial applications," *Photonics Spectra*, vol. 38, no. 10, pp. 105–108, 2004.

[197] LaserComponents, "High power pulsed laser diodes 1550-series." `https://www.lasercomponents.com/fileadmin/user_upload/home/Datasheets/lc-pld/highpower_905d3j08.pdf`, 2015. Accessed: 2021-01-14.

[198] H. Zhong, T. Duan, H. Lan, M. Zhou, and F. Gao, "Review of low-cost photoacoustic sensing and imaging based on laser diode and light-emitting diode," *Sensors (Switzerland)*, vol. 18, no. 7, pp. 20–22, 2018.

[199] Q. Yao, Y. Ding, G. Liu, and L. Zeng, "Low-cost photoacoustic imaging systems based on laser diode and light-emitting diode excitation," *Journal of Innovative Optical Health Sciences*, vol. 10, no. 4, pp. 1–13, 2017.

[200] L. R. Prade, *Optoacoustic mesoscopy in the frequency domain using laser diodes*. PhD thesis, School of Electrical and Computer Engineering, Technical University of Munich, 2018.

[201] A. Stylogiannis, L. Prade, A. Buehler, J. Aguirre, G. Sergiadis, and V. Ntziachristos, "Continuous wave laser diodes enable fast optoacoustic imaging," *Photoacoustics*, vol. 9, pp. 31 – 38, 2018.

[202] M. Erfanzadeh and Q. Zhu, "Photoacoustic imaging with low-cost sources; a review," *Photoacoustics*, vol. 14, pp. 1 – 11, 2019.

[203] Q. Yao, Y. Ding, G. Liu, and L. Zeng, "Low-cost photoacoustic imaging systems based on laser diode and light-emitting diode excitation," *Journal of Innovative Optical Health Sciences*, vol. 10, no. 04, p. 1730003, 2017.

[204] H. Zhong, T. Duan, H. Lan, M. Zhou, and F. Gao, "Review of Low-Cost Photoacoustic Sensing and Imaging Based on Laser Diode and Light-Emitting Diode," *Sensors*, vol. 18, p. 2264, jul 2018.

[205] T. J. Allen and P. C. Beard, "High power visible light emitting diodes as pulsed excitation sources for biomedical photoacoustics," *Biomed. Opt. Express*, vol. 7, pp. 1260–1270, Apr 2016.

[206] Y. Zhu, G. Xu, J. Yuan, J. Jo, G. Gandikota, H. Demirci, T. Agano, N. Sato, Y. Shigeta, and X. Wang, "Light Emitting Diodes based Photoacoustic Imaging and Potential Clinical Applications," *Scientific Reports*, vol. 8, no. 1, p. 9885, 2018.

[207] T. J. Allen and P. C. Beard, "Pulsed near-infrared laser diode excitation system for biomedical photoacoustic imaging," *Opt. Lett.*, vol. 31, pp. 3462–3464, Dec 2006.

[208] K. Daoudi, P. van den Berg, O. Rabot, A. Kohl, S. Tisserand, P. Brands, and W. Steenbergen, "Handheld probe integrating laser diode and ultrasound transducer array for ultrasound/photoacoustic dual modality imaging," *Opt. Express*, vol. 22, pp. 26365–26374, Oct 2014.

[209] P. K. Upputuri and M. Pramanik, "Performance characterization of low-cost, high-speed, portable pulsed laser diode photoacoustic tomography (pld-pat) system," *Biomed. Opt. Express*, vol. 6, pp. 4118–4129, Oct 2015.

[210] L. Zeng, G. Liu, D. Yang, and X. Ji, "Portable optical-resolution photoacoustic microscopy with a pulsed laser diode excitation," *Applied Physics Letters*, vol. 102, no. 5, p. 053704, 2013.

[211] T. Wang, S. Nandy, H. S. Salehi, P. D. Kumavor, and Q. Zhu, "A low-cost photoacoustic microscopy system with a laser diode excitation," *Biomed. Opt. Express*, vol. 5, pp. 3053–3058, Sep 2014.

[212] L. Zeng, G. Liu, D. Yang, and X. Ji, "3d-visual laser-diode-based photoacoustic imaging," *Opt. Express*, vol. 20, pp. 1237–1246, Jan 2012.

[213] A. Hariri, A. Fatima, N. Mohammadian, S. Mahmoodkalayeh, M. A. Ansari, N. Bely, and M. R. N. Avanaki, "Development of low-cost photoacoustic imaging systems using very low-energy pulsed laser diodes," *Journal of Biomedical Optics*, vol. 22, no. 7, pp. 1 – 8, 2017.

[214] L. Zeng, Z. Piao, S. Huang, W. Jia, and Z. Chen, "Label-free optical-resolution photoacoustic microscopy of superficial microvasculature using a compact visible laser diode excitation," *Optics Express*, vol. 23, no. 24, pp. 31026–31033, 2015.

[215] M.-L. Li and P.-H. Wang, "Optical resolution photoacoustic microscopy using a Blu-ray DVD pickup head," in *Photons Plus Ultrasound: Imaging and Sensing 2014* (A. A. Oraevsky and L. V. Wang, eds.), vol. 8943, pp. 178 – 183, International Society for Optics and Photonics, SPIE, 2014.

[216] K. I. Maslov and L. V. Wang, "Photoacoustic imaging of biological tissue with intensity-modulated continuous-wave laser," *Journal of Biomedical Optics*, vol. 13, no. 2, pp. 1 – 5, 2008.

[217] A. Kilpelä and J. Kostamovaara, "Laser pulser for a time-of-flight laser radar," *Review of Scientific Instruments*, vol. 68, no. 6, pp. 2253–2258, 1997.

[218] M. Omar, D. Soliman, J. Gateau, and V. Ntziachristos, "Ultrawideband reflection-mode optoacoustic mesoscopy," *Opt. Lett.*, vol. 39, pp. 3911–3914, Jul 2014.

[219] H. He, S. Mandal, A. Buehler, X. L. Dean-Ben, D. Razansky, and V. Ntziachristos, "Improving optoacoustic image quality via geometric pixel super-resolution approach," *IEEE Transactions on Medical Imaging*, vol. 35, pp. 812–818, 2016.

[220] F. C. Delori, R. H. Webb, and D. H. Sliney, "Maximum permissible exposures for ocular safety (ANSI 2000), with emphasis on ophthalmic devices," *Journal of the Optical Society of America A*, vol. 24, no. 5, p. 1250, 2007.

[221] M. Ziegler, M. Hempel, H. E. Larsen, J. W. Tomm, P. E. Andersen, S. Clausen, S. N. Elliott, and T. Elsaesser, "Physical limits of semiconductor laser operation: A time-resolved analysis of catastrophic optical damage," *Applied Physics Letters*, vol. 97, no. 2, p. 021110, 2010.

[222] M. B. Sanayeh, P. Brick, W. Schmid, B. Mayer, M. Müller, M. Reufer, K. Streubel, M. Ziegler, J. W. Tomm, and G. Bacher, "The physics of catastrophic optical damage in high-power AlGaInP laser diodes," in *Semiconductor Lasers and Laser Dynamics III* (K. P. Panajotov, M. Sciamanna, A. A. Valle, and R. Michalzik, eds.), vol. 6997, pp. 26 – 37, International Society for Optics and Photonics, SPIE, 2008.

[223] M. Bou Sanayeh, *Catastrophic Optical Damage in High-Power AlGaInP Diode Lasers*. PhD thesis, Faculty of Engineering, Univesrity of Duisburg - Essen, Aug 2008.

[224] J. Xia, J. Yao, and L. V. Wang, "Photoacoustic tomography: principles and advances," *Electromagnetic waves (Cambridge, Mass.)*, vol. 147, pp. 1–22, 2014.

[225] E. W. Stein, K. Maslov, and L. V. Wang, "Noninvasive, in vivo imaging of the mouse brain using photoacoustic microscopy," *Journal of Applied Physics*, vol. 105, no. 10, p. 102027, 2009.

[226] A. Stylogiannis, L. Prade, S. Glasl, Q. Mustafa, C. Zakian, and V. Ntziachristos, "Frequency wavelength multiplexed optoacoustic tomography," *Nature Communications*, vol. 13, no. 1, p. 4448, 2022.

[227] W. Zijlstra and A. Buursma, "Spectrophotometry of hemoglobin: Absorption spectra of bovine oxyhemoglobin, deoxyhemoglobin, carboxyhemoglobin, and methemoglobin," *Comparative Biochemistry and Physiology Part B: Biochemistry and Molecular Biology*, vol. 118, no. 4, pp. 743 – 749, 1997.

[228] M. Z. bin Hussein, A. H. Yahaya, and L. M. Ping, "Dye-interleaved nanocomposite: Evan's blue in the lamella of mg–al-layered double hydroxide," *Dyes and Pigments*, vol. 63, no. 2, pp. 135 – 140, 2004.

[229] J. Hed, C. Dahlgren, and I. Rundquist, "A simple fluorescence technique to stain the plasma membrane of human neutrophils," *Histochemistry*, vol. 79, no. 1, pp. 105–110, 1983.

[230] M. L. Landsman, G. Kwant, G. A. Mook, and W. G. Zijlstra, "Light absorbing properties, stability, and spectral stabilization of indocyanine green," *Journal of Applied Physiology*, vol. 40, no. 4, pp. 575–583, 1976.

[231] S. T. Thurman, "Otf estimation using a siemens star target," in *Imaging and Applied Optics*, p. IMC5, Optical Society of America, 2011.

[232] C. Loebich, D. Wueller, B. Klingen, and A. Jaeger, "Digital camera resolution measurements using sinusoidal Siemens stars," in *Digital Photography III* (R. A. Martin, J. M. DiCarlo, and N. Sampat, eds.), vol. 6502, pp. 214 – 224, International Society for Optics and Photonics, SPIE, 2007.

[233] K. P. Köstli, M. Frenz, H. Bebie, and H. P. Weber, "Temporal backward projection of optoacoustic pressure transients using fourier transform methods," *Physics in Medicine and Biology*, vol. 46, pp. 1863–1872, jun 2001.

[234] M. Omar, J. Rebling, K. Wicker, T. Schmitt-Manderbach, M. Schwarz, J. Gateau, H. López-Schier, T. Mappes, and V. Ntziachristos, "Optical imaging of post-embryonic zebrafish using multi orientation raster scan optoacoustic mesoscopy," *Light: Science & Applications*, vol. 6, no. 1, pp. e16186–e16186, 2017.

[235] K. B. Chowdhury, M. Bader, C. Dehner, D. Jüstel, and V. Ntziachristos, "Individual transducer impulse response characterization method to improve image quality of array-based handheld optoacoustic tomography," *Opt. Lett.*, vol. 46, pp. 1–4, Jan 2021.

[236] A. F. Frangi, W. J. Niessen, K. L. Vincken, and M. A. Viergever, "Multiscale vessel enhancement filtering," in *Medical Image Computing and Computer-Assisted Intervention — MICCAI'98* (W. M. Wells, A. Colchester, and S. Delp, eds.), (Berlin, Heidelberg), pp. 130–137, Springer Berlin Heidelberg, 1998.

[237] A. Longo, S. Morscher, J. M. Najafababdi, D. Jüstel, C. Zakian, and V. Ntziachristos, "Assessment of hessian-based frangi vesselness filter in optoacoustic imaging," *Photoacoustics*, vol. 20, p. 100200, 2020.

[238] S. Kellnberger, N. C. Deliolanis, D. Queirós, G. Sergiadis, and V. Ntziachristos, "In vivo frequency domain optoacoustic tomography," *Optics Letters*, vol. 37, no. 16, pp. 3423–3425, 2012.

[239] P. Mohajerani, S. Kellnberger, and V. Ntziachristos, "Frequency domain optoacoustic tomography using amplitude and phase," *Photoacoustics*, vol. 2, no. 3, pp. 111–118, 2014.

[240] S. Telenkov, A. Mandelis, B. Lashkari, and M. Forcht, "Frequency-domain photothermoacoustics: Alternative imaging modality of biological tissues," *Journal of Applied Physics*, vol. 105, no. 10, 2009.

[241] A. Mandelis and X. Guo, "Wavelength-modulated differential photothermal radiometry: Theory and experimental applications to glucose detection in water," *Physical Review E - Statistical, Nonlinear, and Soft Matter Physics*, vol. 84, no. 4, pp. 1–14, 2011.

[242] B. Lashkari, S. S. Sean Choi, M. E. Khosroshahi, E. Dovlo, and A. Mandelis, "Simultaneous dual-wavelength photoacoustic radar imaging using waveform engineering with mismatched frequency modulated excitation," *Optics Letters*, vol. 40, no. 7, p. 1145, 2015.

[243] S. Kellnberger, D. Soliman, G. J. Tserevelakis, M. Seeger, H. Yang, A. Karlas, L. Prade, M. Omar, and V. Ntziachristos, "Optoacoustic microscopy at multiple discrete frequencies," *Light: Science and Applications*, vol. 7, no. 1, 2018.

[244] Z. Molnar and M. Nemeth, "Monitoring of tissue oxygenation: An everyday clinical challenge," *Frontiers in Medicine*, vol. 4, no. JAN, pp. 1–6, 2017.

[245] M. Seeger, D. Soliman, J. Aguirre, G. Diot, J. Wierzbowski, and V. Ntziachristos, "Pushing the boundaries of optoacoustic microscopy by total impulse response characterization," *Nature Communications*, vol. 11, no. 1, p. 2910, 2020.

[246] X. L. Deán-Ben and D. Razansky, "On the link between the speckle free nature of optoacoustics and visibility of structures in limited-view tomography," *Photoacoustics*, vol. 4, no. 4, pp. 133 – 140, 2016.

[247] M. P. Mienkina, C.-S. Friedrich, N. C. Gerhardt, M. F. Beckmann, M. F. Schiffner, M. R. Hofmann, and G. Schmitz, "Multispectral photoacoustic coded excitation imaging using unipolar orthogonal golay codes," *Opt. Express*, vol. 18, pp. 9076–9087, Apr 2010.

[248] A. Stylogiannis, L. Riobo, L. Prade, S. Glasl, sabine Klein, G. Lucidi, M. Fuchs, D. Saur, and V. Ntziachristos, "A low-cost single-point optoacoustic sensor for spectroscopic measurement of local vascular oxygenation," *Optics Letters*, vol. 45, no. 24, pp. 6579–6582, 2020.

[249] I. Yoshiya, Y. Shimada, and K. Tanaka, "Spectrophotometric monitoring of arterial oxygen saturation in the fingertip," *Medical & Biological Engineering & Computing*, vol. 18, no. 1, pp. 27–32, 1980.

[250] A. C. RALSTON, R. K. WEBB, and W. B. RUNCIMAN, "Potential errors in pulse oximetry: I. Pulse oximeter evaluation," *Anaesthesia*, vol. 46, no. 3, pp. 202–206, 1991.

[251] H. Lee, H. Ko, and J. Lee, "Reflectance pulse oximetry: Practical issues and limitations," *ICT Express*, vol. 2, no. 4, pp. 195–198, 2016.

[252] V. De Santis and M. Singer, "Tissue oxygen tension monitoring of organ perfusion: Rationale, methodologies, and literature review," *British Journal of Anaesthesia*, vol. 115, no. 3, pp. 357–365, 2015.

[253] A. Carreau, B. E. Hafny-Rahbi, A. Matejuk, C. Grillon, and C. Kieda, "Why is the partial oxygen pressure of human tissues a crucial parameter? Small molecules and hypoxia," *Journal of Cellular and Molecular Medicine*, vol. 15, no. 6, pp. 1239–1253, 2011.

[254] G. L. Semenza, "Oxygen Sensing, Hypoxia-Inducible Factors, and Disease Pathophysiology," *Annual Review of Pathology: Mechanisms of Disease*, vol. 9, no. 1, pp. 47–71, 2014.

[255] I. Serganova, J. Humm, C. Ling, and R. Blasberg, "Tumor hypoxia imaging," *Clinical Cancer Research*, vol. 12, no. 18, pp. 5260–5264, 2006.

[256] E. P. Rivers, D. S. Ander, and D. Powell, "Central venous oxygen saturation monitoring in the critically ill patient," *Current Opinion in Critical Care*, vol. 7, no. 3, pp. 204–211, 2001.

[257] T. W. Scheeren, P. Schober, and L. A. Schwarte, "Monitoring tissue oxygenation by near infrared spectroscopy (NIRS): Background and current applications," *Journal of Clinical Monitoring and Computing*, vol. 26, no. 4, pp. 279–287, 2012.

[258] N. Chiang, O. A. Rodda, J. Sleigh, and T. Vasudevan, "Perioperative warming, oxygen, and Ilomedin on oxygenation and healing in infrainguinal bypass surgery," *Journal of Surgical Research*, vol. 220, no. October 2013, pp. 197–205, 2017.

[259] E. GmbH and Co.KG, "Eschweiler combi line 2 blood gas analyzer." `https://www.eschweiler-kiel.de/wp-content/uploads/2019/02/combiline2_en_110219-web-1.pdf`. Accessed: 2020-01-14.

[260] J. R. Griffiths and S. P. Robinson, "The OxyLite: A fibre-optic oxygen sensor," *British Journal of Radiology*, vol. 72, no. JUL., pp. 627–630, 1999.

[261] O. O. Ltd., "Oxylite pro." https://www.oxford-optronix.com/uploads/wysiwyg_editor/files/OxyLite%20flyer%202017a.pdf. Accessed: 2021-01-14.

[262] O. O. Ltd., "Oxylite pro." https://www.google.com/url?sa=t&rct=j&q=&esrc=s&source=web&cd=&ved=2ahUKEwiMk9n7zpvuAhUyy4UKHfMRCbwQFjABegQIBBAC&url=http%3A%2F%2Fwww.bio-d.co.kr%2Fkor%2Fprd%2Fprd_down.php%3Fidx%3D203%26check%3Dpdf&usg=AOvVaw2iE0zHnpx0qJd-qtvw21Rj. Accessed: 2021-01-14.

[263] A. Pellicer and M. d. C. Bravo, "Near-infrared spectroscopy: A methodology-focused review," *Seminars in Fetal and Neonatal Medicine*, vol. 16, no. 1, pp. 42–49, 2011.

[264] E. D. Chan, M. M. Chan, and M. M. Chan, "Pulse oximetry: Understanding its basic principles facilitates appreciation of its limitations," *Respiratory Medicine*, vol. 107, no. 6, pp. 789–799, 2013.

[265] M. Ferrari, L. Mottola, and V. Quaresima, "Principles, techniques, and limitations of near infrared spectroscopy," *Canadian Journal of Applied Physiology*, vol. 29, no. 4, pp. 463–487, 2004.

[266] M. G. Lopez, P. Pandharipande, J. Morse, M. S. Shotwell, G. L. Milne, M. Pretorius, A. D. Shaw, L. J. Roberts, and F. T. Billings, "Intraoperative cerebral oxygenation, oxidative injury, and delirium following cardiac surgery," *Free Radical Biology and Medicine*, vol. 103, no. December 2016, pp. 192–198, 2017.

[267] S. Ogoh, K. Sato, K. Okazaki, T. Miyamoto, F. Secher, H. Sørensen, P. Rasmussen, and N. H. Secher, "A decrease in spatially resolved near-infrared spectroscopy-determined frontal lobe tissue oxygenation by phenylephrine reflects reduced skin blood flow," *Anesthesia and Analgesia*, vol. 118, no. 4, pp. 823–829, 2014.

[268] M. Khan, C. G. Pretty, A. C. Amies, R. Elliott, Y. S. Chiew, G. M. Shaw, and J. G. Chase, "Analysing the effects of cold, normal, and warm digits on transmittance pulse oximetry," *Biomedical Signal Processing and Control*, vol. 26, pp. 34–41, 2016.

[269] B. Ning, M. J. Kennedy, A. J. Dixon, N. Sun, R. Cao, B. T. Soetikno, R. Chen, Q. Zhou, K. Kirk Shung, J. A. Hossack, and S. Hu, "Simultaneous photoacoustic microscopy of microvascular anatomy, oxygen saturation, and blood flow," *Optics Letters*, vol. 40, no. 6, p. 910, 2015.

[270] K. Sei, M. Fujita, T. Hirasawa, S. Okawa, T. Kushibiki, H. Sasa, K. Furuya, and M. Ishihara, "Measurement of blood-oxygen saturation using a photoacoustic technique in the rabbit hypoxemia model," *Journal of Clinical Monitoring and Computing*, vol. 33, no. 2, pp. 269–279, 2019.

[271] M. Gehrung, S. E. Bohndiek, and J. Brunker, "Development of a blood oxygenation phantom for photoacoustic tomography combined with online pO2 detection and flow spectrometry," *Journal of Biomedical Optics*, vol. 24, no. 12, p. 1, 2019.

[272] M. W. Schellenberg and H. K. Hunt, "Hand-held optoacoustic imaging: A review," *Photoacoustics*, vol. 11, no. June, pp. 14–27, 2018.

[273] A. Hariri, J. Lemaster, J. Wang, A. K. S. Jeevarathinam, D. L. Chao, and J. V. Jokerst, "The characterization of an economic and portable LED-based photoacoustic imaging system to facilitate molecular imaging," *Photoacoustics*, vol. 9, pp. 10–20, 2018.

[274] S. Liu, K. Tang, H. Jin, R. Zhang, T. T. H. Kim, and Y. Zheng, "Continuous wave laser excitation based portable optoacoustic imaging system for melanoma detection," *BioCAS 2019 - Biomedical Circuits and Systems Conference, Proceedings*, pp. 0–3, 2019.

[275] M. Erfanzadeh, P. D. Kumavor, and Q. Zhu, "Laser scanning laser diode photoacoustic microscopy system," *Photoacoustics*, vol. 9, pp. 1–9, 2018.

[276] G. Spanner and R. Niessner, "Noninvasive determination of blood constituents using an array of modulated laser diodes and a photoacoustic sensor head," *Fresenius' Journal of Analytical Chemistry*, vol. 355, no. 3-4, pp. 327–328, 1996.

[277] A. Ray, J. R. Rajian, Y.-E. K. Lee, X. Wang, and R. Kopelman, "Lifetime-based photoacoustic oxygen sensing in vivo," *Journal of Biomedical Optics*, vol. 17, no. 5, p. 057004, 2012.

[278] J. P. Besson, S. Schilt, and L. Thévenaz, "Multi-gas sensing based on photoacoustic spectroscopy using tunable laser diodes," *Spectrochimica Acta - Part A: Molecular and Biomolecular Spectroscopy*, vol. 60, no. 14, pp. 3449–3456, 2004.

[279] P. Breitegger, B. Schweighofer, H. Wegleiter, M. Knoll, B. Lang, and A. Bergmann, "Towards low-cost QEPAS sensors for nitrogen dioxide detection," *Photoacoustics*, vol. 18, no. January, p. 100169, 2020.

[280] M. Wolff, H. G. Groninga, and H. Harde, "Photoacoustic sensor for medical diagnostics," *Smart Medical and Biomedical Sensor Technology*, vol. 5261, no. May, p. 50, 2004.

[281] G. R. Kelman, "Digital computer subroutine for the conversion of oxygen tension into saturation.," *Journal of applied physiology*, vol. 21, no. 4, pp. 1375–1376, 1966.

[282] V. Perekatova, P. Subochev, M. Kleshnin, and I. Turchin, "Optimal wavelengths for optoacoustic measurements of blood oxygen saturation in biological tissues," *Biomedical Optics Express*, vol. 7, no. 10, p. 3979, 2016.

[283] G. Wissmeyer, D. Soliman, R. Shnaiderman, A. Rosenthal, and V. Ntziachristos, "All-optical optoacoustic microscope based on wideband pulse interferometry," *Opt. Lett.*, vol. 41, pp. 1953–1956, May 2016.

[284] R. Shnaiderman, G. Wissmeyer, O. Ülgen, Q. Mustafa, A. Chmyrov, and V. Ntziachristos, "A submicrometre silicon-on-insulator resonator for ultrasound detection," *Nature*, vol. 585, no. 7825, pp. 372–378, 2020.

[285] G. Wissmeyer, M. A. Pleitez, A. Rosenthal, and V. Ntziachristos, "Looking at sound: optoacoustics with all-optical ultrasound detection," *Light: Science & Applications*, vol. 7, no. 1, p. 53, 2018.

[286] J. Y. Sim, C. G. Ahn, E. J. Jeong, and B. K. Kim, "In vivo Microscopic Photoacoustic Spectroscopy for Non-Invasive Glucose Monitoring Invulnerable to Skin Secretion Products," *Scientific Reports*, vol. 8, no. 1, pp. 1–11, 2018.

[287] Y. Ma, "Review of recent advances in qepas-based trace gas sensing," *Applied Sciences (Switzerland)*, vol. 8, no. 10, 2018.

[288] P. Patimisco, G. Scamarcio, F. K. Tittel, and V. Spagnolo, "Quartz-enhanced photoacoustic spectroscopy: A review," *Sensors (Switzerland)*, vol. 14, no. 4, pp. 6165–6206, 2014.

[289] A. Stylogiannis, N. Kousias, A. Kontses, L. Ntziachristos, and V. Ntziachristos, "A low-cost optoacoustic sensor for environmental monitoring," *Sensors*, vol. 21, no. 4, 2021.

[290] V. Ntziachristos, L. Ntziachristos, A. Stylogiannis, N. Kousias, and A. Kontses, "An apparatus with a high sensitivity optical absorption sensor and a method of use thereof for environmental applications." Patent GR20200100657, Filed: October 2020.

[291] T. C. Bond, S. J. Doherty, D. W. Fahey, P. M. Forster, T. Berntsen, B. J. DeAngelo, M. G. Flanner, S. Ghan, B. Kärcher, D. Koch, S. Kinne, Y. Kondo, P. K. Quinn, M. C. Sarofim, M. G. Schultz, M. Schulz, C. Venkataraman, H. Zhang, S. Zhang, N. Bellouin, S. K. Guttikunda, P. K. Hopke, M. Z. Jacobson, J. W. Kaiser, Z. Klimont, U. Lohmann, J. P. Schwarz, D. Shindell, T. Storelvmo, S. G. Warren, and C. S. Zender, "Bounding the role of black carbon in the climate system: A scientific assessment," *J. Geophys. Res. Atmos.*, vol. 118, no. 11, pp. 5380–5552, 2013.

[292] Masson-Delmotte, V. Zhai, H.-O. Pörtner, D. Roberts, J. Skea, P. Shukla, A. Pirani, W. Moufouma-Okia, C. Péan, R. Pidcock, S. Connors, J. Matthews, Y. Chen, X. Zhou, M. Gomis, E. Lonnoy, T. Maycock, M. Tignor, and T. W. (eds.), "Global warming of 1.5°c. an ipcc special report on the impacts of global warming of 1.5°c above pre-industrial levels and related global greenhouse gas emission pathways, in the context of strengthening the global response to the threat of climate change, sustainable development, and efforts to eradicate poverty," tech. rep., International Panel on Climate Change, 2019.

[293] K. L. Jansen, T. V. Larson, J. Q. Koenig, T. F. Mar, C. Fields, J. Stewart, and M. Lippmann, "Associations between health effects and particulate matter and black carbon in subjects with respiratory disease," *Environmental health perspectives*, vol. 113, pp. 1741–1746, dec 2005.

[294] N. A. Janssen, M. E. Gerlofs-Nijland, T. Lanki, R. O. Salonen, F. Cassee, G. Hoek, P. Fischer, B. Brunekreef, and M. Krzyzanowski, "Health effects of black carbon," tech. rep., World Health Organization, 2012.

[295] A. Lükewille, "Status of black carbon monitoring in ambient air in europe," tech. rep., European Environmental Agency, 2013.

[296] B. Weinhold, "Global bang for the buck: Cutting black carbon and methane benefits both health and climate," *Environmental Health Perspectives*, vol. 120, no. 6, pp. a245–a245, 2012.

[297] H. Rosen and A. D. A. Hansen, "Role of combustion-generated carbon particles in the absorption of solar radiation in the arctic haze," *Geophysical Research Letters*, vol. 11, no. 5, pp. 461–464, 1984.

[298] M. G. Flanner, C. S. Zender, J. T. Randerson, and P. J. Rasch, "Present-day climate forcing and response from black carbon in snow," *Journal of Geophysical Research Atmospheres*, vol. 112, no. 11, pp. 1–17, 2007.

[299] V. Ramanathan and G. Carmichael, "Global and regional climate changes due to black carbon," *Nature Geoscience*, vol. 1, no. 4, pp. 221–227, 2008.

[300] Z. A. Mansurov, "Soot Formation in Combustion Processes (Review)," *Combustion, Explosion and Shock Waves*, vol. 41, no. 6, p. 727, 2005.

[301] I. Glassman, "Soot formation in combustion processes," *Symposium (International) on Combustion*, vol. 22, no. 1, pp. 295 – 311, 1989.

[302] D. A. Lack, J. Thuesen, M. R. Elliot, F. Stuer-Lauridsen, S. B. Overgaard, and D. Kristensen, "Investigation of appropriate control measures (abatement technologies) to reduce black carbon emissions from international shipping," tech. rep., International Maritime Organization, 2015.

[303] O. A. Popoola, D. Carruthers, C. Lad, V. B. Bright, M. I. Mead, M. E. Stettler, J. R. Saffell, and R. L. Jones, "Use of networks of low cost air quality sensors to quantify air quality in urban settings," *Atmospheric Environment*, vol. 194, pp. 58 – 70, 2018.

[304] J. Duyzer, D. van den Hout, P. Zandveld, and S. van Ratingen, "Representativeness of air quality monitoring networks," *Atmospheric Environment*, vol. 104, pp. 88 – 101, 2015.

[305] W. Jiao, G. Hagler, R. Williams, R. Sharpe, R. Brown, D. Garver, R. Judge, M. Caudill, J. Rickard, M. Davis, L. Weinstock, S. Zimmer-Dauphinee, and K. Buckley, "Community air sensor network (cairsense) project: evaluation of low-cost sensor performance in a suburban environment in the southeastern united states," *Atmospheric Measurement Techniques*, vol. 9, no. 11, pp. 5281–5292, 2016.

[306] TSI, "Ultrafine condensation particle counter." `https://www.tsi.com/discontinued-products/ultrafine-condensation-particle-counter-3776/`. Accesed: 2021-01-14.

[307] K. Iida, M. R. Stolzenburg, and P. H. McMurry, "Effect of working fluid on sub-2 nm particle detection with a laminar flow ultrafine condensation particle counter," *Aerosol Science and Technology*, vol. 43, no. 1, pp. 81–96, 2009.

[308] L. Ntziachristos, P. Fragkiadoulakis, Z. Samaras, K. Janka, and J. Tikkanen, "Exhaust particle sensor for obd application," in *SAE Technical Paper*, SAE International, 04 2011.

[309] L. Ntziachristos, S. Amanatidis, Z. Samaras, K. Janka, and J. Tikkanen, "Application of the pegasor particle sensor for the measurement of mass and particle number emissions," *SAE Int. J. Fuels Lubr.*, vol. 6, pp. 521–531, 04 2013.

[310] J. Heintzenberg and R. J. Charlson, "Design and applications of the integrating nephelometer: A review," *Journal of Atmospheric and Oceanic Technology*, vol. 13, no. 5, pp. 987 – 1000, 01 Oct. 1996.

[311] B. Giechaskiel, M. Maricq, L. Ntziachristos, C. Dardiotis, X. Wang, H. Axmann, A. Bergmann, and W. Schindler, "Review of motor vehicle particulate emissions sampling and measurement: From smoke and filter mass to particle number," *Journal of Aerosol Science*, vol. 67, pp. 48–86, 2014.

[312] D. M. Roessler and F. R. Faxvog, "Opacity of black smoke: calculated variation with particle size and refractive index," *Appl. Opt.*, vol. 18, pp. 1399–1403, May 1979.

[313] D. M. Roessler and F. R. Faxvog, "Opacity of black smoke: calculated variation with particle size and refractive index: erratum," *Appl. Opt.*, vol. 18, pp. 2099–2099, Jul 1979.

[314] T. C. Bond, T. L. Anderson, and D. Campbell, "Calibration and intercomparison of filter-based measurements of visible light absorption by aerosols," *Aerosol Science and Technology*, vol. 30, no. 6, pp. 582–600, 1999.

[315] T. C. Bond and R. W. Bergstrom, "Light absorption by carbonaceous particles: An investigative review," *Aerosol Science and Technology*, vol. 40, no. 1, pp. 27–67, 2006.

[316] J. J. Caubel, T. E. Cados, and T. W. Kirchstetter, "A new black carbon sensor for dense air quality monitoring networks," *Sensors (Switzerland)*, vol. 18, no. 3, pp. 1–18, 2018.

[317] R. Hadef, K. P. Geigle, W. Meier, and M. Aigner, "Soot characterization with laser-induced incandescence applied to a laminar premixed ethylene–air flame," *International Journal of Thermal Sciences*, vol. 49, no. 8, pp. 1457 – 1467, 2010.

[318] P. Patimisco, G. Scamarcio, F. K. Tittel, and V. Spagnolo, "Quartz-enhanced photoacoustic spectroscopy: A review," *Sensors (Switzerland)*, vol. 14, no. 4, pp. 6165–6206, 2014.

[319] A. Elia, P. M. Lugarà, C. di Franco, and V. Spagnolo, "Photoacoustic techniques for trace gas sensing based on semiconductor laser sources," *Sensors*, vol. 9, no. 12, pp. 9616–9628, 2009.

[320] AVL, "Mss - avl micro soot sensor." `https://www.avl.com/emission-measurement/-/asset_publisher/gYjUpY19vEA8/content/mssplus-avl-micro-soot-sensor`. Accesed: 2021-01-14.

[321] A. Miklós, P. Hess, and Z. Bozóki, "Application of acoustic resonators in photoacoustic trace gas analysis and metrology," *Review of Scientific Instruments*, vol. 72, no. 4, pp. 1937–1955, 2001.

[322] A. Petzold and R. Niessner, "Photoacoustic soot sensor for in-situ black carbon monitoring," *Applied Physics B*, vol. 63, no. 2, pp. 191–197, 1996.

[323] L. Krauml, Z. Bozoki, and R. Niessner, "Characterisation of a mobile photoacoustic sensor for atmospheric black carbon monitoring," *Analytical Sciences/Supplements*, vol. 17icpp, pp. s563–s566, 2002.

[324] L. Lust, "Photoacoustic sensor with mirror," 2014. U.S. Patent US8848191B2.

[325] V. Spagnolo, A. A. Kosterev, L. Dong, R. Lewicki, and F. K. Tittel, "NO trace gas sensor based on quartz-enhanced photoacoustic spectroscopy and external cavity quantum cascade laser," *Applied Physics B*, vol. 100, no. 1, pp. 125–130, 2010.

[326] V. Spagnolo, P. Patimisco, R. Pennetta, A. Sampaolo, G. Scamarcio, M. S. Vitiello, and F. K. Tittel, "THz Quartz-enhanced photoacoustic sensor for H_2S trace gas detection," *Optics Express*, vol. 23, no. 6, p. 7574, 2015.

[327] L. Dong, A. A. Kosterev, D. Thomazy, and F. K. Tittel, "QEPAS spectrophones: Design, optimization, and performance," *Applied Physics B: Lasers and Optics*, vol. 100, no. 3, pp. 627–635, 2010.

[328] V. Spagnolo, P. Patimisco, S. Borri, G. Scamarcio, B. E. Bernacki, and J. Kriesel, "Mid-infrared fiber-coupled QCL-QEPAS sensor," *Applied Physics B: Lasers and Optics*, vol. 112, no. 1, pp. 25–33, 2013.

[329] R. Shnaiderman, G. Wissmeyer, M. Seeger, D. Soliman, H. Estrada, D. Razansky, A. Rosenthal, and V. Ntziachristos, "Fiber interferometer for hybrid optical and optoacoustic intravital microscopy," *Optica*, vol. 4, pp. 1180–1187, Oct 2017.

[330] C. W. Hinds, *Aerosol Technology: Properties, Behavior, and Measurement of Airborne Particles*. Wiley, 2nd ed., 1999. ISBN:978-0-471-19410-1.

[331] W. Schneider, K. G. Moortgat, S. G. Tyndall, and P. J. Burrows, "Absorption cross-sections of no2 in the uv and visible region (200 – 700 nm) at 298 k," *Journal of Photochemistry and Photobiology A: Chemistry*, vol. 40, no. 2, pp. 195 – 217, 1987.

[332] M. Duquesnoy, G. Aoust, J. M. Melkonian, R. Lévy, M. Raybaut, and A. Godard, "Quartz enhanced photoacoustic spectroscopy based on a custom quartz tuning fork," *Sensors (Switzerland)*, vol. 19, no. 6, pp. 1–10, 2019.

[333] X. Dai, H. Yang, and H. Jiang, "In vivo photoacoustic imaging of vasculature with a low-cost miniature light emitting diode excitation," *Opt. Lett.*, vol. 42, pp. 1456–1459, Apr 2017.

[334] A. Stylogiannis, M. Seeger, L. Prade, S. Glasl, and V. Ntziachristos, "Optoacoustic microscopy with over-driven continuous wave laser diodes." Under preparation.

[335] Picolas GmbH, "Impedance of laser diodes inductive behaviour." `https://picolas.de/de/impedance-of-laser-diodes-inductive-behaviour/`. Accessed: 2021-01-22.

[336] Pico Technology Limited. `https://www.picotech.com/oscilloscope/3000/usb3-oscilloscope-logic-analyzer`. Accessed: 2021-01-22.

Eidesstattliche Erklärung

Ich erkläre an Eides statt, dass Ich die bei der promotionsführenden Einrichtung

Fakultät für Elektrotechnik und Informationstechnik

der TUM zur Promotionsprüfung vorgelegte Arbeit mit der Titel:

Development of Laser Diode Excitation System for Optoacoustic Imaging and Sensing

in Lehrstuhl für Biologische Bildgebung unter der Anleitung und Betreuung durch:

Prof. Dr. Vasilis Ntziachristos

ohne sonstige Hilfe erstellt und bei der Abfassung nur die gemäß § 6 Ab. 6 und 7 Satz 2 angebotenen Hilfsmittel benutzt habe.

- ☒ Ich habe keine Organization eingeschaltet, die gegen Entgelt Betreuerinnen und Betreuer für die Anfertigung von Dissertationen sucht, oder die mir obliegenden Pflichten hinsichtlich der Prüfungsleitungen für mich ganz oder teilweise erledigt.
- ☒ Ich habe die Dissertation in dieser oder ähnlicher Form in keinen anderen Prüfungsverfahren als Prüfungsleistung vorgelegt
- ☐ Die vollständige Dissertation wurde in TUM Bibliothek veröffentlicht.
  Die promotionführende Einrichtung Fakultät für Elektrotechnik und Informationstechnik hat der Veröffentlichung zugestimmt.
- ☒ Ich habe den angestrebten Doktorgrad noch nicht erworben und bin nicht in einem früheren Promotionsverfahren für den angestrebten Doktorgrad andgültig gescheitert.
- ☐ Ich habe bereits am _____ bei der Fakultät für _____
  _____
  der Hochschule _____
  unter Vorlage einer Dissertation mit dem Thema _____
  _____
  die Zulassung zur Promotion beantragt mit dem Ergebniss:_____

Die öffentlich zugängliche Promotionsordnung der TUM ist mir bekannt, insbesondere habe ich die Bedeutung von § 28 (Nichtigkeit der Promotion) und § 29 (Entzug des Doktorgrades) zur Kenntnis gennomen. Ich bin mir der Konsequenzen einer falschen Eidestattlichen Erklärung bewusst.

Mit der Aufnahme meiner personenbezogenen Daten in die Alumni-Datei bei der TUM bin ich ☒ einverstanden, ☐ nicht verstanden.

Antonios Stylogiannis München, Monday 1st August, 2022

_____